Machine Learning-Based Classification of Cardiac Diseases Using Spectral and Non-linear Analysis of Electrocardiogram Signals

Henok Mezemr Besfat

A Ph.D. Dissertation Submitted to the Department of Electronics and Communication Engineering

College of Electrical Engineering and Computing

Presented in Partial Fulfillment of the Requirement for the Degree of Doctor of Philosophy in Electronics and Communication Engineering

Office of Graduate Studies

Adama Science and Technology University

June, 2025

Adama, Ethiopia

Machine Learning-Based Classification of Cardiac Diseases Using Spectral and Non-linear Analysis of Electrocardiogram Signals

Henok Mezemr Besfat

Main Supervisor: **Dr. Demissie Jobir Gelmecha**

Co-supervisor: **Dr. Ram Sewak Singh**

A Dissertation Submitted to the Department of Electronics and Communication Engineering

College of Electrical Engineering and Computing

Presented in Partial Fulfillment of the Requirement for the Degree of Doctor of Philosophy in Electronics and Communication Engineering

Office of Graduate Studies

Adama Science and Technology University

June, 2025

Adama, Ethiopia

DECLARATION

I hereby declare that this Dissertation entitled *"**Machine Learning-Based Classification of Cardiac Diseases Using Spectral and Non-linear Analysis of Electrocardiogram Signals**"* is my original work. That is, it has not been submitted the award of any academic degree, diploma or certificate in any other university. All sources of materials used for this dissertation have been duly acknowledged through appropriate citations.

Name of Student	Signature	Date

RECOMMENDATION

We, the supervisors of this dissertation, hereby certify that we have read the dissertation entitled *"**Machine Learning-Based Classification of Cardiac Diseases Using Spectral and Nonlinear Analysis of Electrocardiogram Signals**"* prepared under our guidance by **Henok Mezemr Besfat** submitted in partial fulfillment of the requirements for the degree of Doctor of Philosophy in Electronics and Communication Engineering. Therefore, we recommend the submission of the dissertation to the department for further review and defense.

Major Supervisor	Signature	Date
Co-supervisor	Signature	Date

APPROVAL PAGE

We here by certify that the recommendation and suggestions made by the board of examiners are appropriately incorporated into the final version of the dissertation entitled ***"Machine Learning-Based Classification of Cardiac Diseases Using Spectral and Non-linear Analysis of Electrocardiogram Signals"*** by **Henok Mezemr Besfat**.

Major Supervisor	Signature	Date
Co-supervisor	Signature	Date

We, the undersigned, members of the Board of Examiners of the dissertation open defense by **Henok Mezemr Besfat** have read and evaluated the dissertation entitled ***"Machine Learning-Based Classification of Cardiac Diseases Using Spectral and Non-linear Analysis of Electrocardiogram Signals"*** and examined the candidate during open defense. This is, therefore, to certify that the dissertation is accepted for partial fulfillment of the requirement of the degree of Doctor of Philosophy in Electronics and Communication Engineering.

Chairperson	Signature	Date
Internal Examiner 1	Signature	Date
Internal Examiner 2	Signature	Date
External Examiner 1	Signature	Date
External Examiner 2	Signature	Date

Finally, approval and acceptance of the dissertation is contingent upon submission of its final copy to the Office of Postgraduate Studies (OPGS) through the candidate's Department Graduate Council (DGC) and College Graduate Committee (CGC).

Department Head	Signature	Date
College Dean	Signature	Date
Office of Postgraduate Studies, Dean	Signature	Date

ACKNOWLEDGMENTS

First and foremost, I would like to express my heartfelt gratitude to the Almighty God for His unwavering guidance and support throughout my life and this academic journey.

I extend my sincere appreciation to my supervisors, Dr. Demissie Jobir Gelmecha and Dr. Ram Sewak Singh, for their invaluable guidance and insightful feedback, which were instrumental in shaping this dissertation.

I would like to express my sincere gratitude to the Department of Electronics and Communication Engineering and all the staff members at the College of Electrical Engineering and Computing (CoEEC) for their encouragement throughout my research journey.

I would also like to acknowledge Dr. Rajaveerapa Devadoss for his dedication in teaching numerous courses and for generously sharing his knowledge without hesitation. I am grateful to my P.hD classmates and friends for their brotherhood. I would like to express my appreciation to Mr. Zewdu Burusa for creating a conducive environment in the lab, which greatly facilitated my research.

I am profoundly grateful to my parents, Liqe Mezemran Mezemr Besfat and Ms. Tinkakie Dinku, for their unconditional love and support during my entire journey. Their encouragement has been a constant source of motivation.

A special thanks goes to my uncle, Mr. Siseraw Dinku, for his steadfast support in my education.

I also wish to thank my sister, Ms. Meaza Mezemr, and my brother, Mr. Andinet Mezemr, for their encouragement and support.

Additionally, I would like to thank all the staff and community at Adama Science and Technology University for their assistance and support.

I am truly thankful to Adama Science and Technology University for providing me with this opportunity to pursue my studies. Lastly, I extend my gratitude to my sponsor, Woldia University, for their support in making this academic endeavor possible.

Thank you all for being a part of this journey.

TABLE OF CONTENTS

DECLARATION i

RECOMMENDATION ii

APPROVAL PAGE iii

APPROVAL OF BOARD OF REVIEWERS v

ACKNOWLEDGMENTS vi

LIST OF TABLES xii

LIST OF FIGURES xiv

ACRONYMS xviii

ABSTRACT xx

CHAPTER 1: INTRODUCTION 1

1.1 Background of the Study . . . 1
1.2 Motivation for the Study . . . 2
1.3 Statement of the Problem . . . 3
1.4 Objectives of the Study . . . 4
1.4.1 General Objective . . . 4
1.4.2 Specific Objectives . . . 4
1.5 Research Questions . . . 5
1.6 Contributions of the Study . . . 5
1.7 Significance of the Study . . . 6
1.8 Delimitation Scope . . . 7
1.9 Framework of the Study . . . 8
1.10 Organization of the Dissertation . . . 8

CHAPTER 2: LITERATURE REVIEW 11

2.1 Introduction . . . 11
2.1.1 The Heart and Its Function . . . 11
2.1.2 The Electrocardiogram Signal . . . 13
2.1.3 Heart Rate Variability and Frequency Components . . . 15
2.1.4 Arrhythmia . . . 17
2.1.4.1 Atrial Arrhythmia . . . 18

2.1.4.2 Ventricular Arrhythmia . . . 19
2.1.4.3 Myocardial Infarction . . . 19
2.1.4.4 Atrioventricular Block . . . 19
2.1.4.5 Coronary Artery . . . 20
2.1.4.6 Congestive Heart Failure . . . 20
2.1.5 Methods for Analysis of Heart Rate Variables Signals . . . 20
2.2 Detection of QRS Complex and Denoising of ECG Signal . . . 22
2.3 Spectral and Non-linear Analysis Methods for the Classification of Cardiac Diseases in Heart Rate Variability Signals . . . 34
2.4 Current Status of Machine Learning Techniques for Classification of Cardiac Diseases . . . 48
2.5 Summary of Literature Review . . . 56

CHAPTER 3: DELINEATION OF QRS FEATURES AND DENOISING OF ECG SIGNAL 58
3.1 Introduction . . . 58
3.2 Materials and Methods . . . 60
3.2.1 Materials . . . 60
3.2.2 Methods . . . 60
3.2.2.1 Maximal Overlap Discrete Wavelet Transform . . . 60
3.2.2.2 Pre-processing . . . 63
3.2.2.3 R-peak Detection . . . 64
3.3 Performance Evaluation . . . 66
3.4 Result and Discussion . . . 66
3.4.1 MIT/BIH database . . . 66
3.4.2 QTDB Database . . . 67
3.4.3 TWADB Database . . . 70
3.5 Summary . . . 73

CHAPTER 4: NON-STATIONARY SPECTRAL AND COHERENCE INVESTIGATION OF CARDIOVASCULAR SIGNALS 75
4.1 Introduction . . . 75
4.2 Material and Methods . . . 78
4.2.1 Database . . . 78
4.2.2 Pre-processing . . . 78
4.2.3 Energy Concentration-Based Optimization of Gaussian Window Reassignment for Time-Frequency Analysis, and Its Application in Analyzing the Non-Stationary Spectral and Coherence of Cardiovascular Signals 80

4.2.3.1 Time-Frequency Analysis . . . 80
4.2.3.2 Reassignment Method . . . 80
4.2.3.3 The Proposed Window . . . 83
4.2.3.4 Optimization Methodology to Select Optimal Parameters . . . 83
4.2.3.5 Non-Stationary Spectral Coherence (NSSC) . . . 84
4.2.3.6 Statistical Analysis . . . 85
4.3 Result and Discussion . . . 85
4.3.1 Result . . . 85
4.3.1.1 Synthetic Test Signals/ Experimental Results . . . 85
4.3.1.2 Robustness Against Noise . . . 92
4.3.1.3 Application on Non-stationary Signals: Spectral Analysis of HRV Signal . . . 95
4.3.1.4 Time-Frequency Coherence Analysis of Cardiovascular Signal/ Simulation Results . . . 96
4.3.2 Discussion . . . 100
4.4 Summary . . . 101

CHAPTER 5: MULTISCALE ENTROPY- DRIVEN MULTI- CLASSIFICATION OF MYOCARDIAL INFARCTION DISEASES BASED ON OPTIMIZED MODIFIED STOCKWELL TIME- FREQUENCY TRANSFORM AND MACHINE LEARNING MODELS 102
5.1 Introduction . . . 102
5.2 Materials and Methods . . . 106
5.2.1 Datasets . . . 106
5.2.2 Pre-processing . . . 107
5.2.3 Proposed Method . . . 107
5.2.4 The Proposed Optimized Modified Stockwell Transform . . . 109
5.2.5 Feature Extraction . . . 110
5.2.5.1 Multiscale-Ap Entropy . . . 112
5.2.5.2 Multiscale-Sample Entropy . . . 113
5.2.5.3 Multiscale-EnoEn Entropy . . . 114
5.2.5.4 Multiscale-Incr Entropy . . . 114
5.2.5.5 Multiscale-Phase Entropy . . . 115
5.2.6 Support Vector Machine . . . 117
5.2.7 Bayesian Optimization Algorithm . . . 117
5.2.8 Adaptive K-Nearest Neighbors . . . 118
5.2.9 Random Forest . . . 118

5.2.10 Extreme Learning Machine . . . 119
5.2.11 Decision Tree . . . 119
5.2.12 Naïve Bayes Model . . . 120
5.3 Result and Discussion . . . 121
5.3.1 Result . . . 121
5.3.2 Discussion . . . 131
5.4 Summary . . . 133

CHAPTER 6: AUTOMATED CLASSIFICATION OF INFERIOR WALL MYOCARDIAL INFARCTION BASED ON TSALLIS ENTROPY AND OPTIMIZED BLOCK LENGTH OF OSELM 134
6.1 Introduction . . . 134
6.2 Materials and Methods . . . 136
6.2.1 Datasets . . . 136
6.2.2 Pre-processing . . . 136
6.2.3 Proposed Method . . . 136
6.2.4 Stationary Wavelet Transform . . . 138
6.2.5 Feature Extraction . . . 141
6.2.6 Tsallis Entropy . . . 141
6.3 Classification . . . 141
6.3.1 Optimum Block Length Online Sequential Extreme Learning Machine . 142
6.4 Result and Discussion . . . 143
6.5 Summary . . . 149

CHAPTER 7: LAYER- FUSION CONVOLUTIONAL NEURAL NETWORK AND MACHINE LEARNING MODEL FOR AUTOMATED CLASSIFICATION OF CAD AND CHF CARDIAC DISEASES 150
7.1 Introduction . . . 150
7.2 Materials and Methods . . . 151
7.2.1 Dataset . . . 151
7.2.2 Pre-processing . . . 153
7.2.3 Deep CNN . . . 155
7.2.4 The Concept of Layer-fusion 1D CNN . . . 155
7.2.5 The structure of 1D-CNN Algorithm . . . 157
7.2.6 Model Training Process . . . 158
7.2.7 Performance Evaluation . . . 159
7.3 Result and Discussion . . . 160
7.3.1 Result . . . 160

7.3.2 Discussion 169
7.4 Summary 170

CONCLUSIONS AND RECOMMENDATIONS **171**

Research Contribution **174**

REFERENCES **176**

LIST OF TABLES

Table 2.1 A summery of various techniques for the detection of QRS in the ECG signal 30
Table 2.2 Cont. . . QRS detection . . . 31
Table 2.3 Cont. . . QRS detection . . . 32
Table 2.4 Cont. . . QRS detection . . . 33
Table 2.5 List of major cardiovascular disease types and a description of each type . . . 35
Table 2.6 A summery of time, spectral, time-frequency, and non-linear analysis of HRV and ECG signals . . . 43
Table 2.7 Cont. . . linear and non-linear analysis . . . 44
Table 2.8 Cont. . . linear and non-linear analysis . . . 45
Table 2.9 Cont. . . linear and non-linear analysis . . . 46
Table 2.10 Cont. . . linear and non-linear analysis . . . 47
Table 2.11 A summery of machine and deep learning models in classification of cardiovascular disease . . . 52
Table 2.12 Cont. . . ML classification . . . 53
Table 2.13 Cont. . . ML classification . . . 54
Table 2.14 Cont. . . ML classification . . . 55
Table 2.15 Performance measures employed in the literature to evaluate and compare the results of various methods . . . 57

Table 3.1 Evaluation of our QRS algorithm for mitdb databases . . . 67
Table 3.2 Evaluation of our QRS algorithm for QTDB databases . . . 69
Table 3.3 Evaluation of our QRS algorithm for aftdb databases . . . 69
Table 3.4 Comparison for mitdb database . . . 72
Table 3.5 Comparison for qtdb database . . . 72
Table 3.6 Comparison for twadb database . . . 72
Table 3.7 Comparison for FANTASIA database . . . 73
Table 3.8 Comparison for AFTDB database . . . 73
Table 3.9 Summary of the proposed work for five database results . . . 73

Table 4.1 PSO parameters for the proposed OptGWRS technique . . . 84
Table 4.2 Mathematical Formulation of STFT, OptADMST, SST, SET, RS, and OptGWRS Techniques . . . 86
Table 4.3 Rényi Entropy of different TFA . . . 89
Table 4.4 Optimized parameters obtained by the proposed method . . . 90
Table 4.5 Maximum energy concentration (Noise free) . . . 91
Table 4.6 Maximum energy concentration ($SNR = 0dB$) . . . 91

Table 4.7 Maximum energy concentration ($SNR = 5dB$) . . . 91
Table 4.8 Computational time (in sec) of different TF techniques (*(**Bold** face indicates better result)*) . . . 92
Table 4.9 Renyi Entropy value at SNR = 5 dB . . . 92
Table 4.10 Renyi Entropy value at SNR = 0 dB . . . 92
Table 4.11 Results of NSSS in low and high frequency band among CAV signals of each class of subjects . . . 100

Table 5.1 Results of optimization parameter measures, Energy concentration and Renyi entropy values for Modified ST with and without the application of EC based-PSO optimization . . . 121
Table 5.2 Weights for the top ten features (the top ranks indicated in descending order) 122
Table 5.3 Calculated mean and std value for the top ten features and eleven arrhythmia groups . . . 124
Table 5.4 P-value for the top ten features and ten arrhythmia groups relative to HC group (**Bold** face indicates not significant features) . . . 124
Table 5.5 Simulation results of various ML models and the proposed model . . . 125
Table 5.6 Computational time required by the different MLs . . . 131
Table 5.7 Comparison of various DL and ML methods for classification of MI arrhythmias 132

Table 6.1 Comparative outcomes for the top 10 features of NR-MI dataset . . . 146
Table 6.2 The Result of the proposed technique with GDA and different activation function (the bold face indicate higher performance at optimal block length) . . . 146
Table 6.3 Comparative analysis of a proposed method for MI classification using ECG signals from the PTB Database . . . 148

Table 7.1 Details of each layer's parameters of the proposed 1D-CNN architecture . . . 158
Table 7.2 AUC-ROC value . . . 163
Table 7.3 Results of the proposed model (**Bold** face- indicates higher performance) . . . 165
Table 7.4 Comparison of existing literature in classification of CAD and CHF arrhythmias 167

LIST OF FIGURES

Figure 1.1 Framework of the proposed approach for the study 9

Figure 2.1 Anatomy of Heart (the arrows indicate the directions of the blood flow into and out of the heart) (Tripathi et al., 2021). 12
Figure 2.2 The basic component of ECG signal for a healthy individual heart (Sörnmo and Laguna, 2005). 14
Figure 2.3 Various examples of sinus rhythms (Soria, 2012). 19
Figure 2.4 The typical MI ECG signal 20
Figure 2.5 The typical CAD ECG signal 20
Figure 2.6 The typical CHF ECG signal 21
Figure 2.7 Structure of the QRS detection 29
Figure 2.8 Structure of the spectral and non-linear analysis of HRV signal 39
Figure 2.9 Structure of the data pre-processing and machine learning model application in classification of cardiovascular diseases 51

Figure 3.1 Decomposition of signal up to $7^{th} level$ 62
Figure 3.2 a) Decomposition of signal by MOWDT, b) Reconstruction of signal by IMODWT 63
Figure 3.3 Block diagram of the proposed work 65
Figure 3.4 (a) Origional ECG signal, (b) decomposed by MOWDT, (c) reconstructed by IMOWDT, (d) ECG denoising (e) R-peak detection for record 111 in MITDB database 68
Figure 3.5 (a) Origional ECG signal, (b) decomposed by MOWDT, (c) reconstructed by IMOWDT, (d) ECG denoising (e) R-peak detection for record sel231 in QTDB database 70
Figure 3.6 (a) Origional ECG signal, (b) decomposed by MOWDT, (c) reconstructed by IMOWDT, (d) ECG denoising (e) R-peak detection for record twa06 in TWADB database 71

Figure 4.1 Framework of the proposed work 77
Figure 4.2 (a) IBI with ectopic beat, (b) IBI after detrending and ecotopic replacement, (c) IBI after resampling 79
Figure 4.3 Proposed block diagram of Optimized Gaussian Window Reassignment TF technique 81
Figure 4.4 Simulation of Synthetic signal $S_1(t)$ (a) Time domain waveform, (b) Instantaneous frequency 86

Figure 4.5 NSS of (a) STFT, (b) OptADMST, (c) SST, (d) SET, (e) RS, (f) OptGWRS of signal $S_1(t)$ . . . 87
Figure 4.6 Simulation of Synthetic signal $S_2(t)$ (a) Time domain waveform, (b) Instantaneous frequency . . . 89
Figure 4.7 Simulation of Synthetic signal $S_3(t)$ (a) Time domain waveform, (b) Instantaneous frequency . . . 89
Figure 4.8 NSS of (a) STFT, (b) OptADMST, (c) SST, (d) SET, (e) RS, (f) OptGWRS of signal $S_2(t)$ . . . 90
Figure 4.9 NSS of (a) STFT, (b) OptADMST, (c) SST, (d) SET, (e) RS, (f) OptGWRS of signal $S_3(t)$ . . . 91
Figure 4.10 NSS of (a) STFT, (b) OptADMST, (c) SST, (d) SET, (e) RS, (f) OptGWRS of signal $S_1(t)$ (SNR = 0dB) . . . 93
Figure 4.11 NSS of (a) STFT, (b) OptADMST, (c) SST, (d) SET, (e) RS, (f) OptGWRS of signal $S_2(t)$ (SNR = 0dB) . . . 93
Figure 4.12 NSS of (a) STFT, (b) OptADMST, (c) SST, (d) SET, (e) RS, (f) OptGWRS of signal $S_3(t)$ (SNR = 0 dB) . . . 94
Figure 4.13 Original CAV signals (a) Heart rate variability, (b) RESP, (c) Arterial pressure interval variability, (d) SABPV . . . 95
Figure 4.14 Spectrum of (a) Heart rate variability, (b) RESP, (c) APIV, (d) systolic arterial BP variability . . . 96
Figure 4.15 NSS maps of cardiovascular signals of a healthy young subject, estimated by OptGWRS row 1 (a - d), by RS, row 2 (e - h) and by SST, row 3 (i - j). 1^{st}, 2^{nd}, 3^{rd}, and 4^{th} columns indicate the spectrum of heart rate variability, RESP, arterial pressure interval variability, and systolic arterial BP variability . . . 97
Figure 4.16 NSSC among HRV and RESP (column-1), HRV and APIV (column-2) and HRV and SABPV (column-3) evaluated by OptGWRS ((row 1), by RS (row 2) and by SST (row 3) . . . 98
Figure 4.17 Strength of Coh(t) evaluated by OptGWRS among HRV and SABPV (row 1), HRV and RESP (row 2) and HRV and APIV (row 3), evaluated in low frequency range (column-1 & 3 for yng and eldy subjects, respectively), and high frequency band (column-2 & 4 for yng and eldy subjects, respectively). 99

Figure 5.1 The proposed framework for analysis of HC and MI classification based on NB, DT, SVM, ELM, A-KNN, BO-SVM, and RF classifiers . . . 106
Figure 5.2 Block diagram of optimized modified Stockwell TF technique using PSO algorithm . . . 108

Figure 5.3 ECG plot of eleven arrhythmias: 1st column indicates time domain plot, 2nd column denotes the respective TF plot based on Modified ST, and 3rd column represent the TF plot based on optimized modified ST. (1st row- HC (DS:0), 2nd row- AMI (DS:1) 3rd row- ALMI (DS:2), 4th row- ASMI (DS:3), 5th row- IMI (DS:4), 6th row- ILMI (DS:5), 7th row- IPMI (DS:6), 8th row- IPLMI (DS:7), 9th row- LMI (DS:8), 10th row- PMI (DS:9),11th row- PLMI(DS:10)) subjects, respectively. ***(DS: indicates dataset).*** 111
Figure 5.4 TF spectrum of an ASMI subject (a) without optimization and (b) with the application of optimization based on energy concentration 112
Figure 5.5 Box plot of top ten features for eleven MI arrhythmias 123
Figure 5.6 KNN accuracy for different K values 129
Figure 5.7 Confusion matrix representation of A-KNN classifier 129
Figure 5.8 Objective function model for the BO-SVM classifier 129
Figure 5.9 Confusion matrix representation of BO-SVM classifier 129
Figure 5.10 Confusion matrix representation of RF classifier 130

Figure 6.1 ECG wave form of IMI and Normal dataset for Lead II (a & d), Lead III (b & e), and Lead AVF (c & f), respectively 137
Figure 6.2 The proposed methodology for analysis of IMI classification based on OBLOSELM classifier 138
Figure 6.3 Six level decomposition using SWT 139
Figure 6.4 Box plot for the top 10 features for NR-MI dataset before reduction by GDA (*N-indicate normalized value, TSA- Tsallis entropy, A-approximate, D- detail, the first 2- indicate squared signal* $X^2[n]$*, the last number indicate decomposition level*) 144
Figure 6.5 Box plot after feature reduction by the GDA with a) Gaussian b) RBF function for NR-MI dataset 144
Figure 6.6 Variation of a) Ac, b) Sp, c) Se, and d) ppv - with number of hidden nodes and block length for OSELM sigmoid activation function and GDA with RBF kernel (**CHNs**-Contributing Hidden Nodes) 145

Figure 7.1 The framework of proposed block diagram for fusion of time-spectral features with 1D-CNN and classification of cardiac diseases with ML 152
Figure 7.2 Plot of (a) Original HRV signal (b) HRV signal with ectopic beat, (c) HRV signal after ectopic beat replacement for a NR subject 153
Figure 7.3 Plot of the time-series and spectral domain for HRV signal (1^st, 2^nd and 3^rd row indicate Normal, CAD, and CHF subjects, column 1 represents the time domain plot and column 2 indicates the corresponding FFT plot) 154
Figure 7.4 The structure of 1D-CNN architecture 157

Figure 7.5 Box plot of the HRV time-series features 160
Figure 7.6 Box plot of the HRV spectral features 161
Figure 7.7 Feature visualizations of (a) The raw input time-series data and (b) After fusion - based on t-SNE 162
Figure 7.8 Performance of the LF-CNN (a) Train and validation accuracy score, (b) Training and validation losses per epoch 162
Figure 7.9 Roc curve of (a) Spectral feature, (b) the LF-CNN model for three arrhythmia classes 164
Figure 7.10 Confusion matrix for (a) Spectral feature of 1DCNN, (b) LF-CNN classification 164
Figure 7.11 Optimized SVM Objective function model for (a) Spectral feature, (b) LF-CNN classification 166
Figure 7.12 Confusion matrix of (a) Spectral feature, (b) Time-spectral features for BO-SVM classifier (**0 - NR, 1 - CAD, and 2 - CHF subjects*) 166
Figure 7.13 Confusion matrix of (a) Spectral feature, (b) Time-spectral features for KNN classifier 167

ACRONYMS

A-KNN	Adaptive K-Nearest Neighbors
AFTDB	AF Termination Challenge Database
ANS	Autonomic Nervous System
APIV	Arterial Pressure Interval Variability
AV	Atrioventricular
BO-SVM	Bayesian Optimization SVM
CAD	Coronary Artery Disease
CHF	Congestive Heart Failure
CVDs	Cardiovascular Diseases
DT	Decision Tree Classifier
ECG	Electrocardiogram
ELM	Extreme Learning Machine
FK	Fejer-Korovkin
FT	Fourier Transform
GDA	Generalized Discriminant Analysis
HRV	Heart Rate Variability
LF-CNN	Layer Fusion Convolutional Neural Network
MI	Myocardial Infarction
MIs	Myocardial Infarctions
MIT/BIH	Massachusetts Institute of Technology/Beth Israel Hospital
ML	Machine Learning
MODWT	Maximal Overlap Discrete Wavelet Transform
MS-ApEn	Multi-scale Approximate entropy
MS-EnoEn	Multi-scale Entropy of entropy
MS-IncEn	Multi-scale Increment entropy
MS-PhasEn	Multi-scale Phase entropy
MS-SampEn	Multi-scale Sample entropy

NB	Naive Bayes
NSR	Normal Sinus Rhythm
NSSC	Non-Stationary Spectral Coherence
OBLOSELM	Optimized Block Length Online Sequential-Extreme Learning Machine
OptGWRS	Optimized Gaussian Window Reassignment
OptMST	Optimized Modified Stockwell Transform
PSO	Particle Swarm Optimization
QTDB	QT Database
RF	Random Forest
SA	Sinoatrial
SABPV	Systolic Arterial Blood Pressure Variability
SCD	Sudden Cardiac Disease
STFT	Short Time Fourier Transform
SVM	Support Vector Machine
SWT	Stationary Wavelet Transform
t-SNE	t-distributed Stochastic Neighbor Embedding
TSAEn	Tsallis entropy
TWADB	T-Wave Alternans Database
WHO	World Health Organization

ABSTRACT

Cardiovascular Diseases (CVDs) are one of the leading health challenges worldwide. According to the World Health Organization (WHO) report, the latest global health estimates indicate that CVDs account for approximately 32% of all deaths globally, resulting in around 17.9 million fatalities annually. Among these deaths, Myocardial Infarction (MI), Coronary Artery Disease (CAD), and Congestive Heart Failure (CHF) present particularly severe outcomes, often occurring without warning and serving as leading causes of death. Most CVDs can be alleviated or prevented if detected and treated in their early stages. Therefore, advancing investigative methods such as spectral and nonlinear, particularly those driven by machine learning, could significantly enhance individual health.

Detecting R peaks within the QRS complex of the Electrocardiogram (ECG) signal is pivotal for accurately diagnosing heart conditions. However, denoising ECG signals and accurately detecting R peaks present significant challenges due to various noise factors such as baseline wander, motion artifacts, muscle contraction noise and power line interference. To address these challenges, this study proposed an efficient R peak detection technique that leverages the Maximal Overlap Discrete Wavelet Transform (MODWT) in combination with the Fejer-Korovkin (FK) wavelet function. The simulation result has shown that the proposed method achieved a sensitivity (Se) of 99.97%, a Positive Prediction (PP) rate of 99.64%, a low Detection Error Rate (DER) of 0.04 for T-Wave Alternans Database (TWADB) and a Se of 99.95%, a PP rate of 99.99%, and an extremely low DER of 0.063 for QT Database (QTDB). After R-peak detection, this study has been extended to Heart Rate Variability (HRV) signal analysis using spectral methods. The non-stationary nature of HRV signals necessitates the adoption of time-frequency methodologies that can capture and portray the temporal changes in frequency components. Further investigating the intricate relationship between cardiovascular signals, including HRV, respiratory (RESP), Systolic Arterial Blood Pressure Variability (SABPV), and Arterial Pressure Interval Variability (APIV) of healthy Young and Elderly subjects to understand cardiovascular control. This study proposed an Optimized Gaussian Window Reassignment (OptGWRS) Time Frequency (TF) technique to capture the characteristics of these signals. The parameters of the Gaussian window are optimized using a Particle Swarm Optimization (PSO) algorithm to maximize the energy concentration of signals in the TF domain. The simulation results have shown that Non-Stationary Spectral Coherence (NSSC) ranges between the HRV and APIV signals in the low frequency band have been significantly reduced ($p=0.000001$) in the elderly group when compared to the young group. In the LF band, the NSSC among HRV and RESP signals have not been influenced by ageing and in the HF band, it is significantly reduced in the elderly compared to the young group ($p =0.0125$).

For Myocardial Infarctions (MIs) detection, the low amplitude and short duration of ECG sig-

nals pose diagnostic challenges. To address these challenges, this study proposed an automated multi-classification model integrating Optimized Modified Stockwell Transform (OptMST), Multi-scale Entropies (MSEns) and Machine Learning (ML) techniques, such as Naive Bayes (NB), Support Vector Machine (SVM), Extreme Learning Machine (ELM), Adaptive K-Nearest Neighbors (A-KNN), Bayesian Optimization SVM (BO-SVM), and Random Forest (RF) to classify ten MI types and healthy controls. Initially, the ECG signal is subjected to OptMST up to four levels of frequency band decomposition. Subsequently, five non-linear features, such as Multi-scale Approximate entropy (MS-ApEn), Multi-scale Sample entropy (MS-SampEn), Multi-scale Entropy of Entropy (MS-EnoEn), Multi-scale Increment Entropy (MS-IncEn), and Multi-scale Phase Entropy (MS PhasEn) are extracted in each frequency band of OptMST coefficients. After this, the ReliefF ranking algorithm is employed to select the top ten features out of twenty, aiming to enhance predictive performance, improve computational efficiency, and reduce the risk of over-fitting of ML. The simulation results demonstrated that the highest classification performance has been achieved by the RF model with an accuracy (Ac) of 98.44%, a recall of 94.6%, a Specificity (Sp) of 98.93%, a Precision (Pr) of 94.67%, and a F-score of 94.62%. Expanding our scope to broader cardiac conditions, a hybrid intelligence system combining Layer Fusion Convolutional Neural Network (LF-CNN) with ML techniques (BO-SVM, KNN, RF) has been proposed to classify CAD and CHF subjects. Time-series and spectral features from HRV data of CAD and CHF subjects have been utilised, with batch normalisation and t-distributed Stochastic Neighbor Embedding (t-SNE) for feature fusion and visualisation. The simulation results demonstrated that the hybrid model achieved an Ac of 99.88%, a Pr of 99.89%, a recall of 99.68%, and an F1-score of 99.79%. This study can advance cardiovascular diagnostics by integrating signal processing with ML, from MODWT-based R peak detection to hybrid LF-CNN-ML systems. These proposed approaches can enhance early identification and classification of cardiac conditions, offering clinicians powerful tools to improve patient outcomes across the CVDs spectrum.

KEY WORDS: *Optimised Modified Stockwell Transform, Deep Convolution Neural Network, Heart Rate Variability, Non-linear analysis, cardiovascular disease classification, machine learning models.*

CHAPTER 1
INTRODUCTION

1.1 Background of the Study

The expenditure on health-related issues in numerous countries' populations is experiencing significant growth, primarily driven by Cardiovascular diseases (CVDs) such as arrhythmia and heart failure, which remain a leading cause of mortality (Singh et al., 2018d). According to the World Health Organization (WHO) report, an alarming number of individuals, approximately 17.9 million people, affected by cardiovascular diseases each year on a global scale, with heart attacks and strokes being the leading causes (Martin et al., 2025; Organization, 2015). A significant portion, approximately one third, of these fatalities tragically transpire prematurely in individuals who are below the age of 70 (Benjamin et al., 2018). The impact of these diseases on both men and women in low-income countries (Yusuf et al., 2014; Prabhakaran et al., 2005), including Ethiopia, is proportionately higher and seems to be even greater compared to middle and high-income countries. Early detection and prevention of heart diseases is the invaluable task that must be done before getting in to a series problem.

Most of deaths caused by CVDs happen all of a sudden, beginning with a ventricular fibrillation which prompts a heart failure known as Sudden Cardiac Disease (SCD). The National Health and Nutrition Examination Survey reported that 20–25% of a sample population above the age of 65 have died due to Congestive Heart Failure (CHF) and 35% of them have suffered from the Coronary Artery Disease (CAD) (Martin et al., 2025). In case of CHF or CAD, plaques and cholesterol accumulates inside the coronary arteries, which imped the flow of blood into heart muscles (Djoussé et al., 2011). Due to this, heart pumping disturbs and may ultimately lead to irregular the heartbeat and hence heart failure (Malik et al., 1996). So, initial stage of CAD and CHF detection is foremost and it needs efficient detection technique and an Electrocardiogram (ECG) or Heart Rate Variability (HRV) Signal analysis methods.

The shift in practical approaches to the expectation of SCD received lot of consideration from leading researchers in recent decades. It was deliberated in numerous works that arrhythmias are responsible for the greater part of the instances of SCD. One essential progress in investigation of arrhythmias was the utilization of long-term recordings and algorithmic techniques to help the cardiologist in recognition of indicative variations in the ECG. The investigation of arrhythmias by novel methods of analysis of the ECG signal is helping us to dissect the heart function. The change of the approaches utilized as part of the investigation of arrhythmias is probably going to help cardiologists in the symptomatic and screening of SCD. The ECG signals, which reflect the electrical activity of the heart, are widely used for diagnosing cardiac

abnormalities. However, the non-stationary nature of ECG signals and the subtle variations associated with different cardiac conditions present notable challenges for traditional analysis methods. This study addresses these challenges by proposing advanced signal processing and machine learning techniques to enhance the classification and interpretation of ECG signals.

The major aim of this study is to improve the performance and efficiency of cardiac abnormality classification through advanced methodologies. The proposed technique integrates multiple pioneering approaches, including time-frequency (TF) analysis, entropy-based feature extraction, and optimized machine learning algorithms. Key contributions of this research include the introduction of a Maximal Overlap Discrete Wavelet Transform (MODWT)-based method for accurate QRS complex detection, validated across five PhysioNet databases, ensuring reliable identification of R-peaks in ECG signals. Additionally, an advanced Non-Stationary Spectral Coherence (NSSC) technique, combined with an optimized Gaussian window reassignment (OptGWRS) method, is proposed to study dynamic relationships between cardiovascular signals such as HRV, blood pressure variability, and respiratory signals. This approach provides insights into Autonomic Nervous System (ANS) regulation and baroreflex sensitivity, particularly highlighting age-related changes in these interactions.

Further, this study introduces an optimized modified Stockwell transform (OptMST) TF method to enhance the resolution of ECG signals in both temporal and spectral domains. By decomposing ECG signals into specific frequency bands, entropy-based features are extracted to capture irregularities and subtle patterns associated with cardiac conditions. To enhance the classification process, a ReliefF ranking algorithm is employed to select the most significant features, reducing redundancy and improving computational efficiency. The study also explores the use of Stationary Wavelet Transform (SWT) and Tsallis entropy (TSAEn) for feature extraction, providing thorough insights into the complexity of ECG data. For the classification, an Optimum block length Online Sequential Extreme Learning machine (OBLOSELM) is proposed, which selects the optimal length to enhance the model performance.

Additionally, a deep convolutional neural network (CNN) model, including layer fusion features, batch normalization, and the Adam optimizer, is proposed to classify conditions such as healthy, CAD, and CHF. The integration of Machine Learning (ML) algorithms such as Bayesian-Optimized Support Vector Machines (BO-SVM), K-nearest Neighbors (KNN), and Random Forests (RF) further enhances classification performance.

1.2 Motivation for the Study

A number of diseases like, Atrial Fibrillation (characterized by lack of P wave), Ventricular Arrhythmias (characterized by longer QRS complex), Ventricular Fibrillation (irregular undu-

lations without QRS complex), Myocardial Infarction (changes in the shape of the T wave), Atrial Flutter (the end of T and beginning of P disappears) (Najarian and Splinter, 2012), CAD, CHF are responsible for higher number of fatalities worldwide. Early and accurate diagnosis is crucial for effective intervention, yet traditional diagnostic methods often face challenges due to the complex and non-stationary nature of cardiac signals. ECG signal analysis remains to be fundamental in CVD detection, but noise interference, low signal amplitudes, and the intricate dynamics of HRV complicate precise interpretation.

Existing techniques for ECG denoising, R peak detection, and arrhythmia classification often lack robustness, which can lead to potential misdiagnoses. Furthermore, conventional time domain and frequency domain analyses do not adequately capture the non-stationary nature of cardiovascular signals, limiting their diagnostic performance. This study is motivated by the growing demand for advanced computational tools that combines signal processing with Artificial Intelligence (AI). By leveraging various transforms, ML, and Deep Learning (DL), this research aimed to develop automated, high-precision systems for the early detection (classification) of CVD, enhancing diagnostic reliability and patient outcomes.

1.3 Statement of the Problem

Cardiovascular diseases such as coronary artery disease, myocardial infraction and heart failure are the leading cause of mortality worldwide. Despite the rising mortality rate attributed to heart illness, it is important to note that this disease remains highly preventable and controllable. Early detection serves as a pivotal factor in improving the recovery prospects of heart disease patients and reducing mortality rates. However, detecting heart diseases in its early stages presents significant challenges due to various factors.

One major challenge is the reliable detection of QRS complexes in the presence of arrhythmias, such as Atrial Fibrillation (AF) or ventricular tachycardia, which alter the shape of the QRS complex. Current methods for detecting R-peaks within the QRS complex are insufficient, necessitating further research to improve performance measures. Additionally, there is a need to explore novel spectral and non-linear features that can accurately capture the dynamics and patterns associated with different cardiac diseases. A new feature extraction methods holds promise in revealing characteristics that can enhance disease characterization.

Machine learning has emerged as a prominent tool for the accurate classification of cardiovascular diseases. However, existing techniques often are not able to achieve high performance due to inappropriate feature selection. Research is required to explore machine learning models that leverage spectral and non-linear analysis for improved classification. Another limitation is the absence of adaptive learning in current models, which struggle to account for changing

ECG patterns.

Furthermore, there is a trade-off between model accuracy and interpretability in artificial intelligence (AI) applications. While DL models such as CNNs achieve high accuracy, their black box nature weakens clinical confidence, as practitioners cannot derive which signal features drive predictions. Existing interpretability methods are also computationally expensive, limiting their practicality.

Frequency domain and time-frequency distribution analysis using Fourier Transform (FT), Short Time Fourier Transform (STFT), Wigner distribution and SPW methods are limited by poor spectrum resolution in Very Low Frequency (VLF), Low Frequency (LF), and High Frequency (HF) range, due to resampling and model misspecification (choosing order). These techniques also do not reduce the noise content of the non-stationary signal. Since these methods are mainly suitable for stationary signals, a technique for spectral and non-linear analysis to extract features from decomposed HRV signals is required.
Based on the recent state of art, the majority of research studies worked on using machine learning such as KNN, SVM, CNN, ANN for automatic classification of cardiovascular diseases. But they have not achieved an accuracy and efficiency level in average of more than 96%, due to inappropriate features. All together, these challenges demonstrate the urgent necessity for an adaptive, interpretable, and clinically-grounded framework that advances beyond conventional CVDs analysis models. A research is required to achieve a better accurate classification by extracting appropriate features from ECG signals.

In this dissertation, a better technique has been developed which can classify cardiovascular diseases more accurately by applying machine learning techniques from spectral and non linear feature decomposition of ECG/HRV signals.

1.4 Objectives of the Study

1.4.1 General Objective

The main objective is to analyse and classify cardiac diseases from spectral and non-linear features using various machine learning techniques.

1.4.2 Specific Objectives

- To develop an efficient spectral method for detection of QRS complexes of ECG signal with reliability in the presence of arrhythmias.
- To develop an efficient spectral analysis technique for HRV signals for different cardiac diseases.

- To analyse non-linear method for accurately capture the specific dynamics and patterns associated with different cardiac diseases.
- To explore machine learning techniques for better classification of cardiac diseases using spectral features.
- To apply machine learning techniques for better classification of cardiac diseases using non-linear features.
- To compare the performance of spectral and non-linear features ensemble with machine learning.

1.5 Research Questions

This study has addressed the following major research questions:

1. How an efficient signal processing technique be developed to reliably detect QRS complexes in ECG signals, particularly in the presence of noise and arrhythmias?
2. What spectral analysis techniques can be developed or improved to accurately characterize ECG/HRV signals for different cardiac diseases?
3. Which non-linear methods can effectively capture the specific dynamics and patterns associated with different cardiac diseases, and how can these methods be optimized for better diagnostic accuracy?
4. What machine learning approaches are most effective for the classification of cardiac diseases using spectral and non-linear features extracted from ECG/HRV signals?

1.6 Contributions of the Study

In this work, the proposed model has provided better classification performance like accuracy, specificity, sensitivity as compared to existing model. Some of the contributions from this work are:

- The proposed method introduced MODWT based detection of QRS complex, and validated on across five physionet databases, ensures accurate identification R-peakes in the ECG signal.

- A NSSC scheme is proposed utilizing an Optimized Gaussian Window Reassignment (OptGWRS) TF technique based on Particle Swarm Optimization (PSO) algorithm to investigate the interaction among HRV, respiratory, Systolic Arterial Blood Pressure Variability (SABPV), and Systolic Arterial Pressure Interval Variability (APIV) signals to understand cardiovascular control and changes in baroreflex sensitivity.

- This study proposed an optimized modified Stockwell transform (S-transform) TF method by extracting five multi-scale entropy measures such as Multi-scale Approximate entropy (MS-ApEn), Multi-scale Sample entropy (MS-SampEn), Multi-scale Entropy of entropy (MS-EnoEn), Multi-scale Increment entropy (MS-IncEn), and Multi-scale Phase entropy (MS-PhasEn) from the decomposed frequency bands of Electrocardiogram (ECG) signals to enhance the resolution of ECG signals in both the temporal and spectral domains. In addition to this, a ReliefF ranking algorithm has been applied to select top ten most relevant features for removing redundant features, improving ML model performance, and reducing computational time. The proposed method's parameters are optimized using PSO algorithm to maximize energy concentration, demonstrating its effectiveness in adapting to variations in individual Myocardial Infractions (MIs) ECG patterns.

- This work presented the use of Stationary Wavelet Transform (SWT) in the decomposition of ECG signals for the classification of Inferior Myocardial Infraction (IMI). A Tsallis entropy (TSAEn) is then employed to extract the features, providing a deeper understanding of the irregularity and complexity inherent in ECG data. Following this, Generalized Discriminant Analysis (GDA) has been applied to reduce the dimensionality of the ranked features. This reduction enhances the efficiency and effectiveness of the analysis, facilitating faster and more accurate processing of ECG signals. Subsequently, the study has proposed an efficient classifier which is based on the Optimized Block Length Online Sequential-Extreme Learning Machine (OBLOSELM) model.

- A layer fusion features based deep CNN model (LF-CNN) has been proposed to effectively extract and fuse features from time-spectral data in classifying Normal, CAD, and CHF. A Rectified Linear Unit (ReLU) activation function, batch normalization, and max pooling layer has been introduced along with the deep CNN model to minimize the computational time of the training , so accelerates the detection speed. To enhance the performance, a machine learning algorithms has been integrated along with the deep CNN, such as BO-SVM, KNN, and RF models.

1.7 Significance of the Study

The significance of the study are stated as follows:

- The Proposed study can assist clinicians in faster identification and diagnosis of patients suffering from cardiac diseases
- Play a vital role in providing early warning information for patients at risk of cardiac diseases by applying early-stage detection
- The applied technique can be used for decreasing the risk of death
- The implementation of this model holds the promise of enhancing clinical decision-making and optimizing the management of cardiac patients by assisting the doctors in taking quick decisions
- Ethiopia is a developing country where many people suffer from cardiac diseases. This study could be beneficial for addressing these health issues in Ethiopia.

1.8 Delimitation Scope

This work has focused on classification of cardiovascular diseases from spectral and non-linear features using machine learning techniques. The specific tasks will mainly focus on: **i)** Detection of R peaks from QRS complex of ECG signal **ii)** Extraction of HRV signals from spectral and non-linear features, separately and **iii)** Classification of cardiac diseases from spectral and non-linear features using ML. The study has focused on:

- Data collection and preprocessing: In the process of data collection and preprocessing, the study aims to collect a diverse range of relevant cardiac data, specifically ECG signals, from a varied group of patients. To ensure the data's quality and reliability, a preprocessing stage will be conducted, focusing on eliminating any unwanted noise or artifacts. This essential step guarantees that the subsequent analysis will be based on clean and accurate input, enabling more precise and meaningful insights for the subsequent analysis
- Feature extraction: Explore spectral analysis techniques, such as wavelet transform to extract meaningful features from the HRV signals. Furthermore, non-linear techniques, like entropy measures, chaos theory, or fractal analysis, will be investigated to capture complex patterns irregularities present in the data.
- ML algorithms: The study will employ a machine learning model to train and classify cardiac data according to the extracted features. By comparing the performance of various algorithms, the study aims to identify the most efficient and accurate approach for classifying cardiac diseases.

1.9 Framework of the Study

The methodology framework presented in this study follows a systematic, multi-stage approach for analyzing cardiovascular signals and detecting cardiac abnormalities. The ECG signal utilized in this thesis has been obtained from Beth Israel Hospital (MIT/BIH) database, QTDB, TWADB, AFTDB, and healthy individuals are taken from Fantasia database for the detection of QRS complex. While, subjects with CAD were obtained from St. Petersburg Institute of Cardiological Technics (Incart), CHF were sourced from the Beth Israel Deaconess Medical Center (BIDMC) congestive heart failure database, and MI data was collected from Physikalisch-Technische Bundesanstalt (PTB) dataset. Similarly, the HRV (R-R interval) was extracted from the ECG signal of the same databases.

For addressing the main objectives of this research work, the process begins with data acquisition from standard PhysioNet databases, followed by signal processing steps including denoising using MODWT, SWT transforms, Flexible Analytic Wavelet Transform (FAWT) and time-frequency analysis through optimized techniques (OptGWRS). The cleaned signals then undergo feature engineering, where both nonlinear features (entropies) and spectral features (LF/HF ratios) are extracted. To enhance model efficiency, dimensionality reduction is performed through feature ranking (such as, Wilcoxon rank-sum test, ReliefF algorithm).

In addition to this, the analysis employs utilization of both machine learning (RF, BO-SVM, A-KNN) and deep learning (LF-CNN) approaches, with optimization via PSO. The framework incorporates validation through standard metrics (accuracy, recall, precision, F1-score) and statistical tests (p-values), ensuring robust performance evaluation. Finally, clinical analysis benchmarks results against existing methods and assesses clinical relevance for real-world applications. This comprehensive pathway integrates signal processing, machine learning, and statistical validation to enable accurate, automated classification of cardiac conditions while maintaining insightfulness for clinical use. For the simulation of the proposed techniques, a MATLAB (version 2023a) and Python software has been employed. The general framework structure of the dissertation is illustrated in Figure 1.1.

1.10 Organization of the Dissertation

The remaining part of the thesis is organized as follows:

Chapter 2 reviews existing techniques for ECG denoising, QRS complex detection, spectral and non-linear feature analysis, and the application of ML models in cardiac disease classification. This section provides critically analyzed gaps in traditional methods and justifies the need for advanced wavelet transforms (MODWT, FAWT, SWT) and hybrid ML/DL models.

Chapter 3 Provides the techniques employed in the delineation of QRS complex and de-

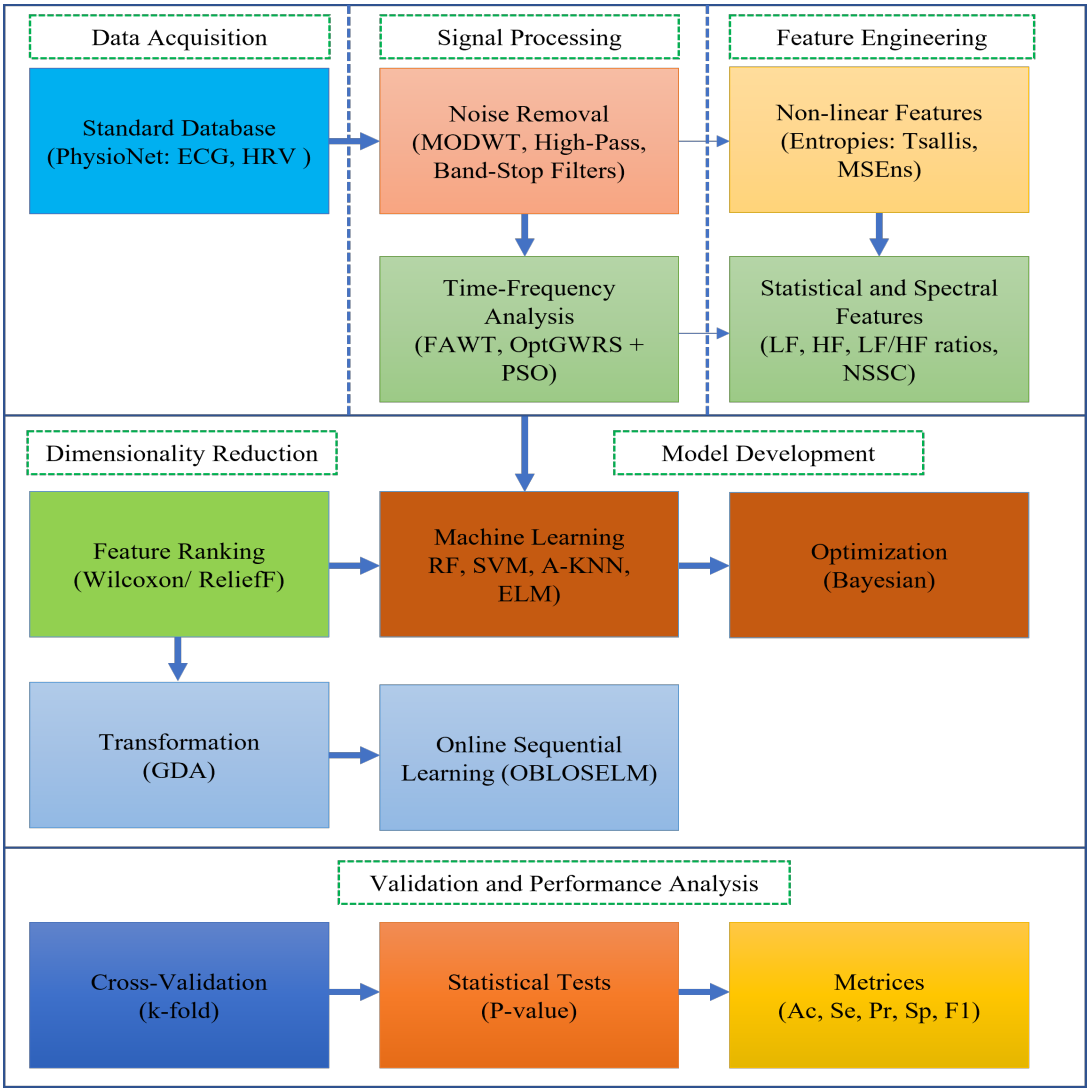

Figure 1.1: Framework of the proposed approach for the study

noising of ECG signal, including DC removal, normalization process, MODWT, and R-peak detection by thresholding adopted from Pan-Tompkins algorithm.

Chapter 4 describes the spectral analysis of healthy young and elderly subjects, and CHF disease utilizing FAWT technique from HRV signal. In addition to this, energy concentration based OptGWRS time-frequency analysis. Its application investigation of the time varying spectral and coherence of cardiovascular signals has been introduced including respiratory, systolic APIV, and SABPV.

Chapter 5 includes the extraction of multi-scale entropy (nonlinear) features, optimized Stockwell time-frequency transform and machine learning models (including, BO-SVM, A-KNN, RF) for the multi-classification of MI diseases.

Chapter 6 presents techniques such as stationary wavelet transform, Tsallis entropy, fea-

ture reduction by GDA, feature selection method utilizing Wilcoxon rank sum test, Fisher score ranking, and OBLOSELM for the automated classification of inferior wall myocardial infraction.

Chapter 7 discusses a hybrid layer fusion convolutional neural network and machine learning framework for the classification of CAD and CHF diseases. The approach involves the leverage of 1-Dimensional (1D)-CNN model for the feature extraction from time-spectral data, ReLU activation function, batch normalization, max pooling layer, Adam optimizer, BO-SVM, KNN, and RF models.

Finally, summarizes key findings and proposes future research directions for real-time deployment.

CHAPTER 2
LITERATURE REVIEW

This chapter reviews the literature on QRS complex detection, spectral and non-linear analysis techniques, and application of machine learning models for classifying various cardiac arrhythmias.

2.1 Introduction

Cardiovascular diseases remains a leading global cause of death and responsible for millions of mortality annually, underscoring the urgent need for early and accurate classification. Traditional diagnostic methods, including coronary angiography, are often invasive and costly, limiting their accessibility. The ECG is a non-invasive tool that records the heart's electrical activity using electrodes. Detecting cardiac abnormalities early through ECG is crucial for reducing worldwide fatalities caused by heart-related conditions.

2.1.1 The Heart and Its Function

Heart is the primary organ of circulatory system in human body located between the lungs in the middle of the chest, responsible for circulating blood through the body (Javeed et al., 2022). The circulatory system, composed of blood vessels, ensures the transportation of blood to and from every corner of the body. As the heart rhythmically beats, it propels the blood throughout the body. This vital fluid carries essential oxygen and nutrients to all organs and tissues, while simultaneously removing unwanted carbon dioxide and waste products, ensuring the overall health and functioning of the body.

The heart performs four main tasks: collecting the blood from all parts of the body that needs to be refined (through veins), pumping it to the lungs, gathering the refined blood from the lungs, and pumping the refined blood back to all parts of the body. As it is shown in Figure 2.1, the heart has four champers (two atria and two ventricles). The two atria are thin-walled chambers that receive blood from the veins. The two ventricles are thick-walled chambers that forcefully pump blood out of the heart. Parts of the heart anatomy include walls, chambers, valves, blood vessels and electrical conduction system.

The heart is composed of three main layers (endocardium, myocardium, and epicardium), has two types of valves (atrioventricular and semilunar), and is regulated by the electrical conduction system, which consists of the sinoatrial and atrioventricular nodes. The human heart is a muscular organ and works as electromechanical pulsatile pump. From the anatomic perspec-

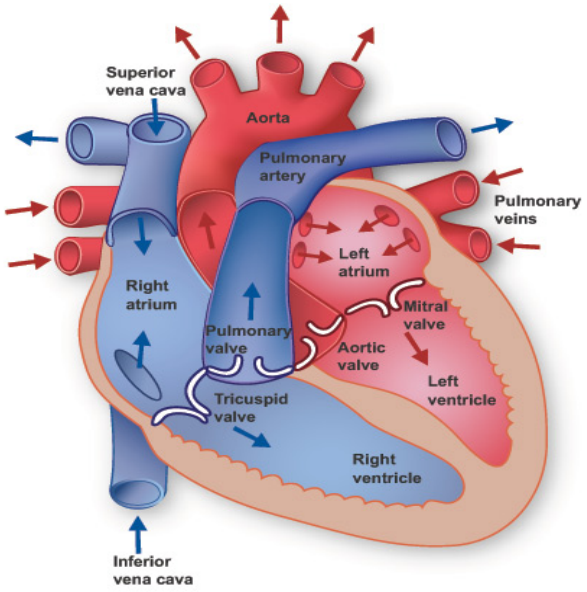

Figure 2.1: Anatomy of Heart (the arrows indicate the directions of the blood flow into and out of the heart) (Tripathi et al., 2021).

tive, as shown in Figure 2.1, there are two separated pumps: one at the right that inflates blood through the lungs organ, and one at the left that inflates blood through the exterior organs. The left pump composed of a left atrium and a left ventricle and the right pump composed of a right atrium and right ventricle. The ventricle is bigger heavy-walled chambers that do most of the work. The atria collect blood from the lungs and venous system and then contract and expel the blood into the ventricle. The ventricle then pumps the blood all through the body or into the lungs (Soria, 2012). There are four valves namely Tricuspid, Mitral, Aortic and Pulmonary valve contained by heart to force the direction of blood. Tricuspid valve links the right ventricle and right atrium. Mitral valve links the left atrium to the left ventricle and has an elliptical orifice. Aortic valve opens between the aorta left and the ventricle (Shah et al., 2009).

The cardiac myocytes have an inimitable capability of automatic electrical impulse generation, which consequence is automatic rhythmicity. An electrical impulse is responsible of the mechanical stimulation of the muscle that provides periodicity of electromechanical pumping of heart. Each cycle is originated by spontaneous generation of an action potential (AP) in the Sino-atrial (SA) node, as it has the fastest electrical impulse generation capability and therefore initiates the heart. The AP is of long duration about 300 ms, which is longer in comparison with the AP of the rest of the cells in the body. The SA node is located by the right atrium nearby the superior vena cava. The electrical impulse, or AP, trekking through both atria and reaching the Atrioventricular (AV) bundle, where is delay by around 0.1s. The AV node transmits the impulse with this delay and spreads over and done with the ventricular myocardium through the AV bundle of His and Purkinje fibres. The delay time permits the atrium to pump blood into the

ventricles. Subsequently, the ventricles are filled with blood and ready to be stimulated. This coordination spreads the electrical impulse from the AV node to the entire ventricular muscle very fast, allowing a synchronized stimulation and subsequently an effective pumping of the blood. This cycle is recurrent up to the decease of the heart. Now we will try to relate the electrical and mechanical behavior of the heart described above.

The activation of the cardiac muscle composed of two phases, contraction and relaxation, or in electrical terms as depolarization and repolarization. As the heart function produces an electrical field, the voltage generated can be recorded by the electrocardiograph from the surface of the body. The heart muscle is equipped with an intricate electrical system that regulates its rhythmic contractions, ensuring the proper circulation of blood throughout the body. However, when this internal electrical signaling is disrupted, it can lead to various abnormalities in heart rate and rhythm. These include accelerated heart rate known as tachycardia, slowed heart rate referred to as bradycardia, or an irregular heartbeat condition called arrhythmia (Singh et al., 2017a).

2.1.2 The Electrocardiogram Signal

The electrocardiogram (ECG) serves as an essential tool for capturing comprehensive cardiac electrical data that provides critical diagnostic information. Clinicians typically perform offline analysis of these recordings, examining the cardiogram to classify different types of cardiac arrhythmias. This essential diagnostic instrument non-invasively records and displays the heart's electrical activity, including both depolarization and repolarization phases, through skin electrodes (Silverman and Willis Hurst, 1992). The electrical activity captured in an ECG results from the sequential processes of depolarization and repolarization of cardiac cells through sodium (Na+) and potassium (K+) ion exchanges (Stanfield et al., 2012). This non-invasive monitoring system captures these electrical potentials at the body surface, acting as a crucial tool for identifying cardiovascular abnormalities. The characteristic waveform morphology and heart rate variability patterns in an ECG provide critical information about cardiac function (Acharya et al., 2007). Deviations from normal rhythm patterns or alterations in waveform characteristics typically indicate arrhythmias, which clinicians can diagnose through careful analysis of ECG recordings (Beheshti et al., 2016). The temporal characteristics and amplitude variations in the P-QRS-T complex of an ECG waveform provide valuable significant diagnostic information about cardiac pathology. Electrocardiographic analysis yields six key clinical insights (Moss and Stern, 1996): i) the position of the cardiac and the relative sizes of its chambers, ii) The source of impulse signals and its propagation pathways. iii) waveform morphology, heart rhythm and conduction abnormalities, iv) location and extent of myocardial ischemia, v) variations in electrolyte levels, and vi) medication effects the cardiovascular system.

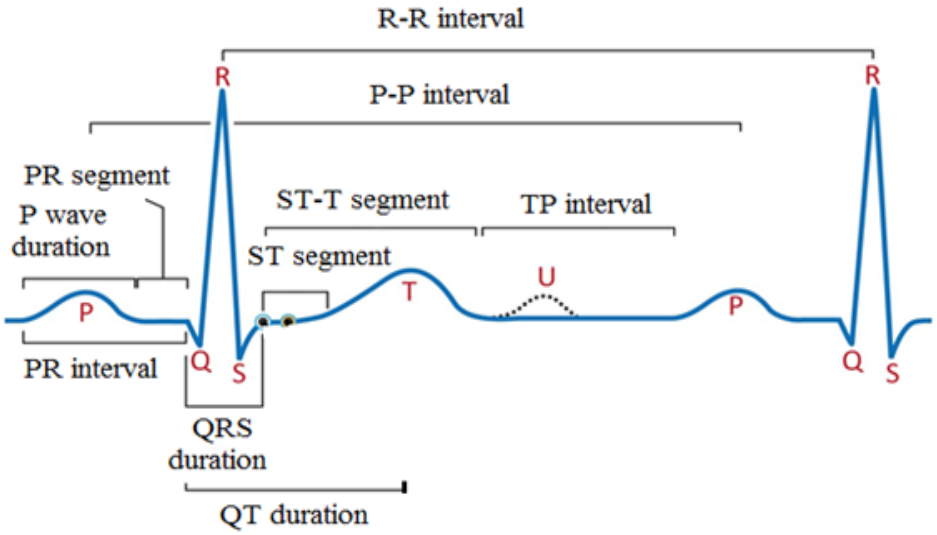

Figure 2.2: The basic component of ECG signal for a healthy individual heart (Sörnmo and Laguna, 2005).

The fundamental components of an ECG waveform are depicted in Figure 2.2. The initial impulse, referred to as the P wave, represents atrial depolarization. This electrical activity originates at the Sinoatrial (SA) node and spreads across both left and right atrial chambers (Sörnmo and Laguna, 2005; Dilaveris et al., 2003). The PR interval (also called PQ interval) indicates the conduction time between atrial and ventricular depolarization. This interval includes a short isoelectric segment known as the PR segment, extending from the end of the P wave to the onset of the QRS complex. The subsequent ventricular depolarization represented as the QRS complex on the electrocardiogram (Durrer, 1968). Significantly, atrial repolarization occurs simultaneously with ventricular depolarization and is consequently masked within the QRS complex. After ventricular depolarization, an isoelectric baseline becomes visible on the ECG tracing. This segment, known as the ST segment, extends from the terminal point of the QRS complex to the onset of the T wave. It represents an electrically inactive period of the cardiac cycle, marking the interval between ventricular depolarization and repolarization. ST segment deviations (either depression or elevation) may indicate signal myocardial injury (Willis Hurst, 1997). The T wave, which signifies ventricular repolarization, consistently appears after the QRS complex. Notably, electrical depolarization occurs before mechanical contraction in the cardiac cycle. Under normal conditions, the T wave should align with the QRS complex polarity and exhibit slight asymmetry. The QT interval signifies the duration from ventricular depolarization onset the completion of repolarization, measured from the start of the Q wave to the end of the T wave (Merritt and Tan, 2012). The duration of this interval varies with

physiological factors including age, gender, and particularly heart rate. Following the T wave, a low-amplitude U wave may appear, reflecting late-phase ventricular repolarization. Notably, the U wave is an inconsistent ECG finding whose absence carries no pathological significance. The U wave becomes more noticeable at lower heart rates (Moss, 1993; Sinha, 2012). For accurate ST segment measurement, the PR segment (not the TP interval) serves as the proper reference point. This baseline reference level represents the heart's isoelectric state between cardiac cycles.

2.1.3 Heart Rate Variability and Frequency Components

Although ECG waveform morphology provides essential diagnostic information, it often proves inadequate for detecting certain cardiac abnormalities (such as CAD) due to subtle variations that are challenging to visually detect. Therefore, advanced signal processing techniques are crucial to extract these intricate electrical patterns from the raw ECG data and it is essential to portray these ECG signals into HRV signals (Hurst, 2006; Acharya et al., 2004).

HRV analysis has emerged as an established methodology with extensive applications in both clinical practice and research domains. This analytical approach offers valuable insights encompassing: (1) Autonomic Nervous System (ANS), (2) cardiovascular risk assessment, (3) diabetic neuropathy evaluation, (4) pharmacological impact studies, and (5) psychological disorder investigations (Acharya et al., 2013; Howorka et al., 2013; Javorka et al., 2008; Salo et al., 1996). HRV quantifies the physiological variation between successive R-R intervals in the QRS complexes of an electrocardiogram. These fluctuations arise from complex interactions between neural regulation and abnormal influences, appearing as distinct rhythmic patterns (Magagnin et al., 2010). HRV dynamics serve as a sensitive indicator of ANS activity, reflecting the continuous interaction between sympathetic (activating) and parasympathetic (inhibitory) modulation of cardiac function.

The sympathetic nervous system exerts its cardiac influence primarily through the neurotransmitters epinephrine and norepinephrine. Released from sympathetic nerve terminals, these catecholamines act directly on the sinoatrial (SA) and atrioventricular (AV) nodes (Reed et al., 2005). Their binding enhances impulse generation at the SA node and accelerates conduction velocity through the AV node, together increasing heart rate. Sympathetic modulation typically manifests over prolonged durations and is quantitatively reflected in the low-frequency (LF) spectral band (0.04-0.15 Hz) of HRV analysis (Akselrod et al., 1981). The spectral power within this band, referred to as LF power (LFp), serves as a measurable indicator of sympathetic activity (Pomeranz et al., 1985). Parasympathetic modulation of cardiac function is facilitated by acetylcholine, a neurotransmitter released from vagal nerve terminals. This cholinergic signaling acts on both the SA and AV nodes, reducing the firing rate of pacemaker cells and

slowing conduction speed, thereby lowering heart rate. Unlike sympathetic effects, parasympathetic influences occur rapidly and are primarily reflected in the high-frequency (HF) spectral band (0.15-0.4 Hz) of HRV. The spectral power within this band (HFp) quantitatively represents vagal tone (Malik et al., 1996). Through power spectral analysis of HRV, the dynamic balance between sympathetic and parasympathetic activity can be evaluated using the LFp/HFp ratio, which serves as an index of autonomic regulation at any given moment (Malpas and Maling, 1990; Scalvini et al., 1998; Sunkaria et al., 2012).

The spectral components of HRV exhibit distinct clustering within specific frequency bands. In healthy individuals, respiratory influences are most notably observed as respiratory sinus arrhythmia, a physiological phenomenon where heart rate cyclically decreases during expiration and increases during inspiration, reflecting vagal modulation of sinoatrial node activity. The respiratory-related spectral band of HRV generally ranges from 0.15 to 0.4 Hz in adults, although this range may extend below 0.15 Hz in neonates and above 1.0 Hz during physical activity (Kamath et al., 1991). Designated as the high-frequency (HF) band (corresponding to 2.5-6 second cycles in adults), these oscillations demonstrate close association with respiratory rhythm (Barbieri et al., 2002) and primarily reflect parasympathetic (vagal) modulation of cardiac function (Rentero et al., 2002). HRV also demonstrates oscillations in the low-frequency (LF) range, typically spanning 0.04 to 0.15 Hz. This band includes a distinct 0.1 Hz component, commonly known as the 10-second rhythm or Mayer wave (Penaz, 1978). Some researchers further categorize this specific frequency range as the mid-frequency (MF) band (Mulder and Mulder, 1981; Mulder, 1992), reflecting its intermediate position in the HRV spectrum. Research suggests that LF components of HRV primarily represents sympathetic nervous system activity (Malliani et al., 1991, 1994). However, current scientific consensus maintains that the LF band (corresponding to >6 second cycles in humans) demonstrates sensitivity to both sympathetic and parasympathetic modulation of cardiac function (Akselrod et al., 1985; Brown et al., 1993; Lanfranchi and Somers, 2002; Malpas, 2002).

Additional HRV oscillations appear in the infra-low frequency range below 0.05 Hz. These spectral components are categorized into distinct bands: very low frequency (VLF) oscillations (0.004-0.04 Hz, corresponding to cycle lengths >25 seconds) and ultra low frequency (ULF) oscillations (<0.004 Hz, signifying cycles >5 hours). (Braga et al., 2002; Overton et al., 2001; Williams et al., 2002). The VLF band of HRV has received less research focus compared to higher or lower frequency oscillations. Potential physiological associations include thermoregulatory processes (Kitney, 1980), plasma renin system activity (Koh et al., 1994; Eckberg, 1985), and various autonomic and humoral regulatory mechanisms involving movement (Porter and Rivkees, 2001), respiration, postural changes, temperature modulation, and arousal states (Aoki et al., 2001; Vornanen et al., 2002). While these associations remain mech-

anistically unclear, VLF oscillations - along with faster HRV components - exhibit significant psychophysiological relevance and clinical diagnostic potential (Malik et al., 1990; Berntson et al., 1997).

Similar to other physiological signals (including respiratory patterns, heart rate, and blood pressure), HRV revealing both non-stationary and non-linear characteristics. These dynamic fluctuations may function as valuable biomarkers, providing insights into existing cardiovascular pathology and predictive information about future cardiac risk (Acharya et al., 2004). Consequently, HRV analysis has emerged as a widely adopted non-invasive clinical tool for evaluating cardiac autonomic regulation and identifying potential cardiovascular disorders (Nikolopoulos et al., 2003; Manis et al., 2007). HRV derived parameters function as important diagnostic biomarkers with broad clinical applications for detecting and characterizing cardiovascular disorders. As a non-invasive evaluation method, HRV analysis provides valuable insights into the functional balance between sympathetic and parasympathetic branches of the ANS (Eckberg, 1983).

2.1.4 Arrhythmia

Cardiac arrhythmias includes all rhythm disturbances deviating from Normal Sinus Rhythm (NSR). NSR originates in the sinoatrial node, propagating through the atria, atrioventricular junction, and ventricular conduction system at physiologically appropriate rates. While the sinus node basically keeps regular discharge patterns at rest, it normally exhibits minor physiological variations. Particularly in pediatric populations, these variations often demonstrate respiratory-phase dependency, resulting in heart rate acceleration during inspiration - a phenomenon referred to as respiratory sinus arrhythmia. In resting adults, NSR is characterized by a heart rate between 60-100 beats per minute (bpm). Deviations from this range represent rhythm abnormalities: sinus tachycardia (>100 bpm) and sinus bradycardia (<60 bpm).

Figure 2.3 denotes characteristic ECG patterns of various arrhythmias. Importantly, normal sinus rhythm displays natural variability throughout the circadian cycle, with sinus tachycardia and bradycardia representing appropriate physiological responses to autonomic stimuli. Elevated rates typically reflect sympathetic activation (e.g., during exercise or stress), while slower rates often suggest vagal predominance (e.g., during sleep or rest). These rate variations constitute normal physiological adaptations rather than pathological arrhythmias when occurring in appropriate contexts. The term arrhythmia does not mean heart beat anomaly, as normal arrhythmias can happen frequently with absolute stability (paroxysmal tachycardia, flutter and so forth.), sometimes the heart showing heart beat in the normal range. On the other hand, some unpredictable rhythms ought not to be thought about arrhythmias (direct inconsistency in the

sinus release, especially when related to breath).

In addition, the classification of cardiac arrhythmias does not necessarily imply underlying pathology. In fact, healthy individuals frequently demonstrate various rhythm disturbances, encompassing both active patterns (such as premature complexes) and passive phenomena (including escape rhythms, mild atrioventricular blocks, and sinus arrhythmia). Clinicians employ different ways to characterize these arrhythmic patterns:

- Location of origin: arrhythmias are alienated into ventricular arrhythmias and supraventricular (containing those having their origin in the atria, AV junction and SA node).
- Underlying mechanism of conduction: arrhythmias may be divided by: 1) irregular formation of electrical impulses, which consist of increased heart automaticity (superfluous parasystolic or systolic mechanism) and triggered electrical impulse activity, and 2) disturbances of conduction and/or decreased automaticity.
- According to clinical point of view: arrhythmias may be incessant, or paroxysmal, or perpetual. In reference to tachyarrhythmia (an instance of a dynamic arrhythmia), paroxysmal tachyarrhythmia befall unexpectedly and generally disappear naturally (for instance AV junction reentrant paroxysmal tachycardia). Incessant tachyarrhythmia is categorized by petite and repetitive runs of ventricular tachycardia or supraventricular. Permanent tachyarrhythmias are continuously present (an example: chronic atrial fibrillation) (World Health Organization, 2012; Patel et al., 2016; Go et al., 2013; INEGI, 2014).

2.1.4.1 Atrial Arrhythmia

Any deviation from the typical ECG recording is considered as a certain cardiac disorder. CVDs encompasses a wide range of conditions affecting the cardiac muscle and the vascular system that supplies essential organs like the heart and brain. Arrhythmia refers to a disruption in the normal sinus rhythm, which can arise from deviations in the initiation of depolarization by pacemaker cells other than those in the sinus (SA) node. This alteration in electrical impulse formation or conduction can lead to the occurrence of an arrhythmia. By engaging in discussions about cardiovascular diseases, we can develop techniques for processing electrocardiograms that have the potential to identify abnormalities at an early stage. Some of the conditions which affect the heart are: Atrial Arrhythmia, Ventricular Arrhythmia, Myocardial Infarction (MI), AV, Coronary Artery (CA), CHF.

Atrial arrhythmia occurs when an electrical impulse repeatedly circulates within the atria, leading to irregularities in the ECG morphology. This can be identified by the presence of abnormal P waves or the absence of distinct P waves, where they coincide with the QRS complex. AF is a specific type of atrial arrhythmia characterized by an irregular and rapid heartbeat, showcasing a disruption in the normal heart rhythm (Najarian and Splinter, 2012).

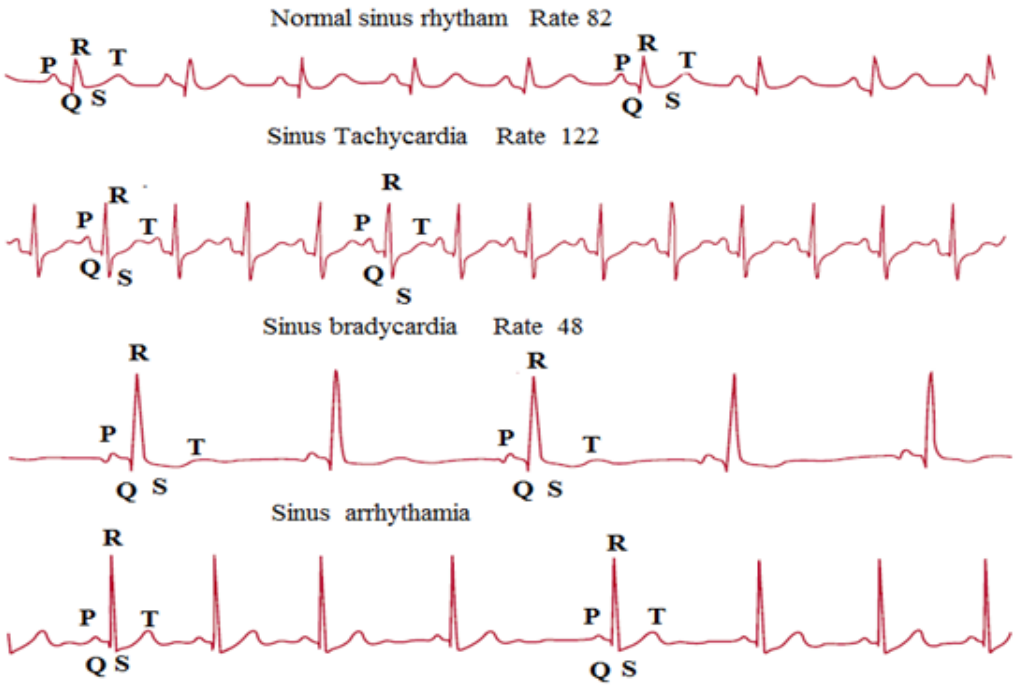

Figure 2.3: Various examples of sinus rhythms (Soria, 2012).

2.1.4.2 Ventricular Arrhythmia

Ventricular arrhythmias occur when the initiation of ventricular activation does not originate from the atrioventricular (A-V) node, leading to a prolonged QRS complex on the electrocardiogram. An abnormal ventricular activation is indicated by a QRS interval lasting longer than 0.1 seconds. Additionally, premature ventricular contractions, which manifest as contractions that occur unusually early, are another characteristic feature of ventricular disturbances (Najarian and Splinter, 2012). Ventricular Arrhythmia includes ventricular tachycardia (VT) and ventricular fibrillation (VF) (Sörnmo and Laguna, 2005). A heart undergoing VF cannot deliver oxygenated blood to the brain.

2.1.4.3 Myocardial Infarction

Myocardial Infarction or heart attack caused when transport of oxygen is terminated in a certain area (and so the heart muscle dies in that region). It happens due to a sudden coronary artery blockage that cuts off oxygen to part of your heart muscle. A typical MI ECG signal is illustrated in Figure 2.4

2.1.4.4 Atrioventricular Block

AV block occurs when the conduction pathway between the SA node and the AV node is disrupted, leading to a mismatch in the contraction timing between the atria and ventricles. As a result, the atria contract at a faster rate than the ventricles, significantly impairing the pumping function of the heart.

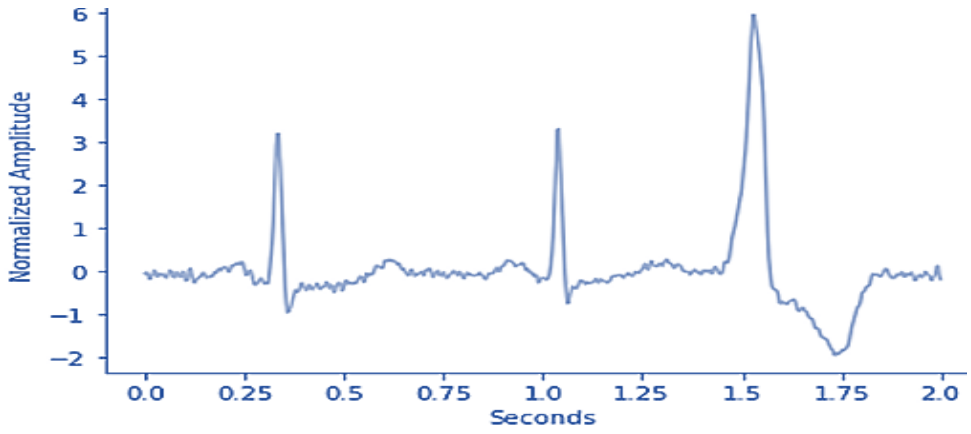

Figure 2.4: The typical MI ECG signal

2.1.4.5 Coronary Artery

Coronary Artery is caused by deposition of plaque in the inner walls of arteries. In this case, the diameter of the arteries decreases and then arteries are not able to supply nutrients and oxygen to heart muscles (Altan et al., 2016). A typical CAD ECG signal is depicted in Figure 2.5

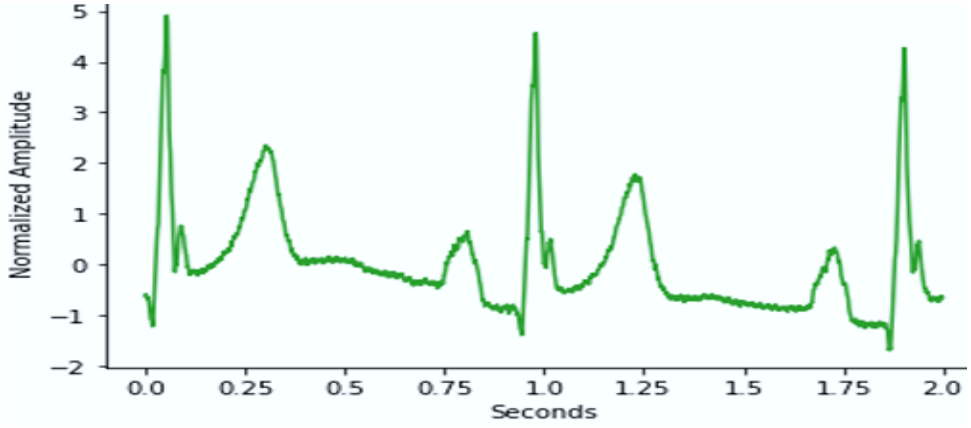

Figure 2.5: The typical CAD ECG signal

2.1.4.6 Congestive Heart Failure

Heart failure occurs when the heart is unable to efficiently pump blood to the body, leading to a diminished ability to deliver sufficient oxygen and nutrients to organs. As a consequence, these organs suffer damage and their functional capacity is reduced (Narin et al., 2014). CHF is a dysfunction of the cardiovascular system that the heart is unable to drain the blood away (Yu and Lee, 2012). A typical CHF ECG signal is shown in Figure 2.6

2.1.5 Methods for Analysis of Heart Rate Variables Signals

There are two basic approaches to quantifying the dynamic characteristics of HRV signals: (i) use of global descriptive statistics to portray the distribution of R-R interval (e.g. vari-

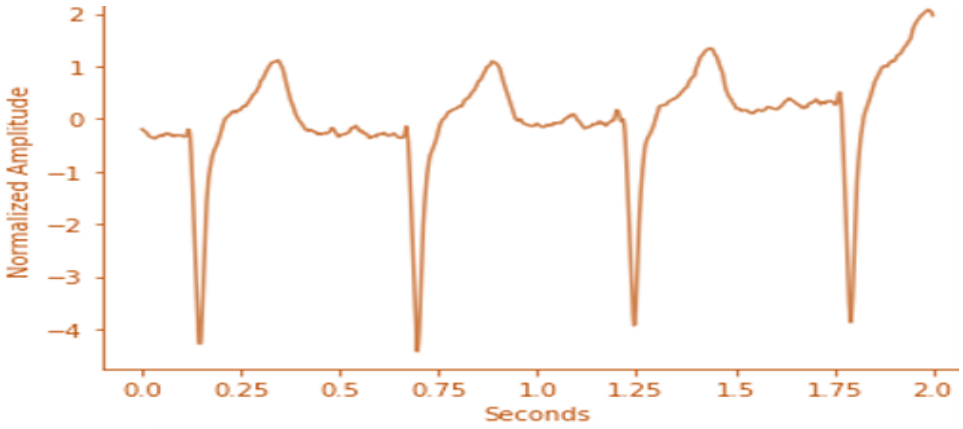

Figure 2.6: The typical CHF ECG signal

ance, range and standard deviation) and (ii) modeling of periodic shapes to extricate particular frequency components of difference that identify with useful techniques or physiological constituents, instance RSA. The first approach statistics mostly contemplate the total population of HRV signals as isolated or independent data samples, whereas second approach focuses on the serial linkages among the data components. These two methodologies are not united with the refinement between time-domain and frequency-domain analysis. Time-domain techniques can be used to express periodic processes, and any frequency-domain technique can be transformed into the time-domain technique if the signals are stationary (Brillinger, 2001). But, the HRV signals are non-stationary time-varying signal from the statistical perspective. Outliers, noise and artifacts affect the sensitivity of the time domain techniques (Acharya et al., 2006). The time domain analysis failed to detect or differentiate the HRV signals, when different rhythmic signals with same means and standard deviations. Hence, time domain analysis is not very useful to analyze the nonlinear and non-stationary signals.

Numerous methods have been employed or proposed over the past several decades for analysis of HRV. However, as the HRV signals have a place with the group of multicomponent non-stationary signals (Wood and Barry, 1996), it is challenge to obtain precise assessments of time-varying spectral signals. This problem can be tackled by an appropriate time–frequency distribution method and resolute the multicomponent behavior of HRV signals. Some of the more commonly employed methods in frequency domain and time-frequency domain are summarized for analysis of arrhythmias in (Malik, 1997; Novak and Novak, 1993; Novak et al., 1995; Huang et al., 1997; Clariá et al., 2000) and graphical depiction of the HRV signal in (Malik, 1995; Azuaje et al., 1999). In recent years, a number of investigators have analyzed the HRV by different advanced digital signal processing methods, statistical methods, box plot and mean and standard deviation and prominence has been given on classification to detect the normal group and diseased group with different classifiers(Acharya et al., 2014; Poddar et al., 2013; Giri et al., 2013; Lee et al., 2007).

2.2 Detection of QRS Complex and Denoising of ECG Signal

CVDs are one of a leading global cause of death, with cardiac arrhythmias playing a major role in life-threatening conditions like heart attacks and strokes (Lin et al., 2010). Accurate diagnosis of these disorders relies primarily on ECG, where the detection of key fiducial points, particularly the QRS complex and R-peaks is essential for identifying arrhythmias and other cardiac abnormalities (Rangayyan and Krishnan, 2024; Kathirvel et al., 2011; Yıldırım et al., 2018). The QRS complex serves as a vital indicator of heart activity, making its precise detection fundamental in ECG-based diagnostics. Accurate detection of the QRS complex in ECG signals is critical for detecting heartbeats, analyzing other ECG components (P-waves, T-waves, RR intervals), diagnosing cardiovascular diseases (CVDs) and cardiac abnormalities (Panahi et al., 2021). However, traditional QRS detection methods face significant challenges, including noise interference (e.g., baseline wander and powerline interference), morphological variations in ECG waveforms, and high computational complexity, limiting their efficiency in real-time applications.

To address this issue, various studies explores different approaches for R-peak (QRS complex) detection, including complete ensemble empirical mode decomposition (CEEMD) (Xie et al., 2021b), adaptive filter (Jain et al., 2017), filter banks (Hamilton and Tompkins, 1986; Adnane et al., 2009; Zhang and Lian, 2009; Afonso et al., 1999; Poli et al., 1995), phasor transform (Martínez et al., 2010), wavelet transforms (WT) (Martínez et al., 2004; Zidelmal et al., 2012; Zeng et al., 2021), integration of WT and hybrid hidden Markovmodels (de Lannoy et al., 2009), DWT (Cesari et al., 2017; Ghaffari et al., 2009), quadratic energy (Hamilton and Tompkins, 1986; Farashi, 2016; Phukpattaranont, 2015), fuzzy clustering, wavelet packets (WPs) (Jia et al., 2020), adaptive threshold (Christov, 2004; Karimipour and Homaeinezhad, 2014), morphology-based approaches (Shimauchi et al., 2021; Friganovic et al., 2018), permutation entropy, moving average filters (Elgendi, 2013; Elgendi et al., 2015; Mansourian et al., 2023; Elgendi et al., 2016), Shannon energy operators (El Bouny et al., 2020; Beyramienanlou, 2021), phase-space reconstruction (PSR) (Hou et al., 2018), correlation analysis-based method (Homaeinezhad et al., 2014) and deep learning. However, WT-based methods face limitations such as rigid wavelet filter bandlimits and the challenge of selecting an optimal mother wavelet. While empirical mode decomposition (EMD) can alleviate wavelet selection issues, its reliance on intrinsic mode functions (IMFs) remains problematic in ambulatory conditions due to the lack of a robust mathematical framework.

The authors of (Chen and Maharatna, 2020) proposed an automated method combining hierarchical clustering (HC) and discrete wavelet transform (DWT) for robust detection of R (QRS complex) and T peaks in ECG signals. The proposed method involves four key stages, including pre-processing, R-peak detection, T-wave boundary detection, and T-peak detection.

In the pre-processing stage, they have utilized 1-30 Hz band-pass to filter the raw ECG signals and normalize to remove noise and baseline wandering. For the R- peak detection, they have utilized HC which groups ECG samples into R and non-R clusters based on amplitude and slope. A template-based approach estimates T-wave boundaries using mean square error (MSE) between the template and detected R-peaks. Subsequently, a DWT was employed for precise T-peak localization using Modulus-Maxima Analysis (MMA).

BayeSlope and an adaptive R-peak detection method has been designed by (De Giovanni et al., 2022) for wearable ECG sensors during high-intensity exercise. The BayeSlope method combines k-means clustering (unsupervised learning), Bayesian filtering, and non-linear normalization to enhance R-peak detection accuracy. Which addresses the challenges encountered in traditional algorithms that fail under the sudden physiological changes (e.g., variable R-peak amplitudes) caused by intense physical activity. An advanced method for detecting R-peaks in ECG signals using a combination of chaos analysis, Independent Component Analysis (ICA), and Principal Component Analysis (PCA) has been presented in (Gupta et al., 2020). This study focused on improving the accuracy of R-peak detection in ECG signals, which is crucial for diagnosing cardiac abnormalities. ICA was used to separate noise and baseline wander from ECG signals in the pre-processing stage. Due to the nonlinear nature of ECG signals, chaos theory had been employed to analyze irregular patterns (feature extraction). Techniques like Lyapunov exponents, time-delay mutual information, and attractor reconstruction are used to characterize the ECG's chaotic behavior. Subsequently, PCA has been applied to reduce dimensionality and enhance R-peak detection by maximizing variance in the data.

The authors of (Habibi et al., 2024) presented an enhanced real-time method for QRS complex detection and ECG signal compression, specifically designed for wearable and IoT-based healthcare applications. The method integrates the Absolute Value Curve Length Transform (A-CLT) with an adaptive threshold algorithm to improve accuracy in detecting QRS complexes. The adaptive thresholding with Finite State Machine (FSM) helps to dynamically adjust the detection thresholds based on local ECG characteristics. The algorithm was optimized for low-power hardware, requiring minimal computational resources and and the performance had been tested on the MIT-BIH Arrhythmia and BIDMC-CHF databases. They have also employed a lossless compression technique using the first derivative of the ECG signal and entropy encoding, which reduces data storage and transmission bandwidth without compromising signal integrity. An adaptive R-peak detection algorithm for wearable ECG signals, addressing challenges like dynamic noise interference and limited computational resources was proposed in (Hao et al., 2022). Their method involves utilization of Brown's exponential smoothing model to dynamically adjusts detection thresholds by analyzing noise levels, R-peak amplitudes, and RR intervals, ensuring robustness in noisy conditions while maintaining compu-

tational efficiency for wearable applications. In the pre-processing stage, ECG signals were segmented into 3-second frames to ensure at least one QRS complex per segment. Following this, a Butterworth filter (8th order, 10–25 Hz) had been used to remove baseline wander and high-frequency noise. Authors in (He et al., 2020) presented an automatic method for detecting QRS complexes in ECG signals using a deep learning approach based on U-Net and bidirectional Long Short-Term Memory (LSTM). To remove baseline wander and high-frequency noise, they have utilized mean filtering and DWT (with db4 wavelet) in the pre-processing stage. The original denoised ECG and its inverted version are then fed into the model to improve detection of both positive and negative R peaks utilizing dual-channel Input. After this, U-Net is used for segmentation, extracting spatial features from ECG signals and Bidirectional LSTM employed to capture temporal dependencies, enhancing context-aware QRS detection.

The research in (Hossain et al., 2019) introduced a novel method for accurately detecting QRS complexes and P waves in ECG signals using the Complete Ensemble Empirical Mode Decomposition with Adaptive Noise (CEEMDAN) approach. The ECG signal is decomposed into intrinsic mode functions (IMFs), and specific modes are selected to reconstruct signals optimized for QRS and P wave detection. Afterward, High-frequency modes (modes 2-5) are used to reconstruct a signal for QRS detection. R-peak candidates are identified from both positive and negative amplitudes, combined, and refined using adaptive thresholds and criteria. All modes except the first (to reduce noise) are used for P wave detection. A robust Digital Fractional Order Differentiator (DFOD) based ECG pre-processor design for QRS detection has been presented in (Nayak et al., 2019). The DFOD is designed using an Antlion Optimization (ALO) algorithm to approximate the ideal fractional order differentiator characteristics. It operates with a fractional order (α) of 0.5, which is experimentally determined to enhance QRS detection accuracy compared to traditional integer-order differentiators.

A real-time QRS detection algorithm for ECG signals has been presented by (Pan and Tompkins, 1985). Their algorithm reliably identified QRS complexes by analyzing slope, amplitude, and width, while using a digital bandpass filter to reduce noise interference. the method processes signals through steps such as bandpass filtering, differentiation, squaring, and moving-window integration, adapting dynamically to changes in ECG morphology and heart rate. In addition to this, it is efficient, implemented in assembly language for microprocessors, and suitable for real-time applications like arrhythmia monitoring. A Modified Pan-Tompkins (MPT) algorithm for QRS complex detection in ECG signals had been proposed in (Rahman et al., 2024). In the pre-processing stage, Notch filter (50 Hz noise removal) and Bandpass filter (1 Hz to 60–500 Hz) were employed. Additionally, to reduce noise and artifacts, ECG signals were segmented into 1200 ms windows, normalized, and standardized. The proposed technique was tested on 8-hour single-lead ECG recordings from healthy sub-

jects using a Movesense wearable device (256 Hz sampling rate). The Standard Pan-Tompkins (SPT) algorithm focuses on filtering, squaring, and adaptive thresholds but lacks Q/S point precision. The MPT algorithm is highly accurate for QRS detection in wearable ECGs and uniquely enables ST segment analysis due to its ability to preserve QRS morphology.

Authors of (Sabor et al., 2022) developed an embedded arrhythmia classifier for wearable devices to enable early detection of abnormal heart rhythms, reducing the need for hospital visits and continuous monitoring. They introduced the Nonlinear Energy Operator (NEO)-compact 1D Convolutional Neural Network (CCNN) algorithm, a lightweight and efficient solution for real-time QRS detection and arrhythmia classification in wearable ECG devices. The method integrates an adaptive NEO-based QRS detector with a CCNN for classification. An embedded algorithm for QRS complex detection in ECG signals, suitable for low-resource microcontrollers in wearable devices and focusing on real-time processing and high accuracy was presented in (Tueche et al., 2021). In the pre-processing step, they have utilized a fourth-order Butterworth bandpass filter (0.5–40 Hz) and a notch filter to remove noise such as baseline drift, powerline interference. Thereafter, the ECG signal is squared to amplify QRS complexes and based on slope, incremental mean slope, and RR-interval time, R-peaks are identified using adaptive thresholds. The Q and S points around each R-peak are also detected using signal derivatives, adaptive thresholds, and trend analysis. The paper in (Yan et al., 2025) introduced an adaptively regularized numerical differentiation method for QRS detection in noisy ECG signals. Their proposed method combines wavelet denoising, Adaptively Weighted Tikhonov Regularization (AWTR)-based numerical differentiation, Hilbert transform, and adaptive thresholding to enhance QRS complexes and suppress noise.

Machine learning model combining wavelet CNN autoencoders and ConvLSTM has been proposed in (Yuen et al., 2020) for detecting QRS complexes in ECG signals from wearable devices. The baseline wander was removed using Butterworth filter (cutoff- 5 Hz)by attenuating low-frequency noise. A two-stage WaveletCNN Auto-encoders was employed to enhance QRS detection in noisy ECG signals. The auto-encoder 1 uses Symlets 4 wavelet (level 3) with CNN for denoising and auto-encoder 2 uses Daubechies 3 wavelet (level 3) to refine QRS gradients. The ConvLSTM combines CNN (spatial feature extraction) and LSTM (temporal modeling) for final QRS detection. Authors in (Zahid et al., 2021) proposed a robust method for R-peak detection in low-quality Holter ECG signals using a 1D Convolutional Neural Network (CNN) with a verification model. A 1D CNN-based encoder-decoder architecture was used to treat R-peak detection as a 1D segmentation problem. The model outputs a pulse train where pulses mark R-peak locations. The research in (Zhao et al., 2021) introduced a robust QRS detection and R-peak identification algorithm designed for wearable ECG sensors. Their method involves utilization of adaptive left-side and right-side thresholds to dynamically adjust

detection sensitivity, improving accuracy in varying conditions. Following that, QRS Watchdog where, a search-back function used to recover missing R-peaks, enhancing robustness has been employed. Thereafter, R-peaks in the original ECG signal were detected by analyzing sharpness and proximity.

A Variational Mode Decomposition (VMD) method has been proposed in (Cao et al., 2023) for simultaneous R-peak detection and noise suppression in ECG signals. A two-stage VMD process was used to remove low-frequency (LF) noise (baseline wander) and enhance the QRS complex. In their approach, parameters like bandwidth control (α) and number of modes (K) are optimized for effective decomposition. The Hilbert Transform (HT) had been used to detect candidate R-peaks by identifying zero-crossing points in the smoothed Shannon Energy (SE) envelope. The paper in (Dhyani et al., 2025) focused on the development and evaluation of a hardware-based QRS complex detection system for ECG signals using Field-Programmable Gate Arrays (FPGAs). Their technique involves pre-processing (downsampling, noise removal via bandstop filtering), feature extraction (derivative, squaring, moving average), and QRS detection using a finite state machine (FSM). The algorithm has been simulated and validated using Xilinx ISE 14.7 and Modelsim 10.0.

An efficient method for QRS complex detection in ECG signals has been proposed in (Sharma and Sunkaria, 2016) utilizing a novel pre-processing techniques and kurtosis based method, which is crucial for diagnosing cardiac conditions. The introduced approach includes mainly the pre-processing and QRS detection stage. In the pre-procesing step, a two stage median filter was used to remove baseline drift, and a Savitzky-Golay (SG) smoothing filter was applied to reduce noise while preserving signal features. Afterward, the third power of the ECG signal has been computed to amplify QRS complexes. Subsequently, the isoelectric line (baseline) was identified using Sauvola's thresholding technique. Finally, the QRS regions have been detected using root mean square (RMS) thresholds. Authors in (Chen and Chuang, 2017) proposed a computationally efficient QRS detection and R point recognition method tailored for single-lead wearable ECG devices. Their approach enhances QRS segments while suppressing P/T waves and baseline wander, enabling accurate heartbeat detection. The proposed technique consists of mainly four key steps, such as: ECG Signal Refreshment (using a 2-second sliding window), signal Enhancement (band-pass filter and zero-sum mask), QRS fiducial point detection, and R Point identification (utilizing QRS templates). In (Sharma et al., 2022), combination of hierarchical clustering and discrete wavelet transform is applied to detect R peak and T wave. A robust QRS detection and R peak identification algorithm is proposed for wearable ECG sensors (Wang et al., 2022). Authors in (Belkadi and Daamouche, 2021) presented an algorithm for QRS complex detection in ECG signals using the Stationary Wavelet Transform (SWT). They have utilized a bandpass filter in a frequency range of [4, 24 Hz], with

Particle Swarm Optimization (PSO), to enhance QRS components and reducing noise. For the MIT-BIH Arrhythmia Database, they obtained 99.83% sensitivity, 99.94% positive predictivity, and 0.228% detection error rate (DER).

The research in (Khamis et al., 2016) generated QRS complex features by combining the signal derivative with its amplitude envelope, subsequent to threshold determination using morphological closing operations with max-min filters. By utilizing a combined adaptive threshold (MFR), two adaptive algorithms had been introduced in (Christov, 2004) for real-time QRS complex detection in ECG signals. MFR is able to make dynamical adjustment to noise, enhance signal quality, and heart rhythm variability to improve detection accuracy. Validating by MIT-BIH Arrhythmia Database (48 records), algorithm 1 achieved Se of 99.69%, Sp of 99.66%, and algorithm 2 yielded Se of 99.74% and Sp of 99.65%. Utilizing the power spectrum of QRS complexes, a method for QRS detection has been presented in (Zidelmal et al., 2012) to distinguish between normal and abnormal beats. Validated on the MIT-BIH arrhythmia database, their method attained a sensitivity of 99.64% and a positive predictivity of 99.82%. The study in (Lu et al., 2018), introduced an improved adaptive threshold algorithm for QRS complex detection in ECG signals, which is a critical step in diagnosing cardiovascular diseases. Their approach involves four basic stages such as pre-processing, peak detection, adaptive threshold detection, and Post-Processing. Tested on the MIT-BIH Arrhythmia database, detection rate of 99.41%, sensitivity of 99.72%, and specificity of 99.69% achieved.

The authors of (Zalabarria et al., 2020) proposed a technique for real-time R-peak detection in noisy ECG signals, suitable for low-cost wearable devices. This study addressed the challenges of noise artifacts (including baseline wander, power-line interference) and arrhythmias while maintaining low computational load. In the pre-processing stage, they have utilized stepped median filtering for baseline wander and a dynamic cutting line for noise elimination. Subsequently, an area over the curve method was employed to identify R-peaks based on QRS complex morphology. Results of 99.54% sensitivity and 99.60% positive predictivity has been obtained by testing on the MIT-BIH Arrhythmia Database. An implementation of QRS enhancement had been presented in (Rodrigues et al., 2021) through double-derivative pre-processing via with finite state machine-driven threshold adaptation. Furthermore, various literature has also reported in the design of real-time ECG monitoring by leveraging a QRS detection technique. The study in (Sharada et al., 2023) proposed a comprehensive cardiac monitoring system designed for remote areas with scarce cardiologists and costly treatments. The method includes ECG signal pre-processing, QRS (Quick Reaction Strike) complex detection, feature extraction, abnormality identification, and beat classification using an outline curve approach.

Integer Haar wavelet transform was employed in (Talukder et al., 2020) to filter ECG

signals and detect R-peak frequencies within the QRS complex, implemented on a Digilent Nexys-4 DDR FPGA board. The proposed design enables direct integration into medical devices or development of specialized internet of things (IoT) systems for biomedical applications. The authors in (Zhang et al., 2020c) presented a Kalman filter-based adaptive threshold method for QRS complex detection that demonstrates high adaptability to peak variations while maintaining low computational cost and memory requirements compared to neural network or transform-domain approaches. FPGA implementation yields real-time performance with 99.30% sensitivity and 99.31% positive predictive accuracy. An FPGA-based system has been introduced in (Meddah et al., 2020) for real-time ECG monitoring and arrhythmia detection, leveraging a QRS detection method derived from the Pan-Tompkins algorithm. Optimized for the Spartan-3E FPGA (Nexys 2) using VHDL in Xilinx ISE 14.2, the system's performance was tested through three comparative analyses to ensure reliability and effectiveness.

For the MIT-BIH arrhythmia and Fantasia databases, the authors of (Modak et al., 2021) achieved a sensitivity of 99.82%, 99.92% and detection error rates of 0.31%, 0.18% in the detection of QRS complex from ECG signal. In the pre-processing stage, two median filters and a moving average filter were applied to reduce baseline wander (while suppressing P and T waves) and smooth the signal (eliminating high frequency noise), respectively. A Max-Min Difference (MMD) algorithm has been employed for the detection of QRS complex which is designed for real time analysis of single-lead ECG signals in the study conducted by (Pandit et al., 2017). In this paper, a sliding window-based strategy was applied to process ECG signals in real-time without storing the entire signal in memory (reducing computational complexity). They obtained Se of 99.62% and positive predictivity of 99.67% throughout five PhysioNet databases (MIT-BIH Arrhythmia, European ST-T, etc.). Authors in (Elgendi, 2013) conducted a fast QRS detection algorithm designed for battery-driven ECG devices and long-term monitoring utilizing band-pass Filtering, squaring function, moving averages, and thresholding techniques. The aim of this study was focusing on developing a computationally efficient QRS detection method suitable for real-time applications and low-power devices.

The work in (Orlandic et al., 2019) employed a relative-energy enhancement filter (long-to-short sliding window energy ratio) for QRS complex detection, utilizing a hysteresis comparator with two adaptive thresholds. A sensitivity of 99.6% and positive predictivity of 99.5% has been achieved in the study conducted by (Martínez et al., 2004). The focus of this work incorporated automatic delineation of ECG signals using the wavelet transform. The paper in (Sharma and Kohli, 2024) proposed a deep learning (DL) model based on a 1D U-Net encoder-decoder architecture to delineate ECG waveform components (P, QRS, T, and U waves) and introduced a post-processing algorithm to refine the results by removing redundant peaks. They validate their approch using QT Database (QTDB) and obtained a performance of 98.45% sen-

sitivity and 91.40% precision on average. While (Aurobinda et al., 2016) employed the Hilbert transform for R-peak detection, it proved ineffective for low-amplitude R waves. Similarly, (He et al., 2017) applied KNN for QRS detection across varying morphologies, but its clinical utility was limited by high computational demands and inherent laziness (Jaafar et al., 2018). Fig. 2.7 demonstrates the overall structure involved in the detection of QRS complex in ECG signal. The summary of various literature in the detection of QRS complex is listed in Table 2.1, 2.2, 2.3, and 2.4.

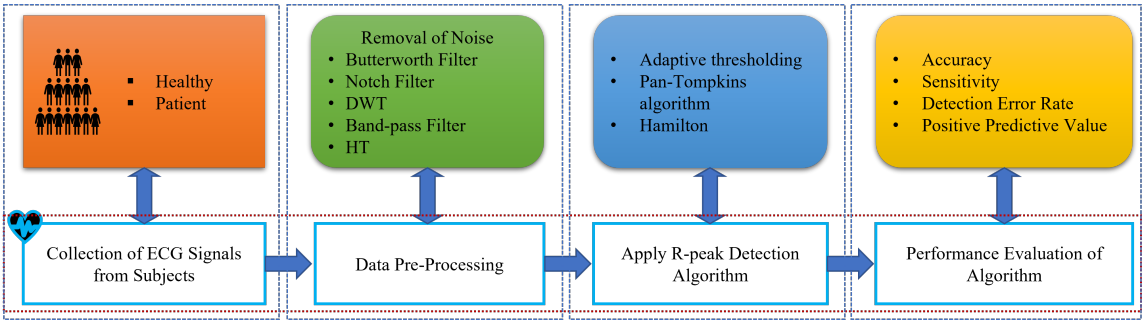

Figure 2.7: Structure of the QRS detection

Despite existing literature reported optimal performance in R-peak detection, limitations in existing QRS complex identification methods suggest further improvement opportunities remain possible.

Table 2.1: A summery of various techniques for the detection of QRS in the ECG signal

Author	Dataset	Methods	Performance Results	Limitations
(Chen and Maharatna, 2020)	• MIT-BIH Arrhythmia Database: 48 records (30-min, 360 Hz) for R-peak detection • QT Database: 105 records (250 Hz) for T-peak evaluation	• R-peak detection: HC (agglomerative, average linkage, Euclidean distance) • T-peak detection: DWT (Haar wavelet) and MMA	• R-peak (MIT-BIH): 99.89% Se, 99.94% +P, 99.83% Acc • T-peak (QT manual): 99.91% Se, 99.38% +P, mean error = 1.4 ± 8.2 ms	• Computationally intensive for real-time use • Performance drops with baseline drift and highly abnormal T-waves • Relies on a fixed ECG template, which may not generalize to all morphologies.
(De Giovanni et al., 2022)	• 20 subjects performing maximal cycling tests, Single-lead, 500 Hz (downsampled to 250 Hz)	• Two-tier adaptive approach: REWARD: Lightweight hysteresis-based R-peak detection BayeSlope: Robust detection	• F1-Score: BayeSlope: 99.3% (best), 98.8% (avg) *Adaptive (REWARD and Baye* Slope): 99.0% (best), 97.9% (avg) REWARD alone: 86.7% (avg). • Energy Consumption: BayeSlope only: 2.08 mJ. Adaptive design: 1.55 mJ (avg), 38.7% energy savings.	• Initialization Sensitivity: BayeSlope requires stable ECG segments for proper initialization • Floating-Point Dependency: Limits deployment on ultra-low-power fixed-point processors • Limited Pathology Testing: Validated only on healthy subjects; performance on arrhythmias is untested
(Gupta et al., 2020)	• MIT-BIH Arrhythmia Database • Ventricular Tachyarrhythmia (VT) Database • Atrial Fibrillation (AF) Termination Challenge Database • American Heart Association (AHA) Database • MIT-BIH Long-Term Database	• Pre-processing: ICA for noise removal • Feature Extraction: Chaos analysis • Detection: PCA for R-peak localization	Se: 99.94%, PP: 99.96%, Acc: 99.91%, DER: 0.088%	• Computational Load: Chaos analysis increases complexity • Dependency on ICA's assumptions: Struggles with correlated noise
(Habibi et al., 2024)	• MIT-BIH Arrhythmia (48 records) • BIDMC-CHF (15 records)	• A-CLT: Simplifies QRS enhancement using absolute differences, Replaces complex operations (e.g., square roots) for hardware efficiency • Adaptive Thresholding with FSM: Dynamically adjusts thresholds based on ECG features • FSM reduces false positives. • Lossless Compression: First-derivative with entropy encoding	• MIT-BIH: Se: 99.69%, P+: 99.60%, F1 Score: 99.63% • BIDMC-CHF: Se: 99.56%, P+: 99.05%, F1: 99.29% • Hardware: FPGA utilization: 1% slices (low-power)	• Limited generalization to extreme arrhythmias • Needs testing on embedded wearables. • Compression Variability: Efficiency depends on signal noise/morphology
(Hao et al., 2022)	• Self-constructed dataset, 80 single-lead ECG recordings (5 minutes each) • 20 healthy individuals, 250 Hz sampling rate	• Preprocessing: Frame splitting and Butterworth bandpass filtering (10-25 Hz) • Threshold Adaptation: Brown's exponential smoothing model with relative error least squares optimization	Precision: 99.6%, Recall: 99.7%, F1-Score: 99.65%	• Limited to young, healthy subjects; untested on arrhythmias or elderly • Evaluated only on Gaussian noise; motion artifacts not addressed • Smoothing coefficients empirically set; may need recalibration for other devices

Table 2.2: Cont. . . QRS detection

Author	Dataset	Methods	Performance Results	Limitations
(He et al., 2020)	• MIT-BIH Arrhythmia Database (MITDB) 44 records (22 train, 22 test), 30-min duration, 360 Hz sampling • CPSC2019 Dataset: 2000 records, 10-sec duration, 500 Hz sampling	• Preprocessing: Mean filtering and DWT for noise removal • Dual-Channel Input: Original + inverted ECG signals to handle negative R peaks • Deep Learning Model: U-Net (segmentation) and bidirectional LSTM (temporal context)	• MITDB: Se: 99.56%, +P: 99.72%, Acc: 99.28% • CPSC2019: Se: 95.13%, +P: 82.03% Acc: 78.73%	• Does not detect other ECG features (P/T waves, ST segments), limiting broader diagnostic applications • Performance drops on highly noisy signals (e.g., CPSC2019 dataset) • Bidirectional LSTM increases processing time; may not be ideal for real-time applications • While robust, the model may require retraining for datasets with significantly different noise profiles or morphologies
(Hossain et al., 2019)	• MIT-BIH Arrhythmia Database (MITDB) • QT Database (QTDB)	• MITDB: CEEMDAN-based QRS detection (modes 2-5) • Adaptive thresholding from positive/negative amplitudes • QTDB: CEEMDAN-based P wave detection (all modes except 1) • Adaptive PR interval search	• MITDB: Se: 99.96%, PPV: 99.89%, Error: 0.15% • QTDB: Se: 99.75%, PPV: 99.47%, Mean P peak error: 4 ms	• Computationally intensive • P peak error slightly higher than some methods • Single-lead dependency • Performance degrades at extreme noise (PPV drops)
(Nayak et al., 2019)	• MITDB • QTDB • European ST-T (EDB) • MIT-BIH ST Change (STDB) • T-Wave Alternans (TWADB) • Supraventricular Arrhythmia (SVDB)	• ALO-optimized DFOD (α=0.5) • Band-pass filter (5–22 Hz) • Hilbert Transform (HT) R-peak detection	• MITDB: Se: 99.95%, PP: 99.94%, DER: 0.11% • QTDB: Se: 99.95%, PP: 99.98%, DER: 0.06% • EDB: Se: 99.87%, PP: 99.86%, DER: 0.27% • STDB:Se: 99.94%, PP: 99.92%, DER: 0.14% • TWADB: Se: 99.43%, PP: 99.25%, DER: 1.32% • SVDB: Se: 99.91%, PP: 99.90%, DER: 0.18%	• Higher computational cost than wavelet-based methods • Limited testing on dynamic QT intervals • Higher FN in high-noise segments (for EDB) • Highest DER among datasets due to noise (for TWADB)
(Pan and Tompkins, 1985)	MIT/BIH Arrhythmia Database (48 half-hour ECG recordings, 24 hours total, >116,000 annotated beats)	Bandpass Filtering (5–12 Hz), Differentiation (5-point derivative), Squaring (nonlinear amplification), Moving-Window Integration (150 ms), Adaptive Thresholding (dual thresholds), T-Wave Discrimination (slope comparison)	• Accuracy: 99.3% • False Positives: 507 (0.437%) • False Negatives: 277 (0.239%) • Total Failures: 0.675%	• The 150-ms window may not optimally handle very wide or narrow QRS complexes (fixed integration window • The algorithm may need optimization for modern real-time applications with higher sampling rates
(Rahman et al., 2024)	Six healthy volunteers (hour single-lead ECG recordings)	• Notch filter (50 Hz removal) and bandpass filter (1 Hz–500 Hz) • Segmentation (1200 ms windows), normalization, and QRS averaging • Wavelet Transform (WT)	Se = 99.98%, Pr = 99.98%, Acc = 99.96%	• Only tested on healthy subjects • The segmentation and averaging steps in MPT may increase processing time compared to SPT • The study does not explicitly assess real-time implementation on low-power wearable devices
(Sabor et al., 2022)	• MIT-BIH Arrhythmia Database (MITD-AR): 48 records (30 min each, 360 Hz), 109,494 annotated beats • QT Database (QTDB): 82 annotated records (15 min each, 250 Hz)	• QRS Detection: Bandpass FIR filter (4–26 Hz): NEO, *Adaptive time-dependent thresholding* • Classification: Compact 1D-CNN, Nested k1,k2 fold cross validation	• QRS Detection: 99.79% se (MITD-AR), R-peak location error (RLE): 7.94 ms • Classification: 97.83% acc (5-class), 96.46% se, 99.25% specificity • Hardware: 46.61 sec for 30 min ECG on STM32F407 (168 MHz), Power: 41.71 mW	• Performance may vary on unseen datasets or ECG morphologies not present in MITD-AR/QTDB • While robust, the method may still be affected by extreme motion artifacts or muscular noise • Further optimization needed for ultra-low-power wearables

Table 2.3: Cont. . . QRS detection

Author	Dataset	Methods	Performance Results	Limitations
(Tueche et al., 2021)	• MIT-BIH Arrhythmia • MIT-BIH Pacemaker • MIT-BIH Normal Sinus	• Pre-processing: Bandpass (0.5-40 Hz) and Notch filter • R-peak detection: Squaring and slope/amplitude tests • Derivative and trend analysis (for Q/S detection)	• MIT-BIH Arrhythmia: Se: 99.65%, PP: 99.69%, F1: 99.67%, Runtime: 16.23 µs/sample • MIT-BIH Pacemaker: Se: 99.76%, PP: 99.71%, F1: 99.73% • MIT-BIH Normal Sinus: Se: 99.74%, PP: 99.93%, F1: 99.83%	• Requires 3s initial delay (Cp) for threshold adaptation • Memory-intensive for ultra-low-power devices • Lack of P/T-wave detection (limited to QRS complex)
(Yan et al., 2025)	• MIT-BIH Arrhythmia (ARR) Database (48 recordings, 30+ mins each) • CPSC 2019 Database (2,000 noisy 10-sec recordings)	• AWTR-based numerical differentiation (adaptive Tikhonov regularization) • Wavelet denoising (coif4) • Hilbert with absolute-value transform • Adaptive thresholding	• MIT-BIH ArrhythmiaDB: Se: 99.90%, P+: 99.91%, DER: 0.20%, Runtime: $3.28x10^{(}-5)$ s/point • CPSC 2019 DB: Se: 93.57%, P+: 93.90%, DER: 12.51%	• Limited testing on extreme noise • Requires parameter tuning (k1,k2) • Not validated on wearable ECG with motion artifacts
(Yuen et al., 2020)	• MIT-BIH Arrhythmia Database (47 subjects, 360 Hz) European ST-T Database (48 patients, upsampled to 360 Hz) • Long Term ST Database (34 patients, upsampled to 360 Hz)	• Butterworth Filter: Removes baseline wander • WaveletCNN Autoencoders: Denoise and enhance QRS complexes • ConvLSTM: Detects QRS complexes using spatiotemporal patterns	• 12 dB SNR: F1=0.9624 (MIT-BIH), 0.97940.9794 (European ST-T) • 0 dB SNR: F1=0.8739 (MIT-BIH), 0.9072 (European ST-T) • SNR:-6 dB: F1=0.7962 (Long Term ST)	• Trained on synthetic noise (NST), may not perform as well on real wearable ECG noise • Fails to detect ventricular tachycardia (low-frequency signals filtered out by Butterworth)
(Zahid et al., 2021)	• CPSC-DB (Noisy Holter ECGs) • MIT-BIH (Clean Clinical ECGs)	• 1D CNN Encoder-Decoder • Verification model (beat similarity and timing check) • Data augmentation (synthetic noise)	• CPSC-DB: F1-score: 99.30%, Recall: 99.69%, Pr: 98.91% • MIT-BIH: F1-score: 99.83%, Recall: 99.85%, Pr: 99.82%	• Not optimized for ultra-low-power devices or multi-lead ECGs • Verification model may struggle with very short RR intervals
(Zhao et al., 2021)	• MITDB (Arrhythmia) • QTDB (Healthy) • NSTDB (Noise Stress) • TWADB (T-Wave Alternans) • FANTASIADB (Healthy) • INCARTDB (12-Lead Arrhythmia) • AFTDB (Atrial Fibrillation) • SVDB (Supraventricular Arrhythmia)	• Bilateral threshold • QRS Watchdog • R-Peak Identifier	• Se: 99.81%, +P: 99.88%, DER: 0.31% • Se: 99.99%, +P: 99.98%, DER: 0.04% • Se: 99.32%, +P: 85.99%, DER: 16.87% • Se: 99.18%, +P: 98.37%,DER: 2.52% • Se: 99.96%, +P: 99.84%, DER: 0.20% • Se: 98.72%, +P: 95.52%, DER: 5.92% • Se: 98.85%, +P: 99.44%, DER: 1.70% • Se: 99.93%, +P: 99.87%, DER: 0.20%	• Slightly higher computational cost • Not tested in extreme noise conditions • Misses some low-amplitude beats • Lags in real-time processing • High false positives in INCARTDB
(Cao et al., 2023)	• MIT-BIH Arrhythmia Database: 48 ECG recordings (360 Hz), includes arrhythmias, noise, and morphological variations • QT Database: 105 ECG signals (250 Hz)	• Preprocessing: Normalization and DC offset removal • VMD-Based Noise Suppression: Stage 1: LF noise removal , Stage 2: QRS enhancement • R-Peak Detection: First-order derivative, SE amplification, HT for zero-crossing R-peak detection	• MIT-BIH: Se = 99.77%, +P = 99.91%, DER = 0.32%, Acc = 99.68% • QT Database: Se = 99.94%, +P = 99.78%, Acc = 99.72% • Denoising: SNR = 24.06 dB	• Struggles with very low-amplitude R-peaks (e.g., missed 13 beats in Record 205) • Performance degrades at low SNR (5-10 dB), where QRS and T-wave amplitudes are distorted • While simpler than search-back methods, VMD iterations may still be demanding for ultra-low-power devices

Table 2.4: Cont. . . QRS detection

Author	Dataset	Methods	Performance Results	Limitations
(Dhyani et al., 2025)	Not explicitly mentioned	• Preprocessing: Downsampling, bandstop (50 Hz), high-pass (<0.5 Hz), and low-pass (30-50 Hz) filtering. • Feature Extraction: Derivative, squaring, moving average integration • Detection: FSM with threshold-based R-peak detection • Implementation: VHDL in Xilinx ISE 14.7, simulated in Modelsim 10.0; tested on Spartan-3E, Virtex-4, Spartan-6, Virtex-5, Virtex-7 FPGAs	• Best FPGA (Virtex-7): Delay = 7.120 ns, Power = 1.95 mW, Frequency = 750 MHz	• Dataset ambiguity: No explicit mention of the ECG dataset used • Unclear performance on ultra-low-power wearables
(Sharma and Sunkaria, 2016)	• Fantasia (FTD) • MIT-BIH Arrhythmia (MIT-AD) • MIT-BIH Normal (MIT-NSD) • CHF (CHFD) • Self-recorded	• Two-stage median filter, Savitzky-Golay smoothing, Kurtosis-based FP reduction • Sauvola's baseline correction • Cubed signal amplification • Isoelectric line detection	• FTD: Se = 99.90%, +P = 99.91%, DER = 0.19%, Ac = 99.81% • MIT-AD: Se = 99.50%, +P = 99.56%, DER = 0.93%, Ac = 99.08% • MIT-NSD: Se = 99.36%, +P = 99.43%, DER = 1.21%, Ac = 98.81% • CHFD: Se = 99.68%, +P = 99.78%, DER = 0.52%, Ac = 99.46% • Self-recorded: Se = 99.97%, +P = 99.99%, DER = 0.04%, Ac = 99.96%	• Limited validation on extreme arrhythmias • Parameter sensitivity (e.g., window sizes) • Baseline drift correction may fail in extreme wander
(Chen and Chuang, 2017)	MIT-BIH Arrhythmia Database (48 half-hour ECG recordings, 360 Hz sampling, includes normal and abnormal rhythms like PVC, LBBB)	• Signal Enhancement: Band-pass filter (0.5-17 Hz) with zero-sum masking for QRS enhancement and P/T wave suppression • QRS Detection: Static thresholds (0.22 crest, -0.2 trough) with four case-based rules for fiducial point detection • R Point Recognition: Four QRS waveform templates and hierarchical detection of S, Ra, and Q points	Se: 99.82%, +P: 99.81%, DER: 0.36%	• Not validated for multi-lead ECG • Fixed thresholds: May fail under extreme noise • Primarily tested on MIT-BIH; lacks clinical trials with wearable motion noise • Limited adaptability to dynamic noise

PPV, +P, and P+ indicate positive predictive value, ALO- Antlion Optimization, DFOD- Digital Fractional Order Differentiator, PVCs- Premature Ventricular Contractions, FPGA- Field-Programmable Gate Array, AST- Adaptive Stockwell Transform, AMST- Adaptive Modified Stockwell Transform, QTV- QT interval variability, GNB- Gaussian naive Bayes, TQWT- Tunable Q Wavelet Transform, ADASYN- Adaptive synthetic sampling approach, FOS- First order statistics, GLCM- Gray Level Co-occurrence Matrix, SFM- Statistical Feature Matrix, FDTA- Fractal Dimension Texture Analysis, GLSZM- Gray Level Size Zone Matrix

2.3 Spectral and Non-linear Analysis Methods for the Classification of Cardiac Diseases in Heart Rate Variability Signals

The autonomic nervous system (ANS) regulates heart rate through the opposing actions of its sympathetic (activating) and parasympathetic (inhibitory) branches. Heart rate variability (HRV) originates from the dynamic interaction between these two systems, reflecting continuous oscillations in heart rate. As a non-invasive measure, HRV works as a quantitative indicator of ANS function, capturing beat-to-beat variations influenced by physiological factors. HRV analysis has emerged as a powerful, non-invasive tool for assessing cardiac autonomic regulation and predicting cardiovascular risks, including sudden cardiac death (SCD), myocardial Infraction, Coronary artery diseases and congestive heart failure (Ziemssen and Siepmann, 2019). The list of various types of cardiovascular diseases and their description has been illustrated on Table 2.5.

Reduced HRV is strongly associated with adverse outcomes, such as severe ventricular arrhythmias and increased mortality following acute myocardial infarction (Electrophysiology, 1996). Traditional linear methods, such as spectral analysis, quantify autonomic activity by evaluating low-frequency (LF) power (0.04–0.15Hz) and high-frequency (HF) power (0.15–0.40Hz) components (Malik et al., 1996). The HF component primarily reflects parasympathetic activity, while the LF power is influenced by both sympathetic and parasympathetic inputs. In addition, the LF/HF ratio provides a key metric for assessing autonomic balance, making HRV a valuable tool for evaluating cardiovascular health and ANS regulation. While time-domain HRV analysis provides computational simplicity, they are unable to differentiate between sympathetic and parasympathetic influences on heart rate variability.

However, recent advancements highlight the importance of non-linear and time-frequency techniques in capturing the complex, dynamic nature of HRV signals. Non-linear methods, including entropy-based measures and detrended fluctuation analysis, provide deeper insights into the chaotic behavior of heart rhythms, while time-frequency analysis enhances the detection of non-stationary features critical for disease diagnosis. Together, these approaches offer a comprehensive framework for evaluating autonomic dysfunction, classifying cardiovascular diseases, and improving clinical prognostication. Despite the simplicity of time-domain HRV measures, their inability to differentiate between sympathetic and parasympathetic contributions underscores the need for advanced analytical techniques. The complexity of the cardiovascular (CAV) system prevents accurate characterization through time or frequency domain

Table 2.5: List of major cardiovascular disease types and a description of each type

CVD Type	Description
Coronary Artery Disease	• The formation of atherosclerotic plaques in coronary arteries results in coronary lumen narrowing that leads to heart blockages and eventually • Resulting from narrowed coronary arteries that provide blood to the heart muscle (Tsipouras et al., 2008), (Libby and Theroux, 2005), (Singh et al., 2021) (Akella and Akella, 2021), (Acharya et al., 2017a), (Kurt et al., 2008) (Jahmunah et al., 2021)
Myocardial Infarction	• Caused by a blockage in one of the coronary arteries, resulting in blood retention and potentially damaging or killing a portion of the heart muscle (Sankari and Adeli, 2011), (Rai and Chatterjee, 2022), (Fan and Watanabe, 2022) (Susič et al., 2024), (Harper and Armelagos, 2010), (Liu et al., 2017) (Mozaffarian et al., 2016)
Congestive Heart Failure	• The malfunction of heart pumping leads to inefficient blood circulation throughout the body • Also known as heart failure • Can arise from hypertension, CAD, and heart valve diseases (Porumb et al., 2020), (Tripathy et al., 2019), (Singh et al., 2024)
Cardiomyopathies	• Related to conditions that affect heart muscle strength leading to reduced blood pumping efficiency • Can be acquired or inherited, and encompasses several types including dilated cardiomyopathy and hypertrophic cardiomyopathy • Refers to a set of diseases that target heart muscle tissue
Peripheral Heart Disease	• Affects blood vessels which provide blood to the arms and legs
Cerebrovascular Disease	• Condition where blood vessels and blood flow to the brain are affected
Congenital Heart Disease	• Present from birth and includes structural abnormalities in the heart • May affect the heart's walls, valves, or blood vessels
Vascular Disease	• Refers to blood vessel abnormalities in arteries and veins throughout the body which can interfere with normal blood circulation

analysis alone. To overcome this challenge, time-frequency (TF) approaches have been developed to accurately monitor changes in HRV spectra (Besfat et al., 2024b; Li et al., 2010). The Fast Fourier Transform (FFT) is commonly used for power spectrum estimation in HRV analysis due to its computational efficiency and high frequency resolution. However, this technique does not offer details about the temporal localization of frequency components in the signals (Alghoul et al., 2017a). To overcome this limitation, various time-frequency analysis tools have been developed for HRV data. These traditional tools, including the short time Fourier transform (STFT), Wigner-Ville distribution (WVD) (Liu et al., 2023a), and wavelet transform (Singh et al., 2017a, 2018a), offer valuable insights into the dynamic nature of HRV, allowing for a more comprehensive understanding of cardiovascular regulation and health.

To overcome the inaccurate TF localization of these techniques, recently Optimized adaptive modified Stockwell transform (OptADMST), Synchroextracting transform (SET), Synchrosqueezing transform (SST), and reassign ment (RS) method has been proposed by different authors. Comparing with all the other time frequency representations (TFRs), the linear STFT is relatively simple (Wang and Veluvolu, 2017a) but the resolution which it can provide is limited in a way due to the Heisenberg-Gabor uncertainty principle. Even though the bilinear Wigner–Ville distribution (WWD) affords the best concentration of chirp signals it experiences appearances of cross-terms that interferes with the representation of signal elements. TF resolution of such classical methods is low; thus making them unable to accurately characterize the non linear behaviors of non-stationary signals. SST is a valuable post-processing time-frequency analysis (TFA) method in non-stationary signal processing, but it suffers with lower TF resolution (TF blurs) for components that exhibit rapid TF variations. Even though SST, SET, and RS provide a better TF localization compared to the classical methods, still they suffer in detecting accurately these subtle changes in the cardiovascular signal.

A key requirement for an effective TFR is achieving sufficient concentration of signal components to accurately represent the signal. Reassignment technique is a TF analysis which provides a higher TF resolution and greater energy concentration of a signal,(Yu et al., 2017; Bakiya et al., 2020; Li et al., 2020b; Rajinikanth et al., 2023). The RS method effectively enhances signal concentration in the TF domain by reallocating energy distribution based on the gravitational center of the energy contribution (Yang et al., 2014; Li, 2022; Auger and Flandrin, 1995; He et al., 2019). RS reassigns the TF spectrogram to the instantaneous frequency trajectory, achieving higher TF resolution (Flandrin et al., 2018; Auger et al., 2013); however, the use of a fixed Gaussian window reduces the clarity of the representation.

The study in (Acharya et al., 2014) aims to differentiate between normal individuals and those with CAD by analyzing HRV signals derived from ECGs. The authors proposed a comprehensive analysis of HRV signals using time-domain features, frequency-domain fea-

tures, and nonlinear methods. The time attributes include mean HRV, RMSSD, NN50, and pNN50 calculations. Frequency feature incorporate the Power spectral density (PSD) across VLF, LF, and HF bands, while the non-linear feature extraction involves Poincaré plots, Recurrence Quantification Analysis (RQA), entropy measures (ApEn, SampEn), Higher Order Spectra (HOS), Detrended Fluctuation Analysis (DFA), Empirical Mode Decomposition (EMD), and correlation dimension. Authors in (Acharya et al., 2017b) proposed an automated method for detecting CAD using ECG signals by leveraging a nonlinear Higher-Order Spectra (HOS) analysis. The noise and baseline wander was removed by using wavelet decomposition in the pre-processing stage. The nonlinear HOS features (bispectrum and cumulants) were employed to capture hidden patterns in ECG data.

An online algorithm for decomposing HRV into its four frequency components such as: High Frequency (HF), Low Frequency (LF), Very Low Frequency (VLF), and Ultra-Low Frequency (ULF) has been presented in (Adamczyk and Polak, 2025). This study introduced an online Variational Mode Decomposition (VMDon) algorithm based on Variational Mode Decomposition (VMD) to decompose HRV signals in real time, enabling continuous ANS assessment. The authors validate VMDon against synthetic and real HRV datasets, comparing it with adaptive VMD (AVMD), Continuous Wavelet Transform (CWT), and Wavelet Package Decomposition (WPD). The paper in (Aggarwal and Kumar, 2022) proposed a ML models to distinguish between CHF and Normal Sinus Rhythm (NSR) patients using HRV signals. The feature selection method includes filter method, wrapper method, and embedded method. They have also employed time domain measures, frequency-Domain measures, and non-linear measures HRV features.

An integrated, portable, and cost effective HRV analysis system named STREME, has been designed for research and clinical use in the study conducted by (Arvind et al., 2020). Their system includes a compact ECG acquisition device (PC-ECG12) and software for HRV analysis, featuring time-domain, frequency-domain, and nonlinear parameters. Authors in (Colak, 2009) conducted the impact of pre-processing steps, such as detrending and ectopic beat correction on the time-frequency analysis and spectral estimation of HRV signals. The aim of their work was to improve the accuracy of HRV analysis for detecting ventricular tachyarrhythmia (VT) or ventricular fibrillation (VF) episodes. Detrending removes slow, nonstationary trends using the smoothness prior method, which acts like a time-varying high-pass filter. While, ectopic beat correction utilizes the Integral Pulse Frequency Modulation (IPFM) model to correct abnormal heartbeats that can distort HRV analysis. The study in (Ebrahimzadeh et al., 2018) proposed a technique to predict Sudden Cardiac Death (SCD) by analyzing ECG and HRV signals. The approach includes linear, nonlinear, and TF analyses to extract discriminating features, accompanied by classification using Multilayer Perceptron (MLP) and k-Nearest

Neighbor (KNN) neural networks. The study in (Estévez et al., 2016) explored the application of different spectral analysis methods to assess HRV, with a main focus on the Lomb-Scargle (L-S) method. This paper compares the L-S method with traditional spectral analysis methods including classic modified periodogram, Welch procedure, and autoregressive Burg method.

The research conducted by (Isler, 2016) aims to distinguish between systolic and diastolic CHF using short term HRV analysis combined with machine learning classifiers. To improve the diagnostic accuracy, they have applied two normalization techniques such as, Heart Rate Normalization (HRN) and Feature Normalization (MINMAX). Then after, a total of 29 HRV features were extracted from time-domain, frequency-domain (FFT, Lomb-Scargle, Wavelet), and nonlinear (Poincaré plot) analyses. Subsequently, they employed Nearest Neighbor (NN) and Multi-Layer Perceptron (MLP) classifires and validated by Leave-one-out cross-validation. HRV features has been utilized for classifying different cardiac conditions (such as normal heart rhythm, arrhythmia, supraventricular arrhythmia, and congestive heart failure) in the study presented by (Jovic and Bogunovic, 2011). This study integrates 11 linear and nonlinear HRV features, incorporating SDNN (standard deviation of R-R intervals), RMSSD (root mean square of successive differences), pNN20 (percentage of successive R-R intervals differing by >20 ms), and HRV triangular index (HTI), spatial filling index (SFI), correlation dimension (D_2), central tendency measure (CTM), and four approximate entropy features (ApEn1-ApEn4).

The paper in (Jovic et al., 2019) investigated the feasibility of accurately detecting CHF using short-term (5-minute) HRV analysis combined with a hybrid feature selection method, combining filter, wrapper, and iterative elimination techniques. Authors in (Kumar et al., 2023) explored the utilization of HRV features derived from ECGs to predict CAD and myocardial infarction (MI) diseases. For the classification of theses arrthymia types, they have leveraged artificial neural networks (ANN) and support vector machines (SVM) based on HRV parameters. The effectiveness of standard long-term HRV measures has been investigated in diagnosing chronic heart failure (CHF) using a classification and Regression Tree (CART) method as reported in (Melillo et al., 2011). This study employed the processes of HRV feature extraction, feature selection, and classification model. An automated method for diagnosing CAD using heart rate signals derived from ECG data has been presented in (Patidar et al., 2015). Their approach leverages the Tunable-Q Wavelet Transform (TQWT) to decompose heart rate signals into sub-bands, followed by feature extraction using a nonlinear measure Centered Correntropy (CC). These features are then transformed utilizing Principal Component Analysis (PCA) and classified based on Least Squares Support Vector Machine (LS-SVM) with various kernel functions (RBF, Morlet, and Mexican hat wavelet).

An investigation of the interchangeability between two spectral analysis methods such as Fast Fourier Transform (FFT, Welch's periodogram with Hanning windowing) and Autoregres-

sive (AR, 16th-order autoregressive model with forward-backward least squares fitting) has been introduced in (Pichon et al., 2006) for assessing HRV in healthy subjects at rest and during orthostatic stress. Utilization of HRV analysis for diagnosis of CAD has been presented by the authors in (Poddar et al., 2015). They derive the HRV features from linear (time and frequency domain) and non-linear methods, followed by dimensionality reduction using Principal Component Analysis (PCA) and classification using machine learning. The study in (Rohila and Sharma, 2020) proposed a non-invasive method to detect the risk of Sudden Cardiac Death (SCD) by analyzing HRV in four subject groups such as NSR, CAD, CHF, SCD patients (1 hour before ventricular fibrillation onset). They have utilized five time-frequency features derived from the Generalized S-transform and uses nonlinear techniques (entropy measures, Poincaré plots, detrended fluctuation analysis) alongside traditional methods, enhancing HRV analysis.

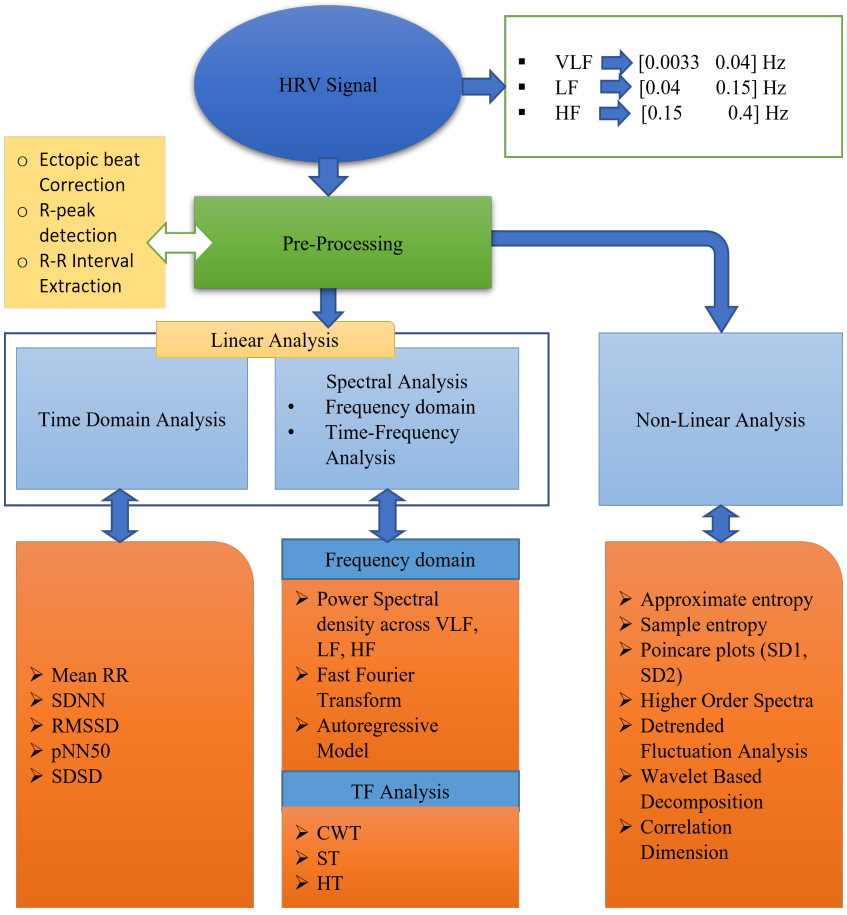

Figure 2.8: Structure of the spectral and non-linear analysis of HRV signal

Investigation of the ability of long-term HRV features to discriminate between low-risk (LRP) and high-risk (HRP) CHF subjects have been reported in (Shahbazi and Asl, 2015). They have also evaluated the impact of feature dimension reduction on classification accuracy. The paper in (Sharma et al., 2019) proposed a method for detecting CAD using ECG signals through time-

frequency analysis. They have employed the Improved Eigenvalue Decomposition of Hankel Matrix and Hilbert Transform (IEVDHM-HT) method to generate Time-Frequency Representations (TFRs) of ECG beats. In their study, three time-frequency-based features such as mixed average time-frequency, frequency average, and time average had been investigated. The authors in (Singh et al., 2017a) proposed an advanced signal processing method, the Adaptive Continuous Morlet Wavelet Transform (ACMWT), for analyzing HRV in both healthy and arrhythmia subjects. The key focus of this study was on enhancing the energy concentration and resolution of time-frequency representations of HRV signals, which are non-stationary and dynamic. Their method incorporates a shape parameter q optimized (q_{opt}) to maximize energy concentration in time-frequency analysis.

A non-invasive method for early detection of Cardiac Artery Disease (CAD) and Cardiac Heart Failure (CHF) has been proposed in (Singh et al., 2018b) using Higher Order Spectra (HOS) analysis of HRV signals. By extracting 10 nonlinear features from HRV data, the paper distinguishes between healthy subjects and patients with CAD or CHF, demonstrating the clinical utility of HOS in cardiac diagnostics. The paper in (Singh et al., 2019) presented a method for detecting arrhythmias using adaptive continuous Morlet wavelet transform (ACMWT) and a back-propagation neural network (BPNN). Their approach focuses on extracting time-frequency (T-F) features (Flatness, Flux, Skewness, Kurtosis, Shannon entropy, Renyi entropy, coefficient of variation) from HRV signals to classify segments as normal or arrhythmic. The paper in (Sinha and Das, 2020) introduced an automated system for diagnosing cardiac arrhythmias using a three-stage feature fusion and classification model based on Discrete Wavelet Transform (DWT). The system aims to distinguish between NSR and various arrhythmias, including ventricular arrhythmias (VF-VT) and atrial arrhythmias (AF and SV), by leveraging nonlinear and statistical features extracted from ECG signals.

The study in (Sood et al., 2016) proposed a computer-assisted method for diagnosing CAD using Heart Rate (HR) signals derived from ECG data. Their method involves usage of Empirical Mode Decomposition (EMD) to decompose HR signals into Intrinsic Mode Functions (IMFs), from which five features are extracted (Second-Order Difference Plot (SODP) area, Analytic Signal Representation (ASR) area, Amplitude Modulation (AM) bandwidth, Frequency Modulation (FM) bandwidth, Fourier-Bessel Expansion (FBE)-based mean frequency). Automated detection of CAD using ML and deep learning techniques has been applied to ECG signals in the study conducted by (Yao et al., 2020). This study aims to improve the automated diagnosis of CAD by leveraging features extracted from the QT interval time-series and ST-T segment waveforms in ECG signals.

In (Chen et al., 2021b), a residual network has been employed to achieve an Accuracy (Acc) of 96.5%, Specificity (Sp) of 95%, recall of 82.4%, and F-score of 82.5%. Authors in

(Fang et al., 2022) obtained Acc of 95.65%, Sp of 90.80%, recall of 97.34%, F-score of 97.07% from PTB database using Multi-Visual Geometry Group (VGG) in CNN model. Moghadam et al. (Moghadam and Asl, 2023) proposes a random forest (RF) algorithm to achieve Acc of 96.54%, recall of 99.74%, and F-score of 97.88%. An accuracy of 82.36% was achieved by (Sopic et al., 2018) through the utilization of time-frequency features and RF classification. The authors of (Han and Shi, 2019) proposed a method that incorporates global energy entropy features derived from the maximal overlap discrete wavelet packet transform (MODWPT) and local morphological features. The classification task is accomplished using SVM, resulting in an Acc of 99.75%. An 85.97% sensitivity (Se), 74.03% specificity and an 86.85% precision (Pr) of the MI detection on ECG signals was found by (Degerli et al., 2021) using SVM classifier.

In study (Zhang et al., 2020a), the author designed a radar-based health-radio technique for the extraction of HRV from the radio-frequency (RF) signal. As it is shown in the paper, the MI detection yielded 81.5% accuracy when using an SVM classifier. Multilead diagnostic attention-based recurrent neural network (MLDA-RNN) was proposed in (Prabhakararao and Dandapat, 2020) to diagnose the severity levels of MI, and an accuracy of 97.79% was observed. In (Sahu and Ray, 2021), for MI detection and localization, an efficient technique using variational mode decomposition (VMD) and regularized neighborhood component analysis (RNCA) is suggested. Overall employing this methodology reached an Ac of 99.82% with the KNN classifier. Furthermore in the study made by (Zhang et al., 2019), harmonic phase distribution was used for the detection of MI. Using logistic regression, the overall parameters were found to be 95.6% for Acc, 96.5% for Se, and 92.7% for Specificity.

HRV signal analysis has become one of the widely adopted non-invasive method for assessing the regulation of the cardiac autonomic function by parasympathetic and sympathetic branches of a nervous system. HRV refers to the natural variations in the time intervals between consecutive heartbeats (R-R in terval), extracted from ECG signal (Arco et al., 2024). It has been used widely in diagnosis of CAD (Abdar et al., 2019; Muhammad et al., 2021), and CHF (İşler and Kuntalp, 2007; Isler et al., 2019; Hussain et al., 2021). This signal is mostly quantified by very low frequency power (VLF), low frequency power (LF), and a high frequency power (HF) segments (components), and these frequency bands are defined in ranges of [0.0033 0.04] Hz, [0.04 0.15] Hz, and [0.15 0.4] Hz, respectively. The application of machine learning and deep learning techniques has demonstrated remarkable out comes in the detection of various cardiac diseases including CAD and CHF arrhythmias (Masetic and Subasi, 2016; Moshawrab et al., 2023; Baghdadi et al., 2023; Ahmed et al., 2023; Honi and Szathmary, 2024; Faust and Acharya, 2021; Wang et al., 2025; Mahananto et al., 2024).

Recently, Convolutional Neural Network (CNN) has been utilized across various applications, including speech recognition, bio-informatics, image classification, facial recognition,

and computer gaming (Yildirim et al., 2019). CNN is capable of automatically extracting and learning valuable features from input data, generating deep features that greatly minimize the require ment of manual feature extraction (Sumalatha et al., 2024). However, effectively training deep CNN necessitates a large dataset to ensure adequate generalization capabilities. The conventional 2D CNN model can be impractical for many real world 1D signal applications, where labeled data is often limited (Kiranyaz et al., 2021).

The summary of various literature in the time, spectral, time-frequency, and non-linear analysis of HRV has been illustrated in Table 2.6, 2.7, 2.8, and 2.9. The structure of the spectral and non-linear analysis methods of HRV signal is illustrated in Fig. 2.8.

Table 2.6: A summery of time, spectral, time-frequency, and non-linear analysis of HRV and ECG signals

Author	Dataset	Methods	Performance Results	Limitations
(Acharya et al., 2014)	• Source: BIOPAC recordings (500 Hz sampling) • Subject: ECG recordings from 10 CAD patients and 10 healthy controls (age range: 40-70 years) • Total data: 61 normal and 82 CAD ECG datasets (1000 samples each)	• Preprocessing: Bandpass (0.3-50 Hz) and notch (50 Hz) filtering • Pan-Tompkins algorithm for R-peak detection • Time-Domain Analysis: mean HR, RMSSD, NN50, and pNN50 • Frequency-Domain Analysis: PSD using Fast Fourier Transform (FFT) and Autoregressive (AR) modeling Freq. bands: VLF, LF, HF, LF/HF ratios • Nonlinear Analysis: Poincaré Plots-SD1 (short-term variability) and SD2 (long-term variability); RQA-Determinism (DET), recurrence rate (REC), mean/max diagonal line lengths, ApEn and SampEn measures, HOS, DFA-Self-similarity index (α); EMD- Intrinsic Mode Functions (IMFs)	• Time-Domain: Lower mean HR (45.6 vs. 52.9 bpm, $p = 0.0008$) and NN50/pNN50 in CAD • Frequency-Domain: Reduced PSD in CAD (VLF/LF bands) • Nonlinear: CAD: Higher RQA parameters (DET: 99.4 vs. 98.4, $p < 0.0001$), lower entropy (ApEn: 1.05 vs. 1.33, $p < 0.0001$); Distinct Poincaré/HOS plots for CAD vs. normal	• Only 10 subjects per group, limiting generalizability • Feature ranges were proposed, but no ML model was built for automated diagnosis • Real-time CAD detection was not tested • Assumed uniform medication impact, which may not hold in practice
(Acharya et al., 2017b)	• Normal ECG signals: Fantasia database (250 Hz) (40 subjects: 20 young, 20 old) • CAD ECG signals: St. Petersburg Institute of Cardiological Technics 12-lead Arrhythmia Database, 257 Hz (7 patients with CAD and hypertension)	• Denoising via Daubechies 6 (db6) wavelet • R-peak detection using Pan-Tompkins • Feature Extraction: Bispectrum (136 features), Cumulants (136 features) • Dimensionality Reduction: PCA • Feature Ranking: Bhattacharyya, entropy, t-test, ROC, Wilcoxon, fuzzy mRMR • Classification: KNN & Decision Tree (DT)	• Bispectrum with KNN: 98.17% acc, 94.57% se, 99.34% spe (13 features) • Cumulants with DT: 98.99% acc, 97.75% se, 99.39% sp (31 features)	• Only 7 CAD patients were used, lacks generalizability • HOS feature extraction and PCA are computationally intensive, potentially limiting real-time applications
(Adamczyk and Polak, 2025)	• Synthetic HRV: Simulated 6-hour signal with known AM/FM-modulated HF, LF, VLF, and ULF components; Added Gaussian noise ($\sigma = 0.01$ s) to mimic real-world variability • Real HRV: Vincent's University Hospital Sleep Dataset (18 subjects, 128 Hz sampling); Apnea-ECG Database (18 subjects, 100 Hz sampling)	• R-peak detection, outlier correction, and cubic spline interpolation • VMDon	• Acc: HF: AVMD (0.941) > VMDon (0.915) > CWT (0.929) > WPD (0.878) • LF: AVMD (0.991) > VMDon (0.975) > CWT (0.985) > WPD (0.945) • VLF: CWT (1.000) > VMDon (0.997) > AVMD (0.994) > WPD (0.988) • ULF: VMDon (1.000) > CWT (0.998) > WPD (0.998) > AVMD (0.990)	• ULF extraction requires a 30-minute window, limiting real-time application • VMDon's HF residuals were higher than AVMD • Limited to overnight HRV; daytime dynamics (e.g., physical activity) were not assessed
(Aggarwal and Kumar, 2022)	• Source: Max Hospital, Mohali (real data) • HRV data from 419 instances (subjects)	• Feature Selection: Filter Method (ANOVA, mutual info, SelectKBest, 33 features), Wrapper Method (SFS, 25 features), Embedded Method (Lasso, 12 features) • HRV Features: Time-domain (SDNN, RMSSD, pNN50), Frequency-domain (ULF, VLF, LF, HF), Non-linear (Poincaré plots, entropy) • ML Classifiers: RF, KNN, SVM, NB, DT	• Best Performance: Filter Method with RF (99.21% acc) • Avg. Acc: Without FS: 86.35%, Filter: 95.40%, wrapper: 94.92%, embedded: 93.81%	• Only 419 instances were used, which may limit generalizability • Performance varies based on the chosen method (filter, wrapper, embedded) • Only traditional ML models were tested
(Arvind et al., 2020)	• Participants: 46 healthy subjects (15 men, 31 women; mean age 27.67 ± 7.75 years) • Recordings: 5-minute resting ECG in a controlled environment (simultaneous capture via STREME and RMS VarioWin)	• The study employed ECG data acquisition -PC-ECG12 hardware (portable, 3-lead). • HRV Parameter Extraction: Time-domain analysis- Mean RR, SDNN, RMSSD, pNN50; • Frequency-domain analysis- LF (0.04-0.15 Hz), HF (0.15-0.4 Hz), LF/HF ratio using FFT-based spectral estimation • Bland-Altman plots to assess agreement in HRV parameters - for validation • Beat detection using a modified Pan-Tompkins algorithm • Cubic spline interpolation for RR interval resampling	• Correlation (r): RMS VarioWin- 0.95-0.99 for all parameters; Kubios HRV- 0.94-0.99 • Bland-Altman: 95% of residuals within agreement limits, confirming minimal bias	• Validation was performed only on healthy indivisuals • Only resting-state HRV was analyzed • Focused on Short-term (5-min) recordings, long-term (24-hour) HRV validation is needed.

Table 2.7: Cont. . . linear and non-linear analysis

Author	Dataset	Methods	Performance Results	Limitations
(Colak, 2009)	• Spontaneous Ventricular Tachyarrhythmia Database (VTA)- from PhysioNet • 135 pairs of R-R interval time series from 78 patients	• Preprocessing: Detrending and ectopic beat correction • Time-Frequency Analysis: Spectrogram (STFT), CWT (Morlet wavelet) • Spectral Analysis: Nonparametric (Periodogram, Welch's periodogram), Parametric (Burg's periodogram (AR model, order p=16))	• CWT: Best time-frequency resolution for ectopic beats and VT/VF localization • Burg's Periodogram: Most accurate PSD, reduces noise by 20 dB in 0.2-0.6 Hz • Welch's Periodogram: Better than standard periodogram but inferior to Burg's	• The IPFM method for ectopic correction is computationally intensive for long Holter recordings • CWT, while powerful, requires careful parameter tuning (e.g., wavelet selection, scales) • Burg's method assumes an AR model, which may not fit all HRV dynamics perfectly • The study focuses on only VT/VF episodes • Spectrogram suffers from fixed resolution limitations
(Ebrahimzadeh et al., 2018)	• MIT-BIH Sudden Cardiac Death Holter Database • 35 SCD subjects • 35 healthy controls	• Preprocessing: Pan-Tompkins QRS detection, RR interval extraction • Feature Extraction: Linear: Time-domain (MNN, SDNN, RMSSD, SDSD, PNN50), Frequency-domain (LF, HF, VLF, LF/HF via Burg's method) Nonlinear: Poincaré plot (SD1, SD2), DFA TF: Smoothed Pseudo Wigner-Ville Distribution (SPWVD), windowed energy features (MAX, MIN, DIF, STD) • Classification: MLP (3-layer), KNN (k=7), Leave-One-Out Cross-Validation (LOOCV)	• MLP Accuracy: 99.73% (1 min before SCD), 96.52% (2 min), 90.37% (3 min), 83.96% (4 min) • KNN Accuracy: 98.32% (1 min), 95.04% (2 min), 88.93% (3 min), 81.49% (4 min) • TF features alone: 99.16% (1 min) vs. linear (74.36%)	• Only 70 subjects (35 SCD, 35 healthy), limiting generalizability • Predictions are reliable only up to 4 minutes before SCD, limiting clinical utility for longer-term prevention • SPWVD and nonlinear analyses are resource-intensive for real-time applications
(Estévez et al., 2016)	• 120 healthy young adults (60 male, 60 female, aged 17-25) participants • ECG recordings (6 min, resting state, spontaneous breathing)	• Pre-processing: Artifact removal, RR interval extraction, spectral analysis; detrending, Butterworth filtering, interpolation • Classic modified periodogram (Hann window), Welch procedure (smoothed periodogram), Autoregressive Burg method (order 25), L-S method	• Absolute PSD: Classic & Welch greater than L-S & Burg • Normalized PSD: L-S: VLF (12.3%), LF (22.9%), HF (34.0%), Burg: Lowest VLF, similar LF/HF to L-S • Mean Frequencies: L-S & Welch aligned for VLF, Burg overestimated HF	• Focused only healthy indivisuals • L-S requires careful IOFAC tuning • The L-S method produces noisy, high-variance spectra, necessitating a smoothing procedure
(Isler, 2016)	• ECG data from Dokuz Eylül University, Faculty of Medicine • 18 systolic and 12 diastolic CHF subjects	• QRS detection based on Pan-Tompkins algorithm • Data pre-processing: HRN- Adjusted RR intervals to a fixed mean heart rate (75 bpm) MINMAX- Scaled features to a [0, 1] range to reduce bias • Time-domain features: Mean RR, SDNN, RMSSD, NN20, PNN20, SDSD • Frequency-domain features: FFT-based Welch periodogram (VLF, LF, HF, LF/HF ratio), Lomb-Scargle periodogram, Wavelet entropy • Nonlinear features: Poincaré plot parameters (SD1, SD2, SD1/SD2 ratio) • Classification: MLP, Nearest Neighbor • Validation: Leave-one-out cross-validation (LOOCV)	• Best Model: MLP with HRN and MINMAX normalization Acc: 96.43%, Se: 93.75%, Sp: 100% • NN Performance: 89.29% acc with HRN and MINMAX	• Small sample size (only 30 patients) • Short-term HRV analysis (5-min segments) may not reflect full autonomic activity • No advanced feature selection

Table 2.8: Cont. . . linear and non-linear analysis

Author	Dataset	Methods	Performance Results	Limitations
(Jovic and Bogunovic, 2011)	• 100 subject records from six PhysioBank databases • Normal rhythm (25), Arrhythmia (25), Supraventricular arrhythmia (25), CHF (25) • 5-minute R-R interval recordings per record	• Feature Extraction: Linear: SDNN, RMSSD, pNN20, HRV triangular index (HTI) Nonlinear: SFI, CTM, correlation dimension (D_2), ApEn1-ApEn4 • Machine Learning: Clustering: K-means, EM Classification: C4.5, Bayesian network, ANN, SVM (linear & squared), Random Forest (RF)	• Best Classifier: Random Forest (RF) – 99.7% (binary), 99.6% (multiclass) • ANN: 99.1% (binary), 91.4% (multiclass) • SVM (squared): 98.9% (binary), 98.4% (multiclass) • Bayesian Network: 98.9% (binary), 99.4% (multiclass) • C4.5: 97.2% (binary), 92.2% (multiclass) • Clustering: ∼50% (multiclass), ∼75% (binary) accuracy	• Only 25 records per class, may lack generalizability • Misclassification risks (e.g., false negatives) not evaluated • Feature Bias: pNN20 used instead of more common pNN50 • Multi-period feature extraction increases computational load
(Jovic et al., 2019)	• 4 PhysioNet databases (NSR1, NSR2, CHF1, CHF2) • 66 healthy (NSR), 42 CHF subjects	• Feature Extraction: 111 HRV features (time/frequency domain, nonlinear, symbolic dynamics) • Feature Selection: Symmetrical Uncertainty (Filter) → Ranked features Naive Bayes Wrapper → Reduced feature set Greedy Iterative Elimination → Final refinement (2-4 features) • Classifiers: RTF, SVM, RF, MLP, k-NN • Validation: LOSOCV (subject-level and feature vector-level)	• RTF/RF: ACC = 90.7%, se = 78.6%, spe = 98.6% (4 features) • SVM: ACC = 88.0%, se = 78.6%, sp = 93.9% (2 features) • Single-Feature Performance: MaxAlphaEn (RTF) achieved 80.6% acc alone	• Clinical deployment requires larger datasets (the study utilizes small number of sample-42 CHF subjects) • Fixed 128/250 Hz sampling may affect spectral features • Linear interpolation may not fully preserve HRV dynamics
(Kumar et al., 2023)	• 70 male subjects (30 controls, 30 CAD, 10 MI) • Lead-II ECG recordings	• Bandpass (0.05-35 Hz) and high-pass (2 Hz) filtering for preprocessing • HRV Feature Extraction: Time-domain → mRR, SDNN, RMSSD, pNN50 Frequency-domain → LF, HF, LF/HF Nonlinear → SD1, SD2, entropy measures • Machine Learning Models: ANN → 3-layer feed-forward, optimized with hidden nodes & learning rates SVM → RBF kernel, hyperparameter tuning (C, γ) Validation → 80% training, 20% testing	• ANN (Time-domain features): 100% acc (CAD vs. Control), 99.6% acc (MI vs. Control), 98.3% (Three-class: Control/CAD/MI) • SVM (Time-domain features): 75.5% (CAD vs. Control), 98.9% (MI vs. Control), 98.7% (Three-class) • Frequency/nonlinear features: Lower accuracy ($\leq$ 88%)	• Small dataset • Time-domain features outperformed others, but their robustness in real-world noisy ECG data remains unverified • The study used resting ECGs
(Melillo et al., 2011)	• Normal individuals (71): MIT-BIH Normal Sinus Rhythm Database (18), Normal Sinus Rhythm RR Interval Database (53) • CHF Patients (39): CHF RR Interval Database (29), BIDMC Congestive Heart Failure Database (10)	• HRV Features: Time-domain (SDNN, RMSSD, SDANN, pNN12/pNN50) and frequency-domain (total power, ULF, VLF, LF, HF, LF/HF) • Feature Selection: Exhaustive search (8,092 combinations) • PSD Estimation: Welch's periodogram and Lomb-Scargle periodogram • Classification: CART with Gini index, 10-fold cross-validation, cost-complexity pruning	• Best Model (total power + RMSSD + SDANN): Se = 89.74%, Sp = 100%, Acc = 96.36%, AUC = 94.87% • Single-Feature Models: SDNN: Se = 87.18%, Sp = 97.18%, SDANN: Se = 82.05%, Sp = 100% • Comparison: Outperformed Asyali's Bayesian classifier (81.82% se) but had lower sensitivity than Isler's wavelet entropy model (100%)	• Small and imbalanced dataset: 71 healthy vs. 39 CHF individuals • Performance may vary with larger, multi-center datasets • Thresholds derived from CART may need validation in real-world settings
(Patidar et al., 2015)	• Source: Iqraa Hospital, Calicut, India • Subjects: 20 (10 normal, 10 CAD) • ECG Recordings: 143 (61 normal, 82 CAD) (500 Hz sampling)	• Pre-processing: R-peaks are detected using the Pan-Tompkins algorithm, • Heart rate signals are derived from RR intervals • Signal Decomposition: TQWT (Q = 24-30) • Feature Extraction: Centered Correntropy - to capture nonlinear dynamics • Feature Transformation: PCA • Classification: LS-SVM with different kernel functions (RBF, Morlet, Mexican hat) • CAD Risk Index: Single-value index derived from PCA features	• Best Kernel: Morlet wavelet (Q = 24-30) Acc: 99.72% ± 0.27%, Se: 99.63% ± 0.40%, Sp: 99.81% ± 0.32%, Matthews Correlation Coefficient (MCC): 0.9956 ± 0.0051 • Comparison: Outperformed DWT, ICA, and other SVM-based methods	• Small Dataset: Only 20 individuals, lacks diversity in age and ethnicity • TQWT and LS-SVM may have computational load for real-time use • Performance may drop with noisy/poor-quality signals • CAD Risk Index requires further validation in clinical trials
(Pichon et al., 2006)	• 56 healthy adults in seated rest; 15 young trained men for orthostatic test	• FFT (Nonparametric), AR (Parametric) • HRV Indices: LF/HF power (ms^2), normalized units (NU) • Statistics: Paired t-tests, Bland-Altman analysis (bias, 95% LoA)	• Correlation: Strong for absolute power (r > 0.9, P < 0.01) but poor for NU/LF-HF ratio • Bland-Altman: HF power (ms^2) → Bias = -160 (FFT > AR), LoA = -642 to +322 • LF/HF ratio: Large discrepancies (e.g., 10.2 AR vs. 4.2 FFT in sitting) • Orthostatic Response: AR detected larger LF increases (2390 vs. 1502 ms^2) and LF/HF shifts (10.9 vs. 5.2)	• Sample Homogeneity: Predominantly young, healthy males in orthostatic test; may not generalize to other populations • Fixed 16th-order AR model may not optimize all datasets • FFT windowing (Hanning) could distort power estimates • Findings may not hold in subjects with arrhythmias or autonomic dysfunction

Table 2.9: Cont. . . linear and non-linear analysis

Author	Dataset	Methods	Performance Results	Limitations
(Poddar et al., 2015)	• 60 healthy males (NR) • 64 CAD subjects • ECG signals (Lead-II) were recorded using a BIOPAC system (500 Hz sampling rate)	• Preprocessing: RR interval extraction, resampling (4 Hz) • Feature Extraction: Time Domain (TD): SDNN, RMSSD, variance, SDSD, CV% Frequency Domain (FD): PSD via FFT/AR (VLF, LF, HF, LF/HF) Non-linear: Poincaré plot (SD1, SD2), ApEn, SampEn • Dimensionality Reduction: PCA • Classification: PNN, KNN, SVM (RBF kernel, optimized via grid search)	• Best Model: PCA-SVM Acc: 91.67%, Se: 86.67% (NOR), 96.67% (CAD) • PCA-KNN: 85.00% accuracy • PCA-PNN: 68.33% accuracy	• Only male subjects were included, limiting generalizability to females • CAD often coexists with diabetes/hypertension, but these were excluded
(Rohila and Sharma, 2020)	• PhysioNet databases: • MIT-BIH Normal Sinus Rhythm (NSRDB, 18 subjects) • Long-Term ST (LTSTDB, 23 CAD subjects) • BIDMC Congestive Heart Failure (CHFDB, 15 CHF subjects) • Sudden Cardiac Death Holter (SDDB, 20 SCD patients, • 1-hour pre-VF ECG) • Total: 76 subjects (912 segments of 5-min ECG each)	• Preprocessing: Noise removal, RR interval extraction • Feature Extraction: Nonlinear HRV → Entropy (Sample, Fuzzy, Permutation, Renyi, Bubble), Poincaré plot (SD1, SD2, SD12, GDE), DFA (α_1) • S-transform time-frequency features (Energy, Mean ST, Entropy) • Classification: SVM (Linear, Quadratic, RBF, Polynomial kernels) DT & Random Forest (RF, 100 trees) Validation: Kruskal-Wallis ANOVA, 10-fold cross-validation	• Best Model (RF): Acc: 91.67%, Se: 83.33%, Sp: 94.64%, Pr: 84.75%	• 76 subjects- Small dataset • Redundant features may affect efficiency - no feature selection • 5-min ECG segments may not suit real-time prediction
(Shahbazi and Asl, 2015)	• Source: Two public Holter databases from PhysioNet Congestive Heart Failure RR Interval Database (29 patients, NYHA I-III) BIDMC Congestive Heart Failure Database (15 patients, NYHA III-IV) • Final Dataset: 10 LRPs (NYHA I-II) and 29 HRPs (NYHA III-IV) after excluding records with <80% NN intervals	• Feature Extraction: Linear HRV → Time-domain (SDNN, RMSSD) and frequency-domain (LF, HF, LF/HF) Nonlinear HRV → ApEn, DFA (α_1), SD1/SD2, CD, Lmax • Feature Selection: p-value < 0.05 • Dimensionality Reduction: Generalized Discriminant Analysis (GDA) • Classifier: k-Nearest Neighbor (KNN, k=5) with leave-one-out cross-validation	• Best Model (Nonlinear + GDA + KNN) Acc: 100%,Se: 100%, Spy: 100% • Features used: 1 (after GDA)	• Only 39 patients (10 LRPs, 29 HRPs)- small & unbalanced dataset • Databases had different ECG sampling rates (128 Hz vs. 250 Hz) • Removed records with <80% NN intervals, reducing dataset size • GDA kernel parameter (σ=1) was not optimized systematically • Results not tested on independent datasets and is not realistic
(Sharma et al., 2019)	• CAD ECG Signals: St. Petersburg Institute of Cardiological Technics 12-lead Arrhythmia Database (7 CAD patients, 30-min recordings, 257 Hz) • Normal ECG Signals: Fantasia Database (40 healthy subjects, 2-hour recordings, upsampled to 257 Hz) • Total Beats: 44,426 CAD beats & 137,587 normal beats	• Preprocessing: Pan-Tompkins R-peak detection, beat segmentation • Time-Frequency Analysis: Improved Eigenvalue Decomposition of • Hankel Matrix & Hilbert Transform (IEVDHM-HT) • Feature Extraction: Three TF-based features such as, mixed average, frequency average, time average, computed globally and locally (9 regions) • Classification: Random Tree & J48 classifiers with 10-fold and leave-one-out cross-validation	• Best Accuracy: 99.93% (J48 classifier, all local features) • Global Features: 99.7% accuracy (Random Tree), 99.15% (J48) • Top Feature: frequency average most discriminative	• Small Dataset: Only 7 CAD patients, limiting generalizability • Computational Cost: IEVDHM-HT may be slow for real-time use • No validation with independent datasets or cardiologists' diagnoses • Complex Features: mixed average, frequency average, and time average lack intuitive clinical interpretation
(Singh et al., 2017a)	• Synthetic Signals: Stationary, non-stationary (slow/fast-varying), and noisy (AWGN, SNR=30 dB) signals simulating HRV dynamics • Real HRV Data: Healthy Young Group (HYG): 14 subjects (23-32 years, Fantasia database) Healthy Elderly Group (HEG): 14 subjects (70-82 years, Fantasia database) Arrhythmia Controlled Medication Group (ARCMG): 14 subjects (54-70 years, MIT-BIH Arrhythmia database) Supraventricular Tachycardia Group (SVTG): 14 subjects (MIT-BIH Supraventricular Arrhythmia database)	• Adaptive Continuous Morlet Wavelet Transform: Introduces shape parameter q optimized for maximum energy concentration, compared against CMWT, ST, AST, and AMST • Preprocessing: R-peak detection (modified Pan-Tompkins algorithm) Ectopic beat correction (cubic spline interpolation) Resampling at 4 Hz • Spectral Analysis: LFp (0.04-0.15 Hz), HFp (0.15-0.4 Hz), and LFp/HFp ratio • Statistical Validation: t-tests ($p < 0.05$) for group comparisons	• Synthetic Signals: ACMWT achieved the highest ECMmax (Energy Concentration Maximum) Robust under noise (SNR=30 dB) • Real HRV Data: Resolution: ACMWT provided clearer time-frequency maps than CMWT, ST, AST, and AMST • Statistical Significance: HYG vs. HEG: $p < 0.0001$ (LFp, HFp decreased in elderly) ARCMG vs. HEG: $p < 0.05$ (LFp, HFp increased due to medication). SVTG vs. others: $p < 0.00001$ (LFp, HFp decreased severely).	• Frequency Range: Limited to 0.02-1 Hz (excludes VLF band) • Parameter Sensitivity: Performance depends on optimal q selection • Computational Cost: Adaptive optimization may increase processing time • Not validated for other cardiovascular conditions (e.g., heart failure)

Table 2.10: Cont. . . linear and non-linear analysis

Author	Dataset	Methods	Performance Results	Limitations
(Singh et al., 2018b)	• Fantasia Database: 20 healthy young (YNG) subjects • St. Petersburg Institute Database: 13 CAD, 15 CHF subjects • Self-Recorded Data (SELF_YNG): 13 healthy subjects	• Preprocessing: Ectopic beat removal, cubic spline interpolation, resampling at 4 Hz • Higher Order Spectra (HOS): Bi-spectral analysis of HRV signals • Extracted Features: 10 nonlinear features (MM, H1-H3, P1-P2, PHE, WCOB1-WCOB2, FLAT) • Statistical Tests: Wilcoxon rank sum test (p-value < 0.05), Bonferroni correction for multiple comparisons	• Statistical Significance: Most features (except PHE) showed $p < 0.0001$ for group distinctions • Healthy vs. Patients: Higher H1, H2, P1, P2, PHE in healthy subjects; lower WCOB2/FLAT • CAD vs. CHF: CAD patients had higher values for most features (except P1, P2, WCOB1) • Box Plots: Visualized clear separability between groups	• Limited dataset sample • PHE Weakness: Insignificant in CAD-CHF comparisons • Computational Cost: HOS analysis is resource-intensive • Lack of classification models for accuracy metrics
(Singh et al., 2019)	• MIT-BIH Arrhythmia Database (48 ECG recordings, 24 hours each, sampled at 250 Hz). • Segmented into 48-interval HRV signals	• Preprocessing: Ectopic beat removal, cubic spline interpolation • Feature Extraction: ACMWT, AST, AMST • Extracted features: Flatness, Flux, Skewness, Kurtosis, Shannon/Renyi entropy, Coefficient of Variation • Classification: Back-Propagation Neural Network (BPNN) with 3 decision rules (Average, Vote, Decision Vote)	• Best Results (Decision Vote Rule): LF Band: Acc = 95.98%, Sp = 96.24%, Se = 89.5% HF Band: Acc = 97.13%, Sp = 96.13%, Se = 94.38% • AUC (ROC): 97.65%	• Ectopic Beat Sensitivity: Performance drops with excessive ectopic beats • Computational Cost: ACMWT and BPNN are resource-intensive • Validated only on MIT-BIH
(Sinha and Das, 2020)	• MIT-BIH Atrial Fibrillation Database (25 recordings, 250 Hz) • MIT-BIH Supraventricular Arrhythmia Database (78 recordings, 360 Hz) • MIT-BIH Normal Sinus Rhythm Database (54 recordings, 128 Hz) • Creighton University Ventricular Tachyarrhythmia • Database (35 recordings, 250 Hz) • Total: 23 AF, 35 VF-VT, 40 SV, and 50 NSR signals	• Preprocessing: Pan-Tompkins R-peak detection, RR interval extraction • Feature Extraction: 5-level DWT (bi-orthogonal wavelet), nonlinear (Hurst exponent, sample entropy) and statistical (mean, kurtosis) features • Feature Fusion: Adaptive weight factors based on p-values & Euclidean distances, creating Integrated Feature Indices (Arrhythmia/Ventricular/ Atrial Index) • Classification: SVM (RBF kernel) with 10-fold cross-validation in a 3-stage model	• Stage 1 (NSR vs. Arrhythmia): Acc = 99.22%, Sen = 99.37%, Sp = 98.91% • Stage 2 (VF-VT vs. Non-VF-VT): Acc = 98.52%, Sen = 98.24%, Sp = 98.76% • Stage 3 (AF vs. SV): Acc = 98.72%, Sen = 98.15%, Sp = 99.10%	• Dataset: Limited to AF/SV/VF-VT; rare arrhythmias untested • Computational Load: DWT and feature fusion may hinder real-time use • Performance may degrade with noisy ECG signals
(Sood et al., 2016)	• ECG recordings from Igraa Hospital, Calicut, Kerala, India (500 Hz sampling rate) • 10 Normal (healthy) and 10 CAD subjects	• Preprocessing: Band-pass (0.3-15 Hz) and notch (50 Hz) filtering R-peak detection using Pan-Tompkins algorithm • Decomposition: Empirical Mode Decomposition (EMD) to extract IMFs Feature Extraction: SODP area, ASR area, AM bandwidth, FM bandwidth, FBE-based mean frequency • Statistical Analysis: Kruskal-Wallis test ($p < 0.05$ for significance)	• AM bandwidth: Most significant • FM bandwidth & FBE mean frequency: Also statistically significant ($p < 0.05$) • SODP & ASR area: Less discriminative (higher p-values) • Best IMF: First IMF (AM bandwidth) was most effective across all signal lengths	• Small dataset (20 subjects) limits generalizability • No machine learning classification (only statistical analysis) • No optimization- manual feature selection
(Yao et al., 2020)	• 200 participants (107 healthy controls, 93 CAD patients) • 5-minute single-lead (Lead I) recordings at 1 kHz	• Feature Extraction: QT/RR interval variability (31 HRV + 19 QTV indices) • Signal decomposition: TQWT (wavelets) + HHT (instantaneous energy/ frequency) • ST-T waveforms: Analyzed using ResNet-18 • Dimensionality Reduction: Statistical tests + PCA (95% variance retained) Classification: • ML models: GNB, SVM, XGBoost • Deep learning: ResNet-18	• Best Model (XGBoost + ResNet-18 fusion): Acc: 96.16%, Se: 95.75%, Sp: 96.40% • QTV features alone (XGBoost): 91.54% accuracy (outperformed HRV) • ST-T only (ResNet-18): 78.46% accuracy (improved when fused)	• Single-lead ECG: Less spatial detail than 12-lead systems • No MI patients or elderly-excluded populations • Manual QT delineation: Potential human error in T-wave detection • Computational cost: ResNet-18 and feature fusion require high resources

2.4 Current Status of Machine Learning Techniques for Classification of Cardiac Diseases

CVD is a critical life-threatening condition and the foremost cause of death globally, as it severely impairs blood vessel function and can lead to serious complications such as coronary artery infections, ultimately resulting in mortality (Roth et al., 2020; Tsipouras et al., 2008; Besfat et al., 2024a). As a result, a trustworthy system needs to be developed for quick and accurate cardiac disease diagnosis to help cardiologists in delivering suitable treatment for their patients. However, the main challenges in cardiac disease detection involves identifying heart disease behavioral patterns from substantial datasets while dealing with time constraints which affect detection response time. Alongside, the advancement of machine learning and deep learning techniques facilitates the analysis of vast and intricate medical data, which then enabling the identification of patterns in disease occurrence and transforming this information into structured data for disease detection (Singh and Mahapatra, 2024), (Singh et al., 2018c).

In recent years, researchers have developed numerous machine learning-based approaches for detecting and classifying cardiac diseases, employing a variety of methodologies and strategies. The study in (Acharya et al., 2016) presented an automated method for detecting and localizing myocardial infarction (MI) by analyzing 12-lead ECG signals. Deep transfer learning-based approach has been proposed in (Alghamdi et al., 2024) for detecting MI using ECG signals, aimed at improving urban healthcare in smart cities. In this study, two modified CNN models, VGG-MI1 (fine-tuned VGG-Net) and VGG-MI2 (VGG-Net as a feature extractor with QG-MSVM classifier), were developed. They have utilized small filter sizes and fewer pooling layers to reduce computational cost and noise sensitivity. In addition, data augmentation (generating additional ECG images) and dropout techniques were applied to mitigate overfitting and enhance robustness. The study in (Barua et al., 2023) introduced a multilevel hybrid handcrafted model named HHF-MUPTT for automated classification of MI using ECG signals. The model architecture Combined multilevel hybrid feature extraction (textural and statistical features) with iterative feature selection and iterative majority voting (IMV) for classification. They have incorporated two methods in their model, such as 1D-Improved Symmetric Binary Pattern (1D-ISBP) and Multilevel Unbalanced Pooling Tree Transformation (MUPTT).

The authors of (Feng et al., 2019) proposed a deep learning approach to classify MI using single-lead ECG signals. In their method, a multi-channel CNN-LSTM model is designed to automatically extract spatial and temporal features from ECG signals without manual feature engineering. The model processes five adjacent heartbeats (3s of data) as input, passing

them through parallel CNN channels to capture spatial features, followed by an LSTM layer to learn temporal dependencies. The network includes 16 layers (convolutional, pooling, dropout, LSTM, and fully connected layers) with ReLU activation and batch normalization. The study in (Hammad et al., 2022) presented an end-to-end deep learning approach using a Convolutional Neural Network (CNN) with focal loss to automatically detect Myocardial Infarction (MI) from ECG signals, addressing the challenge of imbalanced data. The focal loss optimization was utilized to mitigate class imbalance by focusing on hard-to-classify samples, improving MI detection accuracy.

Detection of inferior myocardial infarction (IMI) has been conducted by (Sharma and Sunkaria, 2018) using stationary wavelet transform (SWT) and machine learning techniques. The ECG signals from leads II, III, and aVF (most sensitive to IMI) has been downsampled and segmented in the pre-processing stage. Their evaluation was based on class-oriented approach (cross-validation) and subject-oriented approach (demonstrated generalization to unseen subjects). The paper in (Sharma and Sunkaria, 2020) developed a method for MI detection and localization using ECG signals, independent of time-domain fiducial markers (e.g., R-wave, Q-wave, ST-segment). A computer-aided diagnostic (CAD) system for detection MI has been presented in (Sridhar et al., 2021) using ECG signals by leveraging pre-processing ECG signals, detecting R-peaks using the Pan-Tompkins algorithm, extracting non-linear features, and classifying the signals using machine learning classifiers like SVM, KNN, Decision Tree, and Probabilistic Neural Network (PNN). Authors in (Zeng and Yuan, 2023) proposed a method for detecting MI using ECG signals by combining signal processing techniques and artificial intelligence. For the synthesis of ECG leads, a 4-dimensional cardiac vector was created by synthesizing standard 12-lead ECG signals with Frank XYZ leads to capture pathological alterations caused by MI. Then after, they perform signal decomposition by utilizing Intrinsic Time-Scale Decomposition (ITD) and DWT. Subsequently, features were extracted based on Phase Space Reconstruction (PSR) and Euclidean Distance (ED). Finally, classification has been performed.

For early prediction of Sudden Cardiac Death (SCD) 1 hour before onset, the authors of (Karimulla and Patra, 2024) has developed a reliable system by analyzing HRV signals derived from ECG data. The focus is on distinguishing between NSR, SCD, CAD, CHF, and Atrial Fibrillation (AF) to improve diagnostic accuracy and save lives. They have extracted 77 features from time domain (RMSSD, SDNN, TINN), frequency domain (VLF, LF, HF power bands), non-linear methods (Sample Entropy, Poincaré plot features), and time-frequency analysis. For the TF analysis, a Constant-Q Non-Stationary Gabor Transform (CQ-NSGT) was utilized to convert HRV signals into 2D images, extracting texture features (GLCM, SFM, FDTA, GLSZM). Following this, a two-stage approach such as Sequential Forward Selection (SFS)

and ANOVA test feature selection has been performed. By utilization of machine learning (SVM) with DWT feature extraction, a classification method was also presented in the paper by (Kumari et al., 2021). The authors in (Nesaragi et al., 2022) introduced a third-order tensor constructed from scalograms (time-frequency representations) derived from heart rate (HR) signals. Each scalogram captures the variability of HR data as a 2D map, and these maps are stacked to form a 3D tensor. Then, Canonical Polyadic (CP) decomposition was applied to the tensor to extract latent features, retaining only the core factor (λ) for its ability to encapsulate higher-order interactions across time, frequency, and time-frames.

A deep learning approach had been proposed in for (Panjaitan et al., 2023) predicting Sudden Cardiac Death (SCD) using HRV derived from ECG signals. This study leverages a Convolutional Neural Network (CNN) model to classify ECG data into five groups: NSR, CAD, CHF, Ventricular Tachycardia (VT), and SCD. A method for detection of CHF was presented in the study conducted by (Rao and Kumar, 2023). Their method involves the Electrocardiomatrix (ECM) technique, which transforms 2D ECG signals into a 3D-colored matrix for enhanced visualization and analysis. The study in (Sun et al., 2024) proposed a multi-modal learning method to enhance the detection of CAD by integrating ECG, Phonocardiogram (PCG), and their coupling signals. They have employed a multi-modal integration method, which combines ECG (electrical activity), PCG (mechanical activity), and a newly generated ECG-PCG coupling signal derived via deconvolution to capture complementary information for CAD detection. A deep learning framework called HeartCare that uses knowledge distillation has been proposed in (Borah et al., 2024) to detect and localize multi-label MI from 12-lead ECG signals. The framework consists of a teacher-student model where a larger, high-performance teacher network trains a smaller, resource-efficient student network to achieve comparable accuracy with reduced computational complexity. The teacher model (complex CNN) extracts morphological features and attention patterns from ECG signals, while the student model (lightweight CNN) mimics the teacher's attention to critical ECG regions (e.g., QRS complexes, ST segments) for MI detection, achieving high accuracy with fewer parameters. Finally, classification of ECG signals has been done in to five super-diagnostic classes such as, Normal (NORM), Conduction Disturbance (CD), ST/T Changes (STTC), Myocardial Infarction (MI), and Hypertrophy (HYP).

By leveraging both multivariate time series classification and connectivity-based features, detection of MI has been introduced in (Jain et al., 2024) using ECG signals. The multi-lead ECG signal was treated as a multivariate time series, and features were extracted using the ROCKET algorithm, which employs random convolutional kernels to capture sequential patterns. A logistic regression classifier was then used for classification. The study in (Zeng et al., 2024) presented an automated framework for detection MI using ECG signals by utilizing hy-

brid signal processing techniques and deterministic learning theory. In their study, they have incorporated methodologies like Shannon Energy Envelope (SEE), Fast and Adaptive Multivariate Empirical Mode Decomposition (FA-MVEMD), deterministic Learning with neural networks. Authors in (Martin et al., 2021) proposed a Long Short-Term Memory (LSTM) neural network architecture for near real-time detection of MI from single-lead (Lead II) ECG signals. This study employed a three-layer LSTM neural network for classification. First two layers (100 LSTM units with tanh activation) used to capture temporal dependencies in ECG signals and the final layer (a single LSTM unit with sigmoid activation) utilized for binary classification (MI vs. healthy control). The summary of various literature in the application of machine and deep learning techniques for cardiovascular disease detection is shown in Table 2.11, 2.12, 2.13, and 2.14. The framework of data pre-processing stage and the application of machine learning models has been depicted in Fig. 2.9 for the detection of CVDs.

Figure 2.9: Structure of the data pre-processing and machine learning model application in classification of cardiovascular diseases

Table 2.11: A summery of machine and deep learning models in classification of cardiovascular disease

Author	Dataset	Methods	Performance Results	Limitations
(Acharya et al., 2016)	• PTB Diagnostic ECG Database (PhysioNet) • 200 subjects (52 normal, 148 MI) • 12-lead ECG • 611,405 beats (125,652 normal, 485,753 MI)	• Preprocessing: Noise removal using (db6) wavelet, R-peak detection via Pan-Tompkins • Feature Extraction: 4-level DWT decomposition, 12 nonlinear features (entropies, signal energy, fractal dimension, etc.) • Feature Selection: t-test & ANOVA for ranking • Classification: KNN (k=5) for binary (normal vs. MI) and multi-class (10 MI types) classification	• Normal vs. MI: 98.80% acc, 99.45% se, 96.27% sp (Lead V5, 47 features) • 10-Class MI Localization: 98.74% acc, 99.55% se, 99.16% sp (Lead V3, 25 features) • Inferior Posterior MI: 99.97% accuracy (Lead V3)	• Performance varies across leads; some MI types may need multi-lead analysis • Extracting 12 nonlinear features is resource-intensive • Needs validation on larger datasets • Rare MI types (e.g., inferior posterior) have fewer samples - class imbalance
(Alghamdi et al., 2024)	• Physikalisch-Technische Bundesanstalt Diagnostic ECG Database • 549 records from 290 subjects (147 MI cases) • Lead II ECG signals sampled at 1000 Hz • 21,092 normal beats & 80,364 MI beats, converted into 128×128 grayscale images	• VGG-MI1: Fine-tuned VGG-Net with a modified 2-unit SoftMax layer. • VGG-MI2: VGG-Net as a feature extractor and QG-MSVM classifier • Data augmentation (cropping & resizing ECG images) • Small filters (3×3) to reduce noise sensitivity • Dropout regularization to prevent overfitting	• VGG-MI1: Accuracy = 99.02%, Se = 98.76%, Sp = 99.17% • VGG-MI2: Accuracy = 99.22%, Se = 99.15%, Sp= 99.49% • Outperformed existing methods (SVM, KNN, wavelet-based approaches)	• High computational cost (deep learning vs. traditional ML) • Limited dataset diversity (only PTB database used) • Single-lead dependency may miss multi-lead MI patterns
(Barua et al., 2023)	• Source: PhysioBank (1000 Hz sampling rate) • Subjects: 200 (148 MI patients, 52 healthy) • Classes: 11 (1 healthy + 10 MI types) • ECG Beats: 49,235 (12-lead, preprocessed) • Segmentation: 651 samples per beat (R-peak centered)	• 1D-ISBP: textural feature extractor (32 features) • Statistical Features: 40 features (entropy, moments, etc.) • MUPTT: Multilevel decomposition using average/max pooling (6 levels) • INCA: Iterative feature selection • 1NN Classifier: Lightweight k-nearest neighbor (k=1) • IMV: Iterative majority voting for final decision	• Best Lead-wise Accuracy: 99.85% (Lead III) • Average Lead-wise Accuracy: 99.40% • IMV Accuracy: 99.94% (top 8 leads)	• Class Imbalance: Some MI classes have very few samples • Feature Dependency: Handcrafted features may lack adaptability • Needs validation in low-resource settings -real-time feasibility
(Feng et al., 2019)	• PTB Database • Records: 549 (148 MI patients, 52 healthy controls) • Leads: I-lead ECG (single-lead) • Segmentation: 600 samples per heartbeat (0.6s, centered on R-peak)	• Preprocessing: Wavelet denoising (Daubechies D6), R-peak detection (Pan-Tompkins), normalization • Model: Multi-channel CNN-LSTM (16 layers total) CNN: 5 parallel branches (9 conv layers, kernel size=5, ReLU) • LSTM: Captures temporal ECG features • Classifier: Softmax (binary: MI vs. normal) • Training: Adam optimizer (LR=0.0001), dropout=0.5, 10-fold cross-validation	Acc: 95.4%, Sen: 98.2%, Spe: 86.5%, F1-score: 96.8%, AUC (ROC): 0.9868, Optimal Input: 5 heartbeats (3s)	• Computational cost: High training time (15s/epoch) • Single-lead focus: Multi-lead ECG could improve robustness • Untested on motion artifacts/poor-quality ECGs • Needs validation on diverse populations
(Hammad et al., 2022)	• PTB ECG dataset from PhysioNet • 549 recordings (290 subjects, 17–85 years) • 368 MI cases, 181 normal cases (imbalanced) • Lead II signals (20s segments, 1000 Hz sampling)	• End-to-end 1D CNN (three blocks, 512 filters per layer, kernel=2, stride=1) • ReLU activation, batch normalization, dropout (rate=0.5) • Focal loss (α=0.5, γ=2) to handle class imbalance • Stratified 5-fold cross-validation for robust evaluation	• With Focal Loss: Acc: 98.84%, Pr: 98.31%, Recall: 97.63%, F1-score: 97.92% • Without Focal Loss:- Acc: 89.72%, Pr: 88.52%, Recall: 81.11%, F1-score: 83.02%	• Limited to Lead II; 12-lead analysis could enhance robustness • No MI localization: Detects presence but not affected heart region • Small dataset: No augmentation or external validation

Table 2.12: Cont. . . ML classification

Author	Dataset	Methods	Performance Results	Limitations
(Sharma and Sunkaria, 2018)	• PTB-DB from PhysioNet • 30 IMI patients and 52 healthy controls (HC) • 12-lead ECG sampled at 1000 Hz, downsampled to 250 Hz • 3,240 IMI segments and 3,037 HC segments after preprocessing	• Preprocessing: Downsampling & segmentation (3.072 s ECG segments) • Feature Extraction: SWT decomposes ECG leads (II, III, aVF) into sub-bands • Features: Sample Entropy, Normalized Sub-band Energy, Log Energy Entropy, Median Slope • Feature Selection: Gain Ratio (GR) for top 10 features • Classification: SVM (RBF kernel) and KNN (K=3,5,7)	• Class-Oriented: SVM: Acc = 98.84%, Se = 99.35%, Sp = 98.29%, AUC = 0.9994 KNN (K=3): Acc = 98.69%, Se = 98.67%, Sp = 98.72%, AUC = 0.9945. • Subject-Oriented (unseen subjects): Avg. Acc = 81.71%, Se = 79.01%, Sp = 79.26%	• Subject-oriented accuracy (81.71%) much lower than class-oriented (98%) • Only 30 IMI patients; needs larger validation • Only leads II, III, aVF used; other leads may improve detection
(Sharma and Sunkaria, 2020)	• PTB Diagnostic ECG Database • 12-lead ECG recordings from 200 subjects (52 healthy, 148 MI patients) • 3,037 healthy and 12,544 MI segments after downsampling and segmentation	• Preprocessing: Downsampling to 250 Hz, 3.072-sec segments Baseline wander removal (2-stage median filter) and SG smoothing • Feature Extraction: SWT with 5th-order Daubechies wavelet • Extracted features: Log Energy Entropy (LEE), Shannon Energy (SEE), Normalized Subband Energy (NSE), Median Slope (MDS), Mean Slope (MNS) • Feature Selection: Fisher Score (F-score) for ranking discriminative features • Classification: k-Nearest Neighbors (kNN) with Mahalanobis/Euclidean distance • ADASYN for handling imbalanced data • 10-fold cross-validation.	• MI Detection: Multi-lead (12 features): AUC = 0.99, Se = 98.62%, Sp = 99.40%, Acc = 99.00% Single-lead (V5, 12 features): AUC = 0.99, Se = 98.34%, Sp = 99.77%, Acc = 99.05% • MI Localization: Multi-lead (5 features): AUC = 0.99, Se = 98.78%, Sp = 99.86%, Acc = 99.76% Single-lead (V3, 8 features): AUC = 0.98, Se = 96.47%, Sp = 99.60%, Acc = 99.28%	• Relies on handcrafted features; deep learning might generalize better - feature dependency • Only tested on PTB database; needs validation on larger, diverse datasets • SWT with kNN may not be optimal for real-time applications - computational load
(Sridhar et al., 2021)	• PTB Diagnostic ECG Database (PhysioBank) • 200 subjects (52 normal, 148 MI) • Lead II ECG, sampled at 1000 Hz • Two-second segments (2000 samples) centered around R-peaks	• Preprocessing: DWT + EMD for noise removal, Pan-Tompkins for R-peak detectio • Feature Extraction: 45 non-linear features (entropy, fractal dimension, recurrence analysis, bispectrum, etc.) • Feature Selection: Student's t-test for ranking significant features • Classification: SVM, KNN, Decision Tree, PNN (10-fold cross-validation)	• Best Model: SVM Acc: 97.96%, Se: 98.89%,Sp: 93.80% • KNN: 97.35% • DT: 95.51% • PNN: 90.44%	• Manual feature extraction (time-consuming) • Single-lead analysis (only Lead II, missing multi-lead correlations) • Computationally expensive (some non-linear features require high processing)
(Zeng and Yuan, 2023)	• PhysioNet PTB Database • 148 MI subjects, 52 healthy controls • 367 MI, 78 healthy heart-beat records • 5 leads (12 standard + 3 Frank XYZ)	• Signal Synthesis: 4D cardiac vector from 12-lead + Frank XYZ leads • Decomposition: ITD (Intrinsic Time-Scale Decomposition) → DWT (Discrete Wavelet Transform, db3) • Feature Extraction: PSR, d=3, tau=1 and ED • Classification: RBF neural networks	Accuracy: 98.20%, Se: 98.37%, Sp: 97.44%, PPV: 99.45%, NPV: 92.68%, MCC: 0.9395	• Fixed parameters (d=3, τ=1) - No adaptive optimization • Computational complexity - May not be real-time feasible • Tested only on a public dataset - No clinical validation

Table 2.13: Cont. . . ML classification

Author	Dataset	Methods	Performance Results	Limitations
(Karimulla and Patra, 2024)	• Source: PhysioNet (MIT-BIH NSRDB, SDDB, LTSTDB, CHFDB, AFDB) • Subjects: 93 total (18 NSR, 20 SCD, 20 CAD, 15 CHF, 20 AF) • Signal Duration: 1-hour ECG recordings • Sampling Rate: 250 Hz (upsampled for NSR)	• Preprocessing: DWT Symlet 6 denoising and Pan-Tompkins R-peak detection, artifact Correction: Median filtering with cubic spline interpolation • Feature Extraction: Time-domain (SDNN, RMSSD, TINN) Frequency-domain (VLF, LF, HF bands) Nonlinear (Sample Entropy, Poincaré plots) T-F analysis: CQ-NSGT and texture features (GLCM, SFM, FDTA, GLSZM) • Feature Selection: ANOVA ($p<0.05$) → Sequential Forward Selection (8 optimal features) • Classification: Gradient Boosting (best performer), RF, SVM, KNN	• Acc: 96.43% (GBC), Sen: 97.14%, Sp: 95.45% • Other Models: RF: 90.38% SVM: 88.71% KNN: 83.84%	• Needs larger dataset validation • CQ-NSGT + SFS may hinder real-time use (computational cost) • Excludes other arrhythmias (e.g., VT) • Hard to interpret clinically (e.g., CQ-NSGT textures) → complex features
(Kumari et al., 2021)	• Sources: MIT-BIH Arrhythmia Database, BIDMC Congestive Heart Failure Database • Classes: Normal Sinus Rhythm (NSR), CHF, Cardiac Arrhythmia (ARR) • Size: 162 ECG recordings (70% training, 30% testing)	• Preprocessing: ECG signal segmentation and normalization • Feature Extraction: Discrete Wavelet Transform (DWT) with Daubechies wavelet (db2), extracting 190 features • Classification: Support Vector Machine (SVM) with a radial basis function (RBF) kernel	• Acc: 95.92%, Pr: 96.11%, Recall: 92.59%, F1-Score: 93.82% • Confusion Matrix: NSR & ARR: 100% recall CHF: 77.78% recall	• Limited arrhythmia types: Only NSR, CHF, and ARR were tested • Feature dependency: Relies heavily on DWT, may not generalize to all ECG anomalies • Small dataset: 162 recordings may not suffice for deep learning • Computational constraints: SVM may need optimization for real-time use • Not tested on other ECG databases
(Nesaragi et al., 2022)	• ECG recordings from IQRAA Hospital, Kerala, India • 20 (10 CAD patients + 10 normal controls) • 143 ECG files (61 normal, 82 CAD) • 500 Hz (15-minute recordings) → sampling rate	• Preprocessing: Band-pass filtering (0.3–15 Hz), R-peak detection (Pan-Tompkins), HRV extraction (255 samples per signal) • Signal Transformation: Scalograms generated via Continuous Wavelet Transform (CWT) with Morlet wavelet Tensor Construction: Third-order tensor ($18 \times 25 \times 10$) from stacked scalograms • Feature Extraction: Canonical Polyadic (CP) decomposition, retaining core factor (λ) as latent features • Classification: Ensemble classifiers (Bagged Trees, RUSBoost) optimized via Bayesian optimization (5-fold CV)	• Best Model: Bagged Trees, Acc: 96.62%, Se: 96.67%, Sp: 96.53%, • Ablation Results: • Direct HRV classification: ∼89% accuracy • Tensor-only (no scalograms): ∼87% accuracy	• Small dataset (20 subjects): Limited generalizability • QRS detection dependency: Noise may degrade performance • Computational cost: Tensor decomposition may hinder real-time use • Binary classification only: No severity grading
(Panjaitan et al., 2023)	• Source: PhysioNet databases • Subjects: 115 subjects (18 NSR, 51 CAD, 15 CHF, 11 VT, 20 SCD) • Signal Duration: 30-minute ECG recordings, segmented into 5-minute intervals (6 segments/ subject)	• Preprocessing: Noise removal using DWT (sym5 wavelet), R-peak detection (Hamilton–Tompkins algorithm) • Feature Extraction: 8 time-domain HRV features (MeanRR, RMSSD, PNN50, SDRR, CVRR, NN50, Min_RR, Max_RR) • Model: 1D-CNN Wavenet (7 hidden layers, learning rate = 0.001, batch size = 128) • Training: 80%-20% split, hyperparameter tuning via grid search	Acc: 99.30%, Se: 97%, Sp: 99.60%, Pr: 97.87%	• Limited features: Only linear HRV features were used (no non-linear/frequency-domain features) • Small dataset: Only 20 SCD cases; may lack generalizability • Computational cost: 1D-CNN Wavenet requires high resources
(Rao and Kumar, 2023)	• BIDMC Congestive Heart Failure Database (PhysioNet) • 15 subjects (11 men, 4 women, aged 22–71) • 1-hour ECG recordings sampled at 250 Hz with 12-bit resolution • Annotations: Normal beats, PACs, PVCs, SVPBs, R-on-T PVCs	• Electrocardiomatrix (ECM): Converts 2D ECG into 3D color-coded matrix (x: time, y: beats, z: amplitude) • Preprocessing: Pan-Tompkins algorithm for noise removal and R-peak detection • Segmentation: ECG split into equal-length segments (two heartbeats each) • Visual Analysis: Manual inspection of color patterns for abnormalities (PACs, PVCs, etc.)	Acc: 96.89%, Sen: 97.53%, Sp: 96.02%, Pr: 99.1%, F1-Score: 97.76%	• Difficulty distinguishing similar beats (e.g., PVCs vs. R-on-T PVCs) • Small dataset (only 15 patients) • No full automation (lacks AI-based classification)

Table 2.14: Cont. . . ML classification

Author	Dataset	Methods	Performance Results	Limitations
(Sun et al., 2024)	• Subjects: 199 (135 CAD patients, 64 non-CAD controls) • Signals: Simultaneous lead-II ECG and PCG	• Preprocessing: Bandpass (0.5–60 Hz for ECG, 20 Hz high-pass for PCG), 50 Hz notch filter, 10-sec segmentation Signal Fusion: ECG-PCG coupling signal via deconvolution • Feature Extraction: Entropy Features: ApEn, SampEn, FuzzyEn, DistEn Recurrence Deep-Coding: Recurrence Plots (RPs) with parallel-input 2D CNN • Feature Selection: PCA (90% variance) and RFE • Classification: SVM (linear/RBF kernels) with 5-fold cross-validation	• Single ECG: 80.41% acc, Single PCG: 86.41% acc, ECG-PCG Coupling: 91.44% acc, ECG+PCG Joint: 90.42% acc • Proposed Multi-Modal (ECG+PCG+Coupling): Acc: 95.96%, Se: 100%, Sp: 87.31%, F1-Score: 92.93%	• Single-lead ECG restricts spatial cardiac analysis • Class imbalance (135 CAD vs. 64 controls) • Computational cost
(Borah et al., 2024)	• PTB-XL Dataset: 21,837 ECG recordings (5 superclasses: NORM, CD, STTC, MI, HYP) • External Validation: SPH Dataset, CPSC 2018 Dataset, Private Indian Dataset (8,000 records)	• Preprocessing: Standardized to 100 Hz, 1,000 data points per sample • Teacher-Student Knowledge Distillation (KD): Teacher Model: Deep CNN with attention mechanisms (38.13 MB) Student Model: Lightweight CNN (7.7 MB) trained via KL divergence and cross-entropy loss • Interpretability: Grad-CAM for attention visualization • Training: Adam optimizer, binary cross-entropy loss, 5-fold cross-validation.	• PTB-XL: 94.25% acc, 0.95 ROC-AUC • External Validation: 95.80% acc, 84.98% se • Model Size: Student model (7.7 MB) vs. Teacher (38.13 MB) • Class-wise ROC-AUC: NORM (0.946), MI (0.946), STTC (0.918), HYP (0.957), CD (0.947)	• Data Imbalance: No explicit handling of rare arrhythmias or noisy ECGs. • Not tested in real-time clinical settings • Struggles with co-occurring conditions (e.g., MI + HYP) → multi-Label Complexity • Hardware: FPGA/edge deployment not implemented. • Lead Dependency: Performance may drop with fewer leads (e.g., 3-lead ECGs)
(Jain et al., 2024)	PTB-XL ECG Dataset (21,837 clinical 12-lead ECGs from 18,885 subjects, 10-second recordings, 500 Hz sampling rate, annotated by cardiologists).	• Multivariate Time Series Model: Uses ROCKET algorithm for feature extraction + logistic regression • Connectivity-Based Model: Extracts relational features (coherence, correlation, PLI, PLV, novel ConnDTW) with CNN/SVM. • Integrated Model: Combines both sequential (ROCKET) and relational (connectivity) features + logistic regression • Lead Reduction: Identifies optimal subset of ECG leads (12, 6, 2, 4)	• Integrated Model: Acc ∼97%, Sen ∼98%, Sp ∼94% • Multivariate Model: Acc ∼96% • Connectivity Model: Acc 95% • 4-Lead Subset: Matches 12-lead performance (∼97% accu) • Outperforms LASSO, ResNet, and 2D-CNN	• Tested only on PTB-XL; needs validation on other datasets (e.g., MIT-BIH) • Requires optimization for low-power devices → real time deployment • Lead Reduction: Further reduction (e.g., 2 leads) may degrade performance
(Zeng et al., 2024)	• PTB Diagnostic ECG Database (PhysioNet) • 549 ECG recordings (148 MI patients, 52 healthy controls) • Lead II signals used • Balanced using SMOTE to handle class imbalance	• Shannon Energy Envelope (SEE): Enhances ECG features by amplifying intermediate-intensity components • FA-MVEMD: Decomposes SEE into IMFs; first two IMFs used for classification. • Deterministic Learning with RBFNNs: Models ECG dynamics and classifies signals based on synchronization errors	• Acc: 99.21% (10-fold cross-validation), Sen: 99.18%, Sp: 99.23%, MCC: 0.984 • Outperformed CNNs, LSTMs, SVMs, and other ML methods	• Only tested on Lead II; multi-lead validation needed • Performance on other databases (e.g., noisy/ambulatory ECGs) untested • Interpretability: Less transparent than traditional feature-based methods
(Martin et al., 2021)	• PTB Diagnostic ECG Database • 148 MI patients, 52 healthy controls Single-lead (Lead II) ECG signals • 1-second heartbeat segments (500ms before and after R-peak) • Subject-split for 10-fold cross-validation	• Preprocessing: 60Hz stop-band filter (removes powerline noise), 500ms moving average filter (removes low-frequency noise), ICA-based R-peak detection • Three-layer LSTM network: First two layers: 100 LSTM units (tanh activation) Final layer: 1 LSTM unit (sigmoid activation) • Training: RMSProp optimizer with L2 regularization, Gradient clipping (5.0), Early stopping (10 epochs patience)	• Acc: 89.56% (±2.79%), Se: 91.88% (±3.13%),Sp: 80.81% (±9.62%) • Processing Time: 40ms per heartbeat (real-time capability) • Comparison: Outperforms other single-lead methods, Lower than multi-lead approaches (e.g., 12-lead CNNs)	• Single-lead limitation: Poor detection of anterior/lateral/posterior MIs • Dataset imbalance: More MI samples (148) than controls (52) → lower specificity • Struggles with poor lead contact/artifacts → noisy ECG handling • Binary classification only: Cannot distinguish MI subtypes or other cardiac diseases

When evaluating the performance of cardiovascular disease detection models, several evaluation metrics need to be used to understand their performance comprehensively. Specifically, analyzing the performance of machine learning models in predicting cardiovascular disease serves a vital purpose for establishing their utility in clinical settings. The key evaluation metrics commonly used for assessing machine learning model performance in detecting cardiovascular disease consists of accuracy, precision (positive predictive value), specificity, sensitivity (recall), F1-score, Matthews correlation coefficient (MCC), the area under the curve (AUC) and receiver operating characteristic (ROC) curve. An analysis of all the gathered articles show the application of at least one performance metric from Table 2.15 for assessing simulation results. The detection capabilities of methods are reflected by these performance metrics. Additionally, the definitions together with mathematical formulas for each performance metric are provided in this table.

where, T_P indicates the number of subjects correctly identified as positive (healthy), T_N refers to the number of individuals accurately identified as negative (abnormal), F_P represents subjects incorrectly categorized as normal when they are actually abnormal, and F_N denotes subjects incorrectly labeled as abnormal when they are actually normal.

2.5 Summary of Literature Review

The literature review chapter covered three areas such as QRS detection, spectral and nonlinear analysis of HRV, and ML applications for various cardiac arrhythmia classification. In the QRS detection, techniques like wavelet transforms, adaptive thresholding, and hybrid algorithms (e.g., HC+DWT) achieved good accuracy but face challenges in real-time applications due to computational intensity and sensitivity to noise. The analysis of spectral and nonlinear HRV demonstrates the effectiveness of features such as entropy, Poincaré plots, and time-frequency methods (e.g., FFT, CWT, Burg's periodogram) for distinguishing conditions such as MI, CAD and CHF, although limitations include small datasets and computational complexity. Traditional spectral HRV analysis also fails to capture nonlinear dynamics in pathological conditions. ML-based approaches for arrhythmia classification, particularly using CNNs, SVMs, and hybrid models, demonstrate better performance (accuracy exceeding 95%) in classifying MI and other cardiac conditions, with advancements in feature fusion and interpretability. However, challenges remain in generalizability across diverse populations (i.e., performance drops in cases of extreme arrhythmias or motion artifacts), high performance, real-time deployment, and handling noisy or imbalanced data. In addition to this, most of the studies focus on binary classification, neglecting multi-classification, which is crucial for clinical decision-making. Overall, these studies highlight the promise of advanced signal processing and ML techniques in cardiac diagnostics while emphasizing the need for robust, scalable solutions.

Table 2.15: Performance measures employed in the literature to evaluate and compare the results of various methods

Evaluation Metric	**Description**	**Mathematical Formula**
Accuracy	Accuracy measures the overall performance of the classification model and it is determined as the ratio of correctly classified subjects to the total number of subjects	Ac = $\frac{T_P+T_N}{T_P+T_N+F_P+F_N}$
Precision	• Represents the portion of Tp predictions among all positive predictions made by the model • It reflects the Accuracy of positive predictions	Pr = $\frac{T_P}{T_P+F_P}$
Recall (Sensitivity)	• Recall measures the ability of a model to correctly distinguish positive instances • It is the ratio of Tp to the total actual positives	Se = $\frac{T_P}{T_P+F_N}$
F1-score	The F1-score serves as a harmonic mean of precision and sensitivity, offering a unified metric that reflects the balance of a classification model's performance	F1-Score = $\frac{2*T_P}{2*T_P+F_P+F_N}$
Specificity	• Specificity evaluates the model's ability to accurately identify subjects who do not have cardiovascular disease (negative cases) • High specificity is crucial for minimizing the occurrence of F_P	Sp = $\frac{T_N}{T_N+F_P}$
Matthews correlation coefficient (MCC)	• MCC signifies the predictive ability of a classifier, indicated by the values that range from -1 to +1 • A value of +1 represents ideal predictions, meanwhile a value of -1 suggests inaccurate predictions entirely, and a value of 0 signifies a classifier is making random predictions	MCC = $\frac{T_P*T_N-F_P*F_N}{\sqrt{((T_P+F_P)(T_P+F_N)(T_N+F_P)(T_N+F_N))}}$
Area under the curve (AUC)	• The AUC quantifies the performance of a prediction model by measuring the region beneath the receiver operating characteristic (ROC) curve	AUC = $\frac{1}{2}(\frac{F_P}{F_P+T_N}+\frac{T_N}{T_N+F_P}$
Receiver Operating Characteristic (ROC) Curve	• Depicting a graphical illustration of the relationship between the true positive rate and the false positive rate • A model demonstrates better performance when its AUC reaches higher values approaching 1	It indicates the plot between sensitivity and specificity

CHAPTER 3

DELINEATION OF QRS FEATURES AND DENOISING OF ECG SIGNAL

3.1 Introduction

The Electrocardiogram signals are widely used for diagnosing various cardiac (Heart) abnormalities. However, these signals are often corrupted by noise and artifacts, which can hinder accurate interpretation and analysis. Effective denoising techniques are essential for enhancing signal quality, while precise delineation of QRS features is crucial for the reliable detection of cardiac events. This chapter focuses on advanced methods for ECG signal denoising and the accurate extraction of QRS complex features. The heart muscle is equipped with an intricate electrical system that regulates its rhythmic contractions, ensuring the proper circulation of blood throughout the body. However, when this internal electrical signaling is disrupted, it can lead to various abnormalities in heart rate and rhythm. These include accelerated heart rate known as tachycardia, slowed heart rate referred to as bradycardia, or an irregular heartbeat condition called arrhythmia (Singh et al., 2017a). The rate and rhythm of the heartbeat are governed by the heart's electrical system. To maintain health of the heart, detecting the parameters of Electrocardiogram signal is a crucial step. The condition of the heart can be known from the ECG signal which is generated from the electrical flow in the heart.

ECG is the recording of the electric activity of the heart in which, most widely used biomedical signal containing the most informative condition in clinical diagnostics of the heart. The ECG signal is generated from the process of depolarization and repolarization of the heart activity in each cycle and is characterized by P, QRS and T peaks. These peaks give information about the cardiac health of a person and are characterized by amplitude, duration, and intervals (Magrupov et al., 2020). The P wave is the result of the depolarization of the atrium. The QRS complex wave is due to the depolarization of ventricle and the repolarization effect is shown by T waves. The values of these parameters are dependent on the rhythm of breathing, the person's state of health, measurement conditions.The analysis of an ECG signal provides vital information for assessing a patient's physical condition and diagnosing cardiovascular diseases.

A number of diseases like, Atrial Fibrillation (characterized by lack of P wave), Ventricular Arrhythmias (characterized by longer QRS complex), Ventricular Fibrillation (irregular undulations without QRS complex), Myocardial Infarction (changes in the shape of the T wave), Atrial Flutter (the end of T and beginning of P disappears) (Najarian and Splinter, 2012) can be diagnosed using ECG. Because of varies types of noise present in the ECG signal, QRS de-

tection is very difficult. Sources of noise can arise from artifacts (due to motion of electrode), baseline wander, muscle noise and powerline interference. As discussed above, detection of the parameters of ECG signal (mainly the QRS complex) is the most crucial and decisive task to know the condition of the heart. Wrong detection leads to false interpretation, and this will cost on the person's life.

A wide range of techniques for analysing ECG signals, incorporating different signal processing methods have been investigated. One of the well-known techniques is investigated by Pan-Tompkins QRS detection algorithm (Pan and Tompkins, 1985). They developed a real time QRS detection by incorporating, band pass filter, differentiation, squaring, moving window integration and adaptive threshold comparison for reliable detection of the QRS complex. (Venkatesh et al., 2023) cardiovascular disease detection is proposed from ECG signals using a neural Network. in (Mondhe, 2022), a machine learning technique is used to detect the cardiovascular disease. In (Chen and Maharatna, 2020), combination of hierarchical clustering and discrete wavelet transform is applied to detect R peak and T wave. A robust QRS detection and R peak identification algorithm is proposed for wearable ECG sensors (Zhao et al., 2021). The methods in this work incorporate peak pre selection, bilateral threshold and R-peak identifier algorithms. R peak detection based on chaos analysis of ECG signal using principal component analysis (PCA) have been developed in (Gupta et al., 2020). Robust arrhythmia classification based on QRS detection and a compact 1D-CNN for Wearable ECG Devices is proposed in (Sabor et al., 2022).

Robust system for R-peak detection in Holter or wearable ECG signals using 1D convolutional neural network is proposed in (Zahid et al., 2021). In (Cao et al., 2023), variational mode decomposition based simultaneous R peak detection and noise suppression for automatic ECG analysis is presented. An adaptive threshold R-peak detection algorithm based on Brown?s exponential smoothing model is proposed in (Hao et al., 2022). Different techniques for QRS complex wave and R peak detection have been addressed based on, BayeSlope, Bayesian filtering, and non-linear normalization is applied to detect the R peaks in the ECG signal (De Giovanni et al., 2022), complete ensemble empirical mode decomposition with adaptive noise (Hossain et al., 2019), combination of Hierarchical clustering and Discrete Wavelet Transform (DWT) (Chen and Maharatna, 2020), infinite impulse response (IIR) type digital fractional order differentiator (DFOD) (Nayak et al., 2019), dual channels based on U-Net and bidirectional long short-term memory (He et al., 2020), wavelet convolutional neural networks (WaveletCNNs) autoencoders and a convolutional long short-term memory (ConvLSTM) (Yuen et al., 2020), embedded algorithm (Tueche et al., 2021), and so many papers apply different techniques.

Extensive research in literature has confirmed that accurately identifying R peaks or the

QRS complex remains a formidable challenge, particularly when dealing with various types of noise as previously discussed. In this study, an investigation of R-peak detection with less computational complexity with more accurate detection scheme is proposed.

3.2 Materials and Methods

3.2.1 Materials

The data collection is done on online available physionet database. From this website, MIT/BIH Arrhythmia (Moody and Mark, 2001), QTDB (Laguna et al., 1997), TWADB (Moody, 2008), AFTDB (Moody, 2004) and FANTASIA databases (Iyengar et al., 1996) are taken for detection of R peak. The denoising of the ECG signal is achieved by utilizing the Fejer-Korovkin (fk) wavelet, which closely resembles the morphology of the ECG signal. In this section, some of the ideas used for simulation of the proposed algorithm are discussed. In this study, we utilized Matlab 2021a for our analysis and experiments.

3.2.2 Methods

3.2.2.1 Maximal Overlap Discrete Wavelet Transform

The Maximal Overlap Discrete Wavelet Transform (MODWT) is an adaptation of the discrete wavelet transform (DWT) that utilizes a linear filtering operation to generate coefficients representing variations across multiple scales (Xiao et al., 2020). This technique enables the analysis of signals at different resolutions. Moreover, MODWT possesses the property of time shift-invariance, meaning that any translation in the input signal corresponds to an equal translation of the wavelet coefficients. As a result, important information is preserved even when the signal undergoes temporal shifts. MODWT is employed to extract both the high frequency (HF) component and the low frequency (LF) component from the original ECG signal (Sundarasekar et al., 2018). The detail coefficients (d) obtained from MODWT represent the high pass representation of the input, capturing the fine-scale variations, while the approximation coefficients (a) represent the low pass representation of the input at each stage, capturing the coarse-scale information. The mathematical derivation of MODWT is obtained from the DWT (Alves et al., 2016).

Let the DWT wavelet filter and scaling filter be $g_{j,l}$ and $h_{j,l}$, respectively. The MODWT wavelet filter $\tilde{h}_{j,l}$ and scaling filter $\tilde{g}_{j,l}$ is obtained as (3.1) and (3.2)

$$\tilde{h}_{j,l} = h_{j,l}/2^{j/2} \tag{3.1}$$

$$\tilde{g}_{j,l} = g_{j,l}/2^{j/2} \tag{3.2}$$

where, l is length of the filter ($l = 1,2,...,L$) and j is the level of decomposition.

Let $a_{j-1,n} = x_n$ be a time series of the original ECG signal, the MODWT pyramid algorithm generates the wavelet (detail) coefficients $d_{j,n}$ (3.3) and scaling (approximation) coefficients $a_{j,n}$ (3.4).

$$d_{j,n} = \sum_{l=0}^{L-1} \tilde{h}_l a_{j-1,(n-2^{j-1}l)modN} \tag{3.3}$$

$$a_{j,n} = \sum_{l=0}^{L-1} \tilde{g}_l a_{j-1,(n-2^{j-1}l)modN} \tag{3.4}$$

Where $\tilde{g}_l = g_l/\sqrt{2}$, $\tilde{h}_l = h_l/\sqrt{2}$, $n = 0,1,2,...,N-1$, and N denotes the length of time series of ECG signal.

Note that, unlike DWT, the coefficients $a_{j,n}$ and $d_{j,n}$ are not generated by down sampling by a factor of two the output of the corresponding filters.

Equation (3.3) and (3.4) can be expressed as a circular filter operations of the original time series x_n using the filters $\tilde{h}_{j,l}$ and $\tilde{g}_{j,l}$ as (3.5) and (3.6)

$$d_{j,n} = \sum_{l=0}^{L_j-1} \tilde{h}_{j,l} x_{n-lmodN} \tag{3.5}$$

$$a_{j,n} = \sum_{l=0}^{L_j-1} \tilde{g}_{j,l} x_{n-lmodN} \tag{3.6}$$

The n^{th} element of the fourth stage approximation and detail coefficients can be calculated by (3.7) and (3.8).

$$d_{4,n} = \sum_{l=0}^{L_4-1} \tilde{h}_{4,l} x_{n-lmodN} \tag{3.7}$$

$$a_{4,n} = \sum_{l=0}^{L_4-1} \tilde{g}_{4,l} x_{n-lmodN} \tag{3.8}$$

Using the inverse pyramid algorithm, the origional ECG signal is recovered as shown in (3.9)

$$a_{j-1,n} = \sum_{l=0}^{L-1} \tilde{h}_l d_{j,n+2^{j-1}lmodN} + \sum_{l=0}^{L-1} \tilde{g}_l a_{j,n+2^{j-1}lmodN} \tag{3.9}$$

where $n = 0,1,...,N-1$.

Unlike DWT, the sequence $a_{j-1,n}$ is not generated by up-sampling the output of the corresponding filters. In DWT, the sample size N is required to be an integer multiple of 2^j. This limitation is avoided by using MODWT. In comparison to DWT, MODWT offers the advantage of significantly improving the alignment between decomposed wavelet and scaling coefficients at each level, aligning them more closely with the original time series (Seo et al., 2017). This enhanced alignment makes it considerably easier to analyze localized signal variations in relation to both scale and time. As a result, the MODWT provides a powerful tool for gaining insights into the intricate dynamics of signals, enabling a more comprehensive understanding of their behavior and characteristics. Considering MIT-BIH arrhythmia data base, sampled at frequency of 360 Hz, the decomposition up to seven level is shown in Fig 3.1. As it can be

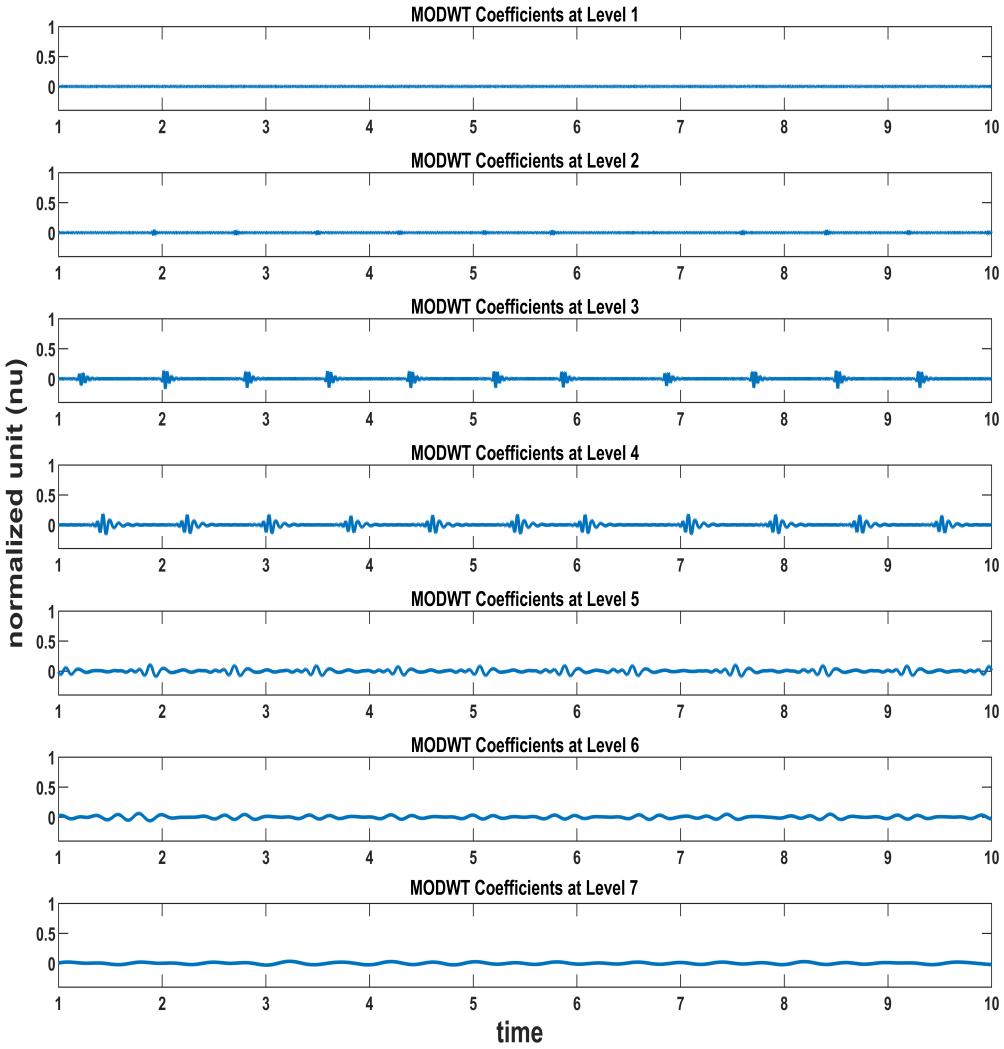

Figure 3.1: Decomposition of signal up to $7^{th} level$

seen from Fig 3.1, the 4^{th} level decomposition keeps the morphology of the signal with out dis-

tortion, compared to other decomposition levels. In this paper, a 4 level decomposition using MOWDT is applied to the signal as shown in Fig 3.2a.

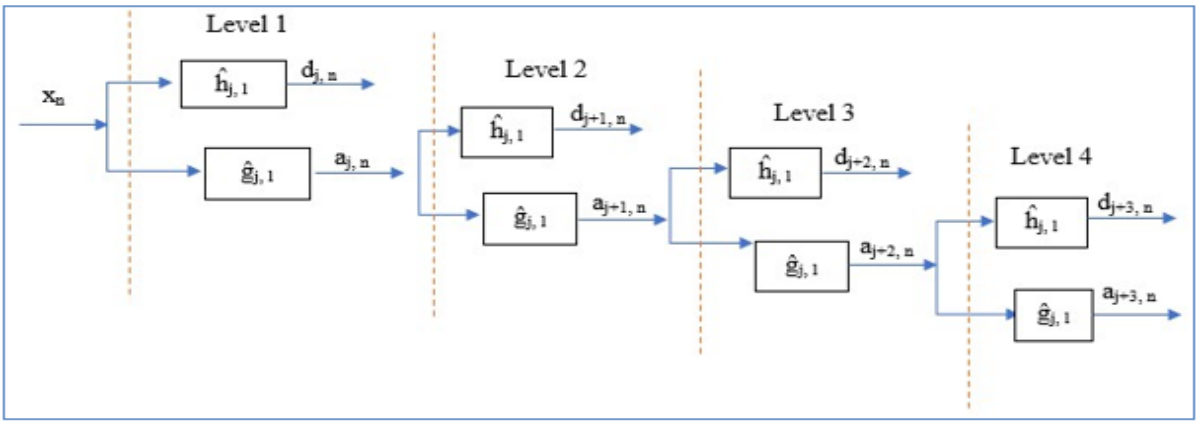

(a)

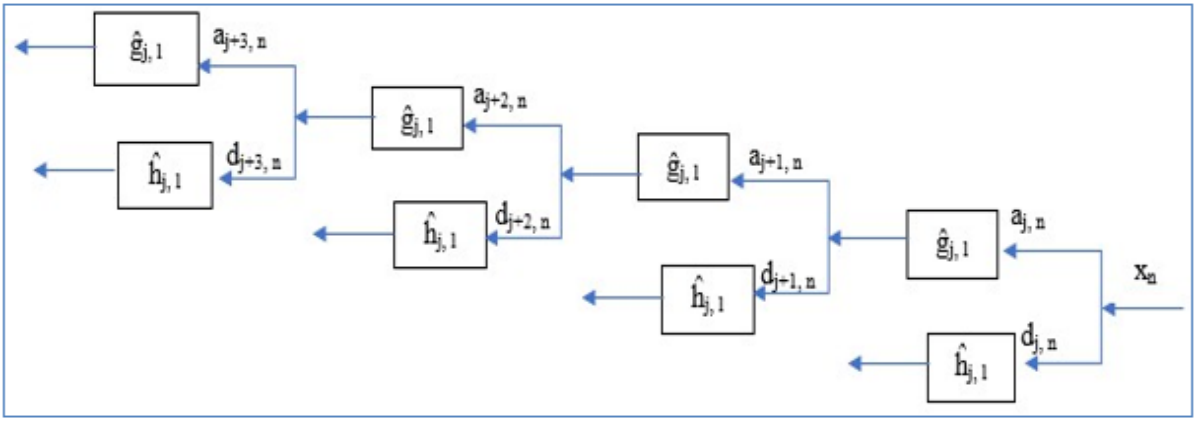

(b)

Figure 3.2: a) Decomposition of signal by MOWDT, b) Reconstruction of signal by IMODWT

The signal reconstruction process employs the Inverse Maximal Overlap Discrete Wavelet Transform (IMODWT), which relies on the coefficients obtained from the Maximal Overlap Discrete Wavelet Transform. The reconstructed ECG signal using IMOWDT is visually depicted in Fig 3.2b.

When selecting a suitable mother wavelet for the analysis of ECG signals, it is crucial to opt for a wavelet that is well-suited to the characteristics of the ECG signal under examination. In this proposed study, the Fejer-Korovkin wavelet family is chosen because shape of this family is match with ECG signal precisely.

3.2.2.2 Pre-processing

The pre processing step filters the noise and enhances the QRS complex of the original ECG signal as shown in Fig 3.3. Before denoising, the signal under goes with DC component re-

moval (X2) and normalization process (X3). The amplitude values of an ECG signal vary depending on factors such as the specific cardiovascular disease, the age, and the gender of an individual. To mitigate the potentially misleading effects caused by these variations during R-peak detection, a normalization process is applied. This process ensures that the ECG signal is adjusted to a consistent baseline, allowing for more accurate and reliable analysis. By normalizing the signal, the focus can shift towards accurately detecting and interpreting the crucial R-peaks, leading to improved insights into the cardiovascular health of the individual.

3.2.2.3 R-peak Detection

The objective of this stage is to locate the R-peaks of ECG signal. After the pre-processing stage, the denoised signal is evaluated in terms of the specified threshold used in our study based on the Pan Tompkins algorithm. This detected R-peak is useful to detect the QRS complex.

Algorithm 1 Decision algorithm for detecting R peak

Input: ECG signal, X
Output: R peak, pkr
Initialize: f_s, N, lev
$ECG \leftarrow x_1$
$threshold = mean(y)$;
$possition\_region \leftarrow (y > threshold * max\_h)$;
$lft = find(difference([0possition\_region]) == 1)$;
$rgt = find(difference([possition\_region0]) == -1)$;
for i=1:length(lft) **do**
    $[R\_value(i)R\_location(i)] = max(x1(lft(i) : rgt(i)))$;
    $R\_location(i) = R\_location(i) - 1 + left(i)$;
    $[Q\_value(i)Q\_location(i)] = min(x1(lft(i) : R\_location(i)))$;
    $Q\_location(i) = Q\_location(i) - 1 + lft(i)$;
    $[S\_value(i)S\_loc(i)] = min(x1(R\_location(i) : rgt(i)))$;
    $S\_location(i) = S\_location(i) - 1 + R\_location(i)$;
end for
$pkr = R\_location(1 : length(R\_location) - 1)$;
$Predicted\_length = length(pkr)$;

The methodology applied in this work is shown in Fig 3.3. The ECG signal is initially loaded and then subjected to preprocessing steps, including DC cancellation, to remove any unwanted components. Subsequently, the signal is normalized to ensure consistency in amplitude values. To analyze the signal further, a 4-level MODWT is applied using the fk22 wavelet function. While there are various wavelet functions available, selecting the most suitable mother wavelet can be a challenging task. However, in this particular study, the fk22 wavelet function is chosen due to its superior performance compared to other wavelet families, enabling more accurate and insightful analysis of the ECG signal. The third and fourth detail coefficients such

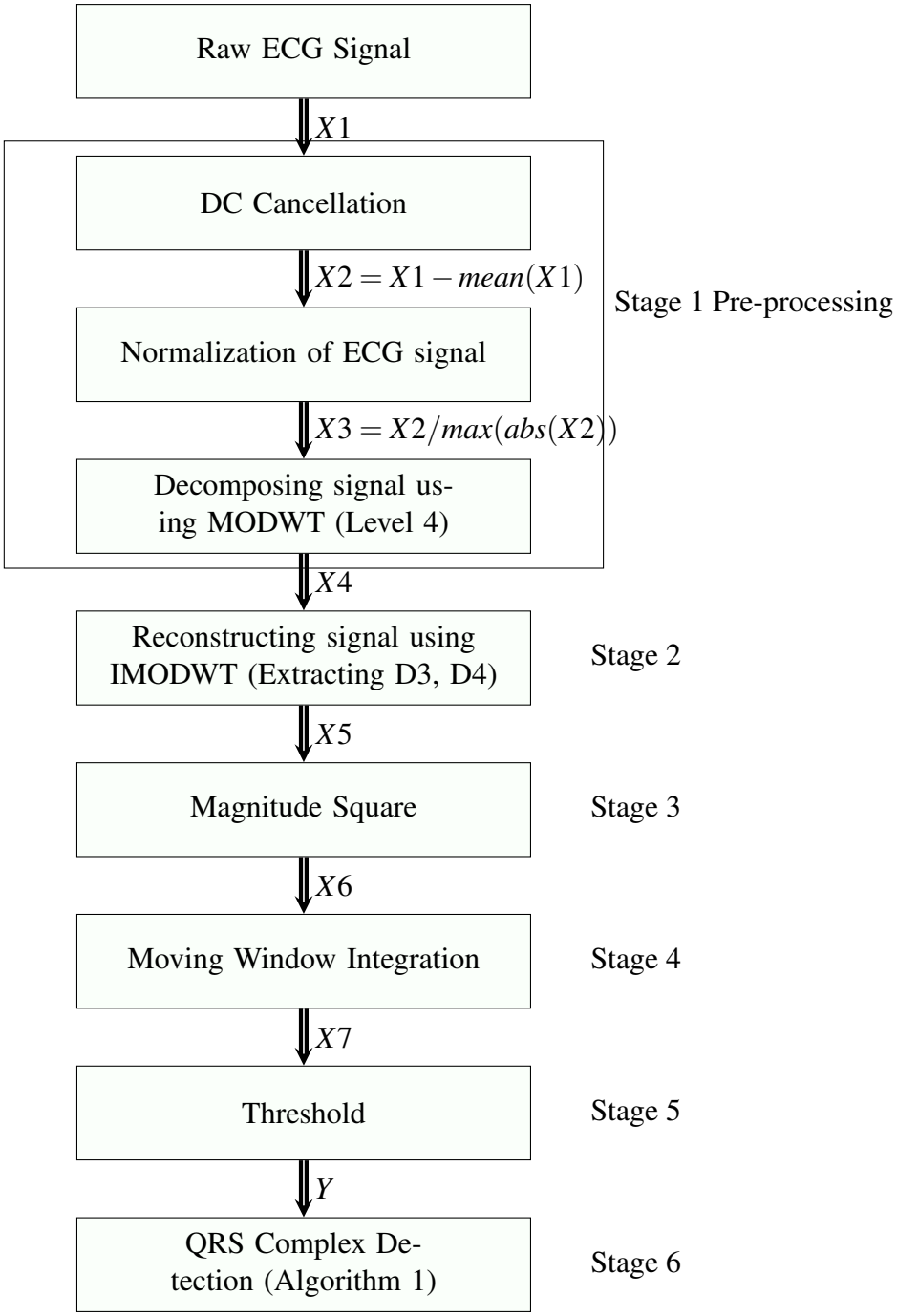

Figure 3.3: Block diagram of the proposed work

as $d_{j+2,n}$ and $d_{j+3,n}$ obtained from MODWT are used to reconstruct the signal using IMODWT. The output of magnitude reconstructed signal X5 is being squared (X6), since there may be a possibility of QRS complex being found in the negative side. After this pre-processing step, a moving window integration is applied to the magnitude square signal to detect the QRS complex. The mean of the samples within each window is computed to obtain a new signal with a

lower sampling rate. By multiplying the mean of the new signal with the maximum value of the original signal, a threshold value is setted. Any sample in the new signal greater than the threshold value is marked as QRS complex sample. From the QRS complex, by finding the minimum and maximum values within the window, required R-peak is identified. Algorithm 1 shows the main steps of R-peak detection used in this work.The method takes ECG signal as an input and it outputs R peaks detected. In line 5, the threshold value is set to be mean of the normalized value of the moving window integration (Y). Length of moving window integration taken is 31. The position of region of R peak is determined if Y is greater than the multiplication of Y and maximum value of Y (i.e max_h). The left and right points are identified by lft and rgt commands in line 7 and 8, respectively. R location is found from maximum of left to right position of the signal considering some offset. In same method, the location of Q and S is determined.

3.3 Performance Evaluation

The proposed method is evaluated for five data bases. The performance of the proposed approach is evaluated based on several merits, including sensitivity (se+), positive prediction (P+), and detection error rate (DER). These evaluation metrics serve as valuable indicators of the approach effectiveness in accurately identifying and predicting relevant outcomes. Sensitivity (recall) is given by (3.10), Positive prediction (precision) is given by (3.11) and DER is given by (3.12), as follows.

$$Se = \frac{TP}{TP+FN} \tag{3.10}$$

$$P+ = \frac{TP}{TP+FP} \tag{3.11}$$

$$DER = \frac{FP+FN}{TB} \tag{3.12}$$

Where, TP is the number of true positive, FN is the number of false negative, FP is the number of false positive, TB is the number of total number of beats annotated in the record.

3.4 Result and Discussion

3.4.1 MIT/BIH database

The Massachusetts Institute of Technology/Beth Israel Hospital (MIT/BIH) arrhythmia database comprises 48 ECG records, with each record containing a two-lead ECG data (channels) span-

ning a duration of 30 hours (equivalent to 650,000 sampling intervals). The sampling frequency for this database is set at 360 Hz, allowing for detailed analysis of the recorded ECG signals. In total, the database contains more than 110,000 beats, providing a rich dataset for arrhythmia research and analysis. The records have been collected from a diverse group of patients, consisting of 22 females and 25 males, spanning an age range of 23 to 89 years. For example, the data numbered as 111 was collected from female having age of 47, with first degree AV block. In this record, there are short bursts of both baseline shifts and muscle noise. Data point 115 was collected from a female individual with an age of 39. The recorded data represents a normal sinus rhythm, with a heart rate ranging between 49 and 87 beats per minute. Performance of proposed algorithm for the MIT-DB database is shown in Table 3.1.

Table 3.1: Evaluation of our QRS algorithm for mitdb databases

Record	**TB**	**FP**	**FN**	**TP**	**Se(%)**	**P+ (%)**	**DER (%)**
100	2272	0	0	2272	100	100	0
101	1864	2	0	1864	100	99.89	0.11
102	2186	0	0	2186	100	100	0
103	2083	0	1	2082	99.95	100	0.05
104	2228	92	9	2219	99.76	97.57	2.73
105	2571	12	3	2568	99.89	99.56	0.55
106	2026	109	69	1957	96.97	95.29	7.81
107	2136	13	1	2135	99.96	99.55	0.49
108	1762	68	20	1742	99.09	97	3.96
.	.	.	.	.	.	.	.
.	.	.	.	.	.	.	.
.	.	.	.	.	.	.	.
233	3078	0	18	3060	99.42	100	0.58
234	2752	0	0	2752	100	100	0
Total	109,443	497	318	109125	99.71	99.55	0.74

For MIT-BIH arrhytma database, since record number 111 has some noises, It is taken for analysis here. The original ECG signal, the signal decomposed by applying MOWDT and R peak detection is shown for recording data of 111 in Fig 3.4. Using 4 GB RAM, intel i5 computer and MATLAB 2021a, the elapsed time it takes is 4.43 seconds.

3.4.2 QTDB Database

QTDB database contains two channels and includes 15 hour records (225,000 sample intervals), sampled at 250 Hz. In QTDB database, 23 records doesn't have R peak annotations and we

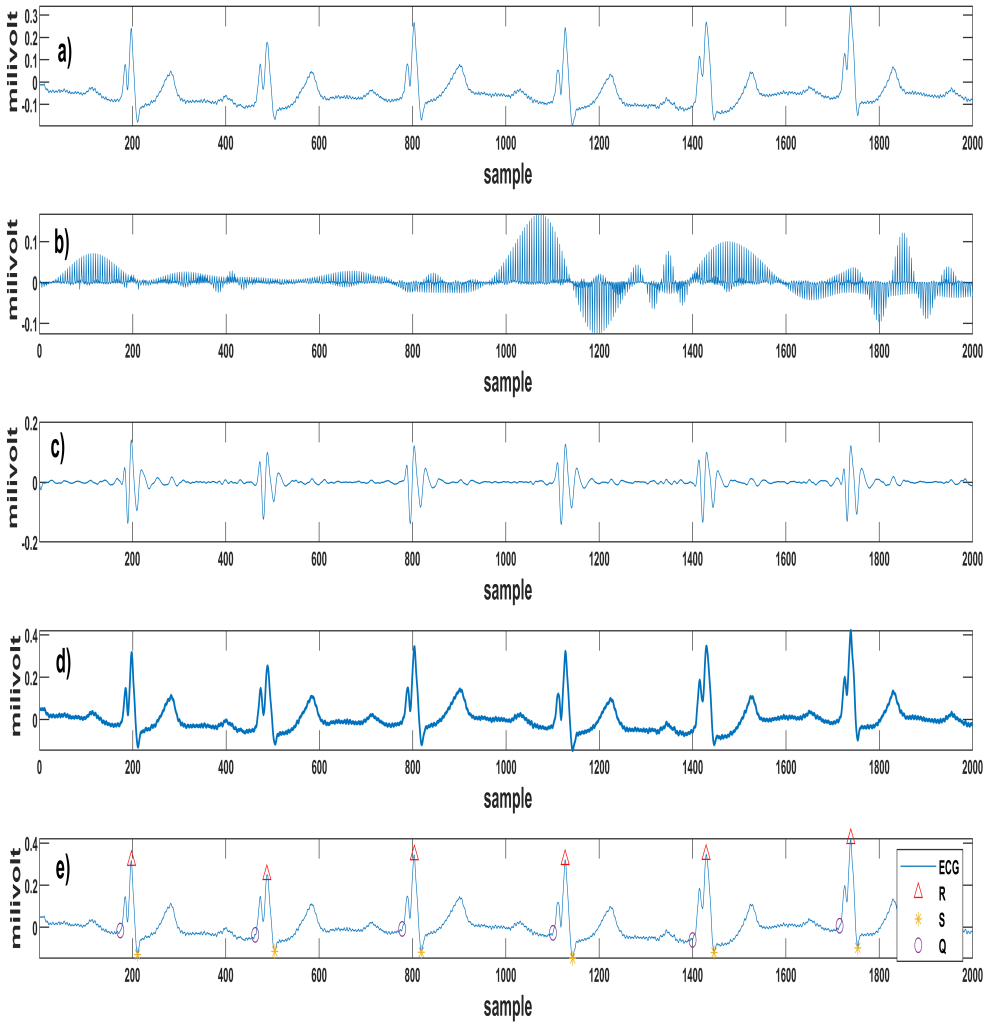

Figure 3.4: (a) Origional ECG signal, (b) decomposed by MOWDT, (c) reconstructed by IMOWDT, (d) ECG denoising (e) R-peak detection for record 111 in MITDB database

doesn't include these signals. Performance of proposed algorithm for the QTDB database is shown in Table 3.2.

Using the proposed algorithm, taking sel231 recording from QTDB database, the R peak detection is shown in Fig 3.5. sel231 is recording of female with age of 72. In this data, AV conduction is quite abnormal with periods of 2:1 AV block. The elapsed time it takes is 1.65524 seconds.

Table 3.2: Evaluation of our QRS algorithm for QTDB databases

Record	**Signal**	**FP**	**FN**	**TP**	**Se(%)**	**P+ (%)**	**DER (%)**
sel100	1133	0	0	1133	100	100	0
sel102	1087	0	0	1087	100	100	0
sel103	1047	0	0	1047	100	100	0
sel104	1108	0	0	1108	100	100	0
sel114	861	0	0	861	100	100	0
sel116	1184	1	0	1184	100	99.92	0.08
sel117	765	0	0	765	100	100	0
sel123	755	0	0	755	100	100	0
sel213	1641	0	1	1640	99.94	100	0.06
.	.	.	.	.	.	.	.
.	.	.	.	.	.	.	.
.	.	.	.	.	.	.	.
sele0612	750	0	0	750	100	100	0
sele0704	1093	0	0	1093	100	100	0
Total	86913	10	51	86862	99.95	99.99	0.06

Table 3.3: Evaluation of our QRS algorithm for aftdb databases

Record	**Signal**	**FP**	**FN**	**TP**	**Se(%)**	**P+ (%)**	**DER (%)**
twa00	140	18	0	140	100	90.22	10.84
twa01	251	2	0	251	100	99.21	0.79
twa02	200	7	2	198	99.27	97.5	3.27
twa03	175	0	0	175	100	100	0
twa04	186	0	0	186	100	100	0
twa05	253	4	0	253	100	98.67	1.35
twa06	246	0	0	246	100	100	0
twa07	209	1	2	207	99.37	99.68	0.95
twa08	148	3	0	148	100	98.14	1.89
.	.	.	.	.	.	.	.
.	.	.	.	.	.	.	.
.	.	.	.	.	.	.	.
twa98	252	0	0	252	100	100	0
twa99	143	0	0	143	100	100	0
Total	18893	72	8	18885	99.98	99.64	0.4

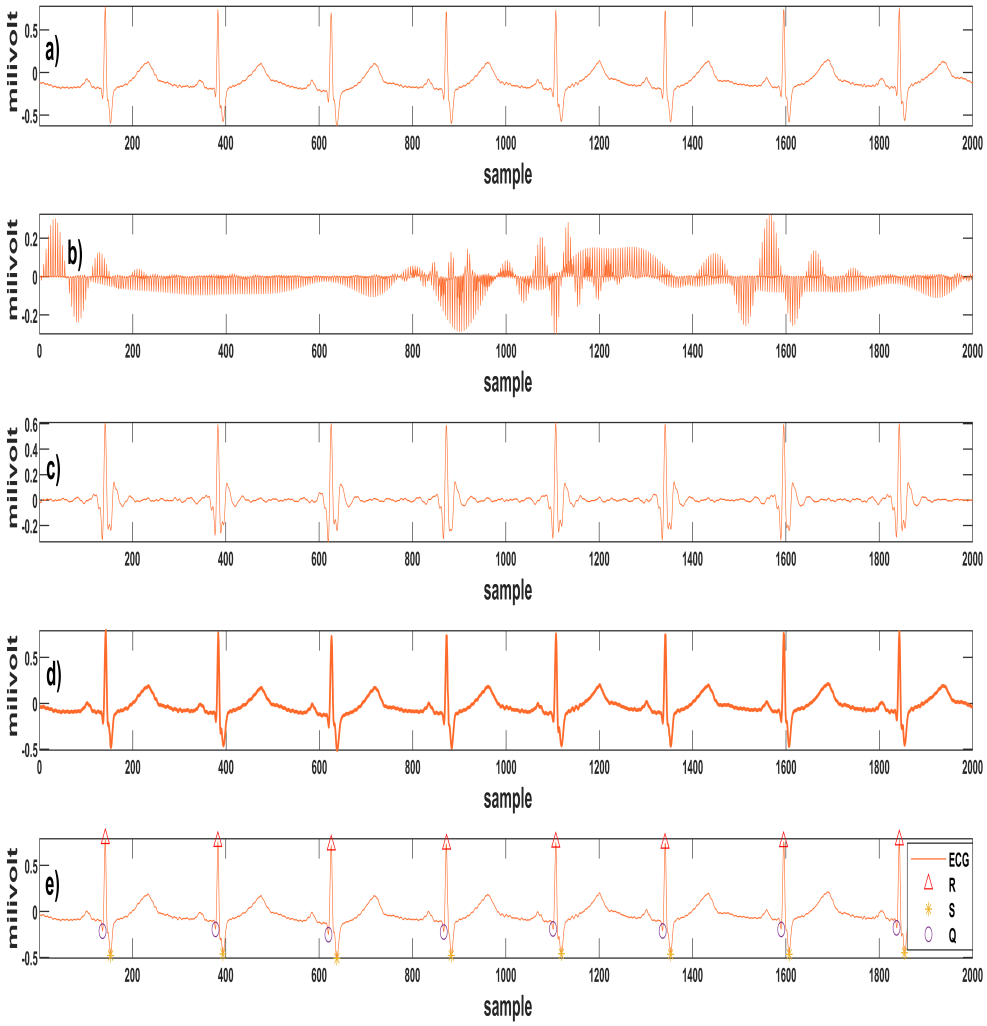

Figure 3.5: (a) Origional ECG signal, (b) decomposed by MOWDT, (c) reconstructed by IMOWDT, (d) ECG denoising (e) R-peak detection for record sel231 in QTDB database

3.4.3 TWADB Database

T-Wave Alternans Database (TWADB) contains around 2 hour recordings (60,000 sample intervals), sampled at 500 Hz. Some of the records contain three channels, but most of the records contain twelve channels. Performance of proposed algorithm for the twadb database is shown in Table 3.3. As shown in Table 3.3, proposed algorithm achieves high sensitivity and +P for TWADB database. R peak detection of ECG signal is shown in Fig 3.6. twa06 record number has 12 channels, in this case channel I is considered. The elapsed time it takes is 1.089 seconds.

From the above results, it can be shown that the proposed algorithm detects R-peak accu-

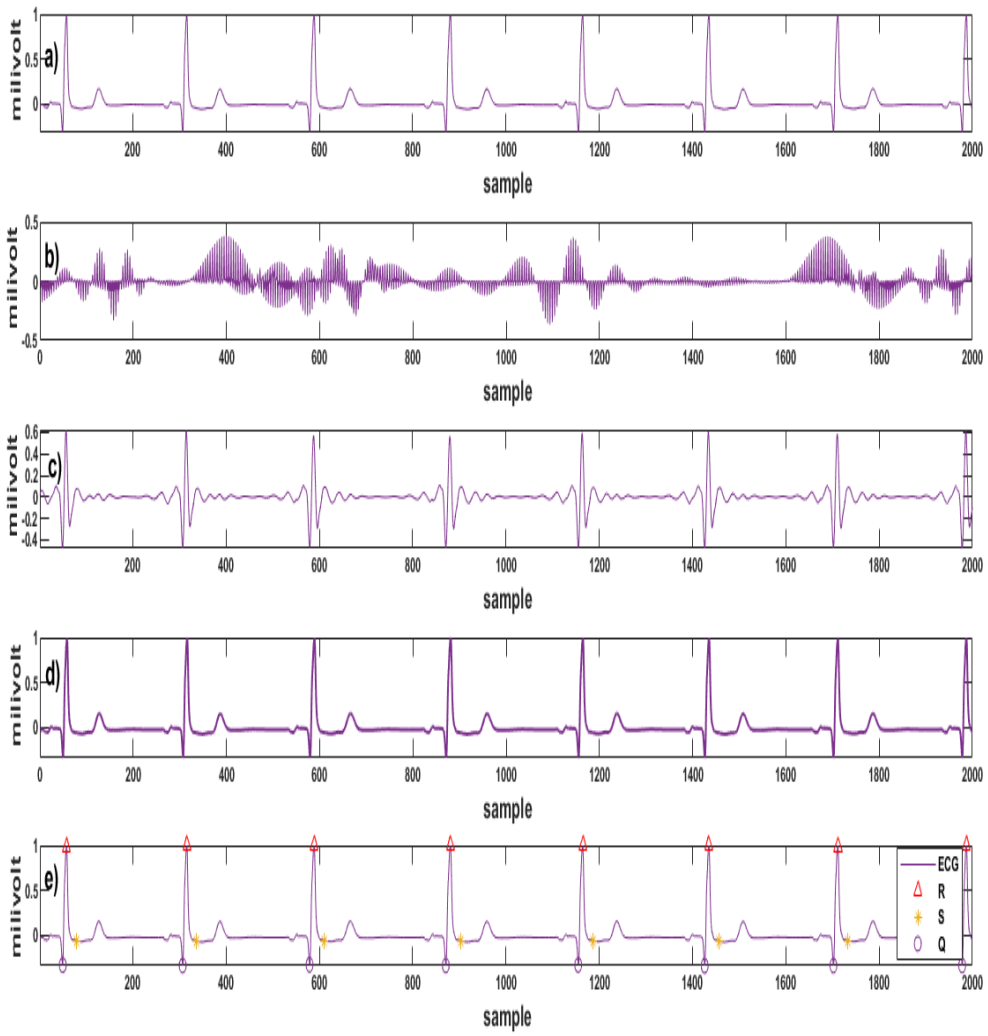

Figure 3.6: (a) Origional ECG signal, (b) decomposed by MOWDT, (c) reconstructed by IMOWDT, (d) ECG denoising (e) R-peak detection for record twa06 in TWADB database

rately. In addition to this, It achieves good result for the parametric measures considered here. Generally, the summary of proposed work for five database results is shown in Table 3.9.

Comparison of the proposed algorithm is compared to other algorithms is listed in Table 3.4, 3.5, 3.6, 3.7 and 3.8. The FANTASIA database encompasses 40 recordings obtained from a diverse group of individuals, including both males and females, with ages ranging from 21 to 85. The recordings are sourced from a total of 32 individuals. The database utilizes a sampling frequency of 250 Hz to capture the intricacies of the recorded signals. Each record spans approximately two hours, equivalent to 1,808,223 sample intervals, and consists of two

Table 3.4: Comparison for mitdb database

S.N	Reference	Year	Total Beats	TP	Se (%)	P+(%)	DER (%)
1	(Pan and Tompkins, 1985)	1985	116,137	115,860	99.76	99.56	0.68
2	(Christov, 2004)	2004	110,050	109,615	99.74	99.65	0.44
3	(Zidelmal et al., 2012)	2012	109,494	109,101	99.64	99.82	0.54
4	(Lu et al., 2018)	2018	109,966	109,653	99.72	99.69	0.59
5	(Zalabarria et al., 2020)	2020	106,581	106,096	99.54	99.6	0.86
6	(Modak et al., 2021)	2021	109,494	109,331	**99.85**	**99.91**	**0.25**
7	(Zhao et al., 2021)	2021	109966		99.81	99.88	0.31
8	Proposed Work	2023	109,443	109,125	99.72	99.55	0.74

Table 3.5: Comparison for qtdb database

S.N	Reference	No. of beats	Se (%)	P+(%)	DER (%)
1	Pan et al. (Pan and Tompkins, 1985)	86995	99.54	99.68	0.77
2	Pandit et al. (Pandit et al., 2017)	86435	99.87	99.91	
3	Elgendi et al. (Elgendi, 2013)	86995	99.97	99.57	
4	Chen et al. (Chen and Maharatna, 2020)	114770	99.92	99.95	
5	Martinez et al. (Martínez et al., 2004)	86892	99.92	99.95	
6	Zhao K et al. (Zhao et al., 2021)	86995	**99.99**	99.98	**0.04**
7	Proposed Work	86913	99.95	**99.99**	0.06

channels. The first channel solely records the breathing rhythm, while the second channel captures the ECG signal.

Table 3.6: Comparison for twadb database

S.N	Reference	No. of beats	Se (%)	P+(%)	DER (%)
1	Pan et al. (Pan and Tompkins, 1985)	18991	96.94	98.21	4.83
2	Elgendi et al. (Elgendi, 2013)	18991	98.69	96.66	4.71
3	Zhao K et al. (Zhao et al., 2021)	18991	99.18	98.37	2.52
4	Proposed Work	18893	**99.97**	**99.64**	**0.4**

AF Termination Challenge Database (AFTDB) database includes two channels two hour records (7680 sampling intervals) with sampling frequency of 128 Hz.

As it can be seen in Table 3.9, the proposed algorithm achieves high sensitivity, +P and low DER for TWADB database and well performs for QTDB database also. The SNR for TWADB database is higher than any other databases.

The performance of ECG analysis heavily relies on the precise and accurate detection of key features such as the QRS complex, as well as the P and T waves. The detection and measurement of these characteristic waves play a crucial role in diagnosing various cardiac functions. For instance, the accurate detection of the QRS complex is essential for determining the heart rate and serves as a reference point for beat alignment. The location of the QRS

Table 3.7: Comparison for FANTASIA database

S.N	Reference	No. of beats	Se (%)	P+(%)	DER (%)
1	Pan et al. (Pan and Tompkins, 1985)	285311	82.7	99.86	17.42
2	Elgendi et al. (Elgendi, 2013)	285311	99.93	99.78	0.29
3	Zhao K et al. (Zhao et al., 2021)	285311	99.96	99.84	0.2
4	Proposed Work	152248	99.75	99.88	0.37

Table 3.8: Comparison for AFTDB database

S.N	Reference	No. of beats	Se (%)	P+(%)	DER (%)
1	Pan et al. (Pan and Tompkins, 1985)	7591	98.99	99.27	1.74
2	Elgendi et al. (Elgendi, 2013)	7591	98.56	99.23	2.2
3	Zhao K et al. (Zhao et al., 2021)	7591	98.85	99.44	1.7
4	Proposed Work	7512	**99.84**	**99.81**	**0.36**

complex is typically represented by the R peak index, aiding in the identification and analysis of important cardiac parameters. After analyzing the data presented in Tables 3.4 through 3.8, it becomes evident that our proposed method outperforms others due to its sensitivity and positive prediction rates for TWADB and QTDB databases. This superior performance is attributed to the versatility of our approach, which leverages wavelet transform, allowing for effective signal denoising and R-peak detection. As a result, the P, T waves, and QRS complex are clearly discernible in the ECG signal, preserving crucial clinical information and enhancing overall evaluation capabilities.

Table 3.9: Summary of the proposed work for five database results

Database	TB	FP	FN	TP	Se(%)	P+ (%)	DER (%)	SNR (dB)
MITDB	109,443	497	318	109,125	99.72	99.55	0.74	35.84
QTDB	86,913	10	51	86,862	99.95	**99.99**	**0.06**	36.96
TWADB	18893	72	8	18885	**99.97**	99.64	0.4	**46.29**
AFTDB	7512	11	14	7498	99.84	99.81	0.36	25.98
FANTASIA	152248	184	391	151857	99.75	99.88	0.37	27.35

3.5 Summary

This chapter presented an efficient method designed for both denoising the ECG signal and accurately detecting R-peaks. Given the presence of various noise sources, the original ECG signal often becomes distorted. To minimize this, first removal of the DC component and normalization of the signal has been done followed by employing wavelet transform for de-noising. After completing the pre-processing steps, a threshold-based approach was employed

for R-peak detection. To validate the efficacy of the proposed method, extensive testing on five distinct PhysioNet databases, namely MITDB, QTDB, TWADB, AFTDB, and FANTASIADB has been conducted. The simulation results have shown that the proposed method achieved a Se+ of 99.97% and P+ of 99.64%, with a DER of 0.403 for the TWADB database, and a Se+ of 99.95%, a P+ of 99.99%, and an exceptionally low DER of 0.063 for the QTDB database. These outcomes demonstrated that the proposed method outperformed in terms of sensitivity for the TWADB database and offers superior positive prediction and lower detection error rates for the considered database. Proposed work stands out as a highly effective method for ECG signal processing and R-peak detection, making it suitable for application to a wide range of ECG datasets.

CHAPTER 4

NON-STATIONARY SPECTRAL AND COHERENCE INVESTIGATION OF CARDIOVASCULAR SIGNALS

4.1 Introduction

Cardiovascular signals such as Heart Rate Variability, Respiratory (RESP), SABPV, and APIV provide critical insights into autonomic and cardiovascular regulation. These inherently non-stationary signals require advanced time-frequency methods for accurate spectral and coherence analysis. Investigating the dynamic interactions among these signals helps understand physiological mechanisms under various conditions. This chapter explores non-stationary spectral and coherence techniques to analyse these cardiovascular signals' interdependence and temporal variability.

Heart rate variability encompasses the natural fluctuations in the time intervals between consecutive heartbeats (Jung et al., 2024), serving as a potential indicators or early warning signs of underlying cardiac conditions (Agrawal et al., 2024). The analysis of HRV (RR-interval) serves as a commonly employed quantitative indicator for assessing the activity of the autonomic nervous system (ANS). The HRV signal spectrum primarily characterized by the spectral components of very low frequency power (VLF), low frequency power (LF), and high frequency (HF) power (Force, 1996). The VLF frequency component is defined in range of 0.0033 to 0.04 Hz. The frequency bands corresponding to LF, and HF components are defined in ranges of LF: 0.04 to 0.15 Hz, and HF: 0.15 to 0.4 Hz, respectively. The frequency band of systolic arterial pressure interval variability (APIV) and systolic arterial blood pressure variability (SABPV) varies in the LF and HF component. While the Respiratory (RESP) signal varies in the high frequency band. The complexity of the cardiovascular (CAV) system prevents accurate characterization through time or frequency domain analysis alone. To overcome this challenge, TF approaches have been developed to accurately monitor changes in HRV spectra (Besfat et al., 2024b). The Fast Fourier Transform (FFT) is commonly used for power spectrum estimation in HRV analysis due to its computational efficiency and high frequency resolution. However, this technique does not offer details about the temporal localization of frequency components in the signals (Alghoul et al., 2017a). To overcome this limitation, various time-frequency analysis tools have been developed for HRV data. These traditional tools, including the short-time Fourier transform (STFT), Wigner-Ville distribution (WVD) (Liu et al., 2023a), and wavelet transform, offer valuable insights into the dynamic nature of HRV, allowing for a more comprehensive understanding of cardiovascular regulation and health. To overcome the inaccurate TF localization of these techniques, recently

Optimized adaptive modified Stockwell transform (OptADMST), Synchroextracting transform (SET), Synchrosqueezing transform (SST), and reassignment (RS) method has been proposed by different authors. Comparing with all the other time frequency representations (TFRs), the linear STFT is relatively simple (Wang and Veluvolu, 2017a) but the resolution which it can provide is limited in a way due to the Heisenberg-Gabor uncertainty principle. Even though the bilinear Wigner–Ville distribution (WWD) affords the best concentration of chirp signals it experiences appearances of cross-terms that interferes with the representation of signal elements. TF resolution of such classical methods is low; thus making them unable to accurately characterize the non-linear behaviors of non-stationary signals. SST is a valuable post-processing time-frequency analysis (TFA) method in non-stationary signal processing, but it suffers with lower TF resolution (TF blurs) for components that exhibit rapid TF variations. Even though SST, SET, and RS provide a better TF localization compared to the classical methods, still they suffer in detecting accurately these subtle changes in the cardiovascular signal.

A key requirement for an effective TFR is achieving sufficient concentration of signal components to accurately represent the signal. The RS method effectively enhances signal concentration in the TF domain by reallocating energy distribution based on the gravitational center of the energy contribution (Yang et al., 2014), (Li, 2022). RS reassigns the TF spectrogram to the instantaneous frequency trajectory, achieving higher TF resolution (Flandrin et al., 2018); however, the use of a fixed Gaussian window reduces the clarity of the representation (Li, 2022). To solve this problem, an optimized RS method on the Gaussian window is proposed based on the energy concentration measure. The proposed TFA method can generate more energy-concentrated TF results than the STFT, OptADMST (Singh et al., 2017a), SST, SET, and RS methods. In many applications, the interdependence between HRV, RESP, SABPV and APIV signals over time, necessitating statistical measures such as non-stationary coherence to reveal these dynamic relationships. Non-stationary spectral coherence (NSSC) is a powerful tool for uncovering functional dynamics among various cardiovascular signals, as it assesses the linear relationship between two simultaneous time series across various frequencies. Characterizing the interactions between the HRV-SABPV signals and HRV-RESP signals is important as it provides valuable insights into the baroreflex and RESP sinus arrhythmia. Additionally, the time-frequency coherence (TFC) between HRV-APIV signals is estimated to determine whether the APIV signal can serve as a surrogate for the HRV signal (Singh et al., 2018a). Traditional methods often suffer from limited TF resolution, resulting in relatively high variance and random errors. Consequently, achieving an adequate resolution and low variance when estimating the TFC of a non-stationary process remains a complex task.

In this study, energy concentration based an optimized Gaussian window RS (OptGWRS) method using a particle swarm optimization (PSO) algorithm has been proposed to achieve a

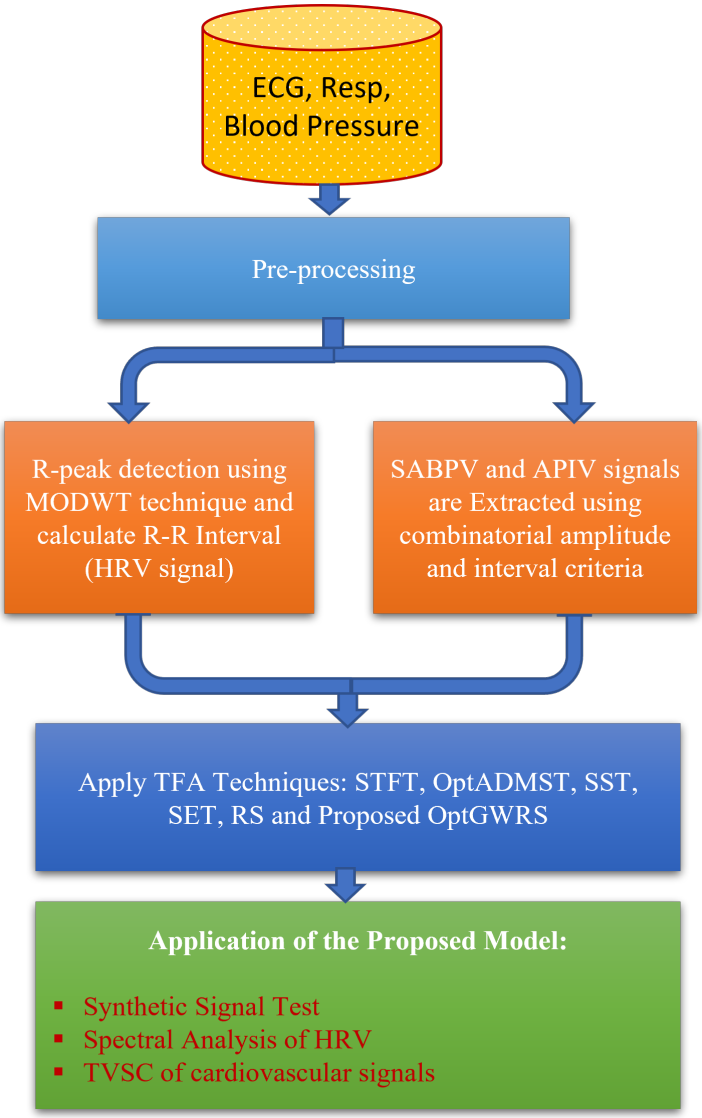

Figure 4.1: Framework of the proposed work

higher TF resolution of non-stationary spectral (NSS) analysis. The performance of the proposed technique is assessed by three synthetic signals which resemble a real HRV, RESP, and blood pressure signals. For the real application of the proposed work, the HRV signal was derived from R-R intervals by applying the MODWT R- peak detection algorithm (Besfat et al., 2024a) to the actual ECG signal, which was obtained from the fantasia database. The RESP signal is also taken from this database. The arterial blood pressure waveforms (SABPV and APIV) are extracted using combinatorial amplitude and interval criteria (Li et al., 2010). Figure 4.1 illustrates the framework of the proposed work. Subsequent sections provide a detailed explanation of the framework. The robustness of the considered TFA method is also evaluated while accounting of two additive white Gaussian noise (AWGN) at signal to noise ratio (SNR) 5dB and 0 dB. In addition to this, the interaction among HRV, RESP, SABPV, and APIV sig-

nals has been investigated by the proposed method for the understanding of the cardiovascular control.

4.2 Material and Methods

In this section, the datasets used and the methodology applied for the spectral analysis of CHF using FAWT from HRV signal has been explained.

4.2.1 Database

The database utilized in this study is sourced from the publicly available PhysioNet database (Goldberger et al., 2000a). For this study, two specific databases were selected to include subjects with different conditions. Subjects with normal cardiac function were obtained from the Fantasia database, and individuals with CHF were sourced from the BIDMC Congestive Heart Failure (chfdb) database.

The Fantasia dataset includes a total of 40 subjects, categorized into two groups: 20 young (yng) patients aged 21 to 34 years and 20 elderly (eldy) patients aged 68 to 85 years (Goldberger et al., 2000b), sampled at 250 Hz. For this study, we consider a time interval of 300 seconds (5 minutes) for each dataset, resulting in a total of 75,000 samples. So, the HRV, RESP, SABPV, and APIV signals are extracted from the Fantasia database and resampled to 4 Hz for the analysis. The APIV and SABPV time series were derived by extracting the minimum and maximum values of the blood pressure (BP) signal on a beat-to-beat basis (Singh et al., 2018a).

4.2.2 Pre-processing

The pre-processing stage aims to optimize the data quality and remove any artifacts that could impact the accuracy and reliability of the analysis. The preprocessing step includes detecting and correcting ectopic beats. First, the outliers are detected by using a median filter. Any HRV value greater than the threshold is detected as an outlier. This technique is robust to noise and effectively removes isolated outliers. Next, the detected ectopic beats are corrected by performing cubic spline replacement. For each detected ectopic beat, it replaces the value with the average of the neighboring HRV values (applying interpolation). Non-stationarity within the HRV signal can lead to a significant dispersion of variance in the lowest frequency range. To address this issue, the detrending process aims to remove any underlying trends or non-stationarity present in the signal, thereby enhancing the accuracy of the analyses. Next, detrending of the HRV signal is done using the *detrend* function and will remove the linear trend from the signal.

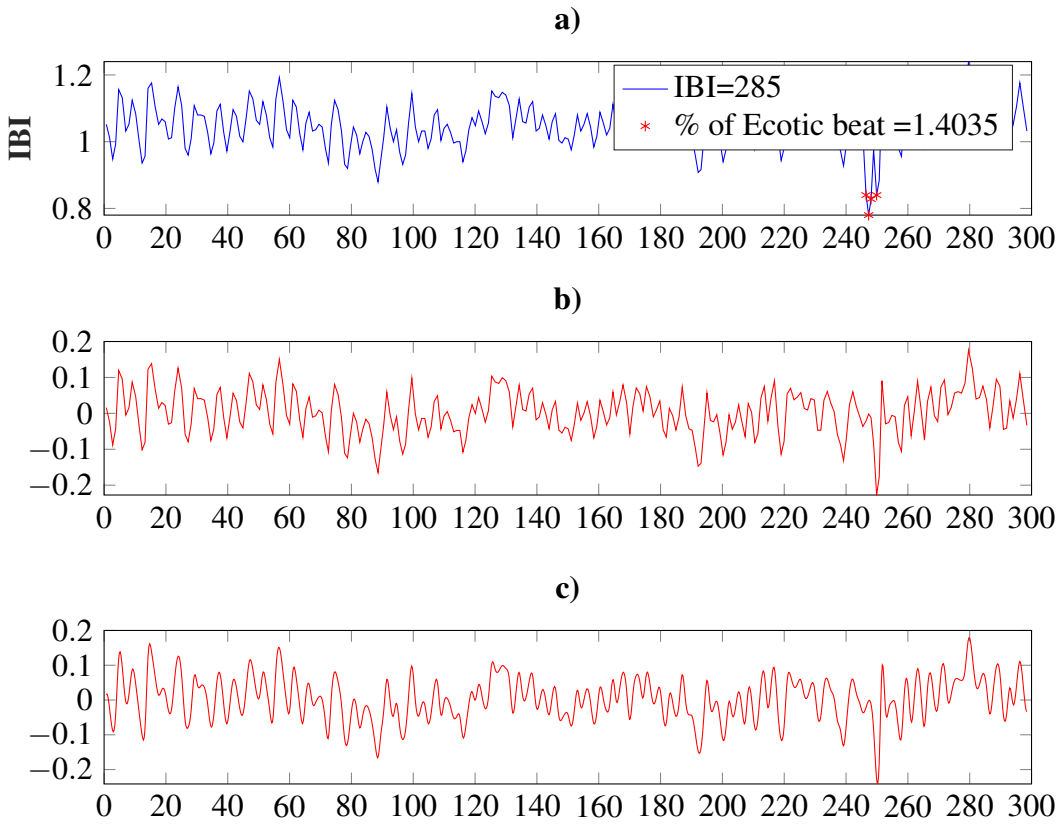

Figure 4.2: (a) IBI with ectopic beat, (b) IBI after detrending and ecotopic replacement, (c) IBI after resampling

The presence of artifacts in the inter-beat interval (RR interval) time series can introduce considerable distortions in the results of HRV analysis (Karimulla and Patra, 2024). Therefore, it is crucial to either correct or exclude all artifacts from the analysis. Common types of artifacts consists of extra, missing or misaligned beat detections, as well as ectopic beats like premature ventricular contractions (PVC) or other arrhythmias. These outliers are detected by using a median filter. The inter-beat-interval (IBI) and the ectopic replacement is displayed on Figure 4.2. Next, the detected ectopic beats are corrected by performing cubic spline replacement. For each detected ectopic beat, it replaces the value with the average of the neighboring HRV values.

4.2.3 Energy Concentration-Based Optimization of Gaussian Window Reassignment for Time-Frequency Analysis, and Its Application in Analyzing the Non-Stationary Spectral and Coherence of Cardiovascular Signals

Before conducting HRV signal analysis, a pre-processing stage is applied to the raw HRV signal. This stage involves detecting and correcting outliers and applying detrending techniques. Outliers, which represent extreme values or sudden spikes caused by abnormal or irregular heartbeats (ectopic beats), are identified and handled. Following the pre-processing step, the OptGWRS transform is utilized to perform spectral analysis of the LF, and HF components. The proposed optimized Gaussian window Reassignment technique is shown in Figure 4.3. The process begins by receiving an input signal and parameters of standard deviation factor (k) and window length (p). A Gaussian window is then generated to prepare for the reassignment TF representation (Eq. 4.6). The RS frequencies are calculated and a TF matrix is constructed. Following this, the energy concentration measure is computed for each parameter (Eq. 4.11). A PSO algorithm (Bai, 2010; Wang et al., 2018; Gad, 2022) is applied to calculate the maximum energy concentration at optimum value of k and p (k_{opt}, p_{opt}). Finally the reassignment TF is calculated at k_{opt}, p_{opt} (Eq. 4.7)

4.2.3.1 Time-Frequency Analysis

Due to the non-stationary nature of the HRV signals, the adoption of TF methodologies becomes essential to capture and characterize the temporal changes in frequency components, enabling a more comprehensive understanding of HRV (Singh et al., 2017a). Conventional TFA methods often produce a blurry TF representation that falls short in accurately capturing the TF features of non-stationary signals. An optimized RS method is introduced in this paper, which employs maximum energy concentration to extract non-stationary components from both the LF and HF components of the HRV signal. This technique is applied to the synthetic signal and real HRV data to validate its effectiveness.

4.2.3.2 Reassignment Method

Reassignment technique is a TF analysis which provides a higher TF resolution and greater energy concentration of a signal, (Yu et al., 2017), (Bakiya et al., 2020), (Li et al., 2020b), (Rajinikanth et al., 2023). Since the RS is a post processing tool for the STFT, the mathematical derivation of RS starts from STFT as:

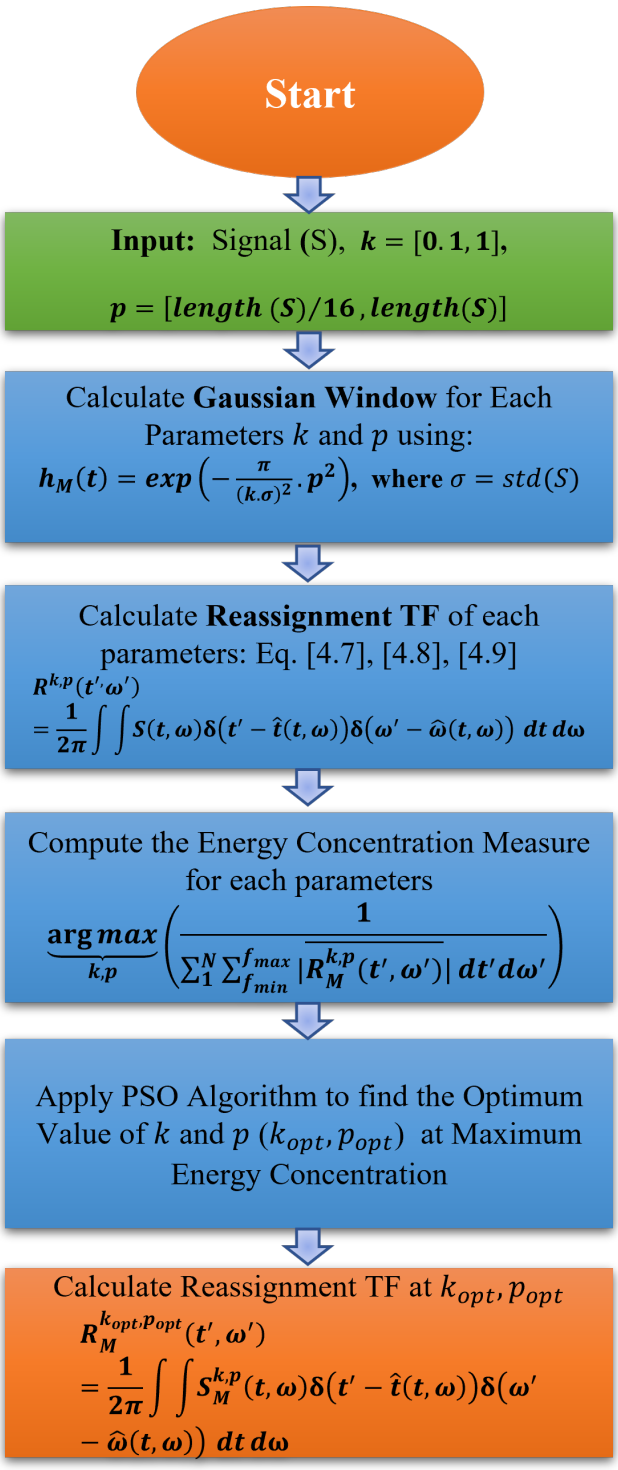

Figure 4.3: Proposed block diagram of Optimized Gaussian Window Reassignment TF technique

Given a signal s, and taking a window g, the STFT of a signal s is given by

$$\text{STFT}(t,\omega) = \int_{-\infty}^{\infty} s(u)h^*(t-u)e^{-i\omega u}\,du \tag{4.1}$$

h(t) is the Gaussian window $\frac{1}{\sqrt{2\pi}\sigma}e^{-\frac{t^2}{2\sigma^2}}$, where σ is the standard deviation which defines the width of the window.

The main objective of the RS is to maximize the energy concentration such that the resolution achieve ideal time frequency (TF_{ideal}) analysis

$$TF_{ideal}(t,\omega) = V(t)\cdot\delta(\omega-\phi'(t)) \tag{4.2}$$

Where, $V(t)$ is the instantaneous amplitude, $\phi'(t)$ represents the instantaneous frequency, which is the first derivative of the instantaneous phase $\phi(t)$.

A technique for refining the value of a TF representation at a given point (t,ω) in the TF plane is set out so as to counteract the effect of smoothing out of signal components. This is made accomplished by shifting the point of attribution of the average to the coordinates $(\hat{t},\hat{\omega})$ in which it is the center of gravity of the energy contributions instead of the point (t,ω) at which the computation takes place. This reassignment brings a change in the TF representation depending on the time point (t' and the frequency point ω') to its new value. To achieve such a higher resolution, the reassignment moves the energy distributed by the spectrogram to the local center of gravity of the TF representation (Auger et al., 2013).

The reassigned time and frequency coordinate can be expressed as

$$\hat{t}(t,\omega) = t - \text{Re}\left\{\frac{STFT_{Th}(t,\omega)STFT^*(t,\omega)}{|STFT(t,\omega)|^2}\right\} \tag{4.3}$$

$$\hat{\omega}(t,\omega) = \omega + \text{Im}\left\{\frac{STFT_{Dh}(t,\omega)STFT^*(t,\omega)}{|STFT(t,\omega)|^2}\right\} \tag{4.4}$$

where STFT(t, ω) is the STFT computed with an analysis window h(t), $STFT_{Th}(t,\omega)$ is the STFT computed with analysis window or smoothing kernel $th(t)$ (i.e time weighted version of, which is a time weighted version of $h(t)$), and $STFT_{Dh}(t,\omega)$ correspond to STFT with smoothing kernels $\frac{d}{dt}h(t)$, (the time derivative of $h(t)$).

By the reassignment technique, the STFT values are reassigned from the original coordinates to the new coordinates as $|S(t,\omega)| \rightarrow R[\hat{t}(t,\omega),\hat{\omega}(t,\omega)]$. Then RS can be written as

$$R^{k,p}(t',\omega') = \frac{1}{2\pi}\int\int S(t,\omega)\delta(t'-\hat{t}(t,\omega))\delta(\omega'-\hat{\omega}(t,\omega))\,dt\,d\omega. \tag{4.5}$$

Where, $\delta(t)$ is a Dirac function, $S(t,\omega)$ is the squared modulus of the STFT (i.e spectrogram). The full derivation of the RM can be found on (He et al., 2019), (Auger and Flandrin, 1995).

It is essential to note that the goal of the RS method is to enhance the sharpness of the localization of signal components by reallocating their energy in the TF plane (i.e., by determining center of the gravity). The initial step in the reassignment approach involves calculating the center of gravity of the signal's energy for each point on the TF plane, represented by $(\hat{t},\hat{\omega})$.

4.2.3.3 The Proposed Window

The size of the Gaussian window is fixed, which can be seen as a limitation since it does not account for the characteristics of the analyzed signal. Adapting the window to the signal would be more beneficial in order to enhance the resolution of the RS method. The Gaussian window can be modified as (Yu et al., 2017)

$$h_M(t) = \exp\left(-\frac{\pi}{(k\cdot\sigma)^2}\cdot p^2\right) \tag{4.6}$$

The introduced parameters, standard deviation factor k and the length of the window p are designed to provide greater flexibility to the Gaussian window. The choice of these parameters greatly affects the quality of the resulting TF representation. To address this issue, the parameters k and p are optimized using a particle swarm optimization algorithm in this study.

Now, The modified RS transform can be expressed as

$$R_M^{k_{opt},p_{opt}}(t',\omega') = \frac{1}{2\pi}\int\int S_M^{k,p}(t,\omega)\delta(t'-\hat{t}(t,\omega))\delta(\omega'-\hat{\omega}(t,\omega))\,dt\,d\omega \tag{4.7}$$

Where, $S_M^{k,p}(t,\omega)$ is the modified spectrogram of the optimized STFT based on $h_M(t)$.

4.2.3.4 Optimization Methodology to Select Optimal Parameters

This study proposes a PSO algorithm for the automatic generation of adaptive parameters (k,p) that take into account the characteristics of the analyzed signal, utilizing an energy concentration measure (ECM) as the objective function applied to the modified RS technique based on (Moukadem et al., 2015). The choice of the value of lower bound L_b and upper bound U_b is based on (Kiliçarslan, 2023).

$$ECM(k,p) = \frac{1}{\int_{-\infty}^{+\infty}\int_{-\infty}^{+\infty}\left|\overline{R_M^{k,p}(t',\omega')}\right|\,dt'\,d\omega'} \tag{4.8}$$

Table 4.1: PSO parameters for the proposed OptGWRS technique

Parameters	**value**
Number of particles	10
Number of iterations	10
Number of dimensions	2
Inertia weight	0.7
Cognitive coefficient	1.5
Social coefficient	1.5
Lower bounds	[0.1, length(S)/16]
Upper bounds	[1, length(S)]

Where, the module of the modified RS-transform is normalized as:

$$\overline{R_M^{k,p}(t',\omega')} = \frac{R_M^{k,p}(t',\omega')}{\int_{-\infty}^{+\infty}\int_{-\infty}^{+\infty}\left|R_M^{k,p}(t',\omega')\right|^2 dt'\,d\omega'} \tag{4.9}$$

Then, the optimization problem can be expressed as follows:

$$\arg\max_{k,p}\left(\frac{1}{\int_{-\infty}^{+\infty}\int_{-\infty}^{+\infty}\left|\overline{R_M^{k,p}(t',\omega')}\right| dt'\,d\omega'}\right) \tag{4.10}$$

Then the overall optimization problem can be written as:

$$\arg\max_{k,p}\left(\frac{1}{\sum_1^N\sum_{f_{\min}}^{f_{\max}}\left|\overline{R_M^{k,p}(t',\omega'}\right| dt'\,d\omega'}\right) \tag{4.11}$$

Where, N is the length of samples of the signal. This can be considered as nonlinear optimization problem with constraints.

The PSO parameters considered in this study are illustrated in Table 4.1.

4.2.3.5 Non-Stationary Spectral Coherence (NSSC)

The NSSC measures the strength of local interrelationship between two non-stationary processes, represented by the signals $X(\tau)$ and $Y(\tau)$. It can be expressed as (Olhede and Walden,

2002).

$$NSSC(\tau,F) = \frac{|Sm\{P_{XY}(\tau,F)\}|}{\sqrt{Sm\{P_{XX}(\tau,F)\}} \times Sm\{P_{YY}(\tau,F)\}}, NSSC(\tau,F) \in [0,1] \tag{4.12}$$

The cross power spectrum P_{XY} is defined as $P_{XY}(\tau,F) = T_{\tau-F}(X) \cdot *T_{\tau-F}(Y)$, P_{XX} and P_{YY} denotes auto cross spectral power of two stochastic processes within the TF domain. The smoothing $Sm\{P_{XY}(\tau,F)\}$ can be defined as $Sm\{P_{XY}(\tau,F)\} = P_{XY}(\tau,F) \otimes \emptyset(\tau,F)$. Where, $Sm\{.\}, T_{\tau-F}\{.\}, \otimes, \emptyset(\tau,F)$ and $*$ signifies smoothing operator, TF transform, convolution, smoothing operator and complex conjugate, respectively.

To mitigate interference and satisfy the Couchy–Schwarch inequality, an elliptical exponential kernel smoothing operator is employed, expressed as:

$$\emptyset(\tau,F) = \exp\left\{-\pi\left[\left(\frac{\nu}{\nu_0}\right)^2 + \left(\frac{\chi}{\chi_0}\right)^2\right]^{2\lambda}\right\} \tag{4.13}$$

The parameters of the operator are chosen as $\nu_0 = 0.8$, $\chi_0 = 0.2$, and $\lambda = 0.3$ based on (Singh et al., 2018a).

4.2.3.6 Statistical Analysis

In analyzing the coherence between two signals, the TF spectral coherence is influenced by parameters such as SNRs, threshold values, and energy concentration, which are essential for its assessment. These dependent parameters necessitate the application of specific statistical analyses to determine the significance of the NSSC evaluations. A statistical analysis of each dataset is performed through the use of a hypothesis test as based on(Singh et al., 2018a).

A Wilcoxon rank sum test was utilized to analyze the coupling among CAV signals in the healthy yng and eldy groups, with statistical significance determined as $P < 0.05$.

4.3 Result and Discussion

4.3.1 Result

4.3.1.1 Synthetic Test Signals/ Experimental Results

In this study, we have utilized synthetic signals that closely resemble cardiovascular signals within the same frequency range, as discussed in studies (Orini et al., 2011), (Singh et al., 2017a), and (Singh et al., 2018a). The study involved conducting performance testing on various TFA methods, including STFT, OptADMST, SST, SET, RS, and the proposed OptGWRS

Table 4.2: Mathematical Formulation of STFT, OptADMST, SST, SET, RS, and OptGWRS Techniques

TF technique	Mathematical expression
STFT	$STFT(t,\omega) = \int_{-\infty}^{\infty} s(u)h^*(t-u)e^{-i\omega u}\,du$
OptADMST	$OST(t,f) = \frac{\lvert f\rvert}{\left(\frac{1}{N}f + d\,\mathrm{var(sign.)}\sqrt{2\pi}\right)} e^{-\frac{f^2t^2}{2(f/N+d\,\mathrm{var(sign.)})^2}}$
SST	$T_s(\omega_l,\beta) = \int_{\{\alpha:\omega f(\alpha,\beta)\in F_l\}} W_s(\alpha,\beta)\alpha^{-3/2}\,d\alpha$
SET	$SET(t,\omega) = G_e(t,\omega)\cdot\delta(\omega-\omega_0(t,\omega))$
RS	$R'(t',\omega') = \frac{1}{2\pi}\int\int S(t,\omega)\delta(t'-\hat{t}(t,\omega))\delta(\omega'-\hat{\omega}(t,\omega))\,dt\,d\omega$
OptGWRS	$R_M^{k,p}(t',\omega') = \frac{1}{2\pi}\int\int S_M^{k,p}(t,\omega)\delta(t'-\hat{t}(t,\omega))\delta(\omega'-\hat{\omega}(t,\omega))\,dt\,d\omega$

d- optimization parameter, $\omega_s(a,b)$- CWT of s(t), a is a scaling factor, b is a shift factor, $G_e(t,\omega)$ indicates STFT

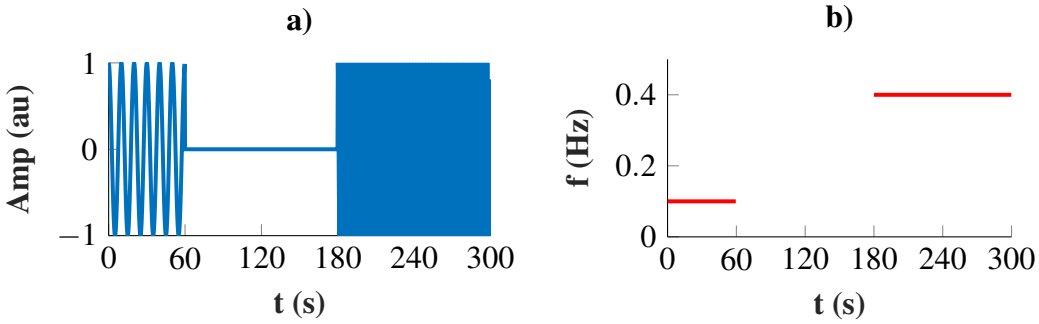

Figure 4.4: Simulation of Synthetic signal $S_1(t)$ (a) Time domain waveform, (b) Instantaneous frequency

approach. The mathematical formulation of the six TF analysis techniques is illustrated in Table 4.2 To assess the effectiveness of these six methods, we have produced three synthetic signals: $S_1(t)$, $S_2(t)$, and $S_3(t)$ signals modeled to resemble cardiovascular signals.

A synthetic signal $S_1(t)$ exhibit distinct characteristics, as it demonstrates stationary behavior with frequency components of $0.1Hz$ within the time range of $0 \leq t < 60$ s, as well as a frequency component of $0.4Hz$ in the interval $180 < t \leq 300$ s.

$$S_1(t) = \begin{cases} \cos(0.2\pi t) & \text{for } 0 \leq t < 60 \text{ s} \\ 0 & \text{for } 60 \leq t \leq 180 \text{ s} \\ \cos(0.8\pi t) & \text{for } 180 < t \leq 300 \text{ s} \end{cases} \tag{4.14}$$

IF is a key feature to understand the time-varying behaviors of the HRV signal. The synthetic signal waveform and IF plot of the signal $S_1(t)$ is shown in Figure 4.4.

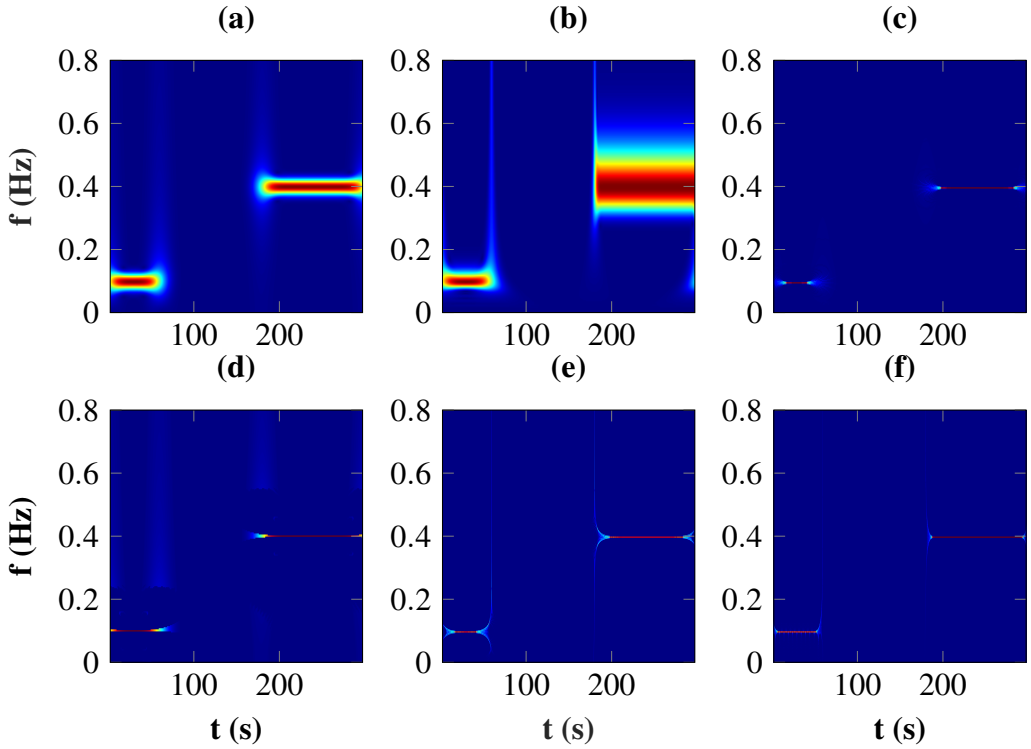

Figure 4.5: NSS of (a) STFT, (b) OptADMST, (c) SST, (d) SET, (e) RS, (f) OptGWRS of signal $S_1(t)$

For the first signal $S_1(t)$, the optimized adaptive modified stockwell transform (OptADMST) exhibits poor time-frequency resolution compared to other time-frequency analysis (TFA) techniques, as illustrated in Figure 4.5b. The time-frequency representation (TFR) obtained using STFT for $S_1(t)$ (Figure 4.5a) also demonstrates inadequate TF localization. Although SST achieves clear frequency resolution, it fails to capture the signal across the entire defined time range. In contrast, the proposed method (OptGWRS) offers good resolution throughout the TF plane. Overall, for signal $S_1(t)$, the proposed approach surpasses the frequency resolution of methods STFT (Figure 4.5a), OptADMST (Figure 4.5b), SST (Figure 1c), SET (Figure 4.5d), and RS (Figure 4.5e), as depicted in Figure 4.5f. The optimized parameters for maximum energy concentration in the proposed technique are 0.2 and 291.56.

The analytical formulas for the standard synthetic signals, $S_2(t)$ and $S_3(t)$, are provided as

$$S_2(t) = \Re\{A_{S2,LF}e^{-i\theta_{S2,LF}(t)} + A_{S2,HF}e^{-i\theta_{S2,HF}(t)}\} \tag{4.15}$$

$$S_3(t) = \Re\{A_{S3,LF}e^{-i\theta_{S3,LF}(t)} + A_{S3,HF}e^{-i\theta_{S3,HF}(t)}\} \tag{4.16}$$

Where, $A_{S2,LF}, A_{S3,LF}$ represent the instantaneous amplitude in LF band of the signal $S_2(t)$ and $S_3(t)$, whereas $A_{S2,HF}, A_{S3,HF}$ in HF band of the signal $S_2(t)$ and $S_3(t)$, respectively.

These, the instantaneous amplitude of the two signals is given by

$$\begin{aligned} A_{S2,LF} &= 4 + 3\sin(2\pi t) \\ A_{S2,HF} &= 4 + \cos(2\pi t) \end{aligned} \tag{4.17}$$

$$\begin{aligned} A_{S3,LF}(t) &= \begin{cases} 0 & \text{for } 60 \leq t \leq 180 \text{ s} \\ 4U(t) & \text{otherwise} \end{cases} \\ A_{S3,HF}(t) &= \begin{cases} 0 & \text{for } 60 \leq t \leq 90 \text{ s } \& \ 240 \leq t \leq 300 \text{ s} \\ 4U(t) & \text{otherwise} \end{cases} \end{aligned} \tag{4.18}$$

$\theta_{S2,LF}$, $\theta_{S2,HF}$ and $\theta_{S3,LF}$, $\theta_{S3,HF}$ $(rad/2/pi)$ represent the instantaneous phase of the signals $S_2(t)$ and $S_3(t)$ in LF and HF bands, respectively, and can band derived as

$$\begin{aligned} \theta_{S2,LF} &= 0.09t + 0.05\sin(4\pi t), \\ \theta_{S2,HF} &= 0.275t + 0.125\sin(4\pi t) \end{aligned} \tag{4.19}$$

$$\begin{aligned} \theta_{S3,LF} &= \theta_{S2,LF}, \\ \theta_{S3,HF} &= \theta_{S2,HF} \end{aligned} \tag{4.20}$$

The instantaneous frequency (IF) can be found from the instantaneous phase by applying the relation of $f = \frac{1}{2\pi}\frac{d\theta}{dt}$ and is given by

$$\begin{aligned} f_{S2,LF}(t) &= \frac{d\theta_{iX,LF}(t)}{2\pi dt} \quad \text{for } 0 \leq t \leq 300 \text{ s} \\ f_{S2,HF}(t) &= \frac{d\theta_{iX,HF}(t)}{2\pi dt} \quad \text{for } 0 \leq t \leq 300 \text{ s} \end{aligned} \tag{4.21}$$

$$\begin{aligned} f_{S3,LF}(t) &= \begin{cases} 0 & \text{for } 60 \leq t \leq 180 \text{ s} \\ \frac{d\theta_{iS3,LF}(t)}{2\pi dt} & \text{otherwise} \end{cases} \\ f_{S3,HF}(t) &= \begin{cases} 0 & \text{for } 60 \leq t \leq 90 \text{ s } \& \ 240 \leq t \leq 300 \text{ s} \\ \frac{d\theta_{iS3,HF}(t)}{2\pi dt} & \text{otherwise} \end{cases} \end{aligned} \tag{4.22}$$

The synthetic signals' waveforms and the IF plot of $S_2(t)$ and $S_3(t)$are presented in Figure 4.6 and Figure 4.7, respectively.

For the signal $S_2(t)$ (Figure 4.8), the methods STFT and OptADMST exhibit poor frequency resolution across the entire frequency band. In the lower frequency range, OptADMST performs better than STFT; however, in the higher frequency range, STFT outperforms OptADMST. Rényi entropy captures the concentration of a distribution which can offer understanding on the manner in which energy is distributed in the TF domain. In this study, the Rényi entropy parameter α is taken as 2.5 based on (Li et al., 2020a)). Although SST yields

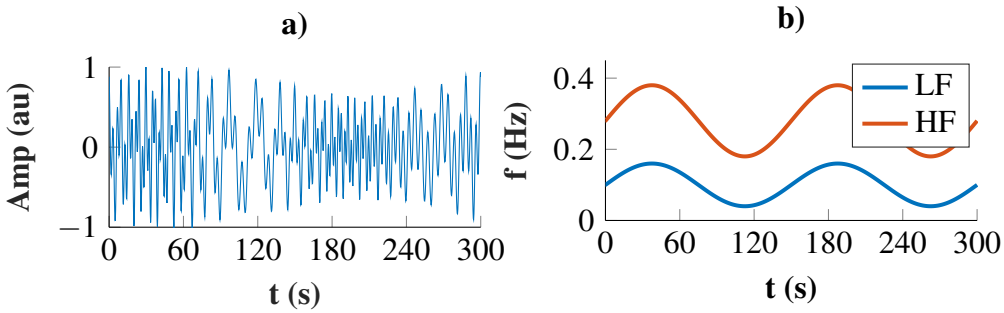

Figure 4.6: Simulation of Synthetic signal $S_2(t)$ (a) Time domain waveform, (b) Instantaneous frequency

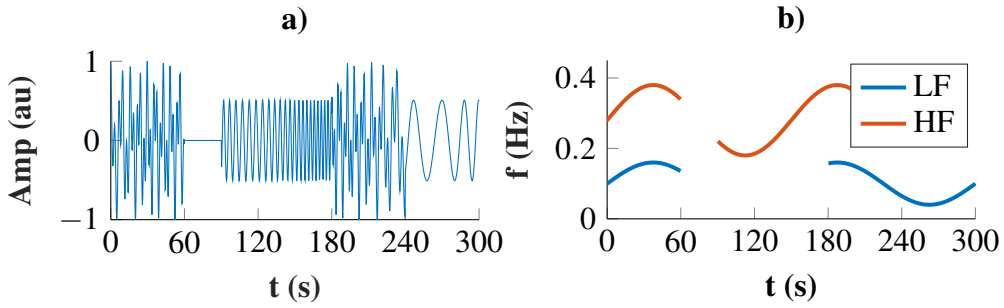

Figure 4.7: Simulation of Synthetic signal $S_3(t)$ (a) Time domain waveform, (b) Instantaneous frequency

a lower Rényi entropy value, as shown in Table 4.3, its spectral visualization indicates that it has overall poor resolution in the higher frequency range compared to SET, RS, and the proposed OptGWRS, as illustrated in Figure 4.8c. In the lower frequency range, SET provides the best TFR across the entire time-frequency plane. Among all methods, the proposed OptGWRS delivers a clear TFR, as seen in Figure 4.8f. The optimized parameters for energy concentration maximization using the proposed technique are 0.3421 and 446.6627. For the synthetic signal $S_3(t)$, the methods STFT and OptADMST demonstrate poor TF localization across both low and high frequencies, as illustrated in Figures 4.9a and 4.9b. In contrast, SST, SET, and RS provide improved TFRs compared to STFT and OptADMST. However, the proposed technique outperforms all others, offering clear TF localization that closely aligns with the ideal TFR across the entire frequency band, as shown in Figure 4.9. The optimized parameters for

Table 4.3: Rényi Entropy of different TFA

Signal	STFT	OptADMST	SST	SET	RS	OptGWRS
$S_1(t)$	13.16	14.71	9.25	9.81	9.31	**8.99**
$S_2(t)$	14.85	15.01	10.58	11.98	10.67	**10.49**
$S_3(t)$	14.67	14.85	10.49	11.82	10.24	**10.15**

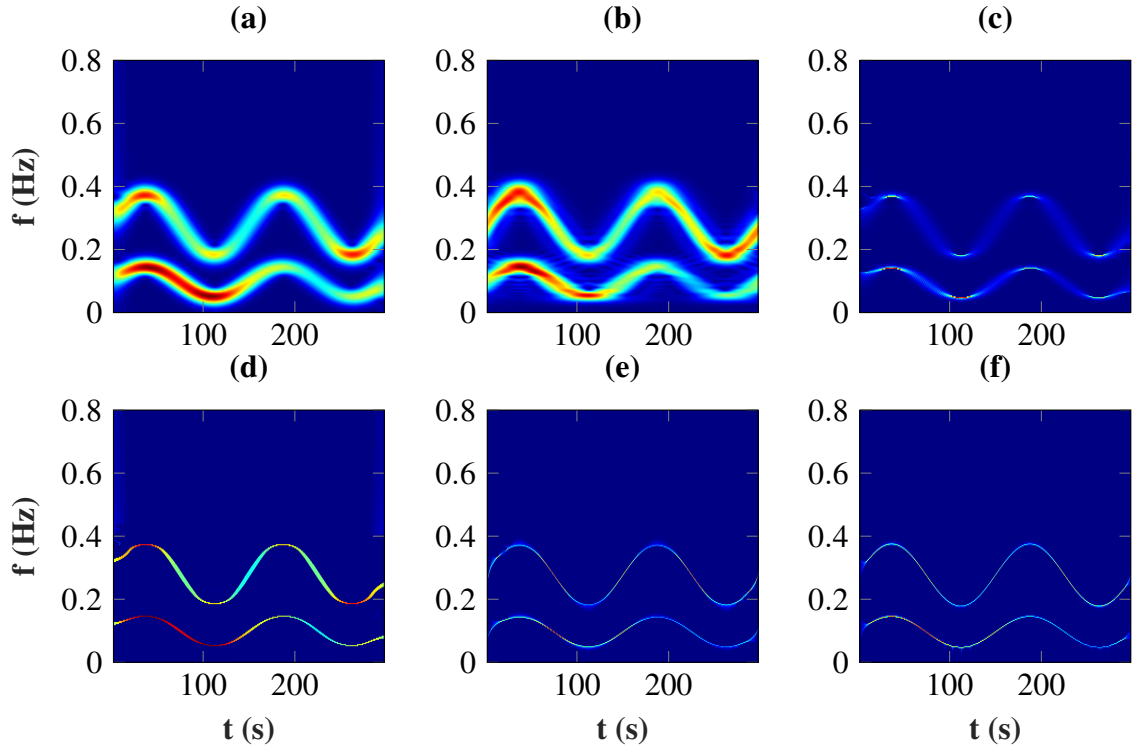

Figure 4.8: NSS of (a) STFT, (b) OptADMST, (c) SST, (d) SET, (e) RS, (f) OptGWRS of signal $S_2(t)$

energy concentration maximization using the proposed technique are 0.24 and 365.25. The optimized parameters of the proposed method for the three considered signals are found by utilizing a PSO algorithm as presented in Table 4.4

Table 4.4: Optimized parameters obtained by the proposed method

Signal	k_{opt}	p_{opt}
$S_1(t)$	0.2	291.56
$S_2(t)$	0.3421	446.6627
$S_3(t)$	0.24	365.25

For the comparison of the proposed method with the other transform techniques, ECM, Renyi entropy, and computational time are considered in this study. A lower value of Rényi entropy achieved through the proposed technique indicates a more concentrated energy distribution in the TF representation shown in Table 4.3.

The specific computational complexity of the different schemes was analyzed with the help of MATLAB 2023a on a computer with the Intel Core i7 CPU and 8GB RAM. The computational time required for signal $S_1(t)$, $S_2(t)$, and $S_3(t)$ is shown in Table 4.8. As it can be

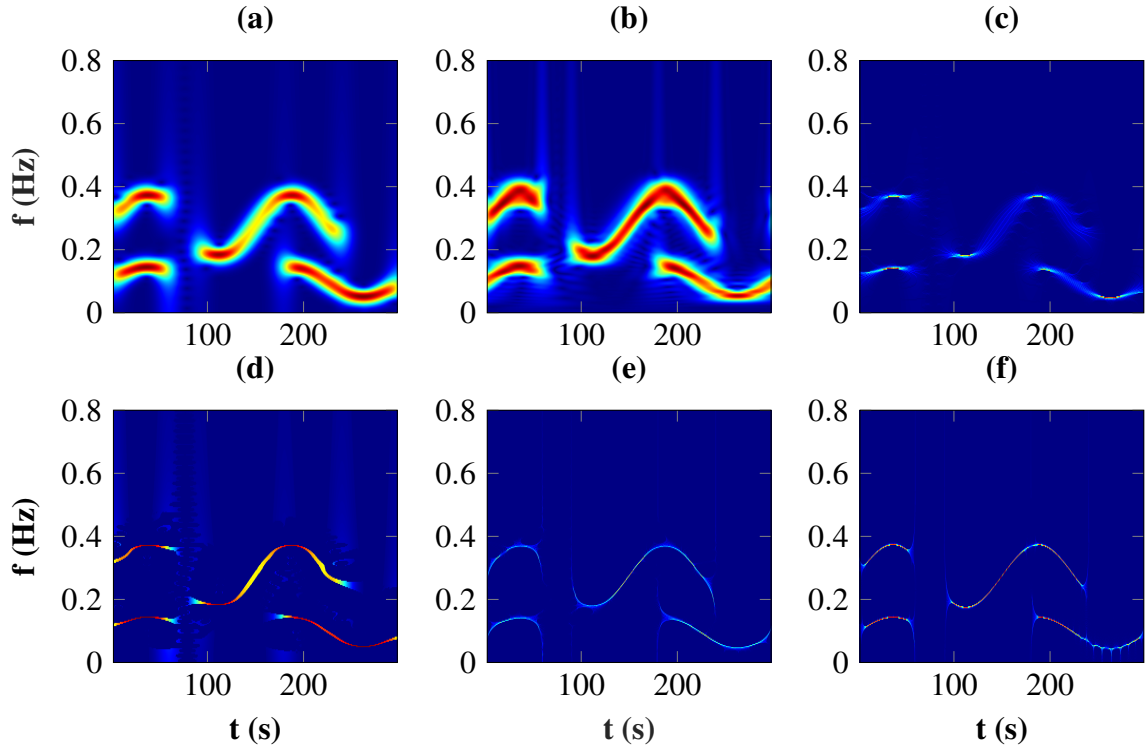

Figure 4.9: NSS of (a) STFT, (b) OptADMST, (c) SST, (d) SET, (e) RS, (f) OptGWRS of signal $S_3(t)$

Table 4.5: Maximum energy concentration (Noise free)

Signal	STFT	OptADMST	SST	SET	RS	OptGWRS
$S_1(t)$	0.005833	0.004334	0.02008	0.009126	0.022978	**0.030225**
$S_2(t)$	0.003809	0.003755	0.006741	0.010401	0.014825	**0.016134**
$S_3(t)$	0.003754	0.003654	0.006576	0.008355	0.013461	**0.017306**

Table 4.6: Maximum energy concentration ($SNR = 0dB$)

Signal	STFT	OptADMST	SST	SET	RS	OptGWRS
$S_1(t)$	0.001431	0.001414	0.002751	0.003632	0.003897	**0.003997**
$S_2(t)$	0.002675	0.002302	0.00476	0.007591	0.00915	**0.010233**
$S_3(t)$	0.002596	0.002213	0.004628	0.006971	0.008644	**0.009855**

Table 4.7: Maximum energy concentration ($SNR = 5dB$)

Signal	STFT	OptADMST	SST	SET	RS	OptGWRS
$S_1(t)$	0.001645	0.001455	0.003642	0.004038	0.004573	**0.005107**
$S_2(t)$	0.003133	0.002802	0.005608	0.009409	0.011357	**0.012725**
$S_3(t)$	0.003016	0.002627	0.005287	0.008234	0.010122	**0.012055**

Table 4.8: Computational time (in sec) of different TF techniques (*(**Bold** face indicates better result)*)

signal	STFT	OptADMST	SST	SET	RS	OptGWRS
$S_1(t)$	0.0215	0.0178	0.0131	**0.0130**	0.0149	0.0140
$S_2(t)$	0.0954	0.1042	0.0192	0.0174	**0.0149**	0.0176
$S_3(t)$	0.0210	**0.0133**	0.0141	0.0149	0.0146	0.0146

Table 4.9: Renyi Entropy value at SNR = 5 dB

Signal	STFT	OptADMST	SST	SET	RS	OptGWRS
$S_1(t)$	14.50648	17.21566	10.02854	11.79347	10.69805	**9.924018**
$S_2(t)$	14.84997	15.03636	10.68735	11.96316	10.5854	**10.54742**
$S_3(t)$	14.71443	14.85335	10.58296	11.84161	10.35882	**10.3463**

shown, when compared to the other TF techniques that have been discussed above, the scheme proposed here has similar computational complexity. The simulation results indicate that the proposed OptGWRS method significantly enhances the energy concentration of signals in the TF domain, achieving the highest concentration compared to other examined transform techniques.

4.3.1.2 Robustness Against Noise

To assess the performance of the OptGWRS method in presence of noisy signals, two different SNRs are applied, first with a SNR of 5 dB (indicating medium level of noise) and second with a SNR of 0 dB (indicating high level of noise). The robustness of the considered TFA techniques was evaluated on the signal $S_1(t)$, $S_2(t)$, and $S_3(t)$ in the presence of AWGN at SNR: 5 dB and 0 dB. For a SNR of 0dB (maximum noise), it can be shown in Figure 4.10, 4.11, and 4.12 the performance of the proposed OptGWRS technique is better than for all the signals considered in this study.

The results of the ECM for the proposed optimized RS technique, as presented in Table 4.7 and 4.6, also indicate a higher value, demonstrating that the proposed method outperforms under noisy conditions. When noise is present in the signal, the OptGWRS method demonstrates

Table 4.10: Renyi Entropy value at SNR = 0 dB

Signal	STFT	OptADMST	SST	SET	RS	OptGWRS
$S_1(t)$	16.05372	17.56968	11.51486	13.53857	12.09267	**11.19665**
$S_2(t)$	14.94838	15.17561	10.72385	12.10124	10.64572	**10.60614**
$S_3(t)$	14.79076	14.97397	10.49824	11.94517	10.38502	**10.25003**

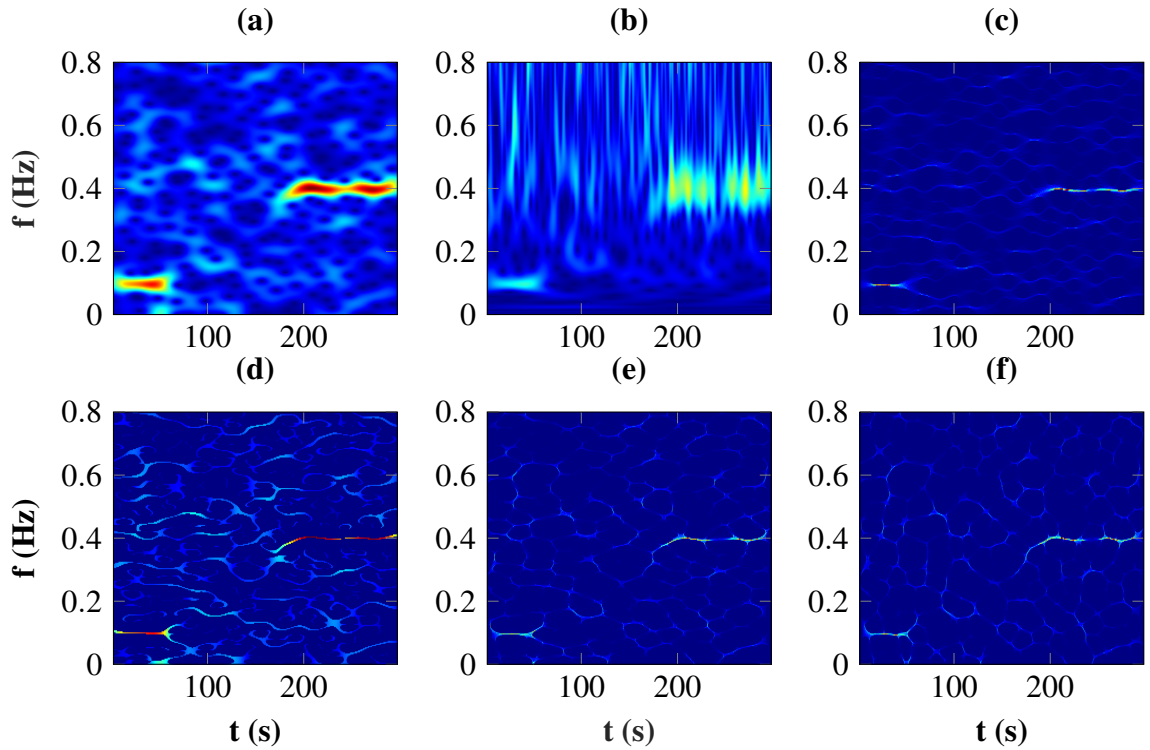

Figure 4.10: NSS of (a) STFT, (b) OptADMST, (c) SST, (d) SET, (e) RS, (f) OptGWRS of signal $S_1(t)$ (SNR = 0dB)

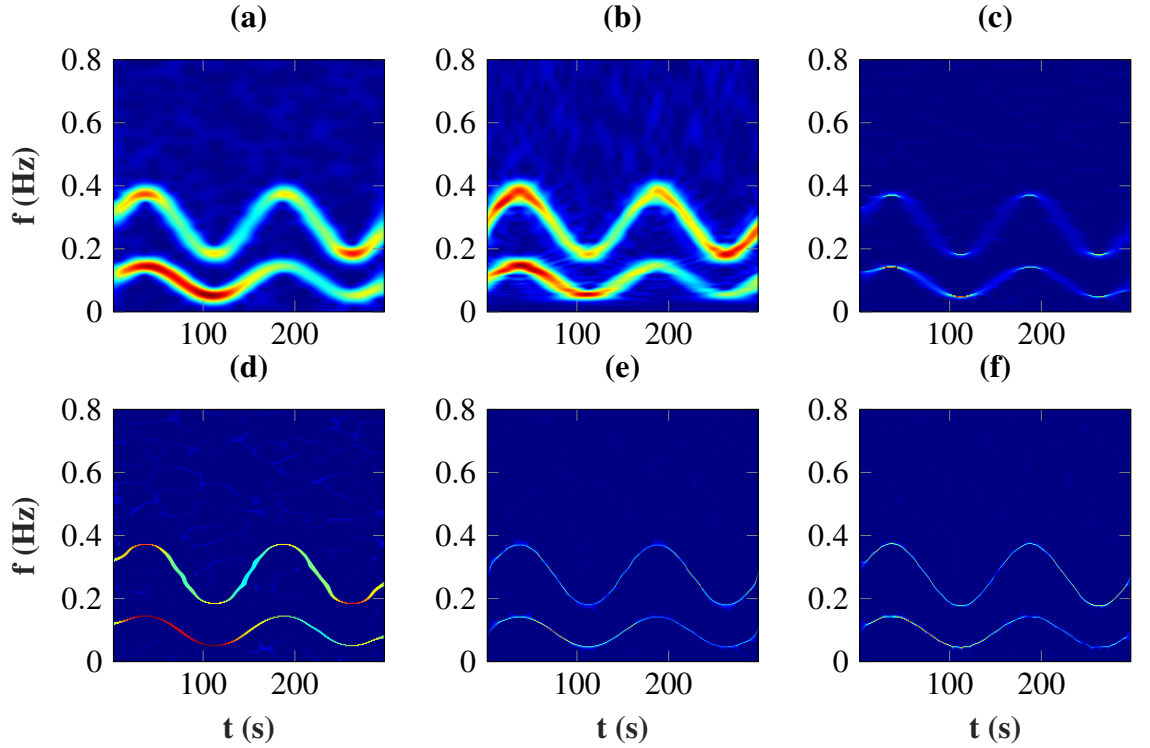

Figure 4.11: NSS of (a) STFT, (b) OptADMST, (c) SST, (d) SET, (e) RS, (f) OptGWRS of signal $S_2(t)$ (SNR = 0dB)

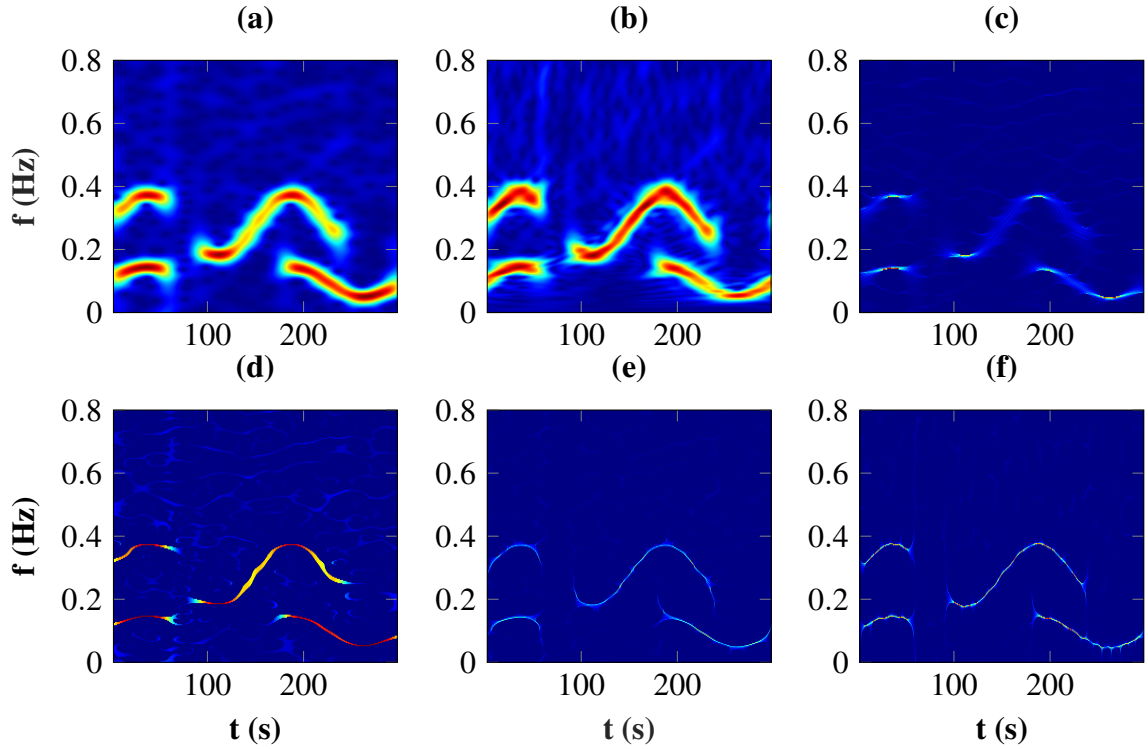

Figure 4.12: NSS of (a) STFT, (b) OptADMST, (c) SST, (d) SET, (e) RS, (f) OptGWRS of signal $S_3(t)$ (SNR = 0 dB)

a better ability of adapting to the noisy signal and hence has a smaller entropy value as shown in Table 4.10 and 4.9. When a high level AWGN (SNR = 0dB) and medium level noise (SNR = 5dB) is introduced to the signal $S_1(t)$, the OptAMDST fails to give a good TF resolution as shown in Figure 4.10. However the visualization of the spectrum demonstrates that the SST, SET, RS techniques offer better TFR under noisy conditions. Nonetheless, the Renyi entropy and ECM values indicate that the proposed technique performs better overall. For the signal $S_2(t)$ and $S_3(t)$, both under high and low levels of noise, the STFT and OptADMST produce broad spectrum where the energy is not concentrated within the defined range, indicating poor TF localization (blurred energy) for both low and high frequency components. The SST and SET techniques suffered some degradation of localization due to noise compared to the RT, as indicated in Figure 4.11 and 4.12. The ECM in Table 4.6 and 4.7, along with the Renyi entropy values in Table 4.10 and 4.9, suggests that the proposed technique is more robust to noise than the other methods in giving a clear TFR. It can be also be demonstrated that as the noise level increases, the entropy value also increases which gives an implication that the presence of noise reduces energy concentration on all the TFA methods. However, the entropies of the OptGWRS technique are slightly lower of all the approaches at both SNR levels. This suggests that despite the increasing noise levels, the proposed OptGWRS method remains effective in accurately capturing transient events.

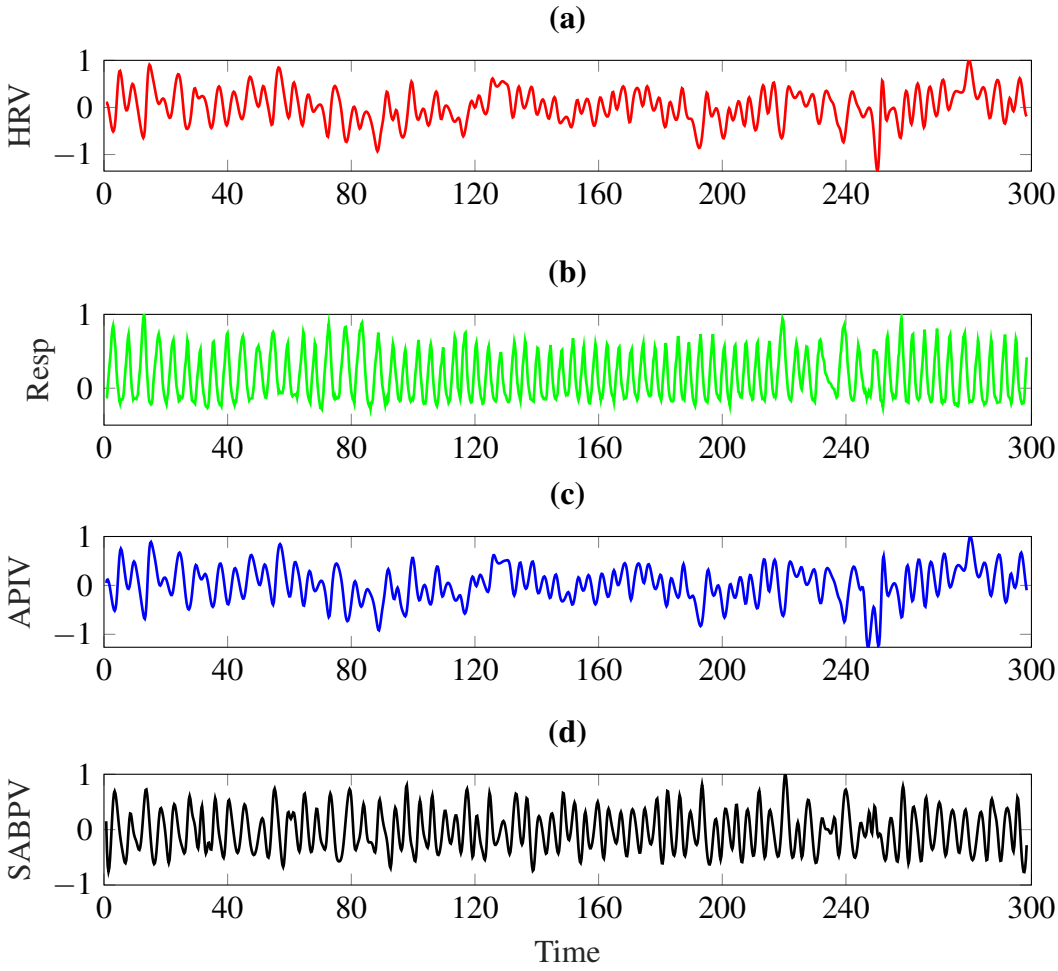

Figure 4.13: Original CAV signals (a) Heart rate variability, (b) RESP, (c) Arterial pressure interval variability, (d) SABPV

4.3.1.3 Application on Non-stationary Signals: Spectral Analysis of HRV Signal

HRV signals contain the essential information about the condition of the heart. The scenarios in HRV signal being non-stationary exhibit time-varying behaviors, making TFA methods the most commonly used approaches to address these variations. The analysis of cardiac signal based solely on human observation is constrained by the clinician's experience, which can limit the reliability of diagnosing cardiac conditions and obtaining comprehensive quantitative and qualitative insights about cardiac activity.

In this paper, a spectral analysis of cardiovascular signal analysis is considered mainly due to its non-invasive tool serving as a potential indicator of the underlying cardiac conditions. The STFT and OptADMST techniques were excluded from the analysis of real cardiovascular signals due to their inability to provide a clear TF representation or high energy concentration for the synthetic signals as discussed above.

4.3.1.4 Time-Frequency Coherence Analysis of Cardiovascular Signal/ Simulation Results

To validate the proposed method, the TF results produced by the OptGWRS, RS, and SST have been applied to HRV, RESP, APIV and SABPV signals. Figure 4.14 displays the spectrum of the different cardio vascular signals; however, it is evident that they do not provide adequate time-varying information regarding the cardio vascular conditions. The STFT and OptADMST

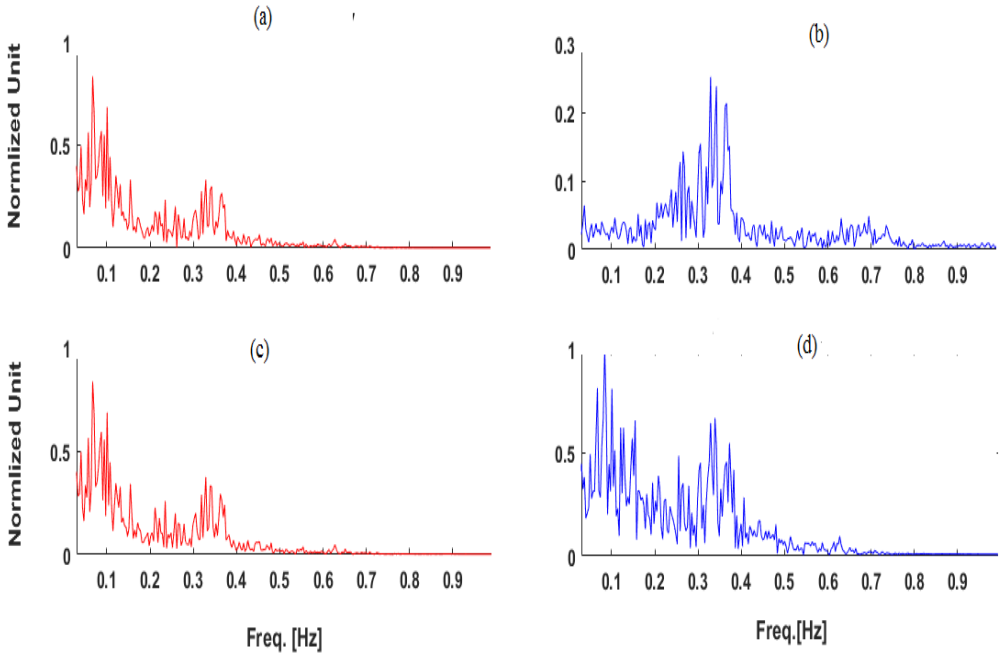

Figure 4.14: Spectrum of (a) Heart rate variability, (b) RESP, (c) APIV, (d) systolic arterial BP variability

techniques cannot accurately characterize time-varying frequencies with concentrated energy. To produce concentrated TF representations, we utilize the SST, RS, and OptGWRS techniques to analyze these signal in this study. The TF representations are illustrated in Figure 4.15; it is evident that the SST results exhibit significant smearing. Although the SST results enhance energy concentration, the TF energy remains somewhat blurred. In Figure 4.15 (row 1), it is clear that the proposed method delivers a notably concentrated TF result i.e the corresponding TF energy smears heavily for the HRV, Resp, APIV and SABPV signal (column 1-4, respectively). The NSS plots were created using OptGWRS (1^{st} row), SST (2^{nd} row), and RS (3^{rd} row).

The energy concentration observed in these NSS estimators highlights several key points: first, there are oscillations in energy concentration within a frequency band of 0.15 to 0.4 Hz,

reflecting typical RESP activity of healthy individuals; second, energy concentration is observed around 0.1 Hz, associated with the mid-frequency (MF) band related to the SABPV or APIV, and third, oscillations in energy concentration occur within a frequency band of 0.04 to 0.15 Hz, referred to as the LF band, potentially linked to various cardiorespiratory mechanisms (Olhede and Walden, 2002). The time varying spectra of the APIV signal is identical to that of the HRV signal, which means that for diagnostic purposes, APIV signals can serve as an effective alternative to HRV signals. The NSS of RS and SST exhibits a lower maximum energy concentration, which results in energy concentration being distributed over a broader region, causing interference among the LF, MF, and HF bands. This interference may lead to a reduced segregation of the LF, mid frequency, and HF attributes within the spectra. It is essential to emphasize that stable LF components (0.009 to 0.119 Hz) are noticeable exclusively by OptGWRS in HRV and APIV, while RS and SST cannot identify them. These stable LF components, specifically at frequencies of 0.026, 0.08, and 0.11 Hz, are associated with the baroreflex regulation of BP. It can be also shown that the RS and SST methods capture the same characteristics for APIV and SABPV signals 4.15(g,k) and (h,l). The application of TF coherence analysis

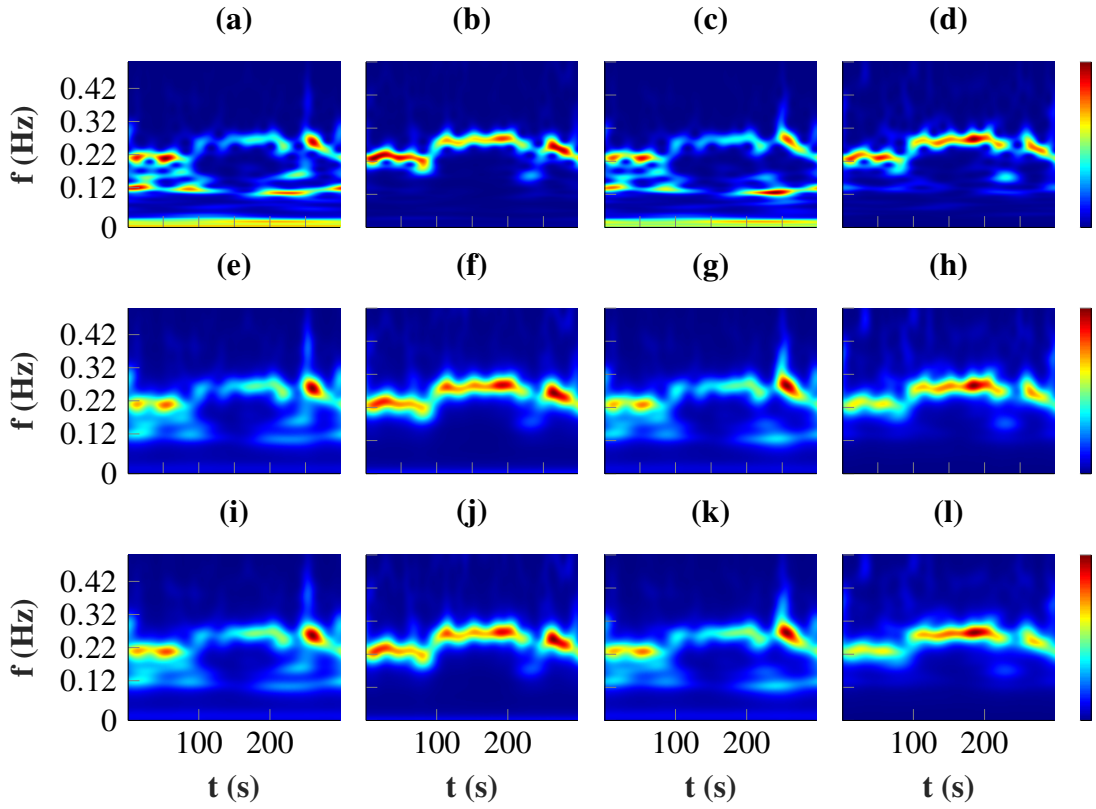

Figure 4.15: NSS maps of cardiovascular signals of a healthy young subject, estimated by OptGWRS row 1 (a - d), by RS, row 2 (e - h) and by SST, row 3 (i - j). 1^{st}, 2^{nd}, 3^{rd}, and 4^{th} columns indicate the spectrum of heart rate variability, RESP, arterial pressure interval variability, and systolic arterial BP variability

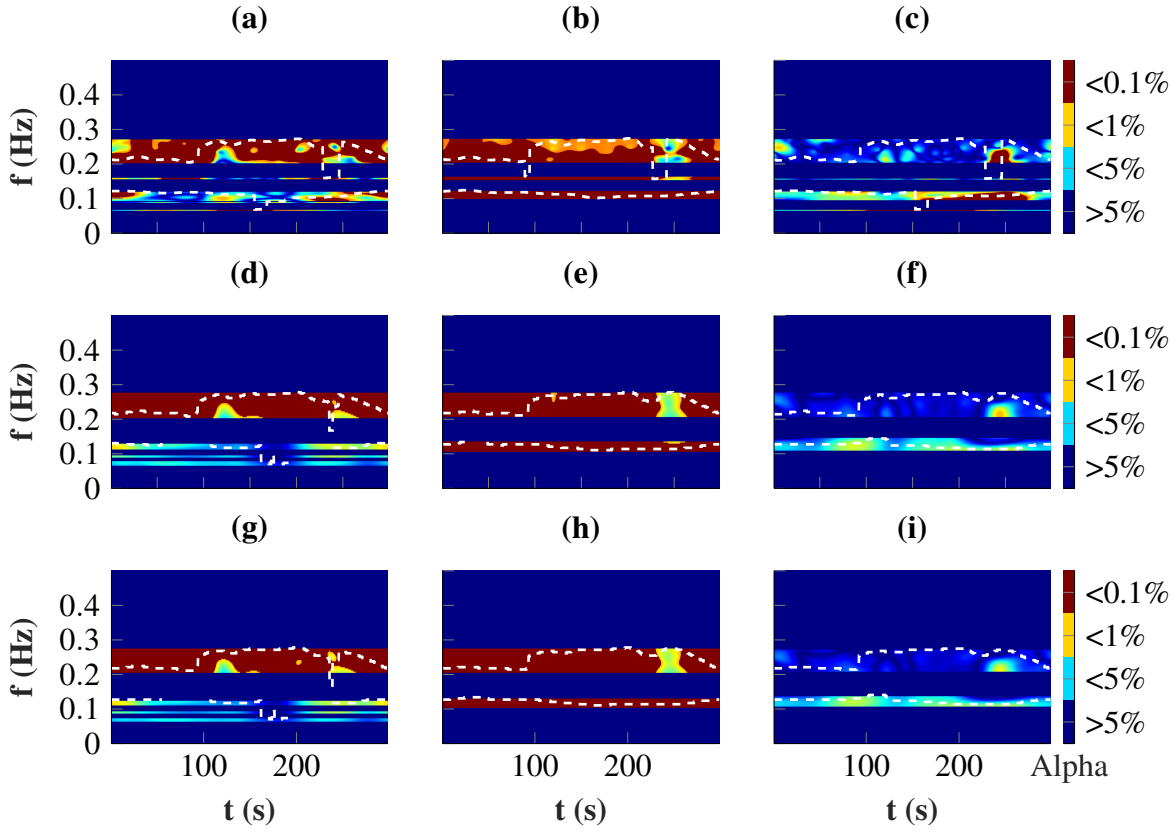

Figure 4.16: NSSC among HRV and RESP (column-1), HRV and APIV (column-2) and HRV and SABPV (column-3) evaluated by OptGWRS ((row 1), by RS (row 2) and by SST (row 3)

serves as a valuable tool for examining the correlation between signals of HRV, RESP, APIV, and SABPV. Figure 4.16 presents NSSC maps that illustrate the significance measure of localized coupling among CAV signals, including HRV-RESP, HRV-SABPV, and HRV-APIV, from a single healthy subject. The coherence among these CAV signals was assessed through the IFs of the LF and HF components, which are indicated by the white dotted lines on the maps. The frequencies of the power spectral components of HRV in the low frequency and high frequency ranges are represented by the white dotted lines on the map and are determined by identifying consistent instantaneous spectral peaks. The IF of the high frequency components of the heart rate variability signal indicate variations in respiratory rate, while the LF components are associated with fluctuations in blood pressure. The coupling among heart rate variability and arterial pressure interval variability, as well as systolic arterial BP variability at frequencies of 0.026, 0.076, 0.1, and 0.11 Hz in the low frequency band, is distinctly identified by OptGWRS, as displayed in Figure 4.16 (b,c). In contrast, the RS estimator only identifies coherence at 0.1 Hz, as illustrated in Figure 4.16 (e,f). Additionally, the coherence across the MF band as assessed by SST is illustrated in Figure 4.16 (h,i). The strength of coherence is influenced by the significance level, α. A lower α value ($\alpha < 5\%$) indicates a higher level of coherence among

CAV signals. In the LF band, HRV, APIV, and ASBPV show a strong correlation. A Wilcoxon rank sum test with a significance threshold of $p < 0.05$ was employed to statistically analyze the median coherence values, Coh(t) in the low frequency and high frequency ranges between the yng and eldy subject groups. In Figure 4.17, the interquartile band and time median trend of coupling, among CAV signals in the low frequency and high frequency ranges are used to illustrate the response patterns of 26 healthy subjects (13 yng and 13 eldy). Table 4.11 presents the statistical results, including the mean of the temporal median trends, while the interquartile range of coherence is highlighted in blue, and the median values are indicated by a black line on the map for all subjects. In young subjects, the average median value of coherence among

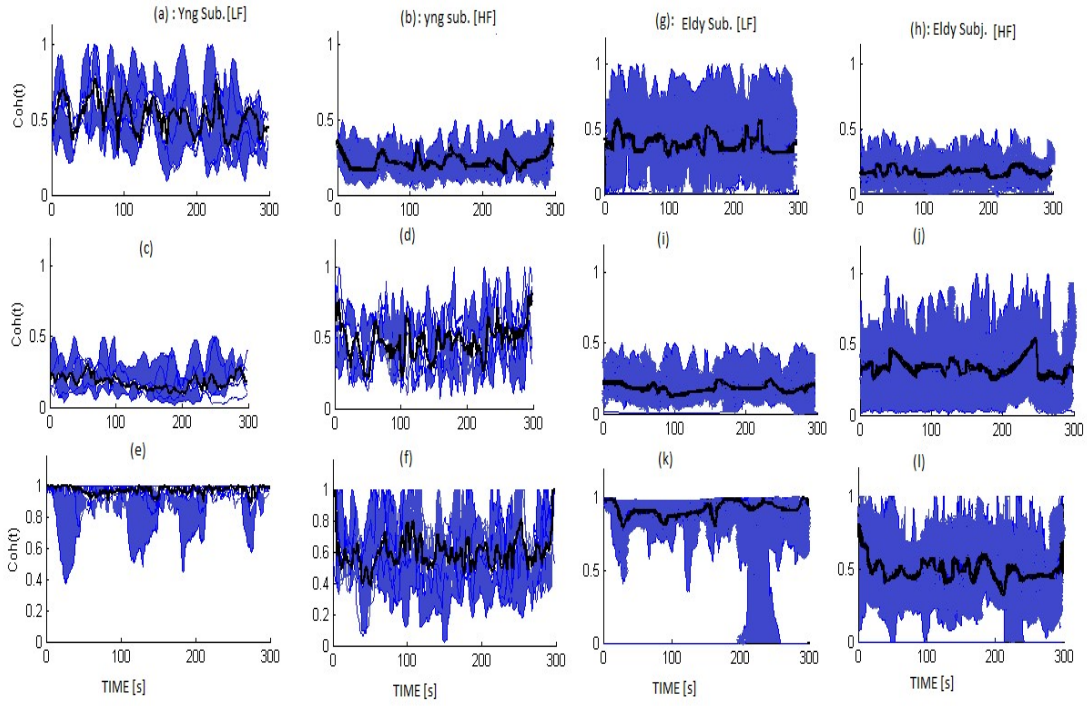

Figure 4.17: Strength of Coh(t) evaluated by OptGWRS among HRV and SABPV (row 1), HRV and RESP (row 2) and HRV and APIV (row 3), evaluated in low frequency range (column-1 & 3 for yng and eldy subjects, respectively), and high frequency band (column-2 & 4 for yng and eldy subjects, respectively).

heart rate and systolic arterial BP - variability signals in the LF and HF bands varied around 0.6412 ± 0.0126 and 0.4768 ± 0.0132, respectively. While in elderly subjects, it oscillated around 0.4817 ± 0.0752 and 0.35512 ± 0.0691 (as shown in Table 4.11). In young subjects, the mean median values of Coh(t) are notably higher, reflecting a stronger coherence between the HRV and SABPV signals. Conversely, elderly subjects exhibit lower mean median values of Coh(t). This disparity indicates that younger individuals may demonstrate better synchronization or interaction between cardiovascular signals compared to older individuals, which could have implications into age-related changes in cardiovascular health and autonomic regulation.

Table 4.11: Results of NSSS in low and high frequency band among CAV signals of each class of subjects

	Low Freq. Range (Avg ± Sd)			**High Freq. Range (Avg ± Sd)**		
Subjects	HRV-SABPV	HRV-RESP	HRV- APIV	HRV- SABPV	HRV-RESP	HRV- APIV
Young	0.6412±0.0126	0.1761±0.0727	0.9781±0.0012	0.4768±0.0132	0.4028±0.0124	0.8064±0.0013
Elderly	0.4817±0.0752	0.1241±0.0617	0.8834±0.0713	0.35512±0.0691	0.3789±0.0644	0.6325±0.0514
P –Value	0.00001	0.125	**0.000001**	0.0001	0.0125	0.0001

The highest coherence value was observed during the interaction between HRV-APIV in the LF band for the young group and for the elderly group, suggesting that the two signals have a functional connection and share similar information about activities. However, this coherence decreased in the HF band for the two subjects.

4.3.2 Discussion

STFT, OptADMST, SST, SET, RS, and OptGWRS techniques has been applied to assess the NSSC of CAV signals. The synthetic signals $S_1(t)$, $S_2(t)$, and $S_3(t)$ was modeled to resemble a real cardiovascular signals. To evaluate the effectiveness of the proposed technique, first these synthetic signals were analyzed by the energy concentration measure and Renyi entropy values. The robustness also measured by introducing a 0 dB and 5 dB AWGN. Under these conditions, the OptGWRS technique outperforms in providing a sharp TF localization compared to other techniques considered in this study. The proposed OptGWRS method successfully localized the TF regions where significant coupling occurs.

A CWT was applied in (Keissar et al., 2009) to analysis the coherence between HRV and respiration signal. In (Orini et al., 2011), characterization of the dynamic interactions among cardiovascular signals was studied by TF coherence. They apply smoothed pseudo-Wigner–Ville distribution (SPWVD) and multitaper spectrogram (MTSP) techniques to localize the TF regions. An energy concentration based NSSC of CAV signals was proposed in (Singh et al., 2018a). They applied an adaptive continuous morlet wavelet transform to investigate the coupling between HRV, RESP, APIV, and SABPV signals. But the methods described in these literature , were not capable to accurately localize TF sections (where signals are locally coupled) due to their inherent limitations, which prevent them from effectively capturing the intricate details of signal variations across both time and frequency. In this paper, energy concentration based Gaussian reassignment TF technique has been proposed to analyze NSS and coherence of CAV signals. The results on synthetic simulated signal and real cardiovascular signals quantifies the performance of proposed work in achieving a sharp localization of the

TF regions.

As it can be shown from the investigation of CAV signals, the HRV and APIV signals were coherent in the HF range all over the respiratory rate, with the capability of this coupling being comparable to that observed among the HRV and RESP signals. It has been demonstrated that the APIV signal can act as a surrogate for the HRV signal. NSSC can therefore be used as a measure of similarity to confirm that one signal and derived measures from it can be used as substitute for the original signals.

The investigation of NSSC has been applied across various fields, including neuroscience, gynecology, and cardiology. In (Guerrero-Mendez and Ruiz-Olaya, 2022; Parmar et al., 2024; Chen et al., 2024), the coherence between Electroencephalography (EEG) and Electromyogram (EMG) signals was studied. The authors utilized coherence to assess the connectivity between the electrical activity of the brain and muscles during the execution of an object manipulation movement. The study in (Guerrero-Mendez et al., 2023) also applied a coherence analysis between EEG and surface EMG.

4.4 Summary

In this chapter, an optimized Gaussian window reassignment technique has proposed based on a PSO algorithm to provide a sharp representation in the TF domain. The experiments conducted on both synthetic and real data for six TFA methods (STFT, OptADMST, SST, SET, RS, and OptGWRS) show that the proposed OptGWRS is effective for instantaneous frequency estimation, enabling the capturing of abrupt changes of these non-stationary signals with rapidly varying frequencies. The simulation results of real signals have shown that the NSSC among HRV and APIV signals is lower in eldly subjects compared with yng subjects in the low frequency and high frequency range. The coupling between heart rate variability and RESP signals in the low frequency band remains largely unaffected by the aging of healthy subjects. In contrast, this coherence in the high frequency range shows a significant decrease ($p = 0.0125$) in eldy subjects compared to yng. Furthermore, the coherence in HRV-SABPV is also significantly lower in both the low and high frequency bands for the yng and eldy subjects. The notable decrease in coupling among CAV signals in eldy subjects might result from the age related degradation of the ANS. It has been shown that integrating the methods with statistical analysis facilitates the accurate localization of the TF regions where significant coupling occurs. The findings of this study are derived from a limited number of subjects available in the Fantasia database, suggesting that access to larger datasets could facilitate a more generalized approach to the issue at hand. For the future the proposed work can be applied in various fields such as neurosciences, cardiology, and gynecology.

CHAPTER 5

MULTISCALE ENTROPY- DRIVEN MULTI- CLASSIFICATION OF MYOCARDIAL INFARCTION DISEASES BASED ON OPTIMIZED MODIFIED STOCKWELL TIME- FREQUENCY TRANSFORM AND MACHINE LEARNING MODELS

5.1 Introduction

MIs is a prevalent form of cardiac (heart) disease that occurs when heart tissue is damaged due to a lack of blood supply to the myocardium, commonly referred to as a heart attack (Rai and Chatterjee, 2022). MIs are a severe and life-threatening heart condition caused by a blockage in one of the coronary arteries, resulting in blood retention and potentially damaging or killing a portion of the heart muscle. This situation is a medical emergency that poses a serious threat to the patient's life and necessities urgent medical intervention (Liu et al., 2017), underscores the critical need for research into detecting MI (Mozaffarian et al., 2016).

Analyzing ECG signals is an efficient approach for the early detection of an MI, as it captures the electrical activity of the heart. This method is not only low-cost but also non-invasive, making it highly suitable for clinical use. MI is identified by specific features on an ECG, including abnormal Q waves, ST-segment elevation, and T-wave inversion. The existence of irregular Q waves indicates a previous transmural MI. Changes in the ST segment are linked to acute ischemia (infarction), resulting from the flow of current between the ischemic and non-ischemic areas, known as an injury current (Hammad et al., 2022). MI can be specifically identified as ST-elevation MI, which is marked by an elevation in the ST-segment of the ECG signal that is generally flat in healthy individuals. This elevation occurs when the repolarization of the ventricles is ineffective, while depolarization proceeds normally, resulting in the ST segment being elevated above the baseline during the transition from ventricular depolarization to repolarization (Sankari and Adeli, 2011). Additionally, certain alterations in T-waves are linked to the post-reperfusion phase. MI can be classified into several types depending on the degree of myocardial necrosis, such as Anterior-MI (AMI), Antero-lateral MI (ALMI), Antero-septal MI (ASMI), Inferior-MI (IMI), Infero-lateral MI (ILMI), Inferior-posterior MI (IPMI), Infero-postero-lateral MI (IPLMI), Lateral-MI (LMI) , Posterior-MI (PMI), and Posterior-lateral MI (PLMI).

Classical time and frequency domain algorithms are inadequate for accurately tracking the non-stationary characteristics of ECG signals, resulting in poor time-frequency (TF) localization (Besfat et al., 2024b). The Stockwell transform (S-transform) provides a frequency-invariant amplitude response, simplifying the interpretation of frequency information compared

to the Wavelet Transform (WT). Additionally, it offers superior time and frequency resolution in TF analysis, surpassing both short time Fourier transform (STFT) and WT methods. The fixed Gaussian window in ST can restrict the analysis of non-stationary signals for effective TF localization. By adjusting the window to align with the signal's characteristics, the TF localization capabilities of ST can be significantly improved to capture abrupt changes in ECG signals. To address this challenge, this paper introduces a modified ST (MST) that employs a particle swarm optimization (PSO) algorithm. PSO is an algorithm motivated by the social behavioral pattern of bird and fish swarms. It simulates how animals in a swarm interact to find food and fulfill their needs (Kiliçarslan, 2023). In PSO, every entity within the population is regarded as a member that represents a potential solution. Particles adjust their positions based on the best-performing particle in the group, with their speed being randomly changed. This iterative process allows particles to improve their positions and speeds at each step, continuing until the optimal global position and speed are identified. In this paper, a PSO algorithm is employed to optimize the hyper-parameters of Stockwell transform. This optimized Modified S-transform (OptMST) facilitates the extraction of TF coefficients across four distinct frequency bands.

The traditional entropy metrics, including approximate entropy (ApEn) and sample entropy (SampEn) quantifies the regularity or unpredictability of a time series on a single scale. However, these measures often fail to capture the multi-scale nature of complex systems, particularly in physiologic data, where dynamics operate across multiple temporal and spatial classes. Multi-scale (MSEn) addresses this limitation by extending entropy analysis to multiple scales, providing a more comprehensive understanding of the system's complexity (Costa et al., 2002; Humeau-Heurtier, 2015).

The ECG signal primarily falls within the frequency range of $[0.05\ 100Hz]$, which is divided into four bands: $F1 = [0\ 5]$, $F2 = [5\ 15]$, $F3 = [15\ 40]$, and $F4 = [40\ 100]$ Hz. The Multi-scale Approximate entropy (MS-ApEn), multi-scale Sample entropy (MS-SampEn), Multi-scale Entropy of entropy (MS-EnoEn), Multi-scale Increment entropy (MS-IncEn), and Multi-scale phase entropy (MS-PhasEn) were applied to these bands to extract a total of twenty features, which has been then used as inputs for a NB, SVM, ELM, A-KNN, BO-SVM, and RF algorithm to classify one HC and ten types of MI cardiovascular diseases.

Several studies have been conducted to automatically detect MI or heart attack by analyzing ECG signals from Physikalisch-Technische Bundesanstalt (PTB) dataset using machine learning and deep learning techniques. Researchers have enhanced the performance of their classifiers by utilizing a diverse range of features, including Wavelet Transform (WT), time-domain attributes, and techniques in particular Principal Component Analysis (PCA), Linear Discriminant Analysis (LDA), and Empirical Mode Decomposition (EMD). Additionally, they have incorporated statistical features, time and frequency domain attributes, Hilbert Trans-

form (HT), and Power Spectral Density (PSD) to improve classification effectiveness (Borah et al., 2024). For instance, Sharma et. al. (Sharma et al., 2015) introduced a MS-Energy and Eigenspace (MEES) method for attribute extraction aimed at detecting and localizing six categories of MI (AMI, ALMI, ASMI, IMI, ILMI, and IPLMI) from multi-lead ECG signals. By employing SVM with a linear kernel, they gained an Accuracy (Ac) of 89%, Sensitivity (Se) of 90.42%, and Specificity of 87.69%. When using a RBF kernel, their performance improved, reaching an Ac of 96%, Se of 93%, and Sp of 99%. In (Acharya et al., 2016), the authors employed a k-nearest neighbor (KNN) model for the automatic detection of normal and MI individuals by extracting 12 non-linear features from 12-lead ECG signals using DWT. They also extracted 47 attributes from lead 11 (V_5) ECG data, attaining a detection accuracy of 98.8%, Se of 99.45%, and Sp of 96.27% for MI.

The authors of (Acharya et al., 2017b) applied convolutional neural network (CNN) model for the automatic identification of healthy and MI ECG beats, analyzing 10,546 normal beats and 40,182 MI beats. They achieved an Ac of 95.22%, Se of 95.49%, and Sp of 94.19% without extracting any features, relying solely on the CNN model. In (Dohare et al., 2018), MI identification using 12-lead ECG signal was proposed. By utilizing Principal Component Analysis (PCA) feature reduction approach and SVM classifier, they achieved Ac of 96.66%, Se of 96.66%, and Sp of 96.66%. Kora et. al. (Kora, 2017) employed a Hybrid Firefly and PSO (FF-PSO) with SVM classifier for the detection of MI condition and they obtained an Ac of 96.7%, Se of 94.45%, and Sp of 95.89%. In (Padhy and Dandapat, 2017), the authors introduced a method for identification and localization of MI from a reduced 2-D multi-lead ECG (MECG) data matrix. They have utilized A third-order tensor structure to exhibit the MECG data in three dimensions. By employing a SVM classifier algorithm, they assured a performance of 95.30% Ac, 96.0% Sp, and 94.6% of Se. The paper (Reasat and Shahnaz, 2017) discusses a shallow CNN for the identification of IMI subjects. They obtained a detection performance of 84.54% accuracy, 85.33% sensitivity, and 84.09% of specificity. Sridhar et. al. (Sridhar et al., 2021) conducted accurate detection of MI using non linear features with ECG signals. By employing SVM classifier, they obtained an AC of 97.96%, Sp of 93.80%, Se of 98.89%. Sadhukhan et. al. (Sadhukhan et al., 2018) presented the use of harmonic phase distribution pattern of the ECG data for MI detection. They applied a threshold-based classification rule and logistic regression classifier for the identification of healthy and MI subjects. Their approach resulted mean detection Ac of 95.6% with Se of 96.5% and Sp of 92.7%. A study in (Sadhukhan et al., 2018) achieved an Ac of 95.6%, Spe of 92.7%, recall of 96.5% by applying a logistic regression (LR) classier to classify normal and MI subjects. Diker et. al. (Diker et al., 2018) proposed the use of morphological, time-domain, and DWT attributes to differentiate MI individuals from normal subjects. They employed a SVM classifier with Genetic algorithm (GA) and obtained a Sp of 88.67%, Ac of 87.80%, and Se of 86.97%. Feng et al. (Feng et al., 2019) conducted a study

to detect normal and MI conditions using CNN classifier with a Recurrent Neural Network (RNN). They achieved Ac of 95.4%, Se of 86.5%, precision of 98.2%, F1-score of 96.8%.

Researchers have extensively utilized different ML and deep learning techniques to identify cardiac diseases (Singh and Mahapatra, 2024; Singh et al., 2018b,c). Despite efforts from various authors, they all highlight that achieving accurate classification remains a significant challenge, with computational time being a major hurdle. This study proposes a classification algorithm that employs NB, Decision Tree Classifier (DT), SVM, ELM, A-KNN, BO-SVM, and RF models to effectively differentiate among a Healthy control (HC) and ten categories of MI arrhythmia datasets.

The main contribution of this study is mentioned as follows:

- This study proposes an optimized modified S-transform TF method to enhance the resolution of ECG signals in both the temporal and spectral domains. The proposed method's parameters are optimized using particle swarm optimization algorithm to maximize energy concentration, demonstrating its effectiveness in adapting to variations in individual ECG patterns.
- The four frequency bands ($F_1, F_2, F_3,$ and F_4) in the pre-processed HC and MIs ECG are decomposed using OptMST, to extract time-varying spectral information related to the P wave, QRS complex, and ST segment of the ECG signal.
- The five entropy measures such as MS-ApEn, MS-SampEn, MS-EnoEn, MS-IncEn, and MS-PhasEn are extracted from the decomposed frequency bands of ECG signals. Each entropy provides four features, resulting in total of twenty features. These features offer valuable insights into data irregularities and facilitate the detection of subtle patterns.
- A ReliefF ranking algorithm has been applied to select top ten most relevant features for removing redundant features, improving ML model performance, and reducing computational time.
- The features are normalized and fed to the input of various ML models and optimal ML is selected based on best performance. To the best of our knowledge, no author has conducted research on eleven cardiac classifications.

5.2 Materials and Methods

5.2.1 Datasets

The MI ECG signal used in this study was sourced from the Physikalisch-Technische Bundesanstalt (PTB) database, offered by the German National Metrology Institute (Goldberger et al., 2000b). This database contains 549 entries from 290 individuals, collected synchronously using 15 leads, comprising a 12-lead ECG ((I, II, III, aVR, aVL, aVF, V1, V2, V3, V4, V5, and V6) and 3 Frank lead vectorcardiogram (VCG). This study focusing exclusively on Lead II ECG

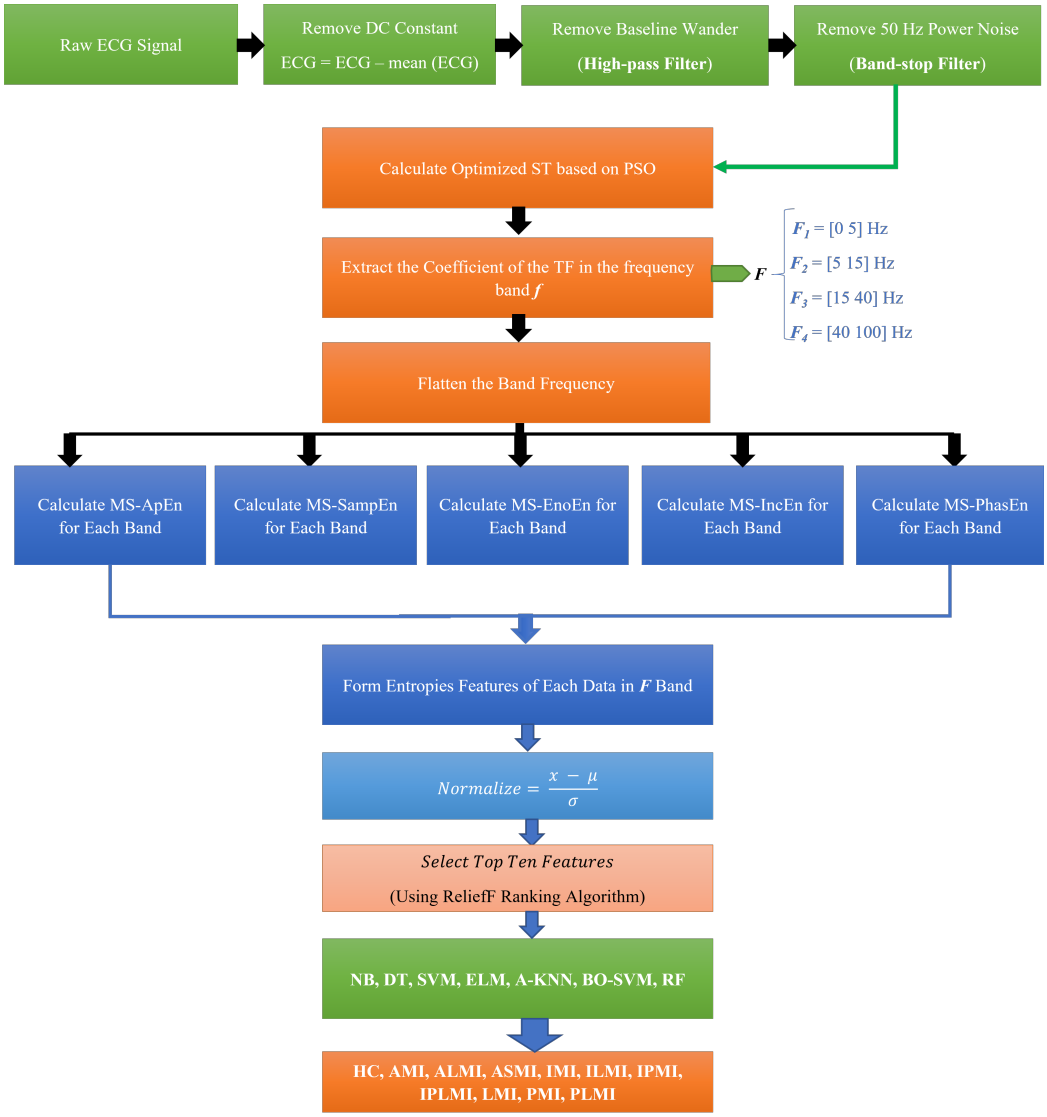

Figure 5.1: The proposed framework for analysis of HC and MI classification based on NB, DT, SVM, ELM, A-KNN, BO-SVM, and RF classifiers

and the ECG signals were sampled at a frequency of 1000 Hz, containing 148 MI subjects (368 records) and 52 individuals in good health (80 records). The ECG signal of MI individuals are

detected to have 10 types of different infarction datasets. To increase the number of datasets, data segmentation has been achieved in this study. Through segmentation, a total of 115,000 samples have been extracted from each subject and divided in to 1000 samples, representing one subject as 115 subjects.

5.2.2 Pre-processing

During the acquisition process, ECG signals can be impacted by baseline drift in the range of 0 to 0.5 Hz and power-line interference within the interval of 50 to 150 Hz. Therefore, the pre-processing stage is vital for effectively detecting cardiac diseases from ECG signals (Besfat et al., 2024a). To eliminate baseline wander, a high-pass filter at 0.5 Hz has been applied, and a band stop filter between 49-51 Hz has been used to remove 50 Hz power line interference.

5.2.3 Proposed Method

Figure 5.1 shows the general block diagram of the proposed framework and it includes four key components: signal pre-processing, nonlinear feature extraction, normalization, feature selection and classification of these features into HC and MI. The preprocessing stage includes removing the DC component and noises from the ECG signal, making it suitable for the feature extraction process. Following this, OptMST based on the PSO algorithm is applied to extract TF coefficients across four frequency bands: 0-5 Hz, 5-15 Hz, 15-40 Hz, and 40-100 Hz. Figure 5.2 illustrates the optimization approach of modified S-transform using PSO algorithm (the explanation of this optimization process is provided in the subsequent section). The frequency bands are then flattened to enhance the analysis and interpretation of the extracted coefficients. By merging multiple frequency bands, this approach captures a wider range of characteristics, potentially resulting in more informative features for further analysis. Subsequently, five entropy features were extracted to form the entropy features for each data point in the F band. From this analysis, a total of twenty features are extracted for each data point in the frequency band F: four attributes derived from MS-Ap, four from MS-SampEn, four from MS-EnoEn, four from MS-IncEn and four from MS-PhasEn entropy. This was followed by the normalization of these attributes to enhance the convergence speed of the model. The normalization involves the mean (μ) and standard deviation (σ) of the data in to consideration, calculated by: $Normalize = (x-\mu)/(\sigma)$. While not all features effectively differentiate between HC and ten types of MI ECG signals, a ReliefF algorithm for ranking the top ten features and a two sample t-test has been employed to identify clinically significant attributes $p < 0.05$. Finally, five classifier algorithms were utilized to distinguish between HC individuals and subjects with MI. In this study, the input attributes (features) are divided using a 10-fold cross-validation, which serves as a robust statistical tool for evaluating any ML classification model.

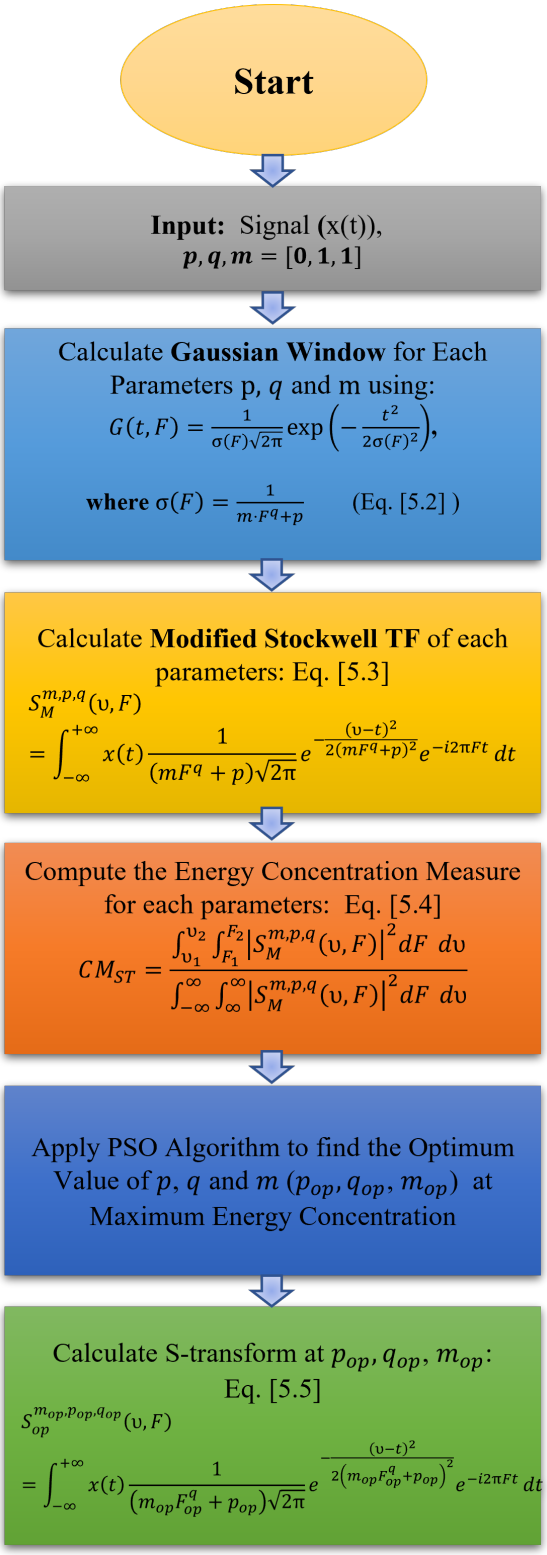

Figure 5.2: Block diagram of optimized modified Stockwell TF technique using PSO algorithm

5.2.4 The Proposed Optimized Modified Stockwell Transform

The ST integrates the features of both the STFT and the CWT. For a time-varying signal x(t), the ST is defined as follows (Das and Ari, 2013):

$$S_x(\upsilon,F)=\int_{-\infty}^{+\infty}x(t)g(t-\upsilon,F)e^{-2\pi jFt}\,dt \tag{5.1}$$

Where $g(t,F)$ denotes a Gaussian function.

The Gaussian window (GW) in the time-frequency domain can be expressed as:

$$G(t,F)=\frac{1}{\sigma(F)\sqrt{2\pi}}\exp\left(-\frac{t^2}{2\sigma(F)^2}\right),\sigma(F)=\frac{1}{m\cdot F^q+p} \tag{5.2}$$

where $\sigma(F)$ denotes the frequency-dependent standard deviation of the GW. The adjustment of the GW parameters in this study adheres to the same strategies described in(Moukadem et al., 2015). The modified ST is given as follows:

$$S_M^{m,p,q}(\upsilon,F)=\int_{-\infty}^{+\infty}x(t)\frac{1}{(mF^q+p)\sqrt{2\pi}}e^{-\frac{(\upsilon-t)^2}{2(mF^q+p)^2}}e^{-i2\pi Ft}\,dt \tag{5.3}$$

The parameters m, p, and q introduced here enhance the flexibility of the GW. To optimize these three parameters, a PSO algorithm has been utilized. In the modified ST without optimization, the parameters m, p, and q are assigned values of 0, 1, and 1, respectively, as these values reflect a standard ST configuration.

The energy concentration measure of the ST can be expressed as:

$$CM_{ST}=\frac{\int_{\upsilon_1}^{\upsilon_2}\int_{F_1}^{F_2}\left|S_M^{m,p,q}(\upsilon,F)\right|^2dF\,d\upsilon}{\int_{-\infty}^{\infty}\int_{\infty}^{\infty}\left|S_M^{m,p,q}(\upsilon,F)\right|^2dF\,d\upsilon} \tag{5.4}$$

where the numerator indicates the energy in the region of interest and the denominator represents the total energy of the signal.

Then, the optimized ST can be computed using the optimized parameters m_{op}, p_{op}, and q_{op}, expressed as:

$$S_{op}^{m_{op},p_{op},q_{op}}(\upsilon,F)=\int_{-\infty}^{+\infty}x(t)\frac{1}{(m_{op}F_{op}^q+p_{op})\sqrt{2\pi}}e^{-\frac{(\upsilon-t)^2}{2(m_{op}F_{op}^q+p_{op})^2}}e^{-i2\pi Ft}\,dt \tag{5.5}$$

The PSO parameters for the proposed OptMST technique include: number of particles = 10, number of iterations = 10, number of dimensions = 3, inertia weight = 0.7, cognitive coefficient =

1.5, social coefficient = 1.5, lower bounds = $[0,0,0]$, and upper bounds = $[8,4,7]$. The selection of the parameters for the PSO algorithm is based on (Kiliçarslan, 2023).

Figure 5.3 displays the original ECG signal alongside the modified ST without optimization and the optimized MST for the eleven arrhythmias. The first column represents the ECG signal, the second column shows its TF representation without optimization (MST), and the third column illustrates the TF representation using energy concentration (EC)-based PSO (OptMST). It is important to note that the y-axis of the OptMST has been adjusted for enhanced visualization, allowing for a clearer representation of how it captures frequency coefficients that the standard MST fails to identify. The TF plot indicates that while the MST can differentiate between the eleven arrhythmias, it does not capture all frequency coefficients. In contrast, the PSO-optimized MST effectively identifies these components, enhancing classification performance.

Figure 5.4(a) and (b) further demonstrates that the TF coefficients in the low frequency band missed by the MST for an ASMI subject are captured by the OptMST, highlighting the superior localization provided by the EC measure compared to the broader (blurred) representation of the MST. The advantages of the EC-based PSO optimized ST are also evident for other arrhythmia subjects, as visualized in Figure 5.3.

5.2.5 Feature Extraction

ECG signals are inherently chaotic and fluctuate over time, which makes nonlinear feature extraction crucial for automatic classification. Traditional time, frequency, and time-frequency analyses fail to capture these variations, whereas nonlinear techniques can effectively identify important characteristics. In this study, several nonlinear features including multiscale-Approximate entropy (MS-ApEn), multiscale-Increment entropy (MS-IncrEn), multiscale-Sample entropy (MS-SampEn), multiscale-Phase entropy (MS-phasEn), and multiscale-Entropy of entropy (MS-EnoEn) has been extracted. By extracting five MSEn from each the four frequency band, a total of twenty features has been obtained. Out of the total 20 features only the top ten features are selected by using a ReliefF ranking algorithm. This algorithm is chosen because it can handle multi-classification problems (eleven classes), less sensitive to noisy data, and can provide a clear ranking of features based on their weights. The top 10 features are also utilized due to their achievement in providing a higher performance measure in the ML.

The first step in MSEn is to coarse-grain the original time series at different scales. This involves calculating the average of the data points over non-overlapping windows of increasing duration, defined by a scale-factor τ (Thuraisingham and Gottwald, 2006). Mathematically,

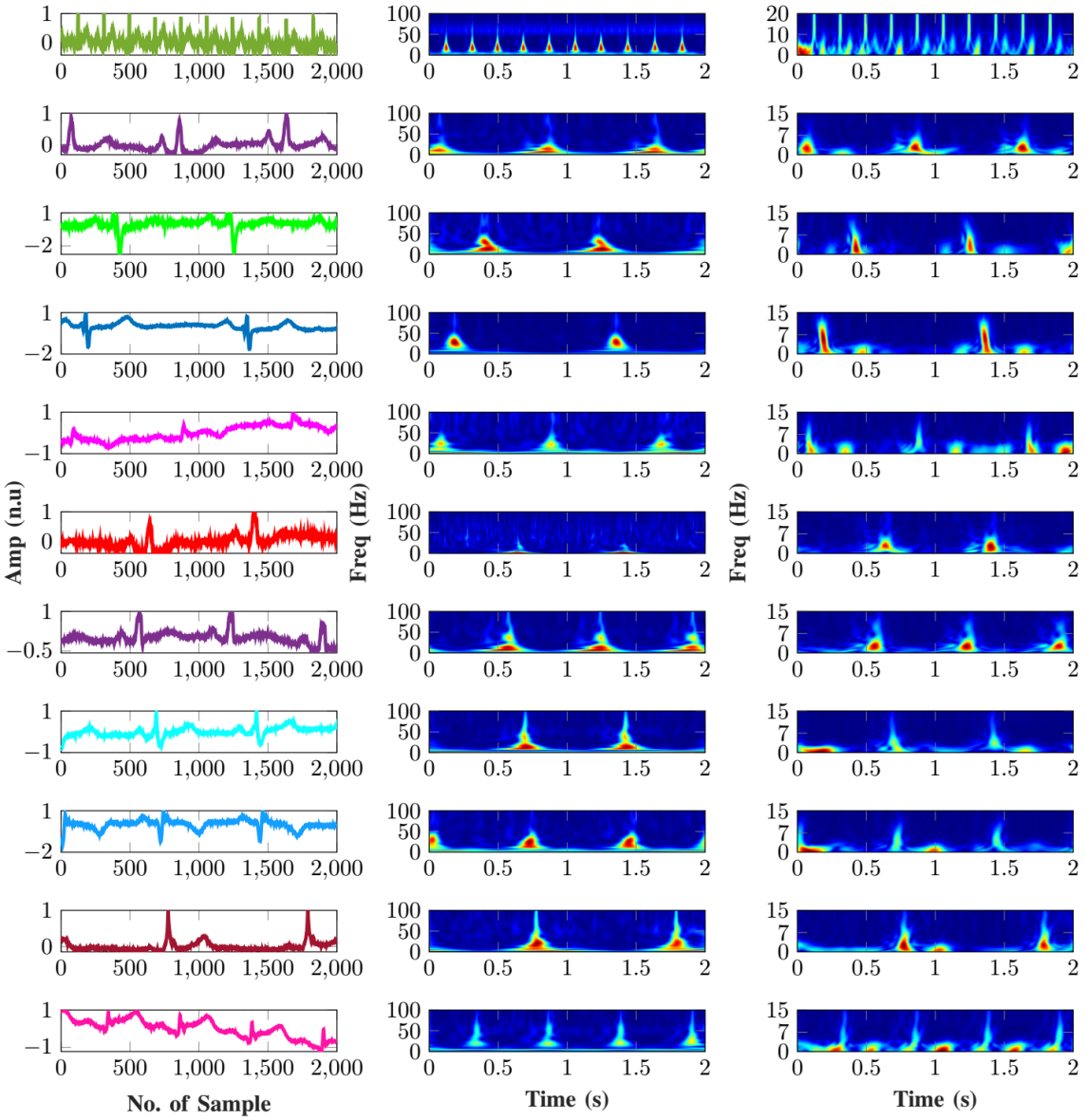

Figure 5.3: ECG plot of eleven arrhythmias: 1st column indicates time domain plot, 2nd column denotes the respective TF plot based on Modified ST, and 3rd column represent the TF plot based on optimized modified ST. (1st row- HC (DS:0), 2nd row- AMI (DS:1) 3rd row- ALMI (DS:2), 4th row- ASMI (DS:3), 5th row- IMI (DS:4), 6th row- ILMI (DS:5), 7th row- IPMI (DS:6), 8th row- IPLMI (DS:7), 9th row- LMI (DS:8), 10th row- PMI (DS:9),11th row- PLMI(DS:10)) subjects, respectively. ***(DS: indicates dataset).***

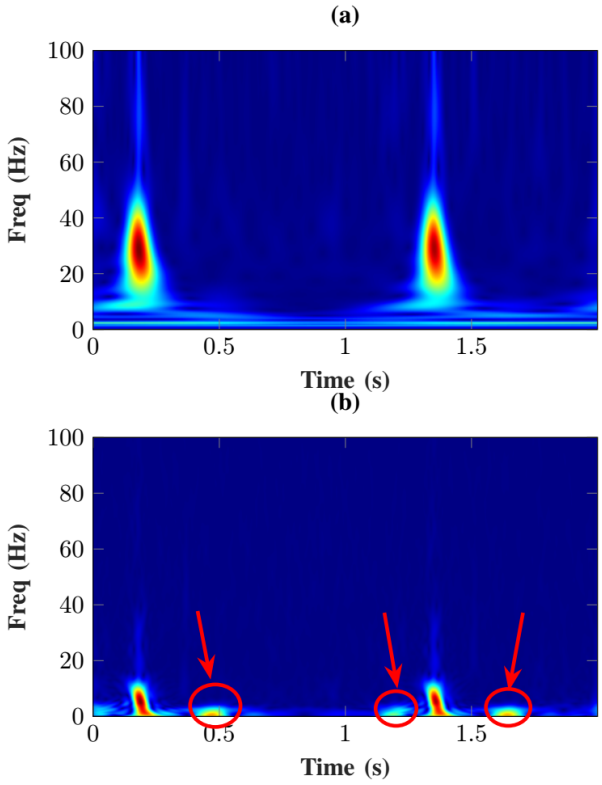

Figure 5.4: TF spectrum of an ASMI subject (a) without optimization and (b) with the application of optimization based on energy concentration

this is formulated as (Costa et al., 2002; Castiglioni et al., 2017):

$$y_j^{(\tau)} = \frac{1}{\tau} \sum_{i=(j-1)\tau+1}^{j\tau} x_i, \quad 1 \leq j \leq \frac{N}{\tau} \tag{5.6}$$

where $y^{(\tau)}$ is the coarse-grained time-series, x_i indicates the original time series, N is the length of the original time-series, and the length of the coarse-grained time series is defined by N/τ. For a value of τ greater than one, the coarse-grained series becomes shorter and smoother, capturing the behavior of the system at larger time scales. After coarse-graining, an entropy metrics such as ApEn, IncEn, SampEn, PhasEn, EnoEn are then calculated for each coarse-grained time series.

5.2.5.1 Multiscale-Ap Entropy

In multi-scale APEn, approximate entropy will be calculated from each coarse-grained time series and it measures the likelihood that matching patterns of data points will remain similar when the pattern length is increased by one (Pham, 2017).

For a time series $x_1, x_2, \cdots, x_N$, construct l-length vectors: $v_l(p) = \{x_p, x_{p+1}, \ldots, x_{p+l-1}\}, \quad 1 \leq$

$p \leq N-l+1$. For each vector $v_l(p)$, count the number of vectors $v_l(q)$ that are similar to $v_l(p)$, i.e., the distance between them is less than or equal to the tolerance level r. The distance is typically the maximum absolute difference between corresponding elements given as:

$$d[v_l(p), v_l(q)] = \max_k \left| x_{p+k} - x_{q+k} \right| \leq r \tag{5.7}$$

where $k = 0, 1, \ldots, l-1$. Letting $C_p^l(r)$ represents the probability of the fraction of vectors $v_l(q)$ that are equivalent to $v_l(p)$, it can be expressed as:

$$C_p^l(r) = \frac{n_p^l(r)}{N-l+1} \tag{5.8}$$

where $n_p^l(r)$ denotes the number of vectors $v_l(q)$ that are matching to the vector $v_l(p)$. For the given time-series of length N, ApEn is calculated by comparing sequences of l consecutive data points to sequences of $l+1$ points (Costa et al., 2005). The ApEn is given by:

$$\begin{aligned} ApEn(l,r,N) &= F^l(r) - F^{(l+1)}(r) \\ &\approx \frac{1}{N-l} \sum_{p=1}^{N-l} \ln \frac{n_p^l}{n_p^{l+1}} \end{aligned} \tag{5.9}$$

where $F^l(r) = 1/(N-l+1) \sum_{p=1}^{N-l+1} \ln C_p^l(r)$ is the average logarithm of the fraction of similar patterns of length l, l indicates embedding dimension (i.e. length of patterns to compare), r denotes tolerance level (a fraction of the standard deviation (std) of the time-series) and N signifies length of time-series.

5.2.5.2 Multiscale-Sample Entropy

Sample entropy is an improvement over ApEn that quantifies the regularity or predictability of the time series designed to be less dependent on the length of the time-series, making it more suitable for analysing physiologic data (Costa et al., 2005; Hu and Liang, 2011). Similar to ApEn, SampEn also compares l and $l+1$ points by excluding self matches and it is described as:

$$SampEn(l,r,N) = -\ln \left(\frac{\beta^{l+1}(r)}{\beta^l(r)} \right) \tag{5.10}$$

where $\beta^l(r) = 1/(N-l) \sum_{p=1}^{N-l} \beta_p^l(r)$ and $\beta_p^l(r) = n_p^l(r)/(N-l)$ denotes the fraction of vectors $v_l(q)$ that are closer to $v_l(p)$.

5.2.5.3 Multiscale-EnoEn Entropy

Entropy of entropy builds on the concept of Shannon entropy and quantifies the diversity of information in a time-series by computing Shannon entropy twice: first to describe the state of the system across a time window, and then to measure the changing of these states across different time scales (Hsu et al., 2017). This double computation of entropy allows EnoEn to capture the complexity of a system in a way that reflects its adaptability.

Considering a time series $\{x_p = x_1, x_2, \cdots, x_N\}$ split into non-overlapping windows (segments) of a length τ. Each segment $W_q^{(\tau)}$ contains τ data points: $\left\{W_q^{(\tau)} = x_{(q-1)\tau+1}, \ldots, x_{(q-1)\tau+\tau}\right\}$. The range of the time-series is divided into s_1 slices, where each slice represents a distinct state of the system. The probability P_{qk} of a data point x_p window $W_q^{(\tau)}$ falling into state index k is obtained as:

$$P_{qk} = \frac{\text{Total number of} x_p \text{in} W_q^{(\tau)} \text{that fall into state} k}{\tau} \tag{5.11}$$

Thereafter, the Shannon entropy $y_q^{(\tau)}$ of window $W_q^{(\tau)}$ is computed as:

$$y_q^{(\tau)} = -\sum_{k=1}^{s_1} P_{qk} \ln P_{qk} \tag{5.12}$$

This represents the information or uncertainty of the system's state within the window.

After computing the Shannon entropy (ShanEn) for each window, we obtain a sequence of entropy values: $\{y_q^{(\tau)}\} = \{y_1^{(\tau)}, y_2^{(\tau)}, \ldots, y_{N/\tau}^{(\tau)}\}$. The range of the entropy values $y_q^{(\tau)}$ is divided into $s_2(\tau)$ levels. The probability P_l of an entropy value $y_q^{(\tau)}$ falling into level index l is given by:

$$P_l = \frac{\text{Tota number of} y_q^{(\tau)} \text{in level} l}{N/\tau}, l = 1, 2, \cdots, s_2 \tag{5.13}$$

Subsequently, the ShanEn of the sequence $y_q^{(\tau)}$ is computed as:

$$EnoEn = -\sum_{l=1}^{s_2} P_l \ln P_l \tag{5.14}$$

This represents the variation of information or the changing of the system's states across different time scales.

5.2.5.4 Multiscale-Incr Entropy

The increment entropy is a new entropy metric utilized for evaluating the intricacy of time-series by considering both the direction and magnitude of changes between adjacent data points

(Liu et al., 2018). Unlike Permutation Entropy (PE), which only considers the order of values, IncrEn incorporates the magnitude of variations, making it more sensitive to subtle changes in the time series.

For a time series x_p, the first step is to construct the increment time series $u(p) = x(p+1) - x(p), 1 \leq p \leq N-1$, where each element $u(p)$ represents the difference between consecutive data points. This increment series $\{u(p)\}$ is the divided in to overlapping vectors of length m_o: $\{U(l) = u(l), u(l+1), \cdots, u(l+m_o-1), 1 \leq p \leq N-m_o\}$. Each vector $V(l)$ represents a segment of the increment series and it is then mapped to a symbolic word w_l which is a sequence of $2m_o$ symbols (one sign and one size for each element in the vector): $w_l = (s_1, q_1, s_2, q_2, \cdots, s_{m_o}, q_{m_o})$, where s represents the sign (direction) of the change (rise, fall, or no change), and q represents the quantifying precision, which determines the number of discrete levels for the magnitude (size). After mapping all vectors to symbolic words, the next step is to count the occurrences of each unique word w_n. The relative frequency $P(w_n)$ of each unique word is then calculated as:

$$P(W_n) = \frac{Q(W_n)}{N - M_o} \tag{5.15}$$

Finally, the IncrEn is computed using the ShanEn formula and is given by:

$$H(m_o) = \frac{1}{m_o - 1} \sum_{n=1}^{(2q+1)^{m_o}} P(W_n) \log P(W_n) \tag{5.16}$$

where $(2q+1)^{m_o}$ is the total number of possible unique words, determined by the number of sign levels (s) and size levels (q), $m_o - 1$ is a normalization factor to ensure that $H(m_o)$ is bounded between 0 and $\frac{m_o log(2q+1)}{m_o - 1}$.

5.2.5.5 Multiscale-Phase Entropy

Phase entropy is utilized as a new measure of entropy that quantifies the distribution of a signal in the Second Order Difference Plot (SODP), which is a two-dimensional phase space that represents the rate of fluctuation (variability) in the signal (Rohila and Sharma, 2019). The SODP offers further information about the dynamics of the system, such as the rate of acceleration or deceleration in the time-series, which is not visible in traditional Poincaré plots.

The key idea behind PhEn is to quantify the multiplicity and rate of fluctuation associated with the signal by analyzing the arrangement of scattered data points in the SODP. Given a time

series $h[n]$, the second-order differences are computed as:

$$\begin{aligned} X[n] &= h[n+1] - h[n] \\ Y[n] &= h[n+2] - h[n+1] \end{aligned} \tag{5.17}$$

where, $X[n]$ represents the first-order difference (the difference between consecutive samples) and $Y[n]$ represents the second-order difference (the difference between consecutive first-order differences). The SODP is a scatter plot of $Y[n]$ against $X[n]$, which offers a visual representation of the rate of fluctuation in the signal.

For each scatter point in the SODP, the slope angle $\theta_s[n]$ is computed with respect to the x-axis. The slope angle is calculated using the four-quadrant arctangent function to ensure that the angle spans the full range from 0 to π.

$$\theta_s[n] = \tan^{-1}\left(\frac{Y[n]}{X[n]}\right) \tag{5.18}$$

Then, the SODP is partitioned into k sectors, each with an angle span of $2\pi/k$ radians. The factor k is a coarse-graining element that defines the resolution of the sectors. For each sector p, the cumulative slope $S_\theta[p]$ is computed by summing the slope angles of all scatter points throughout that sector:

$$S_\theta[p] = \sum_{q=1}^{M_p} \theta[q], p = 1, 2, \cdots, k \tag{5.19}$$

where M_p is the total of scattered points in the p^{th} sector. The probability distribution $P(p)$ within every sector is determined by normalizing the cumulative slope of each sector by the total cumulative slope of all sectors:

$$P(p) = \frac{S_{\theta_s}[p]}{\sum_{p=1}^{k} S_{\theta_s}[p]} \tag{5.20}$$

where the $P(p)$ is the probability of the p^{th} sector. Finally, the PhEn is computed as the Shannon entropy of the probability distribution π:

$$PhEn = -\sum_{p=1}^{k} P(p) \log P(p) \tag{5.21}$$

where, PhEn assesses the multiplicity and rate of variability in the signal and the ShanEn measures the uncertainty or information content in the distribution of slopes across the sectors.

5.2.6 Support Vector Machine

The Support Vector Machine (SVM) algorithm distinguishes positive and negative samples by realizing the optimal hyperplane that increases the separation between the two categories (Injadat et al., 2018). It utilizes kernel methods to transform data vectors into a higher-dimensional space, enhancing classification accuracy. The SVM algorithm aims to improve the geometric separation between categories, making it particularly effective for classification. It effectively addresses overfitting and can handle nonlinear and high-dimensional data, enhancing its detection capabilities (Ramadevi and Das, 2024).

For a non-separable training dataset h_p, y_p, the issue of identifying the optimal separating hyperplane can be expressed as:

$$\min \frac{1}{2}\|w_v\|^2 + C\sum_{p=1}^{n} \varsigma_p, \tag{5.22}$$

$$y_p\left[(w_v \cdot h_p) + b\right] - 1 + \varsigma_p \geq 0, \tag{5.23}$$

Where, w_v denotes the weight vector of the separating hyperplane, C indicates a slack penalty that determines the level of penalty applied for mis-classified samples, ς_p represents slack variables, $y_p \in \{+1, -1\}$, $p = 1, 2, \ldots, n$, Eqn. 5.22 represent constraint function, and Eqn. 5.23 denotes objection condition.

5.2.7 Bayesian Optimization Algorithm

This study employs a Bayesian optimization method to optimize the hyperparameters of the SVM model, emphasizing its superior performance compared to other optimization methods like PSO and genetic algorithm (GA) (Xie et al., 2021a). The primary concepts utilized for parameter optimization in this technique include the Gaussian process (GP), Bayesian theorem and acquisition function (Greenhill et al., 2020). The optimization process is iterative, where the surrogate model is updated based on previous evaluation results in each iteration. The acquisition function is then used to choose the next hyperparameter configuration to test, continuing this cycle until the objective function is minimized (Joy et al., 2016). The BO algorithm typically encounters the following problem scenarios:

$$H^* = \arg_{h \in V} \max f(h) \tag{5.24}$$

where V represents the candidate set of h.

The BO algorithm generates a new value for each hyperparameter, entirely replacing the

original value obtained through the optimization process. Subsequently, a new hybrid model known as BO-SVM is created.

5.2.8 Adaptive K-Nearest Neighbors

K–Nearest Neighbors (KNN) is a very simple bust effective classification algorithm known for its high stability, which assigns a class to an instance by examining the majority category of its K nearest neighbors (Injadat et al., 2018). In the standard KNN algorithm, the value of K is typically chosen by the user and remains fixed throughout the process. In contrast, adaptive k-NN dynamically selects the optimal value of K based on the dataset i.e., by evaluating the effectiveness of K-NN algorithm for different values of K and choosing the one that maximizes a performance metric. This study uses Euclidean distance as the distance measure and identifies the optimal value of M through experiments ranging from 1 to 10, as defined by:

$$ED(x,y) = \sqrt{\sum_{p=1}^{n} |x_p - y_p|^2} \tag{5.25}$$

where, $x = x_1, x_2, x_3, \cdots, x_n$ and $y = y_1, y_2, y_3, \cdots, y_n$ denotes feature vectors of two points, x_p and y_p are categorical values (the p_{th} attributes of x and y, respectively), n denotes the number of attributes of the vector input in the data.

5.2.9 Random Forest

The Random Forest (RF) is an ensemble learning model that integrates multiple decision tree (DT) classifiers to predict class labels(Breiman, 2001). Each tree operates independently on randomly sampled data, and their predictions are aggregated using a majority voting system. When a new data point is observed, it is evaluated by all DTs, and the category with the highest votes is designated as the final prediction (Muhammad et al., 2023).

The decision function can be expressed as (Liu et al., 2012):

$$C(x) = \underset{Y}{\operatorname{argmax}} \sum_{p=1}^{k} I(c_p(h) = Y) \tag{5.26}$$

where, C(x) is aggregate of classification model, c_p is a single DT model, $c_1(x), c_2(x), c_3(x), \cdots, c_k(h)$ represents a sequence of classifiers that are used to create multiple classification models, $I(\cdot)$ denotes the indicator function, and Y represents the output variable. Equation 5.26 illustrates that the decision function counts the number of classifiers that agree on a particular class label Y for the input h.

In this paper, we utilized Bag method and selected a forest size of 100 trees, as this configuration yielded highest performance results.

5.2.10 Extreme Learning Machine

The Extreme Learning Machine (ELM) model demonstrates rapid learning capabilities and efficient computational performance (Singh et al., 2018d). For a dataset X = $\{(x_p, y_p)|x_p \in \mathbb{R}^N, y_p \in \mathbb{R}^M, p = 1,\ldots,N\}$, the mathematical function of the ELM can be represented as:

$$\sum_{n=1}^{L} \beta_n \sigma(w_n \cdot x_p + b_n) = y_p, \tag{5.27}$$

Here, L represents total number of neurons in hidden layer of the ELM. While, N signifies the number of training samples, w_n- weight vector, b_n- bias, and $\sigma(\cdot)$ represents the activation function. The function output can be given by:

$$y_i = \sum_{n=1}^{L} \beta_n h_n(x) = h(x)W, \tag{5.28}$$

where W represents the output weight matrix of the output layer, and $h(x)$ denotes a non-linear attribute mapping. The above relation-ship can be represented as follows:

$$HW = Y \tag{5.29}$$

where, H represents the output matrix of hidden layer and Y denotes the target data matrix.

5.2.11 Decision Tree

Decision Tree (DT) is a supervised learning technique that performs more efficiently and rapidly with large datasets by evaluating the information gain and entropy of each feature (Rehman Javed et al., 2022). Entropy, $H(X)$ measures the unpredictability or randomness (impurity) within a database and information gain (IG) is defined as the reduction in entropy achieved by changing a dataset (Mahesh et al., 2022). DT selects features for splitting based on greater information gain and reduced entropy. The information and entropy for each attribute are evaluated by the following expressions:

$$\text{Entropy} = H(X) = -\sum_{p=1}^{q} P_p \log P_p \tag{5.30}$$

where P_p represent the probability of X belonging to class p in the dataset.

$$IG(C,x_i) = H(C) - H(C|x_p) \tag{5.31}$$

where $IG(C,x_p)$ represents the information gain of feature x_p, C indicates classification classes, and x_p denotes the features in the dataset. The IG can also be also rewritten as (Mienye and Jere, 2024):

$$IG(S,X) = H(S) - \sum_{v \in \text{Values}(X)} \frac{|S_v|}{|S|} H(S_v) \tag{5.32}$$

where S is a collection of examples (dataset), Values(X) is possible values of attribute X, X is an attribute, S_v is the subset of S for which attribute X has value v.

5.2.12 Naïve Bayes Model

Naïve Bayes (NB) model is a simple probabilistic classifier that is founded on Bays' theorem. Its primary objective is to classify the categories of unlabeled instances using the principles of the Bayesian theorem (Lu et al., 2019).

The Bayesian theorem can be formulated as follows:

$$P(L_c|X) = \frac{P(X|L_c)P(L_c)}{\sum_c P(X|L_c)P(L_c)} \tag{5.33}$$

where X refers to unlabeled instance, L_c indicates a set of class labels, $P(L_c)$ denotes the prior probability of L_c, $P(X|L_c)$ is the conditional probability of X under the condition of L_c.

The NB model operates under the assumption that all features are independent (naive) of one another, allowing the aforementioned expression to be represented as follows (Chen et al., 2021a):

$$P(X|L_c) = P(x_1,x_2,x_3,\cdots,x_d|L_c) = \prod_{j=1}^{d} P(x_j|L_c) \tag{5.34}$$

where $X = x_1,x_2,x_3,\cdots,x_d$ is a feature vector and d signifies the dimension of the input dataset.

The Bayesian method for classifying a new instance involves assigning the most probable target value f_{MPV}, which is determined by the following expression (Zhang and Li, 2007; Chen et al., 2020):

$$f_{MPV} = \arg\max_{L_c \in L} P(L_c|X) \tag{5.35}$$

Based on the laws of independent probability, the Bayesian classifier becomes:

$$f_{NB}(X) = \arg\max_{L_c \in L} P(L_c) \prod_{j=1}^{d} P(x_j|L_c) \tag{5.36}$$

where the function $f_{NB}(X)$ is called Naive Bayes classifier or simply NB.

5.3 Result and Discussion

5.3.1 Result

The energy concentration measurement of the MST and the proposed optimized MST are listed in Table 5.1. It confirmed that the proposed OptMST time-frequency technique achieves maximum energy concentration (ECM). This indicates that the technique provides clearer and more precise information regarding the signal's behavior over time and frequency, facilitating the extraction of distinct signal features. Furthermore, it allows for a more compact representation of the signal, requiring fewer coefficients or components to capture essential information. The Gaussian window regulation parameters (such as p, q, and m) for the non-optimized MST are set to 0, 1, and 1, respectively, reflecting a typical ST configuration. In contrast, the optimized MST employs different optimal parameter (p_{opt}, q_{opt}, and m_{opt}) values for the eleven datasets, resulting in enhanced energy concentration. Additionally, the Renyi entropy measures of the proposed method yield lower values compared to the non-optimized MST, demonstrating that the proposed TF transform achieves high resolution and robustness against noise.

Table 5.1: Results of optimization parameter measures, Energy concentration and Renyi entropy values for Modified ST with and without the application of EC based-PSO optimization

Dataset	Optimum Parameter values			Energy Concentration values		Renyi Entropy measures	
				without optimization	with optimization		
	p_opt	q_opt	m_opt	p, q, m = [0, 1, 1]	(ECM)	without optimization	with optimization
DS:0	0.050936	3.04983536	3.701827167	0.001547125	0.001696685	16.83770058	16.01991293
DS:1	0.222791	3.06835371	4.598538235	0.002618633	0.002866387	14.99225858	14.18168191
DS:2	0.048406	3.096462786	4.539335439	0.001454846	0.002576208	15.14867707	13.7505453
DS:3	0.121412	3.001661153	4.685522258	0.002901596	0.003117969	14.12666661	14.07859748
DS:4	0.048143	3.121097796	3.885549716	0.001576007	0.002397639	15.61072805	14.40523105
DS:5	0.610723	3.114804135	3.761416868	0.000326786	0.002026987	15.25284736	13.6265943
DS:6	0.719073	3.080131079	3.904994761	0.001576484	0.002506342	15.27361912	14.08998916
DS:7	0.043726	3.084785368	4.416883498	0.001506141	0.003147326	14.96655116	13.69911422
DS:8	0.048503	3.088760681	4.623951051	0.001197438	0.002942173	15.28732762	13.80909156
DS:9	0.253383	3.080156421	4.567821981	0.001541972	0.002655047	15.26859415	14.06067149
DS:10	0.045752	3.11825873	4.561914508	0.002566186	0.002698834	14.94197935	14.6491958

The effectiveness of the proposed method is validated using ECG data from one HC in-

Table 5.2: Weights for the top ten features (the top ranks indicated in descending order)

Top 10 Features	**Feature weights**
f2: MS-PhasEn	0.017772
f4: MS-PhasEn	0.012757
f3: MS-PhasEn	0.011336
f2: MS-EnoEn	0.008534
f2: MS-IncEn	0.006563
f4: MS-EnoEn	0.006247
f1: MS-EnoEn	0.006021
f3: MS-EnoEn	0.005172
f1: MS-ApEn	4.85E-03
f1: MS-SampEn	0.004235

dividual and ten MI subjects from the PTB database. To ensure a comprehensive comparison with existing studies and to assess the effectiveness of the proposed approach, performance metrics such as Ac, Sp, recall, and F-score have been employed.

From the total of 20 features, only 10 have been selected using the Relieff ranking method (Reyes et al., 2015; Urbanowicz et al., 2018). The ReliefF algorithm can handle multi-classification problems and assigns a weight to each feature, which reflects its relevance to the target variable. According to this ranking, the MS-PhasEn extracted from the second frequency band (f2) is identified as the top ranked feature, with a corresponding weight value of 0.017772, as shown in Table 5.2. The second-ranked feature is the MS-phasEn from the fourth frequency band (f4), which has a weight value of 0.012757. Similarly, the tenth feature selected is the MS-SampEn extracted from the first frequency band of the ECG signal with a progressively lower weight value of 0.004235. For the top ten features, the positive weight value indicates that the feature is relevant for distinguishing between groups.

The whisker plot (box plot) of the top ten features derived from ECG signals, as shown in Figure 5.5, depicts the data distribution of the top ten features, illustrating the statistical measures such as the median (red line), quartiles, and potential outliers. From the box plot, it is evident that the top ten ranked features demonstrate a clear distinction among the eleven groups, making them suitable for ML to accurately classify these groups. This graphical representation ensures that extracting features from five multi-scale entropy (MSEn) measures yields better

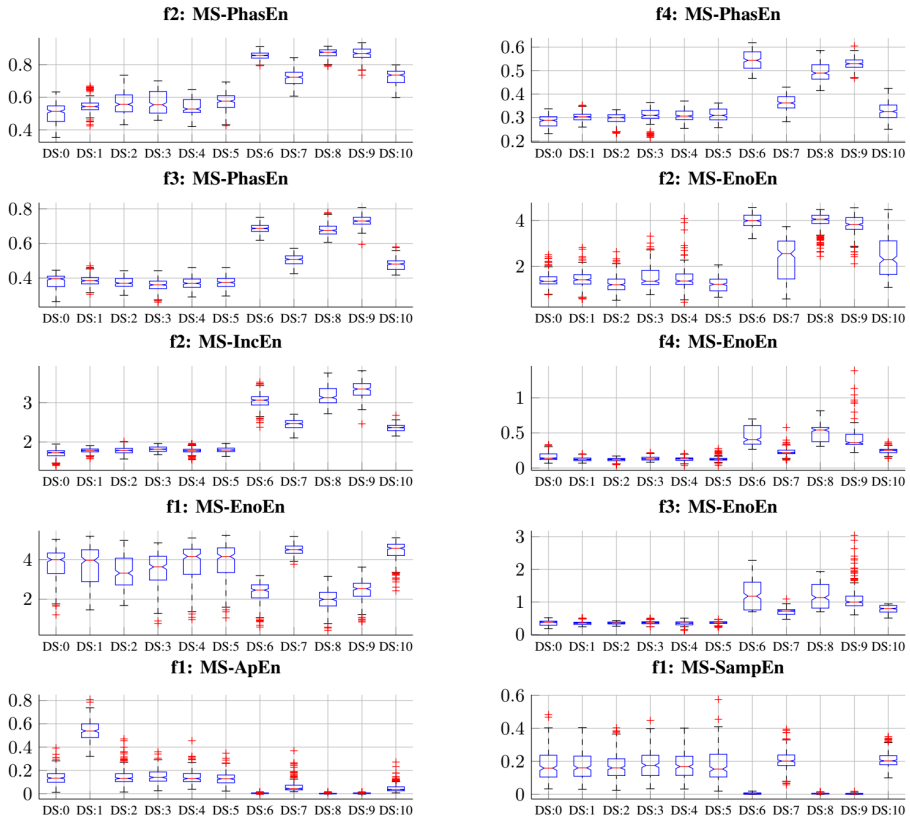

Figure 5.5: Box plot of top ten features for eleven MI arrhythmias

performance compared to using fewer entropy. Additionally, it is essential to extract MSEn from the four frequency bands, as the top ten features include both the four frequency bands and five MSEn.

The mean and std value of the top ten features for the eleven arrhythmia groups has been illustrated in Table 5.3 for further understanding of the distribution of features. The mean defines the central tendency (value) of the feature's distribution, calculated by summing all the values of the feature and dividing by the total number of observations. The std measures the amount of variation or dispersion in the feature's values, quantifying how much the values deviate from the mean. As it can be seen, the top ten features have a distinct mean value and it is relatively higher in HC compared to the mean values of other MI types. The small std value for each group indicates the feature values are not significant around the mean, suggesting a low spread or low variability of the data in each group.

The P-value illustrated in Table 5.4 represent the statistical significance ($P < 0.05$) of the ten MI subjects assessed in relation to HC subject. The P-value is calculated using a two sample t-test. As it can be seen, the P-value between HC and ten MI groups indicate a statistical significance for the first feature. The features such as f3:MS-PhasEn, f2:MS-EnoEn, f1:MS-EnoEn, f3:MS-EnoEn, and f1:MS-SampEn does not support a significant relationship between

Table 5.3: Calculated mean and std value for the top ten features and eleven arrhythmia groups

Features		Arrhythmia Type										
		DS:0	**DS:1**	**DS:2**	**DS:3**	**DS:4**	**DS:5**	**DS:6**	**DS:7**	**DS:8**	**DS:9**	**DS:10**
f2: MS-PhasEn	**mean**	0.50276	0.54601	0.563828	0.566988	0.543186	0.571459	0.85504	0.72011	0.871024	0.867944	0.721229
	± std	0.065983	0.039828	0.066654	0.070629	0.050341	0.058414	0.022767	0.047665	0.026137	0.034436	0.048433
f4: MS-PhasEn	**mean**	0.286188	0.302216	0.29513	0.309711	0.308015	0.312138	0.544708	0.363715	0.493745	0.529478	0.32887
	± std	0.024715	0.019957	0.022931	0.028479	0.025124	0.026664	0.039942	0.032226	0.037105	0.022471	0.040787
f3: MS-PhasEn	**mean**	0.382164	0.382237	0.372139	0.357021	0.370515	0.374116	0.686925	0.505489	0.679003	0.730532	0.478998
	± std	0.03849	0.032848	0.031803	0.034548	0.036402	0.03481	0.024522	0.030627	0.034353	0.029464	0.033061
f2: MS-EnoEn	**mean**	1.433045	1.429096	1.227529	1.48448	1.466404	1.239682	3.999884	2.309308	3.970323	3.831733	2.45142
	± std	0.293291	0.376289	0.340279	0.466126	0.483189	0.347117	0.298045	0.904505	0.380567	0.412549	0.899653
f2: MS-IncEn	**mean**	1.71012	1.780138	1.78655	1.816409	1.784065	1.797297	3.040762	2.45044	3.174104	3.332584	2.363947
	± std	0.123002	0.054897	0.092181	0.067556	0.073689	0.075313	0.18979	0.116115	0.227259	0.219281	0.091014
f4: MS-EnoEn	**mean**	0.162405	0.125768	0.118726	0.134852	0.128426	0.128073	0.453001	0.226671	0.495368	0.424545	0.245685
	± std	0.059743	0.027152	0.023307	0.028369	0.026307	0.028022	0.133283	0.053312	0.108961	0.146668	0.037345
f1: MS-EnoEn	**mean**	3.782231	3.668794	3.388134	3.459703	3.855813	3.892702	2.299193	4.500991	1.968525	2.449442	4.412581
	± std	0.748	1.004058	0.848565	0.959893	0.873315	0.889068	0.568977	0.250485	0.528904	0.521784	0.490891
f3: MS-EnoEn	**mean**	0.35556	0.350267	0.355583	0.365222	0.344264	0.363814	1.211733	0.706065	1.184664	1.09984	0.779826
	± std	0.082244	0.057292	0.038704	0.051084	0.06479	0.050304	0.48051	0.114543	0.348408	0.383647	0.120865
f1: MS-ApEn	**mean**	0.138014	0.541415	0.143145	0.148597	0.141997	0.132257	0.00293	0.061498	0.001198	0.002827	0.047658
	± std	0.060135	0.088238	0.066012	0.060189	0.058524	0.055229	0.003524	0.049979	0.002972	0.003469	0.036245
f1: MS-SampEn	**mean**	0.179655	0.176198	0.173986	0.184032	0.179418	0.173997	0.005016	0.205043	0.004538	0.003723	0.209508
	± std	0.092086	0.086708	0.083824	0.08668	0.083026	0.097558	0.004511	0.057603	0.003433	0.003724	0.050136

Table 5.4: P-value for the top ten features and ten arrhythmia groups relative to HC group (**Bold** face indicates not significant features)

Features	P-value (Using two-sample t-test)									
	DS:0-DS:1	**DS:0-DS:2**	**DS:0-DS:3**	**DS:0-DS:4**	**DS:0-DS:5**	**DS:0-DS:6**	**DS:0-DS:7**	**DS:0-DS:8**	**DS:0-DS:9**	**DS:0-DS:10**
f2: MS-PhasEn	2.49E-16	5.6E-21	1.04E-21	7.16E-13	2.48E-28	4.1E-263	1.9E-153	3.1E-268	6.5E-258	2.2E-153
f4: MS-PhasEn	1.18E-13	6.74E-05	1.61E-19	2.77E-19	1.81E-24	3.4E-279	1.6E-105	2.6E-248	0	1.65E-35
f3: MS-PhasEn	**0.982571**	0.002461	7.9E-13	0.000923	0.019106	0	8.7E-144	1.7E-287	0	1.7E-105
f2: MS-EnoEn	**0.900156**	1.36E-11	0.157338	**0.371241**	2.79E-10	1.1E-299	3.2E-37	1.7E-271	1.5E-251	1.55E-47
f2: MS-IncEn	2.35E-14	2.53E-13	5.2E-27	3.64E-14	1.65E-18	1.1E-291	4.1E-237	1.3E-284	0	8.4E-233
f4: MS-EnoEn	3.45E-16	1.26E-22	6.28E-10	2.18E-14	2.24E-14	6.4E-111	9.99E-30	5.4E-154	4.21E-88	7.82E-55
f1: MS-EnoEn	**0.170106**	1.96E-07	6.82E-05	**0.332318**	**0.149996**	1.06E-82	1.5E-36	2.8E-110	1.73E-74	6.07E-24
f3: MS-EnoEn	**0.423671**	**0.99684**	**0.130836**	**0.102476**	**0.194796**	4.18E-95	1.7E-142	4.9E-132	1E-104	1.2E-166
f1: MS-ApEn	5.42E-211	**0.38395**	**0.059879**	**0.471982**	**0.285463**	2.1E-127	5.82E-41	2.7E-129	1.6E-127	3.55E-62
f1: MS-SampEn	**0.678668**	**0.490253**	**0.599963**	**0.97687**	**0.522739**	1.6E-104	0.000434	6.1E-105	1.6E-105	1.93E-05

HC and AMI, as the P-value is greater than 0.05.

In this study, the MSEn features has been fed to various machine learning algorithms such as NB, SVM, DT, ELM, A-KNN, BO-SVM and RF. The average recall (sensitivity), precision, and F-score value of the NB model provides a poor result compared to all other ML models, as shown in Table 5.5. The accuracy and specificity value for class 1 (AMI) is higher compared to the other classes. The SVM utilizing linear kernel achieved an average Ac of 94.68%, Sp of 97.07%, recall of 70.75%, Pr of 70.65%, and F-score of 70.63%. A polynomial kernel provides a higher performance in comparison withe linear and radial basis function (RBF) kernel, as illustrated in Table 5.5. In the ELM model, utilizing a sigmoid activation function and 300 number of hidden nodes achieved an average Ac of 96.32%, Sp of 97.98%, recall of 79.76%, Pr of 80.32%, and F-score of 79.8%. Similarly, the performance measure for class 1 is higher relative to the other classes.

Table 5.5: Simulation results of various ML models and the proposed model

Class	Accuracy	Recall	Specificity	Precision	F-Score
	Classifier: NB				
DS: 0	0.9427	0.6304	0.9739	0.7073	0.6667
DS: 1	0.9901	1.0000	0.9891	0.9020	0.9485
DS: 2	0.8874	0.4130	0.9348	0.3878	0.4000
DS: 3	0.9071	0.5652	0.9413	0.4906	0.5253
DS: 4	0.9170	0.4783	0.9609	0.5500	0.5116
DS: 5	0.8933	0.3696	0.9457	0.4048	0.3864
DS: 6	0.9585	0.7826	0.9761	0.7660	0.7742
DS: 7	0.9625	0.9348	0.9652	0.7288	0.8190
DS: 8	0.9644	0.7609	0.9848	0.8333	0.7955
DS: 9	0.9625	0.8261	0.9761	0.7755	0.8000
DS: 10	0.9625	0.6522	0.9935	0.9091	0.7595
Avg.	94.07%	67.39%	96.74%	67.77%	67.15%
	Classifier: SVM (Kernel-linear)				
DS: 0	0.9368	0.6739	0.9630	0.6458	0.6596
DS: 1	0.9941	0.9565	0.9978	0.9778	0.9670
DS: 2	0.8972	0.3696	0.9500	0.4250	0.3953
DS: 3	0.9269	0.6522	0.9543	0.5882	0.6186
DS: 4	0.9091	0.4565	0.9543	0.5000	0.4773
DS: 5	0.9091	0.5435	0.9457	0.5000	0.5208

Continued on next page

Table 5.5 Continued from previous page

Class	Accuracy	Recall	Specificity	Precision	F-Score
DS: 6	0.9664	0.8478	0.9783	0.7959	0.8211
DS: 7	0.9644	0.7826	0.9826	0.8182	0.8000
DS: 8	0.9822	0.8913	0.9913	0.9111	0.9011
DS: 9	0.9644	0.7826	0.9826	0.8182	0.8000
DS: 10	0.9644	0.8261	0.9783	0.7917	0.8085
Avg.	94.68%	70.75%	97.07%	70.65%	70.63%
			Classifier: DT		
DS: 0	0.9644	0.8478	0.9761	0.78	0.8125
DS: 1	0.9960	0.9783	0.9978	0.9783	0.9783
DS: 2	0.9644	0.7391	0.987	0.85	0.7907
DS: 3	0.9407	0.6087	0.9739	0.7	0.6512
DS: 4	0.9289	0.6087	0.9609	0.6087	0.6087
DS: 5	0.9328	0.7174	0.9543	0.6111	0.66
DS: 6	0.9644	0.8696	0.9739	0.7692	0.8163
DS: 7	0.9644	0.7609	0.9848	0.8333	0.7955
DS: 8	0.9585	0.8043	0.9739	0.7551	0.7789
DS: 9	0.9585	0.6739	0.987	0.8378	0.747
DS: 10	0.9644	0.8478	0.9761	0.78	0.8125
Avg.	95.80%	76.88%	97.69%	77.30%	76.83%
			Classifier: ELM (Sigmoid activation, # of hidden node = 300)		
DS: 0	0.9601	0.7652	0.9796	0.7940	0.7776
DS: 1	0.9957	0.9957	0.9957	0.9592	0.9767
DS: 2	0.9285	0.6783	0.9535	0.5991	0.6340
DS: 3	0.9510	0.6565	0.9804	0.7711	0.7084
DS: 4	0.9237	0.5870	0.9574	0.5793	0.5804
DS: 5	0.9316	0.6304	0.9617	0.6304	0.6280
DS: 6	0.9771	0.8696	0.9878	0.8840	0.8731
DS: 7	0.9889	0.9522	0.9926	0.9282	0.9399
DS: 8	0.9798	0.8913	0.9887	0.8933	0.8899
DS: 9	0.9704	0.8304	0.9843	0.8413	0.8344
DS: 10	0.9885	0.9174	0.9957	0.9550	0.9357
Avg.	96.32%	79.76%	97.98%	80.32%	79.80%
			Classifier: SVM (Kernel- RBF)		

Continued on next page

Table 5.5 Continued from previous page

Class	Accuracy	Recall	Specificity	Precision	F-Score
DS: 0	0.9625	0.7391	0.9848	0.8293	0.7816
DS: 1	0.9980	1	0.9978	0.9787	0.9892
DS: 2	0.9229	0.5652	0.9587	0.5778	0.5714
DS: 3	0.9447	0.6739	0.9717	0.7045	0.6889
DS: 4	0.9427	0.7609	0.9609	0.6604	0.7071
DS: 5	0.9130	0.5217	0.9522	0.5217	0.5217
DS: 6	0.9921	0.9565	0.9957	0.9565	0.9565
DS: 7	0.9862	0.9565	0.9891	0.898	0.9263
DS: 8	0.9901	0.9783	0.9913	0.9184	0.9474
DS: 9	0.9802	0.8696	0.9913	0.9091	0.8889
DS: 10	0.9881	0.8913	0.9978	0.9762	0.9318
Avg.	96.55%	81.03%	98.10%	81.19%	81.01%
			Classifier: SVM (Kernel- Polynomial)		
DS: 0	0.9625	0.7609	0.9826	0.814	0.7865
DS: 1	0.9960	1	0.9957	0.9583	0.9787
DS: 2	0.9348	0.5652	0.9717	0.6667	0.6118
DS: 3	0.9526	0.7391	0.9739	0.7391	0.7391
DS: 4	0.9447	0.7174	0.9674	0.6875	0.7021
DS: 5	0.9368	0.7174	0.9587	0.6346	0.6735
DS: 6	0.9822	0.9348	0.987	0.8776	0.9053
DS: 7	0.9842	0.9783	0.9848	0.8654	0.9184
DS: 8	0.9862	0.9565	0.9891	0.898	0.9263
DS: 9	0.9723	0.7826	0.9913	0.9	0.8372
DS: 10	0.9842	0.8478	0.9978	0.975	0.907
Avg.	96.69%	81.82%	98.18%	81.97%	81.69%
			Classifier: A-KNN		
DS: 0	0.9769	0.9313	0.9891	0.8723	0.9008
DS: 1	0.998	1	0.9978	1	1
DS: 2	0.9489	0.9009	0.9478	0.8904	0.8956
DS: 3	0.9605	0.8922	0.9804	0.9033	0.8977
DS: 4	0.9408	0.8852	0.9674	0.8912	0.8882
DS: 5	0.9427	0.9074	0.9674	0.8811	0.8941
DS: 6	0.9783	0.9296	0.9826	0.9091	0.9192
DS: 7	0.9961	0.913	0.9978	0.9545	0.9333

Continued on next page

Table 5.5 Continued from previous page

Class	Accuracy	Recall	Specificity	Precision	F-Score
DS: 8	0.9784	0.9313	0.9783	0.9167	0.9239
DS: 9	0.9704	0.9348	0.9935	0.9556	0.9451
DS: 10	0.988	0.9565	1	0.9167	0.9362
Avg.	**97.08%**	**92.57%**	**98.20%**	**91.74%**	**92.13%**
			Classifier: BO-SVM		
DS: 0	0.9883	0.9091	0.987	0.9118	0.9104
DS: 1	1	1	1	0.9787	0.9892
DS: 2	0.9527	0.901	0.9609	0.8962	0.8986
DS: 3	0.9665	0.9109	0.987	0.9055	0.9082
DS: 4	0.9428	0.8852	0.9696	0.8991	0.8921
DS: 5	0.9419	0.8957	0.9543	0.9009	0.8983
DS: 6	0.9802	0.9348	0.9913	0.9131	0.9238
DS: 7	0.9798	1	0.9957	0.9787	0.9892
DS: 8	0.9843	0.9296	0.9826	0.921	0.9253
DS: 9	0.9901	0.9194	0.9957	0.9189	0.9191
DS: 10	0.9854	0.9783	0.9923	1	0.9890
Avg.	**97.38%**	**93.31%**	**98.33%**	**92.94%**	**93.12%**
			Classifier: RF		
DS: 0	0.9869	0.9296	0.9957	0.9524	0.9409
DS: 1	0.9980	0.9783	1	1	0.9890
DS: 2	0.9883	0.9348	0.9826	0.9331	0.9339
DS: 3	0.9743	0.9261	0.9891	0.9237	0.9249
DS: 4	0.9684	0.9313	0.9761	0.9085	0.9198
DS: 5	0.9854	0.9261	0.9891	0.9437	0.9348
DS: 6	0.9823	0.9496	0.9826	0.9233	0.9363
DS: 7	0.9952	1	0.9957	0.9583	0.9787
DS: 8	0.9873	0.9496	0.9891	0.9489	0.9492
DS: 9	0.9664	0.9243	0.9826	0.9222	0.9232
DS: 10	0.9960	0.9565	1	1	0.9778
Avg.	**98.44%**	**94.60%**	**98.93%**	**94.67%**	**94.62%**

For the A-KNN model, a higher performance has been achieved for the best K value of $k = 1$ as depicted in Figure 5.6. The obtained average Ac, recall, Sp, Pr, and F-score is 97.08%,

92.57%, 98.20%, 91.74%, and 92.13%, respectively. The higher Ac value obtained by A-KNN model compared to NB, SVM (for linear, rbf, and polynomial kernel), DT, and ELM models, suggests that this model is reliable overall, with fewer misclassifications across both positive and negative cases. This model has been also able to achieve a higher recall, Pr, and F-score value of 100% for DS:1 (AMI). The confusion matrix of the A-KNN model has been illustrated

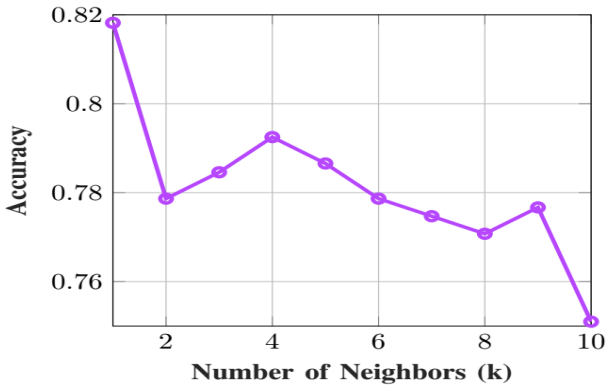

Figure 5.6: KNN accuracy for different K values

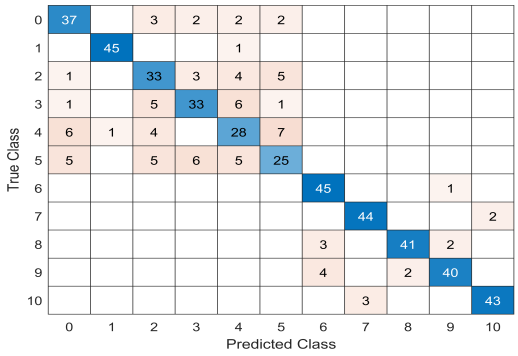

Figure 5.7: Confusion matrix representation of A-KNN classifier

in Figure 5.7.

An average Ac of 97.38%, recall of 93.31%, Sp of 98.33%, Pr of 92.94%, and F-score of 93.12% has been obtained utilizing the BO-SVM ML model. A Sp of 98.33% illustrates that 98.33% of HC individuals are correctly identified as not having an MI condition. In Figure

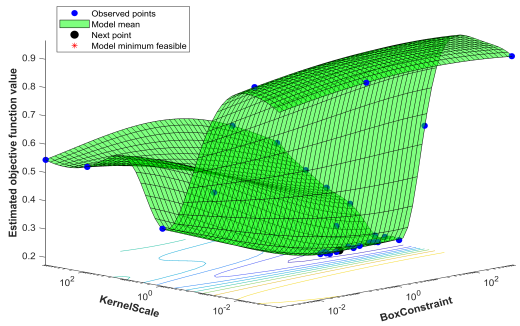

Figure 5.8: Objective function model for the BO-SVM classifier

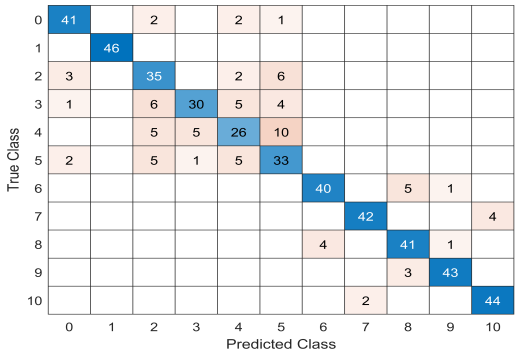

Figure 5.9: Confusion matrix representation of BO-SVM classifier

5.8, it can be seen that the BO optimizes the parameters C (box constraint) and γ (kernel size) to minimize the cost function of the SVM model. The values obtained for the parameter C is 25.751, for γ is 1.4968, and estimated objective function value is 0.17482. This suggests that the optimization process has been significantly enhances the model's performance compare to the standard SVM model, as illustrated in Table 5.5.

The performance of the RF algorithm is superior over the aforementioned ML models and resulted an average Ac of 98.44%, recall of 94.60%, Sp of 98.93%, Pr of 94.67%, and F-score of 94.62%. The Ac and Sp values for all ML models illustrate outstanding achievement in comparison to other metrics, signifying that utilization of MSEn features serves a crucial role to the overall accuracy of the classification. The higher Sp value suggests that these ML models are better at correctly identifying individuals who do not have MI conditions. This is particularly important in avoiding false positives, where healthy individuals are erroneously diagnosed as having an MI condition. Which is crucial to avoid unnecessary treatments or anxiety for subjects who are actually healthy.

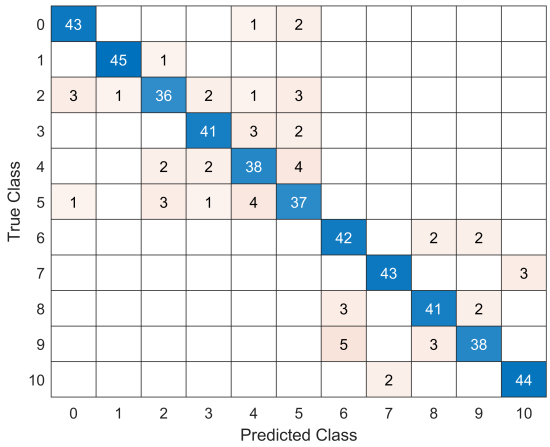

Figure 5.10: Confusion matrix representation of RF classifier

The confusion matrix for the three ML models such as A-KNN (Figure 5.7), BO-SVM (Figure 5.9), and RF (Figure 5.10) demonstrates also that the RF classifier attains superior accuracy compared to the other two models. Overall, these three models outperformed better performance than the other ML models included in our study. Among them, RF ranks highest in performance, followed by BO-SVM in second place and A-KNN in third, as represented by the green, blue and yellow colors in Table 5.5, respectively.

The effectiveness of the classifier algorithms also assessed by the computational time required by these models as shown in Table 5.6. For the simulation, an HP computer with Intel (R) Core (TM) i7-8700 CPU 3.20 GHz processor has been utilized. The time needed for the BO-SVM model to classify the eleven arrhythmias is longer than that of other models. The DT, NB and A-KNN algorithms require less time to run the simulations. In comparison, the elapsed time for the RF is shorter than that of the SVM, ELM, and BO-SVM models, indicating that the proposed RF method offers comparable efficiency.

Table 5.6: Computational time required by the different MLs

Classifier	Computational time (Sec)
NB	27.4883
SVM	235.3545
DT	25.4474
ELM	702.7802
A-KNN	62.7716
BO-SVM	10413.13
RF	157.9376

5.3.2 Discussion

Various methods for classification of MI in ECG signals are listed in Table 5.7 and it has presented a comparison of results from several published studies alongside the current proposed approach.

The authors in (Liu et al., 2017) proposed a multi-lead ECG based MI detection from the PTB database. By leveraging a CNN classifier, they attained an accuracy of 96%, specificity of 97.37%, and sensitivity of 95.40%. Lui et. al. (Lui and Chow, 2018) introduced multi-classification of MI by combining CNN and recurrent neural network (RNN). They obtained a specificity of 97.7%, sensitivity of 92.4%, F1-score of 94.6%, and PPV of 97.2% utilizing CNN with Long short-term memory (LSTM). Martin et al. (Martin et al., 2021) proposed an LSTM classifier for myocardial infarction detection, achieving an accuracy of 89.56%, specificity of 80.81%, and recall of 91.88%. Moghadam et al. (Moghadam and Asl, 2023) proposed a random forest (RF) model that yielded an Ac of 96.54%, a recall of 99.74%, and an F-score of 97.88%. For training and validation set, a PTB-XL database was utilized in a study (Chen et al., 2021b). The dataset incorporates 21,837 clinical 12-lead ECGs from 18,885 subjects. A residual network has been employed to achieve an Ac of 96.5%, specificity of 95%, recall of 82.4%, and an F-score of 82.5% by extracting 4,096 samples from the data of every ECG lead. The authors in (Fang et al., 2022) achieved an accuracy of 95.65%, specificity of 90.80%, recall of 97.34%, and an F-score of 97.07% using a Multi-Visual Geometry Group (VGG) CNN model on the PTB database. In study (Jain et al., 2024), a multivariate sequential features were extracted from multi-lead ECG signal by modeling as a multivariate time series. They validate the performance of their approach by employing PTB-XL dataset, as it comprises many number of ECG signals, and logistic regression (LR) classifier, achieved an accuracy of 95.4%, specificity of 89.1%, and recall of 97.9%, using a one-lead (lead 12) ECG signal. A residual CNN algorithm was employed for automated Occlusion MI (OMI) detection from self

Table 5.7: Comparison of various DL and ML methods for classification of MI arrhythmias

Author	Dataset (# of type)	Features	Classifiers	Performance (%)		
				Ac	Se	Sp
(Acharya et al., 2017b)	HC : 10546 Segmented data MI : 40182 (1 type) Segmented data	ECG data	CNN	95.22	95.49	94.19
(Reasat and Shahnaz, 2017)	HC : 52 MI : 148 (1 type)	ECG data	Shallow CNN	84.54	85.33	84.09
(Padhy and Dandapat, 2017)	HC : 52 MI : 148 (5 types)	Tensor MECG	SVM	95.3	94.6	96
(Kora, 2017)	HC : 18 MI : 26 (1 type)	ECG beat, FFPSO	SVM	96.7	94.45	95.89
(Liu et al., 2017)	HC AMI (3 types)	ECG data	Multilead-CNN	96.00	95.40	97.37
(Sadhukhan et al., 2018)	HC : 52 MI : 148 (1 type)	ECG leads	Logistic Regression	95.6	96.5	92.7
(Dohare et al., 2018)	HC : 60 records MI (1) : 60 (1 type)	P duration, QRS duration, ST-T complex interval and QT interval Interval features, PCA	SVM	96.96	96.96	96.96
(Lui and Chow, 2018)	HC : 52 MI : 148 (1 type)	ECG data	CNN-LSTM	-	92.4	97.7
(Diker et al., 2018)	HC : 52 MI : 148 (1 type)	Morphological, time-domain and DWT features	SVM with GA	87.8	86.97	88.67
(Feng et al., 2019)	HC : 52 MI : 148 (1 type)	ECG data	CNN+RNN	95.4	-	86.5
(Sridhar et al., 2021)	HC : 52 MI : 148 (1 type)	Various non-linear entropy features, DWT	SVM	97.96	-	93.8
(Chen et al., 2021b)	MI (1) : PTB-XL	-	Residual network	96.50	82.40	95.00
(Martin et al., 2021)	HC : 52 MI : 148 (1 type)	ECG data	LSTM	89.56	91.88	80.81
(Fang et al., 2022)	PTB-XL	ECG data	Multi-VGG in CNN	95.65	97.34	90.80
(Moghadam and Asl, 2023)	HC : 52 MI : 148 (1 type)	Morphological , interval, amplitude, and angle between waves features	RF	96.54	-	-
(Jain et al., 2024)	MI : PTB-XL (1 type)	Multivariate sequential feature	Logistic Regression	95.40	97.90	89.10
(Riek et al., 2024)	OMI : Self-recorded (1 type)		Residual CNN	94.70	74.70	96.30
Proposed	HC: 52 (230 Segmented data) MI : 148 (10 types) (2300 Segmented data)	MS-ApEn, MS-SampEn MS-EnoEn, MS-IncEn MS-PhasEn, OptMST	A-KNN BO-SVM RF	97.08 97.38 **98.44**	92.57 93.31 **94.60**	98.20 98.33 **98.93**

collected 12 lead ECG recording in study (Riek et al., 2024). The dataset includes 10,893 ECG data from 7,297 OMI subjects, achieving an accuracy of 94.7%, specificity of 96.3%, recall of 74.7%, and an F-score of 68.1%.

The results strongly indicate the effectiveness of the proposed technique, demonstrating significant performance improvements. It is important to note that most existing literature has focused on a limited number of MI classifications, whereas this study addresses 11 different types of HC-MI classifications. Despite the larger number of groups, the proposed ML model achieve superior performance. Notably, the proposed RF model outperforms those in existing literature, yielding better classification results through the analysis of ECG signals, as illustrated in Table 5.7.

5.4 Summary

This chapter has discussed the critical issue of detecting MI diseases promptly using ECG signals, eliminating the need for human intervention. ECG signal is highly specific for diagnosing MI and plays a crucial role in the diagnostic process. Prompt and accurate identification of MI allows for timely treatments, such as coronary intervention therapy, which can help preserve myocardial tissue and improve patient outcomes. To handle this issue, it has been introduced OptMST, various MSEn features, and ML models. Among them the BO-SVM, A-KNN, and RF models provided a higher performance in classifying eleven different arrhythmia groups, compared to methods found in recent literature. This proposed method can be contributed to the advancement of automatic cardiac health monitoring for early and accurate classification of MIs.

CHAPTER 6

AUTOMATED CLASSIFICATION OF INFERIOR WALL MYOCARDIAL INFARCTION BASED ON TSALLIS ENTROPY AND OPTIMIZED BLOCK LENGTH OF OSELM

6.1 Introduction

Inferior Wall Myocardial Infarction (IWMI) is a serious cardiac condition that requires timely and accurate detection for effective clinical intervention. Traditional diagnostic approaches can be time-consuming and variable, underscoring the need for automated solutions. This chapter presents an efficient IWMI classification method that leverages non-linear Tsallis entropy for feature extraction from decomposed ECG signal using Stationary Wavelet Transform (SWT) and an Optimized Block Length Online Sequential Extreme Learning Machine (OB-OSELM) for robust classification. The proposed approach aims to enhance diagnostic accuracy while ensuring computational efficiency for real-time applications.

To address the issue of translation invariance in the Discrete Wavelet Transform (DWT), the SWT was introduced as a modified version. Leveraging these remarkable properties, SWT has been utilized in this study to decompose the ECG signal for analysis of IMI diseases. Machine learning (ML) at present is rapidly gaining significant traction across various fields, and in healthcare where it finds its application in disease diagnosis. Most traditional diagnostic procedures are time-consuming, costly, and above all, manual. The emerging of ML applications in the medical field has brought forth cost-effective and adaptable ML-based systems for cardiac diagnosis (Weimann and Conrad, 2024).

Several methods have been proposed in the literature for automatic detection and classification of cardiac arrhythmia from ECG signals. Sharma et al. (Sharma and Sunkaria, 2018) conducted a study that specifically targeted the detection of IMI using a combination of the SWT and KNN algorithm. They achieved an accuracy (Ac) of 98.69% in detecting IMI. Padhy et al. (Padhy and Dandapat, 2017) employed singular value decomposition and wavelet entropy for feature extraction, followed by classification using SVM, achieving an Ac of 95.3%. An accuracy of 82.36% was achieved by (Sopic et al., 2018) through the utilization of time-frequency features and RF classification. The paper by (Han and Shi, 2019) proposes a method that incorporates global energy entropy features derived from the maximal overlap discrete wavelet packet transform (MODWPT) and local morphological features. The classification task is accomplished using SVM, resulting in an Ac of 99.75%. An 85.97% sensitivity, 74.03% specificity and an 86.85% precision of the MI detection on ECG signals was found by (Degerli et al., 2021) using SVM classifier. Extraction of nonlinear features, proposed by (Sridhar et al.,

2021) yielded an Ac of 97.96%, Se of 98.89%, and Sp of 93.80% for the detection of MI. An SVM classifier was utilized for this purpose. For the automated MI detection of in the work done in (Hammad et al., 2022), a deep convolutional neural network (CNN) was used. By using the focal loss, the network obtained an overall Ac of 98.84%, precision of 98.31%, F1 score of 97.92%, and recall of 97.63%. In the study that applied ultrashort-term heart rate variability (HRV) for MI detection and classification to (Shahnawaz and Dawood, 2021) ANN based classifier was effective and had good performance. For the evaluation, the Ac was 99.1%, Se was 100% and Sp was 98.1%. In study (Zhang et al., 2020a), the author designed a radar-based health-radio technique for the extraction of HRV from the radio-frequency (RF) signal. As it is shown in the paper, the MI detection yielded 81.5% accuracy when using an SVM classifier.

Multi-lead diagnostic attention-based recurrent neural network (MLDA-RNN) was proposed in (Prabhakararao and Dandapat, 2020) to diagnose the severity levels of MI, and an accuracy of 97.79% was observed. In (Sahu and Ray, 2021), for MI detection and localization, an efficient technique using variational mode decomposition (VMD) and regularized neighborhood component analysis (RNCA) is suggested. Overall employing this methodology reached an Ac of 99.82% with the KNN classifier. Furthermore in the study made by (Zhang et al., 2019), harmonic phase distribution was used for the detection of MI. Using logistic regression, the overall parameters were found to be 95.6 % for Ac , 96.5 % for Se, and 92.7 % for Sp. In the study (Zeng and Yuan, 2023), the author has presented a dynamical estimator classifier and a feature extraction algorithm for detection of MI which comprises of Intrinsic time-scale decomposition (ITD), DWT, Phase space reconstruction (PSR), and Euclidian distance (ED). MI identification was suggested by the authors in (Zeng et al., 2024) by means of Shannon energy envelope (SEE), Fast and adaptive multivariate empirical mode decomposition (FA-MVEMD), and determinstic learning. From it, they extract four features which they use to improve the detection functionality.

Despite being conducted by different authors, these studies demonstrate performance improvements in classifying cardiac diseases, with computational time remaining a significant challenge. The contributions of this chapter are summarized as: a) This study presents the use of SWT in the decomposition of ECG signals. This approach provides significant improvements in feature extraction, and the localization of abnormalities, thereby enhancing the adaptability to individual variations in ECG patterns. b) The research employs TSAEn for feature extraction from decomposed ECG signals. This method provides a deeper understanding of the irregularity and complexity inherent in ECG data, allowing for the detection of subtle patterns. c) The study applies GDA to reduce the dimensionality of the ranked features. This reduction enhances the efficiency and effectiveness of the analysis, facilitating faster and more accurate processing of ECG signals. d) This study has proposed an efficient classifier which is based

on the Optimum Block Length Online Sequential Extreme Learning Machine (OBLOSELM) model. Thus, the proposed Optimum block length (OBL) in OSELM helps to find the optimal relationship between the number of hidden nodes and the performance parameters of the learning model. This classifier significantly improves the diagnostic accuracy for detecting IMI abnormalities in ECG signals, contributing to better clinical outcomes.

6.2 Materials and Methods

This section discusses the dataset utilized and the approach employed in the IMI identification system.

6.2.1 Datasets

In this study, the Physikalisch-Technische Bundesanstalt (PTB) dataset has been utilized to analyse the characteristics of IMI cardiac diseases. This database is publicly available on PhysioNet database (Goldberger et al., 2000b). This dataset encompasses ECG recordings from 290 individuals: 52 healthy patients, 148 diagnosed with myocardial infarction, and 68 with other heart conditions. The data are sampled at 1000 Hz. Out of the total of 148 MI patients, 30 of them are diagnosed with IMI.

6.2.2 Pre-processing

ECG signals present power-line interference and baseline wander when acquired by attaching skin electrodes on the body. Basically, the pre-processing stage is a crucial step in analyzing and extracting important information significant from ECG signals (Wang et al., 2024). In this paper, a pre-processing stage has been used according to the method that was explained in detail in (Sharma and Sunkaria, 2018). This stage involves a two-stage median filter and the Savitzky–Golay (SG) smoothing filter to remove the baseline wander and make the output signal smoother. This filtered signal is then referred as X[n] after being filtered using an SG-filter.

6.2.3 Proposed Method

The ECG signal wave form of a healthy (NR) and unhealthy (IMI) dataset is shown in Figure 6.1. This visual representation indicates the distinctive waveform patterns observed in the NR and IMI subjects' ECG signals.

In the initial stage, a raw ECG signal is acquired and subsequently subjected to a pre-processing technique to enhance its quality. The pre-processed signal is then decomposed into

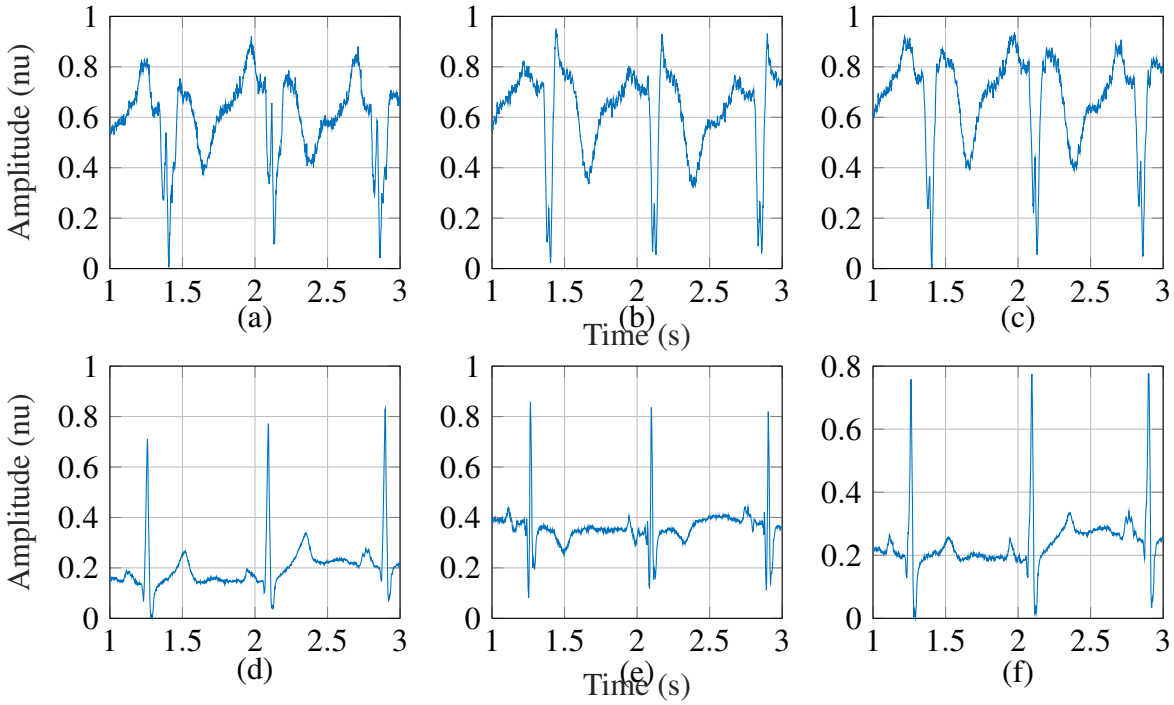

Figure 6.1: ECG wave form of IMI and Normal dataset for Lead II (a & d), Lead III (b & e), and Lead AVF (c & f), respectively

six different frequency components for a detailed examination by using SWT. Further more, a TSAEn features are extracted at each decomposition level for IMI classification, as depicted in Fig 6.2. While not all features demonstrate effective discrimination between normal and IMI ECG signals, a Wilcoxon rank sum test is utilized to identify clinically significant features $p < 0.05$. Following this, the selected features are ranked using the Fisher score feature ranking algorithm. GDA is then used to reduce the dimensionality of the ranked features. GDA not only reduces the feature space but also improves classification accuracy by selecting the most informative features from the ranked list (Singh et al., 2018d). In the specific case of classifying normal subjects and IMI subjects, GDA is applied, followed by the utilization of the OBLOSELM classifier for the final classification. To ensure effective generalization and performance on unseen database, it is crucial to validate a machine learning model. In the classification process, a randomly selected 80% ($60+20$ Validation) of the data is used for training, while the remaining 20% is reserved for testing. The performance parameters were calculated based on a 10-fold cross-validation scheme with repetition of 100 to enhance the robustness and efficiency of the machine learning algorithms. Such iterative learning was performed in this study using 1000-folds over various data sets to ensure comprehensive testing and evaluation. Average performance statistics were calculated for each dataset while performing this extensive testing.

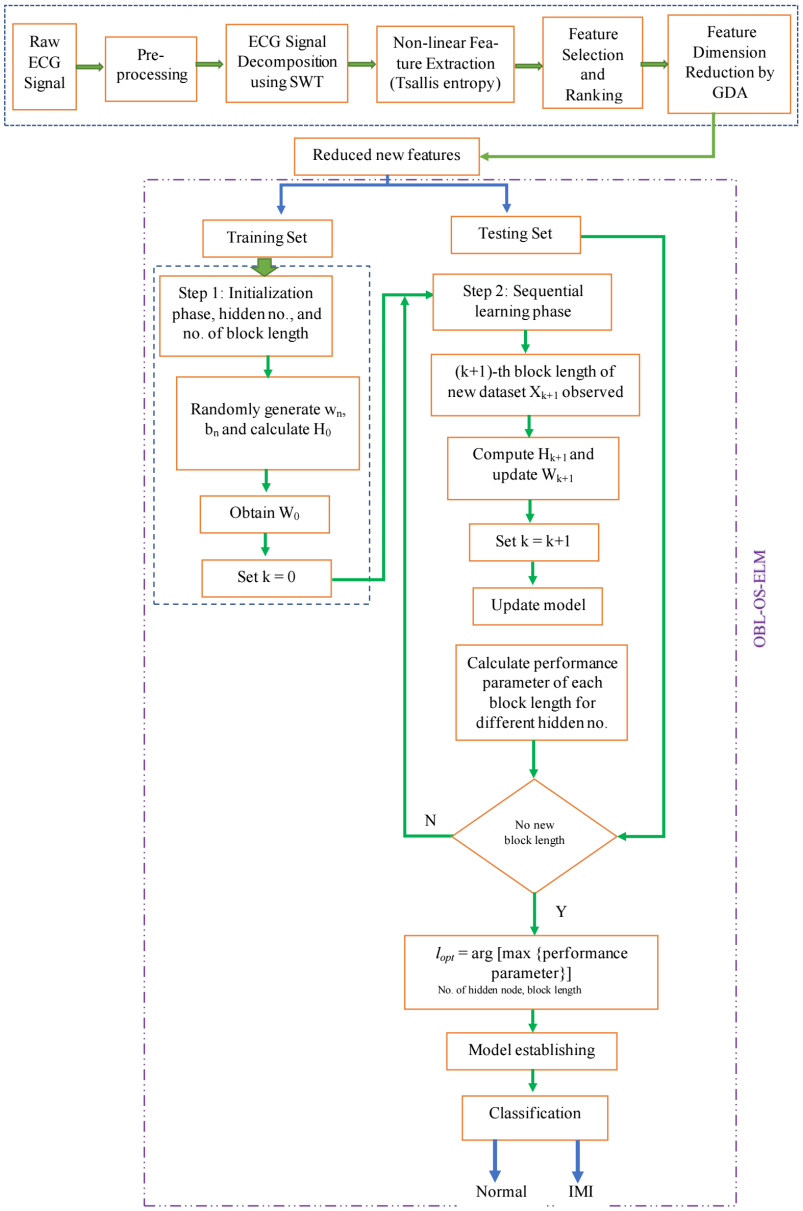

Figure 6.2: The proposed methodology for analysis of IMI classification based on OBLOSELM classifier

6.2.4 Stationary Wavelet Transform

In this study, stationary wavelet transform technique is employed for efficient classification of IMI because of its decomposition capabilities, translation invariance, and ability to maintain temporal resolution as the original signal. In the SWT, the input signal undergoes convolution with both a low-pass filter $h(n)$ and a high-pass filter $g(n)$, similar to the DWT. However, unlike the DWT, the SWT does not perform decimation to obtain wavelet coefficients for different sub-bands. This distinction allows the SWT to maintain the same number of samples and preserve shift invariance, enhancing its effectiveness in various signal analysis tasks. In the SWT, the

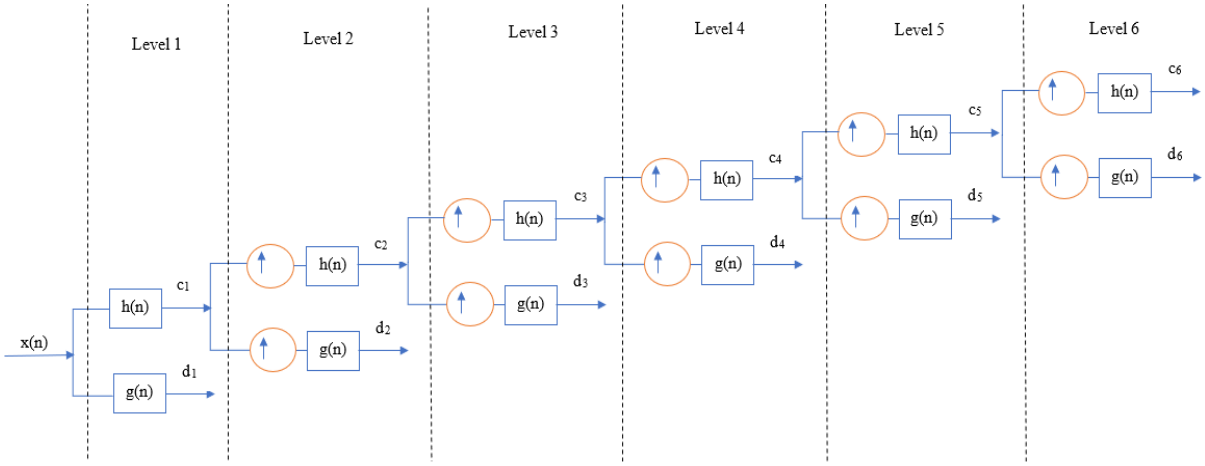

Figure 6.3: Six level decomposition using SWT

input signal undergoes convolution with both a low-pass filter $h(n)$ and a high-pass filter $g(n)$, similar to the DWT. However, unlike the DWT, the SWT does not perform decimation to obtain wavelet coefficients for different sub-bands. This distinction allows the SWT to maintain the same number of samples and preserve shift invariance, enhancing its effectiveness in various signal analysis tasks. In order to perform SWT decomposition, the length of the signal must be a multiple of 2^n, where n represents the number of samples. If the signal's length does not meet this requirement, zero-padding is applied to the signal. Performing a time-invariant wavelet transform involves up-sampling the filter coefficients of both the high-pass filters and low-pass filters, as illustrated in Fig 6.3.

The wavelet transform of a signal $x(t)$ can be expressed as follows:

$$\mathscr{W}(p,q) = \int_{-\infty}^{\infty} x(t) \frac{1}{\sqrt{p}} \phi^*(\frac{t-q}{p}) dt \tag{6.1}$$

the function $\mathscr{W}(p,q)$ represents the continuous wavelet transform (CWT) of a signal $x(t)$, where p and q are the scale and shift (dyadic) parameters, respectively. In the case of DWT, the scale parameter and shift parameter are discretized, taking on specific values such as $p = 2^n$, and $q = 2^n m$, respectively. The DWT of $x(t)$ is given by:

$$\mathscr{W}(m,n) = \int_{-\infty}^{\infty} x(t) \frac{1}{\sqrt{2^n}} \phi^*(2^{-n}t - m) dt \tag{6.2}$$

where, n indicates the decomposition level and m is the discrete time index.

At each step n, scaling function $\psi(t)$ can be defined as

$$\psi_{n,m}(t) = 2^{-n/2} \psi(2^{-n}t - m) \tag{6.3}$$

and, the mother wavelet $\phi(t)$ is then defined by

$$\phi_{n,m}(t) = 2^{-n/2}\phi(2^{-n}t - m) \tag{6.4}$$

The discrete approximation coefficient at a resolution 2^n can be derived as (Zhong and Oyadiji, 2011)

$$c_{n,m} = \langle f(t), \psi_{n,m}(x)\rangle = \int_{-\infty}^{\infty} 2^{-n/2} f(t)\psi^*(2^{-n}t - m)dt \tag{6.5}$$

The detail coefficients at a resolution 2^n are derived as

$$d_{n,m} = \langle f(t), 2^{-n/2}\psi(2^{-n}t - m)\rangle \tag{6.6}$$

Now, $c_{n+1,m}$ can be found by direct computation from $c_{n,m}$ as

$$c_{n+1,m} = \sum_{k=-\infty}^{\infty} h(k-2m)c_{n,k} \tag{6.7}$$

similarly, $d_{n+1,m}$ are computed as

$$d_{n+1,m} = \sum_{k=-\infty}^{\infty} g(k-2m)c_{n,k} \tag{6.8}$$

where h_k and g_k are the impulse responses of low-pass and high-pass filters, respectively. The SWT does not employ decimation on the original data, resulting in a redundant representation of the signal. A redundant decomposition can be obtained as

$$\tilde{c}_{n,m} = \langle f(t), \frac{1}{2^{n/2}}\psi(\frac{t-m}{2^n})\rangle \tag{6.9}$$

$$\tilde{d}_{n,m} = \langle f(t), \frac{1}{2^{n/2}}\phi(\frac{t-m}{2^n})\rangle \tag{6.10}$$

where $\tilde{c}_{n,m}$ and $\tilde{d}_{n,m}$ are the discrete approximation coefficient and detail coefficient, respectively.

The approximation coefficient of SWT is given by

$$\tilde{c}_{n+1,m} = \sum_{l=-\infty}^{\infty} h(l)\tilde{c}_{n,m+2^m l} \tag{6.11}$$

Similarly, detail coefficient of the SWT can be derived as

$$\tilde{d}_{n+1,m} = \sum_{l=-\infty}^{\infty} h(l)\tilde{d}_{n,m+2^n l} \tag{6.12}$$

Here, The SWT is employed to perform decomposition in to six level of the pre-processed ECG signal $X[n]$ and its square signal $X^2[n]$ (Sharma and Sunkaria, 2018).

6.2.5 Feature Extraction

In this study, the wavelet coefficients are computed at each decomposition level, and the TSAEn is extracted from these coefficients. This feature extraction process is performed on both the pre-processed signal $X[n]$ and its squared version $X^2[n]$, resulting in a total of 72 features. Through the utilization of feature selection methods such as the Wilcoxon rank sum test and Fisher score ranking technique, 10 features are chosen for further analysis. Then after this process, extracted TSAEn features are fed to the OBLOSELM classifier to accurately classify the IMI. In order to demonstrate the enhanced classification process resulting from performing dimension reduction using GDA, the classification is conducted both with and without GDA applied.

6.2.6 Tsallis Entropy

As ECG signals exhibit non-linearity, non-stationarity, and time variance characteristics, this paper employs TSAEnt to harness these features and accurately measure the irregularity and complexity of the signals. TSAEn is a nonextensive (exhibiting non-additive property) entropy (Zhang et al., 2009), (Suyari, 2004), (Furuichi, 2005). Given the probability distribution $p_i = p(X = i), i = 1, 2, \cdots, W$. The equation of TSAEn is provided by

$$S_q(X) = \frac{1}{q-1}(1 - \sum_{i=1}^{W} P_i^q) \tag{6.13}$$

Where, X indicates sample of the decomposed signal $q \in \mathbb{R}^+$, $W \in \mathbb{N}$, p_i is the probability that the signal belongs to a considered interval.

6.3 Classification

Classification involves assigning data to predefined categories by mapping the attribute set to specific class labels. In this paper, the OBLOSELM classification algorithm is utilized, where classification is accomplished using mapping functions generated from a labeled training dataset. Furthermore, the classification process includes the design of a decision boundary to effectively separate the two classes of NR and IMI.

6.3.1 Optimum Block Length Online Sequential Extreme Learning Machine

The ELM algorithm is already discussed in chapter 5. The OSELM algorithm, derived from ELM, uses the sequential learning approach that incorporates the fast learning advantage of ELM with the updating features of online learning strategies so that it can learn from only newly arriving data (Cao et al., 2019). This makes OSELM as a highly promising solution for addressing computational cost and accuracy performance concerns in handling datasets. The training process of OSELM consists of the initialization phase and the online sequential learning phase (Zhang et al., 2018), (Dou et al., 2020).

Step 1. Initialization phase, number of block length, and hidden number

During the initialization phase, number of block length, and hidden number of OSELM, the algorithm computes the initial hidden layer output matrix H_0 and the initial output weights W_0.

Given a training set $X = (x_i, y_i), i = 1, 2, \cdots, N$ and hidden layer nodes L, a data set X_0 can be constructed from X: $X_0 = (x_i, y_i), i = 1, 2, \cdots, N_0$, where $N_0 \geq L$,

1. To start, the input weights w_n and biases b_n are randomly generated, and then the initial hidden layer output matrix H_0 is calculated.
2. Obtain the initial output weight value W_0 by the application of generalized inverse theory such that $W_0 = P_0 H_0^T Y_0$, where, $P_0 = (H_0^T H_0)^{-1}$, $Y_0 = (y_1, y_2, \cdots, y_{N_0})^T$, Y_0 is the target output matrix.
3. Set initial $k = 0$

Step 2. Sequential learning phase

During the sequential learning phase, OSELM computes the hidden layer output matrix H_{k+1} and the output weights W_{k+1}.

1. The training data $X_{k+1} = \{(x_i, y_i), i = (\sum_{j=0}^{k+1} N_j) + 1, \cdots, \sum_{j=0}^{k+1} N_j\}$ is the adding in the $(k+1)^{th}$ learning (chunk of new observations). Where, N_j is the number of j^{th} chunk data (block length) employed for training OSELM model and N_{k+1} indicates the adding data number in the $(k+1)^{th}$.
2. Calculate the hidden layer output matrix H_{k+1} of new learning data.
3. Set $Y_{k+1} = [y_{(\sum_{j=0}^{k} N_j)+1}, \cdots, y_{\sum_{j=0}^{k+1} N_j}]^T$, Y_{k+1} denotes the labels of the new dataset.

4. Update the output weight W_{k+1} according to:

$$W_{k+1} = W_k + P_k H_{k+1}^T (T_{k+1} - H_{k+1}^T W_k) \tag{6.14}$$

The iterative matrix,

$$P_{k+1} = P_k - P_k H_{k+1}^T (I + H_{k+1} P_k H_{k+1}^T)^{-1} H_{k+1} P_k \tag{6.15}$$

5. Set $k = k+1$ and go back to step 2 until all the new data are learned.

6. Calculate the performance parameters, including accuracy, sensitivity, specificity, and positive predictive value for each block length and go back to step 1 until all the considered block length.

7. Find optimal block length (l_{opt}) as:

$$l_{\text{opt}} = \arg \max_{\substack{\text{block length,} \\ \text{hidden no.}}} \{\text{performance parameter}\} \tag{6.16}$$

8. Find the performance parameter at l_{opt}. This is known as OBLOSELM

6.4 Result and Discussion

To assess the effectiveness of the proposed approach, ECG signals from the PTB database are utilized, comprising both NR (healthy) and IMI subjects (unhealthy). The performance of the proposed method is evaluated through the use of confusion matrix, including Se, Sp, Ac, and Positive Predictive Value (PPV). In order to comprehend the statistical analysis, a box plot illustrating ten features of the NR-IMI dataset for the squared signal $X^2[n]$ has been displayed in Fig 6.4. The box plot is useful to visualize the scattering and skewness of a sample group. A detailed description of the structure and labeling of a box plot is provided in (Singh et al., 2021). The features extracted from the decomposition of the squared signal $X^2[n]$ gives a better distinguishable difference between the two classes. To reduce the dimensionality of attributes, GDA has been utilized. This approach not only reduces the dimension of the input attributes but also enables effective discrimination of features. Fig 6.5 shows after GDA reduction using RBF kernel function. As it can be shown, the features of NR and MI are very distinct. The median of the IMI group is noticeably different from the median of the NR group by GDA, indicating a significant difference in the feature's values between the healthy and unhealthy subjects.

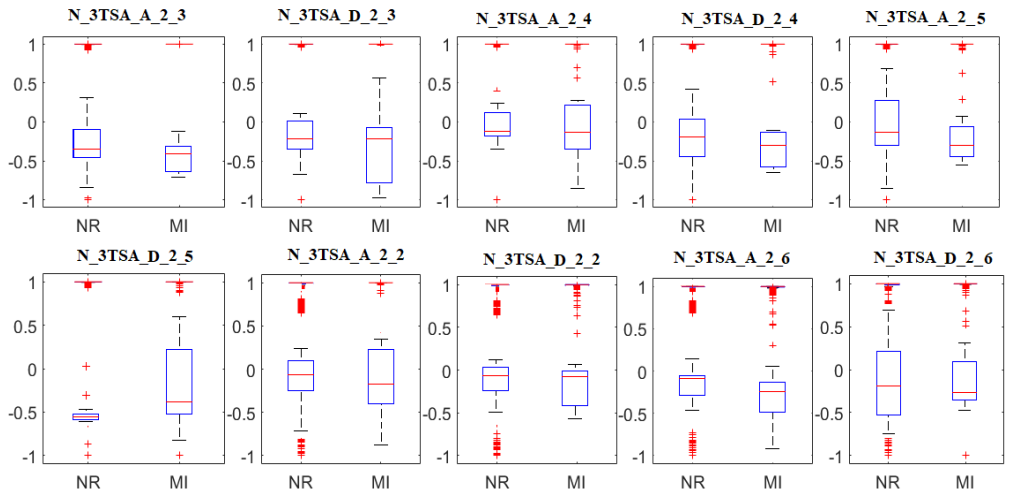

Figure 6.4: Box plot for the top 10 features for NR-MI dataset before reduction by GDA (*N-indicate normalized value, TSA- Tsallis entropy, A-approximate, D- detail, the first 2- indicate squared signal* $X^2[n]$*, the last number indicate decomposition level*)

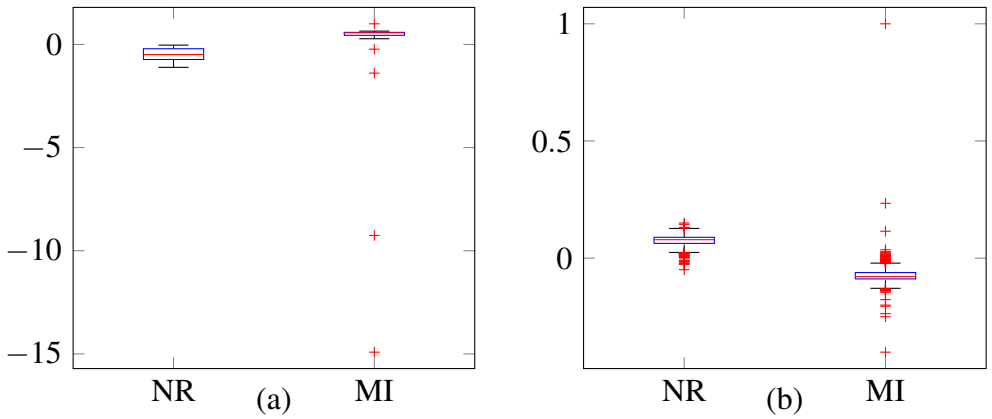

Figure 6.5: Box plot after feature reduction by the GDA with a) Gaussian b) RBF function for NR-MI dataset

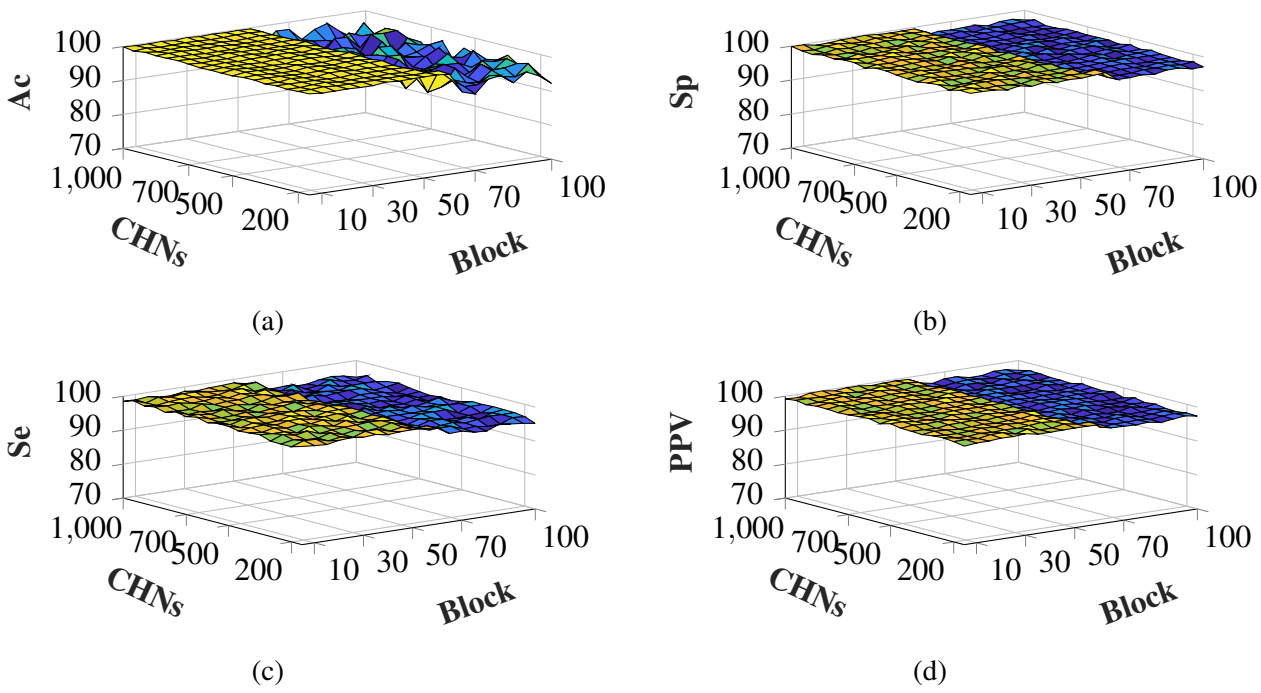

Figure 6.6: Variation of a) Ac, b) Sp, c) Se, and d) ppv - with number of hidden nodes and block length for OSELM sigmoid activation function and GDA with RBF kernel (**CHNs**-Contributing Hidden Nodes)

Fig 6.6 illustrates the different classification metrics, including Ac, Se, Sp, and ppv, in relation to block sizes and the number of contributing hidden nodes for the OBLOSELM classifier and the GDA feature reduction scheme with various activation functions. Upon thorough analysis of the impact of varying block size on these parameters, it becomes evident that their values remain largely unchanged even with an increase in block size. The simulation graph suggests that using fewer than 50 blocks is relevant for the successful classification of Normal and IMI subjects. In order to gain a thorough understanding of the distinctions among the NR-IMI groups, various statistical measures, including mean values, standard deviations, and p-values, are provided in addition to the box plot. The mean serves as a measure of the data's central tendency, capturing its average value, while the standard deviation(S.D) conveys the extent of dispersion or variability around that mean. A larger S.D between IMI and NR dataset shows that the measurements are closer to the mean, suggesting greater variability within the group. The mean, S.D and p-value of 10 features of two classes are shown in Table 6.1. It can be demonstrated that the mean value of the features shows a higher value for IMI subjects than the NR subjects. The p-values for the top 10 features were calculated using the Wilcoxon rank-sum method. The results reveal that the Tsallis features exhibit p-values significantly lower than 0.05 for the considered datasets. This suggests that the Tsallis features are well-suited for recognizing the considered datasets. All the top ten features exhibit significant measurement of

Table 6.1: Comparative outcomes for the top 10 features of NR-MI dataset

Features		N_3TSA_A_2_3	N_3TSA_D_2_3	N_3TSA_A_2_4	N_3TSA_D_2_4	N_3TSA_A_2_5	N_3TSA_D_2_5	N_3TSA_A_2_2	N_3TSA_D_2_2	N_3TSA_A_2_6	N_3TSA_D_2_6
IMI	Mean	0.99954	0.99971	0.99981	0.99960	0.99980	0.99960	0.99864	0.99797	0.99900	0.99731
	±S.D.	9.11E-04	5.63E-04	3.73E-04	7.79E-04	3.84E-04	7.63E-04	2.10E-02	3.45E-02	1.31E-02	4.37E-02
NR	Mean	0.95875	0.97253	0.98034	0.96147	0.98069	0.96118	0.94537	0.94452	0.94634	0.94412
	±S.D.	0.23692	0.15980	0.11816	0.22327	0.11667	0.22520	0.26462	0.26634	0.26420	0.26191
p-value		1.09E-04	1.25E-04	1.88E-04	3.52E-04	2.57E-03	2.31E-02	3.10E-02	5.59E-02	9.00E-03	2.55E-03

variation between the two classes. The larger differences in mean values and lower p-values observed in TSA features, as depicted in Table 6.1, provide informative indicators for identifying NR and IMI conditions.

The results of the proposed technique with GDA for different activation function are depicted in Table 6.2. It is evident that by increasing the number of hidden nodes to 500, all

Table 6.2: The Result of the proposed technique with GDA and different activation function (the bold face indicate higher performance at optimal block length)

No. of Hidden Nodes	Ac				Se				Sp				ppv			
	Block				Block				Block				Block			
	5	10	20	40	5	10	20	40	5	10	20	40	5	10	20	40
GDA with RBF Kernal and OBLOSELM with Sigmoid Activation																
50	99.9	99.91	99.91	99.89	99.8	99.82	99.81	99.79	100	100	100	100	100	100	100	100
100	99.91	99.92	99.91	99.9	99.83	99.83	99.83	99.81	100	100	100	100	100	100	100	100
150	99.9	99.92	99.91	99.92	99.8	99.83	99.83	99.84	100	100	100	100	100	100	100	100
200	99.92	99.91	**99.93**	99.91	99.83	99.82	**99.86**	99.81	100	100	**100**	100	100	100	**100**	100
500	99.93	99.92	99.93	99.92	99.86	99.84	99.86	99.84	100	100	100	100	100	100	100	100
GDA with RBF Kernal and OBLOSELM with Hardlim Activation																
50	87.28	92.56	87.14	84.88	93.75	95.35	93.09	91.23	80.79	89.92	81.33	78.8	93.12	93.22	88.36	86.93
100	97.51	95.51	93.91	95.79	97.99	95.94	98.26	96.65	97.01	95.09	89.63	94.99	98	96.42	93.04	96.53
150	97.88	98.66	97.8	97.26	98.69	98.9	96.78	98.4	97.1	98.41	98.81	96.11	97.62	98.74	99.09	97.49
200	99	99.02	98.9	99.13	99.1	99.41	98.38	98.66	98.87	98.64	99.45	99.6	99.12	98.97	99.51	99.66
500	99.9	**99.93**	99.93	99.9	99.81	**99.86**	99.85	99.81	100	**100**	100	100	100	**100**	100	100
GDA with RBF Kernal and OBLOSELM with Sine Activation																
50	99.91	99.9	99.9	99.9	99.83	99.81	99.79	99.79	100	100	100	100	100	100	100	100
100	99.9	99.9	99.89	99.9	99.8	99.79	99.79	99.79	100	100	100	100	100	100	100	100
150	99.9	99.9	99.9	99.9	99.8	99.8	99.81	99.8	100	100	100	100	100	100	100	100
200	99.9	99.9	99.9	**99.93**	99.8	99.81	99.8	**99.85**	100	100	100	**100**	100	100	100	**100**
500	99.91	99.88	99.91	99.91	99.82	99.77	99.81	99.83	100	100	100	100	100	100	100	100

performance metrics exhibit higher values compared to a lower number of hidden nodes. Moreover, there is no substantial change in these metrics for an increasing number of blocks. The performance results presented in this section are based on the value of l_{opt} obtained for a specific value of hidden nodes. Notably, the proposed technique achieves remarkable results for

different configurations. The application of GDA with a Gaussian kernel and sigmoid activation results Ac of 98.91%, Se of 98.62%, Sp of 99.21% and ppv of 99.2% at l_{opt} 5 and 100 hidden nodes. As it is evident from Figure 6.5a, this result also shows the Gaussian kernel exhibits relatively poor performance in distinguishing between the two groups. While, application of GDA with RBF kernel and sigmoid activation at 20 l_{opt} and 200 hidden nodes provides a relatively better Ac of 99.93%, Se of 99.86%, Sp of 100%, and ppv of 100%, compared to Gaussian kernel for the same activation function. So, the GDA with RBF kernel has better performance in classifying the two groups, due to its ability in distinguishing the features of NR and MI.

For a hardlim activation function, GDA with Gaussian kernel gives Ac of 98.52%, Se of 98.01%, Sp of 99.04%,and ppv of 99.04% for l_{opt} value of 5 and 100 hidden nodes. This number of hidden node ensures faster computation compared to a higher number of nodes. At a value of l_{opt} 20 and hidden nodes 500, GDA with a Gaussian kernel and RBF activation function demonstrates an Ac of 98.91%, a Se of 98.63%, a Sp of 99.19%, and a ppv of 99.2%. Similarly, GDA with a Gaussian kernel and a sine activation achieves an Ac of 98.94%, Se of 98.65%, Sp of 99.24%, ppv of 99.24%. In addition, it is important to highlight the outstanding performance of the GDA technique when combined with the RBF kernel and different activation functions. Specifically, GDA with a RBF kernel and sigmoid activation demonstrates remarkable performance in terms of Ac, achieving a score of 99.93% indicating a high level of correct classification. It also exhibits Se of 99.86%, Sp of 100%, and ppv of 100% at l_{opt} value of 20 and 100 number of hidden nodes. Sp value of 100% indicates indicate that the OBLOSELM correctly identifies all subjects who are truly free of the IMI condition. Similarly, GDA with RBF kernel and hardlim activation achieves a high Ac of 99.93%, along with Se of 99.86%, Sp of 100%, and ppv of 100% at 10 l_{opt} and 500 hidden nodes. For other values of block lengths and hidden nodes, it doesn't provide a consistent value of maximum ppv. Additionally, Given that the l_{opt} is obtained as 40 for 200 hidden nodes, GDA with a RBF kernel and sine activation achieves an Ac of 99.93%, Se of 99.85%, Sp100%, and ppv 100%. A ppv value of 100% indicates that if the test result is positive, the subject is certain to have the condition. In essence, ppv represents the probability that an individual has the condition given a positive test result. Conversely, when GDA is not applied, the performance of the OBLOSELM with various activation functions is notably poorer. For instance, OBLOSELM with sigmoid activation achieves an Ac of 89.07%, Se of 98.2%, Sp of 79.96%, and ppv of 83.03% at l_{opt} 5 and hidden nodes 200. Similarly, OBLOSELM with RBF activation achieves an Ac of 89.34%, Se of 98.44%, Sp of 80.24%, and ppv of 83.3% at 500 hidden nodes and l_{opt} of 5. At l_{opt} value of 20 and 200 hidden nodes, OBLOSELM with sine activation achieves an Ac of 89.35%, Se of 98.26%, Sp of 80.45%, and ppv of 83.4%.

Finally, OBLOSELM with hardlim activation performs the poorest, achieving an Ac of 79.45%, Se of 92.61%, Sp of 66.3%, and ppv of 73.45% at 5 l_{opt} and 500 hidden number of nodes. The application of GDA with RBF kernel function, combined with sigmoid or sine activation functions, consistently yields higher accuracy, sensitivity, specificity, and positive predictive value, demonstrating the effectiveness of the proposed technique. The results explicate on the crucial role played by the choice of kernel function and activation function in determining the system's performance. The better performance achieved by the proposed technique, specifically utilizing GDA with the RBF kernel function and sigmoid activation function, suggests that this particular combination enables the model to effectively capture and leverage nonlinear relationships in the data. Comparison of the developed method with some of the existing

Table 6.3: Comparative analysis of a proposed method for MI classification using ECG signals from the PTB Database

Classifier/ methodology	Dataset records (leads)	Features	Evaluation parameters
SVM (Sridhar et al., 2021)	148 MI, 52 NR (1)	Nonlinear features	Ac=97.96 Se= 98.89 Sp=93.80
ANN (Shahnawaz and Dawood, 2021)	148 MI, 52 NR (1)	Time, frequency ,nonlinear HRV analysis features	Ac=99.1 Se= 100 Sp= 98.1
Dynamical estimators (Zeng and Yuan, 2023)	367 MI, NR 78	ITD, DWT, PSR and ED	Ac= 98.20 Se= 98.37 Sp= 97.44
Dynamical estimators (Zeng et al., 2024)	367 MI, 390 NR	SEE + FA-MVEMD	Ac= 99.21 Se= 99.18 Sp= 99.23
OBL-OS-ELM **Proposed**	3240 IMI, 3037 NR (3)	SWT/ Tsallis entropy	Ac= 99.93 Se= 99.86 Sp= 100 ppv= 100

state-of-the-art techniques is listed in Table 6.3. The effectiveness of the proposed technique is compared with the SVM (Sridhar et al., 2021) based method, ANN (Shahnawaz and Dawood, 2021), ITD, DWT, PSR and ED (Zeng and Yuan, 2023), SEE+FA-MVEMD (Zeng et al., 2024). The limitations in these literature include the need for considering large datasets and higher accuracy. Notably, our study employed a much larger dataset as compared to the previous works in the literature. As it can be seen in Table 6.3, the proposed OBLOSELM method outperforms in classifying IMI and yields a better classification results through the analysis of ECG signals.

The detection of IWMI using techniques such as Tsallis entropy and OBLOSELM is vital in clinical practice to allow early diagnosis of this type of heart attack to enhance patient's therapy initiation, decrease diagnostic burden within an emergency department, in addition to effective tracking of the high risk patients. This paper proposed a framework to diagnose ECG signals using Tsallis entropy for analysing the non-linear heart dynamics, optimized block length for improved real-time efficiency of OSELM; all of which together will contribute to enhance the response times with high accuracy and in managing the IWMI diagnosis.

6.5 Summary

This study has introduced an automated method for detecting IMI cardiac disease from ECG signals using combination of SWT, TSAEn and OBLOSELM machine learning.In order to elevate the performance and accuracy of the OBLOSELM classifier, feature reduction technique such as GDA and optimum block length have been employed. The effectiveness of the proposed approach, employing GDA with a RBF kernel and OBLOSELM with sigmoid activation function results a substantial improvement when compared to methods proposed in recent literature. This research can be contributed to advancing the field of cardiac health monitoring, offering a robust framework for early and precise detection of ischemic myocardial infarction using non-invasive ECG analysis.

CHAPTER 7

LAYER- FUSION CONVOLUTIONAL NEURAL NETWORK AND MACHINE LEARNING MODEL FOR AUTOMATED CLASSIFICATION OF CAD AND CHF CARDIAC DISEASES

7.1 Introduction

This chapter introduces a hybrid framework combining a layer-fusion Convolutional Neural Network (CNN) with traditional machine learning classifiers for the automated classification of CAD and CHF. To ensure robustness and clinical relevance, the proposed model is trained and evaluated using publicly available ECG datasets, such as the PhysioNet databases. Performance metrics, including accuracy, sensitivity, specificity, and F1-score, validate the model, demonstrating its potential for real-time clinical decision support in intelligent cardiac care systems.

Recently, Convolutional Neural Network has been utilized across various applications, including speech recognition, bio-informatics, image classification, facial recognition, and computer gaming (Yildirim et al., 2019). CNN is capable of automatically extracting and learning valuable features from input data, generating deep features that greatly minimize the requirement of manual feature extraction (Sumalatha et al., 2024). In this study, a 1D convolutional CNN model has been proposed. This approach not only enhances classification performance but also reduces computation time. A performance evaluation of the proposed model has been carried out using accuracy (Ac) as well as precision (Pr), recall (sensitivity), F1-score, and Area Under the Curve (AUC) metrics.

While existing solutions exhibit considerable potential, there is still a need to enhance the classification accuracy of cardiac arrhythmias. This study proposes a layer fusion (LF) feature approach utilizing a deep CNN model to enhance the classification capabilities and improve the computation speed for three types of cardiac arrhythmias (such as Normal, CAD, and CHF). The LF features include the original time-series HRV signal and its Fast Fourier Transform (FFT) i.e. spectral features. The model includes 1D convolution layer, batch normalization, Relu activation function, and max pooling layer to enhance the classification performance.

The main contributions of this chapter are as follows:

- Time series data and spectral features are extracted from the pre-processed HRV signal. These features play a vital role in providing meaningful information for analysis, and then utilized as an input for the 1D CNN model.
- A layer fusion features based deep CNN model has been proposed to effectively extract

and fuse features from time-spectral data, enhancing performance parameters of ML in classifying Normal, CAD, and CHF.

- A Rectified Linear Unit (Relu) activation function, batch normalization, and max pooling layer has been introduced along with the deep CNN model to minimize the computational time of the training , so accelerates the classification speed.
- To improve the classification performance and computation efficiency, Adam optimizer is applied with a cross entropy loss function.
- Furthermore, to enhance the classification performance, we integrate machine learning algorithms along with the deep CNN, such as BO-SVM, KNN, and RF models.

7.2 Materials and Methods

This study proposes an end-to-end architecture derived from a deep CNN (1D-CNN) approach, BO-SVM, KNN, and RF machine learning models to the automatic classification of Normal, CAD, and CHF arrhythmias using HRV data. A 1D-CNN is proposed as it provides faster high performance classification. The block diagram of the proposed method is shown in Fig. 7.1. It consists of four major stages: (i) the pre-processing stage which aims to generate HRV data from the ECG signal by detecting R-peaks in the ECG signal and calculating the corresponding R-R intervals (resulting in the derived HRV signals); (ii) extraction of spectral and time series data features from the pre-processed HRV data (Normal, CAD, and CHF) and normalization of these features; (iii) the application of the 1D-CNN model to process the spectral and time series features, aimed at optimizing and enhancing performance for the deep CNN stage; (iv) the fusion and classification stage, which includes fusion of the two features, training (to create a classification model) and testing, respectively. The attributes obtained from the deep CNN model are then feed to ML algorithms in particular BO-SVM, KNN, and RF in order to enhance the classification performance.

7.2.1 Dataset

This study employs HRV data derived from ECG signals of participants sourced from the Fantasia, St. Petersburg Institute of Cardiological Technics (Incart), and Beth Israel Deaconess Medical Center (BIDMC) congestive Heart failure (BIDMC-CHF) databases (Goldberger et al., 2000b). The Fantasia database comprises recordings from 40 normal (healthy) individuals (20 young and 20 elderly), with the sampling frequency of 250 Hz; however, due to an erroneous recording from one young participant, only 39 healthy subjects are included in this analysis.

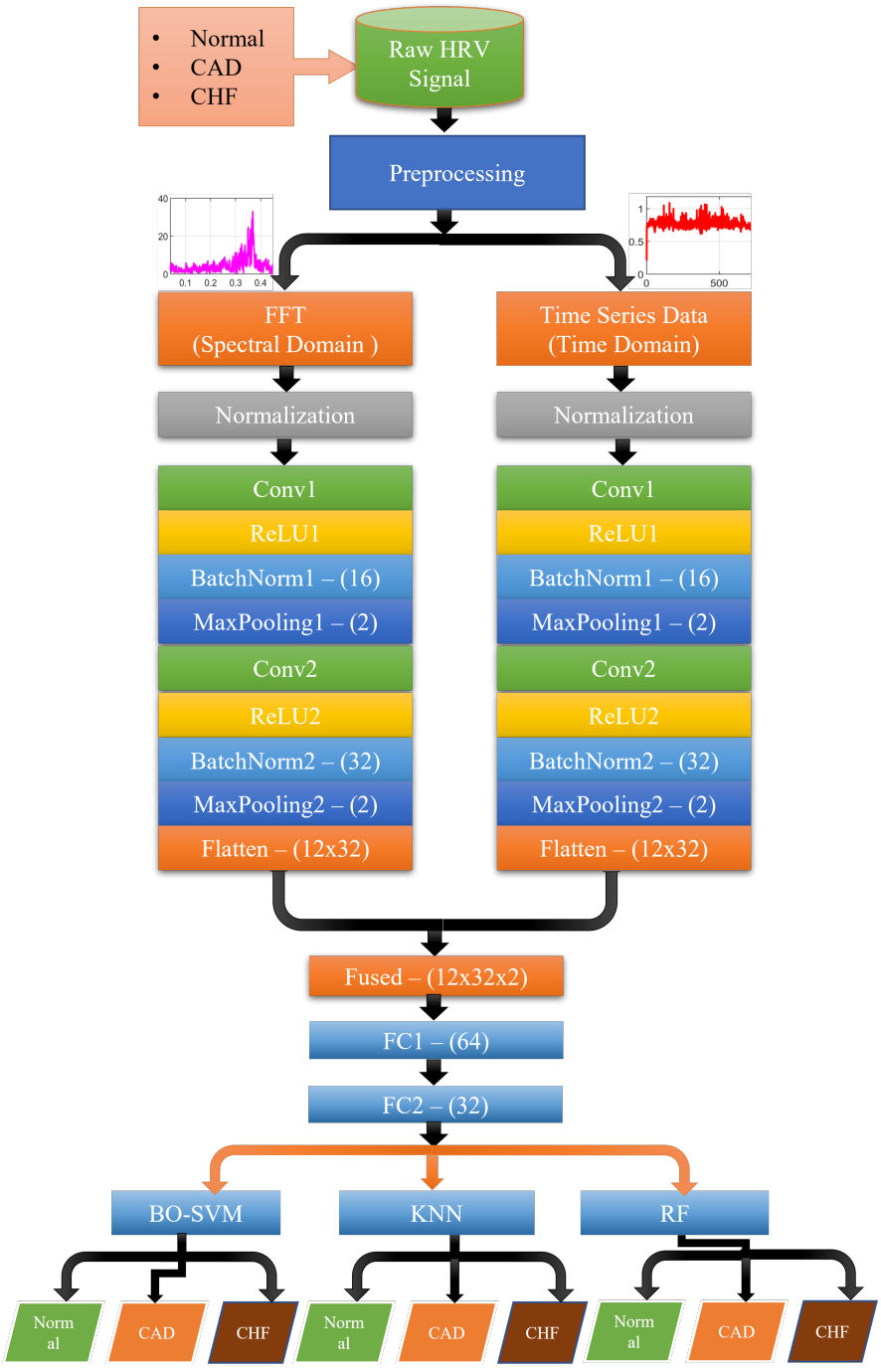

Figure 7.1: The framework of proposed block diagram for fusion of time-spectral features with 1D-CNN and classification of cardiac diseases with ML

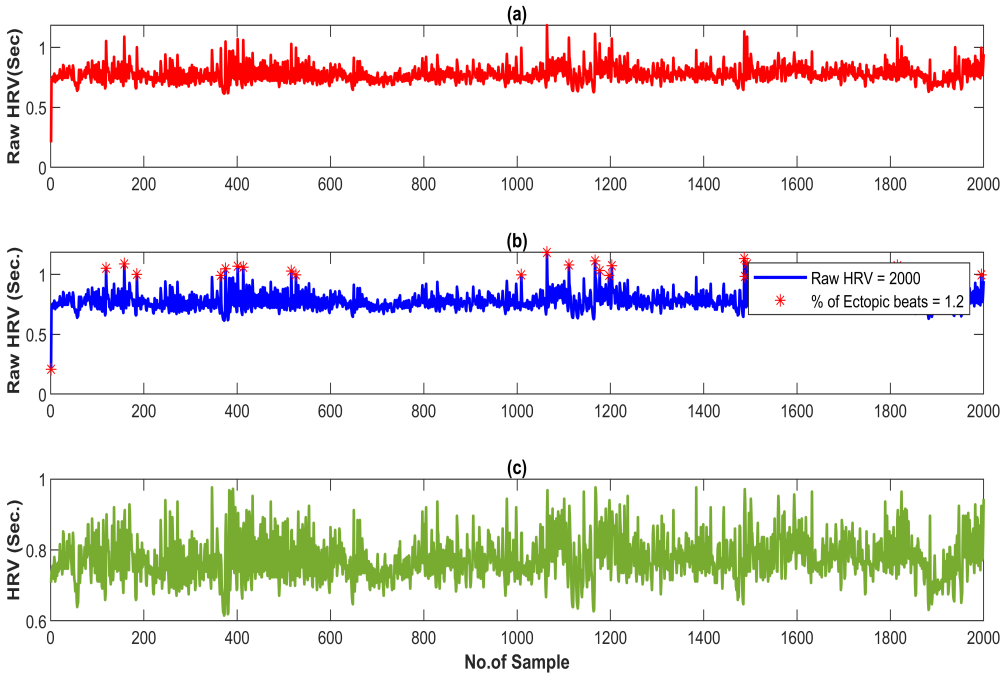

Figure 7.2: Plot of (a) Original HRV signal (b) HRV signal with ectopic beat, (c) HRV signal after ectopic beat replacement for a NR subject

The Incart database incorporates 75 annotated recordings sampled at 257 Hz, which include 13 subjects diagnosed with CAD and the BIDMC-CHF database comprises recordings from 19 subjects, all diagnosed with severe congestive heart failure, and its sampling frequency is 250 Hz. To enhance the dataset for deep CNN model training, segmentation has been performed to each 2000-sample recording, dividing it into 50-sample segments, which resulted in 40 segments per subject. This process expanded the dataset of healthy individuals to 1,560, CAD to 520, and CHF to 760 subjects. The R-peaks in the ECG signals has been detected through the use of a MODWT technique (Besfat et al., 2024a), and the R-R intervals (HRV) were subsequently calculated for each subject. Then, the HRV signal is resampled to 4 Hz.

7.2.2 Pre-processing

HRV signal analysis can be significantly affected by the presence of artifacts or ectopic beats, necessitating a pre-processing step. In this study, a median filter is utilized to detect these outliers, followed by the application of detrending and cubic spline interpolation to correct them (Singh et al., 2018b; Besfat et al., 2024b). For each detected ectopic beats, its value is replaced with the average of the neighboring HRV values, thereby enhancing the analysis of the signal.

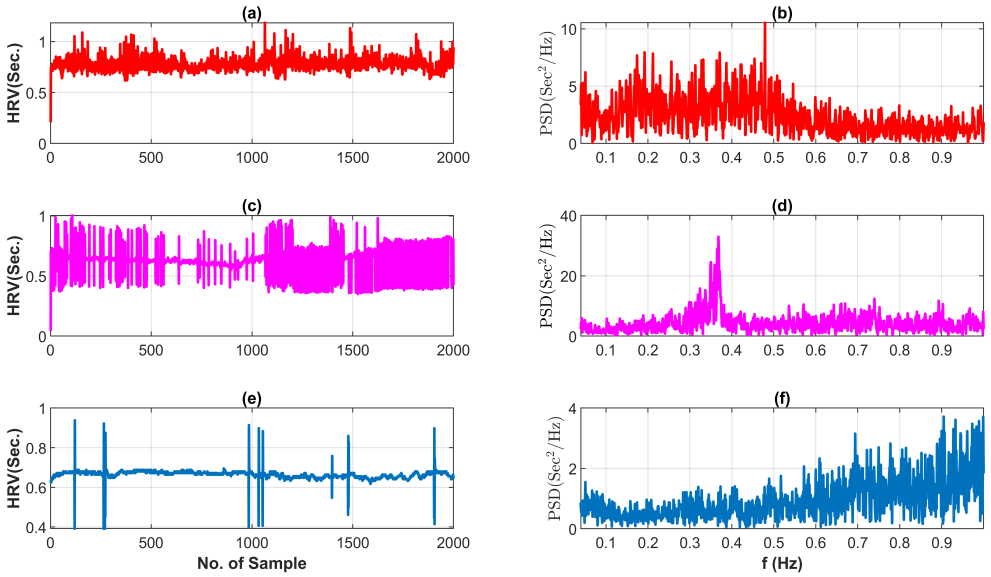

Figure 7.3: Plot of the time-series and spectral domain for HRV signal (1^st, 2^nd and 3^rd row indicate Normal, CAD, and CHF subjects, column 1 represents the time domain plot and column 2 indicates the corresponding FFT plot)

Fig. 7.2 illustrates the plots of the original HRV signal containing an ectopic beat and the processed signal after replacing the ectopic beat, respectively. Analysis of the 2000 HRV samples reveals that 1.2 % of the beats are ectopic. These outliers are distinctly visible as points that deviate significantly from the rest of the signal, highlighting the efficacy of the pre-processing method used in identifying these anomalies. After the extraction of spectral and time-series features, the data has been normalized (re-scaled) from the original range and the values lies in the range $[0,1]$. For this purpose, Min-Max normalization method has been applied and expressed as:

$$H_i^N = \frac{H_i - H_{min}}{H_{max} - H_{min}} \tag{7.1}$$

where, H_i is each data point in the dataset to be normalized and H is the entire HRV dataset features.

The time-series data and its FFT plot of the HRV data for the three cardiac arrhythmias are illustrated in Fig. 7.3 As it can be demonstrated from Fig. 7.3(a) and (c), the NR subject data indicates a more uniform variation in the R-R interval compared to the CHF individual data, which has an almost constant R-R interval. In contrast, the variation in the R-R interval of the CAD data is more variable, as shown in Fig. 7.3 (b). The power spectral density (PSD) variation of the NR individual data shows a high power in the LF and HF bands, whereas for the CAD subject data, the power variation is higher in the HF band only, with very low power in the other bands.

7.2.3 Deep CNN

The CNN is a deep learning model characterized by multiple stacked layers that emulate the functioning of neurons in the human brain. Deep CNN has demonstrated to be very effective for feature extraction and learning, and it has been applied in numerous studies. The feature extraction process in CNN consists of multiple hidden layers, comprising 1D convolutional layers, pooling layers, and ReLU activation functions (Panjaitan et al., 2023). The output from each conv layers learned non-linear features using the non-saturating activation function (ReLU function) and was subsequently batch-normalized. Therefore, the automated extraction process is enhanced by the convolutional (conv) and pooling layers, while the fully connected layer (dense layer) along with a softmax activation function helps in performing the classification output. In the conv layers, the ReLu function is utilized because it allows faster convergence compared to the tanh function in deep learning applications (Wang and Chen, 2019). Furthermore, max-pooling has been shown to outperform average-pooling; Consequently, max-pooling is implemented in the pooling layer of this study.

7.2.4 The Concept of Layer-fusion 1D CNN

The concept of layer-fusion 1D-CNN adopted in this paper is based on the frame work established in (Qiu et al., 2019). To improve feature diversity, the LF1D-CNN is introduced for the automatic classification of cardiac arrhythmias, utilizing both the original HRV signals (h(n)) and their corresponding frequency information (H(n)) as inputs. By leveraging LF1D-CNN, features from various layers of two parts (sub-models) get concatenated.

Letting h(n) represent the HRV signal, the respective FFT can be formulated as

$$H(n) = \sum_{n=0}^{N} h(n) e^{j\frac{2\pi n}{N}} \tag{7.2}$$

Where l = 0, 1, . . . , N-1 and N represents the length of h(n). By defining $H_m = \{h(n), H(n)\}$, the output of the 1D convolutional layer can be expressed as:

$$C_v = f(W^l * H + b^l) \tag{7.3}$$

where $W^l = W_h^l, W_H^l$ signifies the weights associated with the convolutional kernel for both h(n) and H(n) in the l^{th} layer, the sign * is the 1D convolution, and $b^l = b_h^l, b_H^l$ indicates the bias term. $f(\cdot)$ denotes ReLU activation function. In this study, to reduce the the likelihood of the vanishing gradient problem, the ReLU function is employed as the activation function. Once after the convolution results are obtained, the max pooling layer is employed to enhance

the output of the units, retaining the maximum value based on the downsampling factor with length d. The length of the feature is then defined as:

$$L_d = \frac{L_c - d}{s_d} + 1 \tag{7.4}$$

where L_c represents the length of C_v and s_d denotes the stride of the downsampling factor. The output of the max-pooling layer is denoted as M_p, and the features from the two sub-models are then combined into what is referred to as the fusion layer. Let F^l denote the features in the l^{th} fusion layer, which can be described as follows:

$$\begin{aligned} F^l &= \max\left(0, f\left(W_h^l * h(n) + b_h^l\right) + f(W_H^l * H(n) + b_H^l)\right) \\ &\leq \max(0, f(W_h^l * h(n) + b_h^r)) + \max(f(W_H^l * H(n) + b_H^l)) \\ &= M_p(h(n)) + M_p(H(n)) \end{aligned} \tag{7.5}$$

where F^l indicates the fused signal. The fusion layer generates a more powerful signal than a single model by integrating spectral and time domain features of HRV signal, which complement each other and provide comprehensive information even when one feature is weak. This integration allows the LF1D-CNN to effectively extract relevant high-level features, ultimately enhancing the classification performance of the three cardiac arrhythmias (Normal, CAD, and CHF). To enhance convergence speed and reduce overfitting, batch normalization is applied and can be defined as

$$BN^l = \gamma^l \frac{F^l - E_{F^l}}{\sqrt{\sigma_{F^l}^2}} + \beta^l \tag{7.6}$$

where E_{F^l} indicates the mean value of F^l and $\sigma_{F^l}^2$ denotes its variance. γ^l and β^l serve as scale and shift parameters, preserving the original distribution of HRV features from distortion. During the classification phase, the softmax function is utilized to map the features, expressed as

$$p(D_l) = \frac{e^{D_i}}{\sum_{i=0}^{I} e^{D_i}} \tag{7.7}$$

where, $p(.)$ signifies the probability score, D_l denotes the output of deep (FC) layer, I is the type of cardiac arrhythmias. The size of the feature map can be calculated as follows:

$$O_l = \frac{I_l - K_s + 2P}{S} + 1 \tag{7.8}$$

where, O_l denotes output length, I_l is input length, K_s signifies kernel Size, P illustrates padding, and S denotes stride (step size).

During the training phase of fused deep CNN model, the cross-entropy loss and the Adam

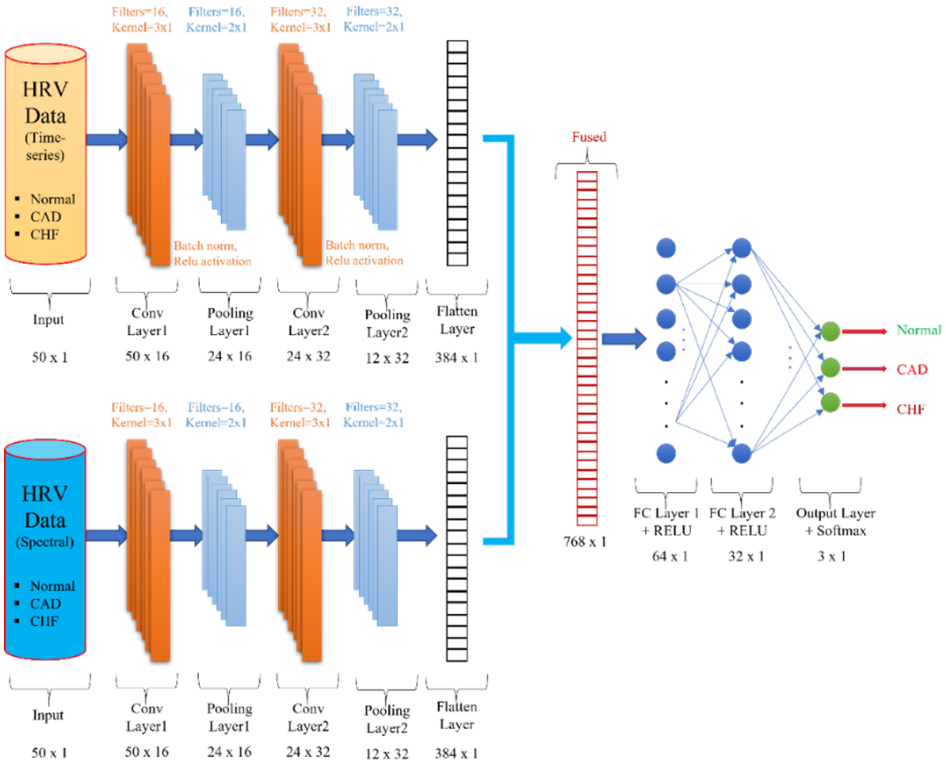

Figure 7.4: The structure of 1D-CNN architecture

optimizer are applied to each layers weight to update the parameters of the model. Once the LF1D-CNN model is trained, it is employed to detect the three arrhythmias.

7.2.5 The structure of 1D-CNN Algorithm

This study proposes a 1D-CNN structure designed for the extraction of features and classification of cardiac diseases, building on the fundamental principles of CNNs. Fig. 7.4 illustrates the proposed 1D-CNN structure, which comprises two conv layers along with two pooling layers (down-sampler), two fully connected (FC) layers, and a softmax layer. The 1D-CNN algorithm processes normalized spectral and time series HRV data directly, utilizing its robust feature extraction capabilities to automatically identify time-spectral features through alternating convolutional and pooling layers, with adaptive feature learning occurring in the fully connected layers. This method removes the necessity for manual feature extraction commonly found in traditional algorithms, enabling efficient end-to-end signal processing. As shown in Fig. 7.4, following the first convolutional layer, the input signals are transformed into a set of feature maps, which are then subjected to down-sampling using max-pooling. This sequence of operations is repeated one times to establish a connection between the features extracted from the final pooling layer and the fully connected layers. In these layers, the features are activated by Relu function before being sent to the softmax layer. For extraction of the frequency (spectral)

domain of features, the size of the conv kernel is 50 x 16 at layer 1 and 24 x 32 at layer 2. The size of the pooling kernel is 24 x 16 and 12 x 32 at layer 1 and 2, respectively. It should be noted that, the size of conv and pooling kernel is also taken the same value for extraction of time series data. After fusion of the spectral and time series features, the architecture includes a first FC layer with 64 nodes, a second dense layer with 32 nodes, and a softmax layer that produces 3 outputs. This model utilizes a fused dataset of spectral (FFT) and time-series signal features (12 x 32 x 2 = 768) as input, enabling automatic classification of cardiac arrhythmias. The details of the stages of spectral/time-series feature extraction is illustrated in Table 7.1.

Table 7.1: Details of each layer's parameters of the proposed 1D-CNN architecture

Layer type	**Kernel size**	**Stride**	**Padding**	**Output Shape**
Conv1	3 x 1	1	1	50 x 16
ReLU1	-	-	-	50 x 16
BatchNorm1	-	-	-	50 x 16
MaxPooling1	2 x 1	-	-	25 x 16
Conv2	3 x 1	1	1	25 x 32
ReLU2	-	-	-	25 x 32
BatchNorm2	-	-	-	25 x 32
MaxPooling2	2 x 1	-	-	12 x 32
Flatten	-	-	-	12 x 32
FC1	-	-	-	64
FC2	-	-	-	32
Softmax/Output	-	-	-	3

The ML techniques such as SVM, BO-SVM, A-KNN, and RF models are already discussed in Chapter 5.

7.2.6 Model Training Process

To build the deep layer fusion CNN model, the fused features data was randomly divided into two portions: 80% for training and 20% for testing. To ensure that the results were not merely coincidental, the number of training rounds was 50 per round (epoch). The loss function used in this study is the cross-entropy loss function since it works well for multi-class classification problems, while the Adam optimizer was chosen for its ability to adaptively fine-tune the learning rate and the initial learning rate is set to 0.0001. In order to monitor the training process the losses and accuracies of the training and validation sets were captured at each epoch. In summary, the HRV fused features was divided into an 80/20 split, and the model was trained for 50 epochs, with a primary emphasis on minimizing cross-entropy loss while leveraging the Adam

optimizer for enhanced performance. The same procedure is also applied For the BO-SVM, KNN, and RF classifiers.

7.2.7 Performance Evaluation

To evaluate the classification effectiveness of the Layer Fusion Convolutional Neural Network LF-CNN, BO-SVM, KNN, and RF model, various performance metrics has been employed, such as Ac, Pr, recall, F1-score, and AUC. These validation parameters are defined as follows:

$$Ac = \frac{T_p + T_n}{T_p + F_n + T_n + F_p} \tag{7.9}$$

where, T_p denotes True positives, T_n indicates True negatives, F_p: False positives, and F_n: False negatives.

Accuracy measures the overall performance of the classification model and it is determined as the ratio of correctly classified subjects to the total number of subjects.

$$Pr = \frac{T_P}{T_P + F_P} \tag{7.10}$$

Precision (positive predictive value) represents the portion of T_p predictions among all positive predictions made by the model. It reflects the Ac of positive predictions.

$$Recall = \frac{T_P}{T_P + F_N} \tag{7.11}$$

Recall (sensitivity) measures the ability of a model to correctly distinguish positive instances. It is the ratio of T_p to the total actual positives.

$$F1 - Score = \frac{2 \times T_P}{2 \times T_P + F_P + F_N} = 2 \times \frac{Precision \times recall}{Precision + recall} \tag{7.12}$$

The F1-score serves as a harmonic mean of precision and sensitivity, offering a unified metric that reflects the balance of a classification model's performance.

where, T_P indicates the number of subjects correctly identified as positive (healthy), T_N refers to the number of individuals accurately identified as negative (abnormal), F_P represents subjects incorrectly categorized as normal when they are actually abnormal, and F_N denotes subjects incorrectly labeled as abnormal when they are actually normal.

7.3 Result and Discussion

7.3.1 Result

The Box (whisker) plot of the time-series and spectral features of the HRV signal for the first ten features has been examined to visualize the statistical distribution of these features, as depicted in Fig.7.5 and Fig. 7.6.

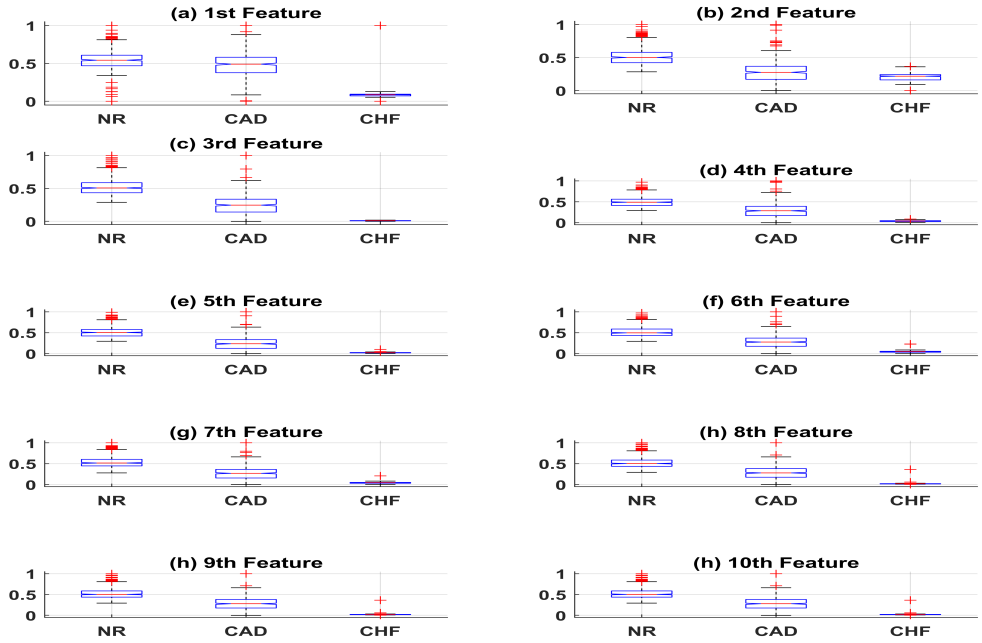

Figure 7.5: Box plot of the HRV time-series features

The red line within the box signifies the middle (median) value of the dataset features, known as median (Q2) component. As it can be observed, the median value of a normal individual is higher than that of CAD and CHF subjects for the time series feature. This suggests that a significant difference in the central tendency of the HRV feature between normal, CAD, and CHF groups. The wide Interquartile range (IQR) in NR and CAD groups indicates high variability (irregularity) in the HRV feature for the time-series data (Fig.7.5), while for the spectral features (Fig. 7.6.), the narrow IQR for the NR and CHF group suggests consistent HRV data. In addition, the narrow whiskers in the spectral features of these groups indicate that most of the data points are clustered closely around the median.

The t-distributed Stochastic Neighbor Embedding (t-SNE) serves as a visualization algorithm that effectively converts high-dimensional Euclidean distances among data points into

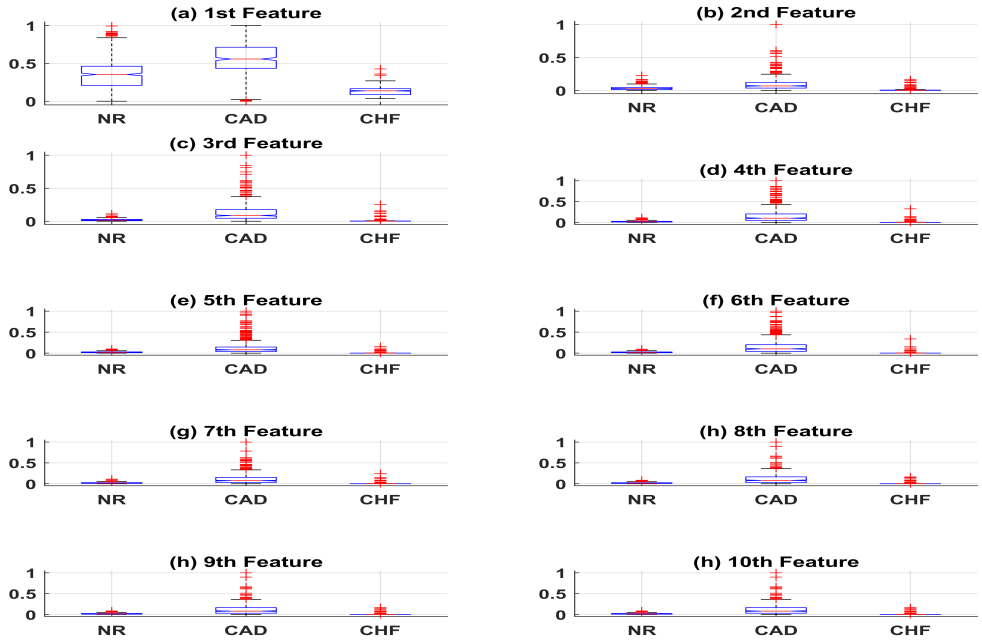

Figure 7.6: Box plot of the HRV spectral features

conditional probabilities, thereby representing their similarity (Wang et al., 2021b). Fig. 7.7 illustrates the visualization results of the features both before and after the application of layer-fusion process.

Upon examining the visualization results of the raw input data, Fig. 7.7(a) reveals that the features of the three cardiac arrhythmias are predominantly indistinguishable from those at the first input layer. It can be seen that there is overlap of the three classes in many areas. The feature distributions of the HRV datasets after the FC layers are visualized in Fig.7.7(b). As it can be seen from this result, the features at the FC layer are distinctly separated and clustered within their respective regions. This visualization result confirms that layer fusion features yield more information compared to single-modal features.

Throughout the 50 epochs of training, the model demonstrated outstanding result, achieving an Ac of 100%, with Pr, F1-score, and recall all also reaching 100%. As shown in Fig. 7.8(a), after 20 epochs the training and validation test of the spectral-time feature demonstrates an accuracy of 100%. This suggests that a model successfully identified the patterns in training dataset and effectively generalized its knowledge to new data instances. Fig.7.8 highlights the model's all over the performance across the 50 epochs, revealing a consistent high accuracy in both the training and validation phases.

Likewise, the model showcased strong performance on the testing dataset, resulting an

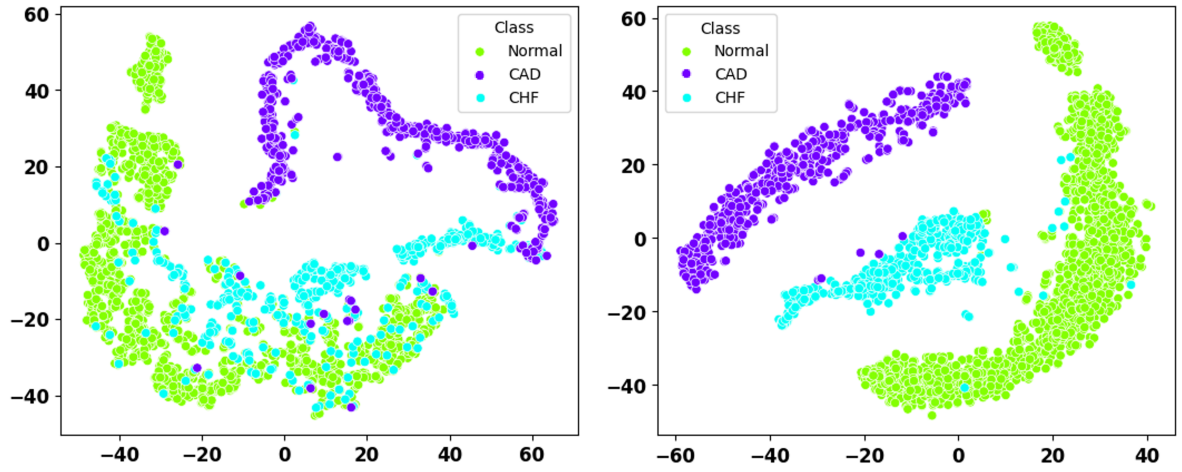

(a) (b)

Figure 7.7: Feature visualizations of (a) The raw input time-series data and (b) After fusion - based on t-SNE

Ac of 97.78%, a Pr of 98.98%, a recall of 98.54%, and an F1-score of 98.87%, as shown in Table 7.3. The decrease in model's loss during training and validation phase is illustrated in Fig. 7.8(b). During the training process, the model's loss progressively reduced, indicating an enhanced capability to predict the values that are closely match with the actual results. The level of a loss reduction emphasizes the model's performance in learning and its improved ability to make predictions. By analyzing these curves, we can assess whether the model is enhancing its predictive skills without simply memorizing the training data. The Ac and the

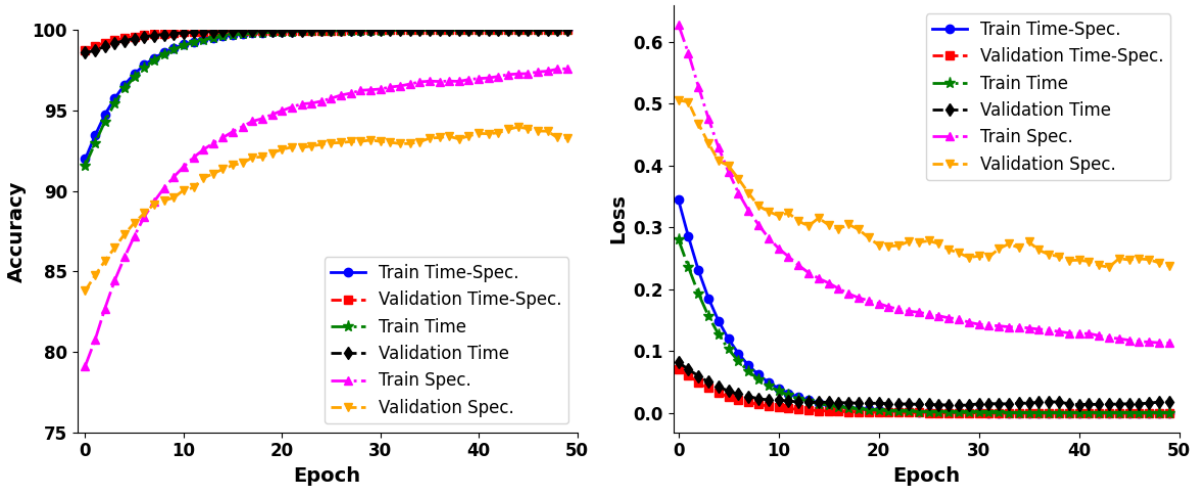

(a) (b)

Figure 7.8: Performance of the LF-CNN (a) Train and validation accuracy score, (b) Training and validation losses per epoch

loss curves are essential in evaluating the learning progression and overall performance of the

ML model as it evolves through time.

The ROC Curves in Fig. 7.9(a) and (b) demonstrate the models' performance across various thresholds, with the y-axis indicating the True Positive Rate (TPR) i.e Se, which indicates how effectively the model identifies subjects with cardiac diseases (true positives), while the x-axis reflects the number of subjects incorrectly classified as false positives (specificity values); thus, a model exhibiting a curve in the upper left corner of the graph, characterized by a higher TPR and a lower false positive rate (FPR), indicates a superior ability to distinguish between the three classes. The TPR is defined as the proportion of correctly identified positive cases calculated by dividing the total positive cases, while the FPR represents the proportion of negative cases incorrectly classified as positive, calculated by dividing the total number of negative cases.

The area under the curve indicates the portion of a square unit, with its value ranging from 0 to 1. An AUC value exceeding 0.5 signifies a distinction, suggesting that a higher AUC reflects a more effective diagnostic tool. Table 7.2 illustrates the performance of the proposed model using the ROC-AUC as an evaluation metric. It is also evident that utilizing combined features leads to improved performance compared to using individual features alone. As presented in

Table 7.2: AUC-ROC value

Features	**Normal**	**CAD**	**CHF**
Time-series	0.9869	0.9868	0.9865
Spectral	0.9385	0.9296	0.9581
Spectral-time	0.9932	0.9932	0.9988

Fig. 7.9 (a) and (b), the AUC values for normal, CAD, and CHF subjects are 0.9385, 0.9296, and 0.9581 when only the spectral feature is considered. However, when the fusion of the two inputs are applied, The AUC value increases to 0.9932, 0.9932, and 0.9988, respectively. In both scenarios, class 2 (CHF) achieves higher AUC value than class 0 (Normal) and class 1 (CAD). These results underscore the effectiveness of the proposed method in differentiating among the three classes.

Additionally, a confusion matrix was employed to provide a comprehensive assessment of the model's classification performance across the Normal, CAD, and CHF classes. Each row of the matrix indicates the actual class results, while each row represents the predicted class results.

Fig. 7.10 presented a confusion matrix which illustrates a visual depiction of the model's

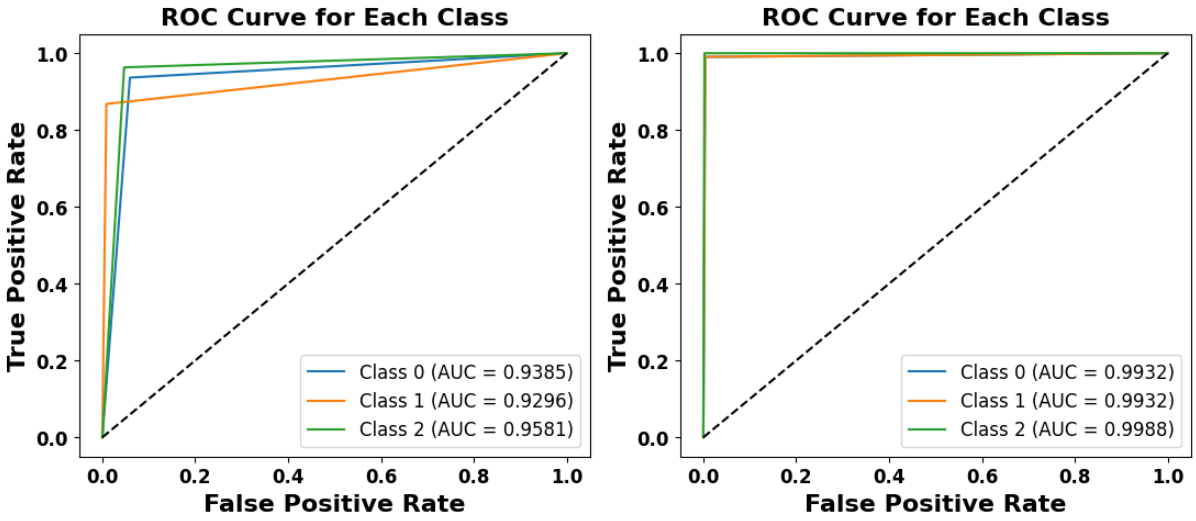

(a) (b)

Figure 7.9: Roc curve of (a) Spectral feature, (b) the LF-CNN model for three arrhythmia classes

performance in detecting the three classes. The confusion matrix provides valuable insights into the frequency of correctly classified instances, including true positives, true negatives, false positives, and false negatives. By analyzing specific values within the matrix, one can interpret the model's accuracy in accurately identifying positive cases. As depicted from Fig.

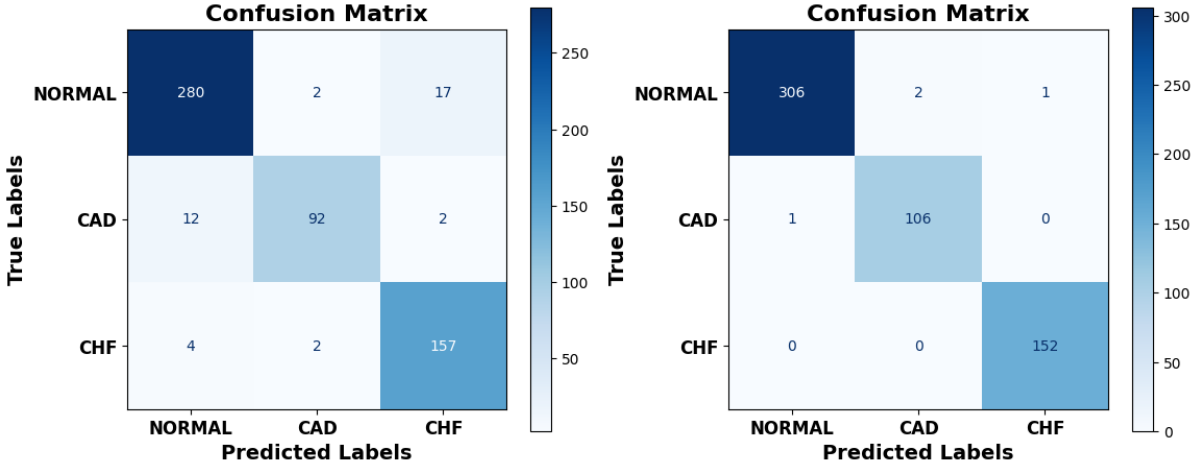

(a) (b)

Figure 7.10: Confusion matrix for (a) Spectral feature of 1DCNN, (b) LF-CNN classification

7.10 (a) and (b), the confusion matrix indicates that the classification of cardiac diseases using the spectral feature perform poorly, whereas the proposed layer-fusion features based deep CNN model demonstrates significantly higher classification performance.

To illustrate the effectiveness of combining Bayesian optimization with SVM model on a

Table 7.3: Results of the proposed model (**Bold** face- indicates higher performance)

Method	Features	Accuracy	Precision	Recall	F1-Score
1-DCNN	Spectral	0.96127	0.93209	0.93545	0.93339
	Time-Spectral	0.96510	0.97884	0.96670	0.97395
LF-1DCNN	Time-Spectral	0.97770	0.98981	0.98539	0.98874
LF-1DCNN +SVM (Kernal linear)	Spectral	0.87089	0.79116	0.82865	0.80067
	Time-Spectral	0.99765	0.99674	0.99371	0.99519
LF-1DCNN+ SVM(RBF)	Spectral	0.92136	0.86769	0.89372	0.87732
	Time-Spectral	0.99296	0.99134	0.98182	0.98630
LF-1DCNN+AdaBoost	Spectral	0.91901	0.83834	0.87578	0.85471
	Time-Spectral	**0.99883**	**0.99679**	**0.99782**	**0.99730**
LF-1DCNN+DT	Spectral	0.94366	0.90058	0.91561	0.90745
	Time-Spectral	0.98592	0.98054	0.96833	0.97381
LF-1DCNN+NB	Spectral	0.78521	0.56135	0.66709	0.54506
	Time-Spectral	0.90610	0.89024	0.84667	0.84758
LF-1DCNN+SVM (Polynomial)	Spectral	0.92488	0.87641	0.90167	0.88467
	Time-Spectral	**0.99883**	**0.99893**	**0.99683**	**0.99787**
LF-1DCNN+BOSVM (RBF)	Spectral	0.95423	0.92336	0.93179	0.92737
	Time-Spectral	**0.99883**	**0.99893**	**0.99683**	**0.99787**
LF-1DCNN+ K-NN (K=3)	Spectral	0.95775	0.90981	0.94139	0.92220
	Time-Spectral	**0.99883**	**0.99893**	**0.99683**	**0.99787**
LF-1DCNN+RF	Spectral	0.95188	0.89974	0.93280	0.91467
	Time-Spectral	**0.99883**	**0.99893**	**0.99683**	**0.99787**

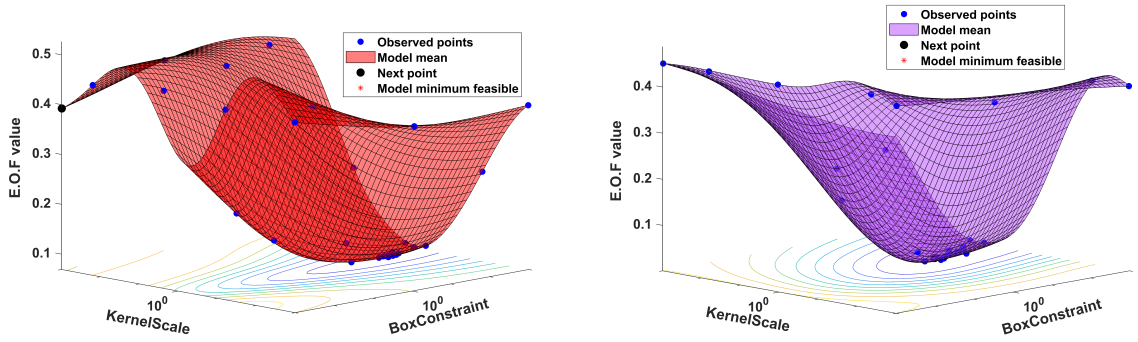

(a) (b)

Figure 7.11: Optimized SVM Objective function model for (a) Spectral feature, (b) LF-CNN classification

training dataset, Fig. 7.11 demonstrate how BO optimizes the parameters C (box constraint) and γ (kernel scale) to minimize the cost function of the SVM. This process highlights the iterative tuning of parameters towards achieving the global minimum. As it can be seen, The values obtained for the parameters C, γ, and Estimated Objective Function (E.O.F) value are 195.75, 0.51, and 0.07, respectively, for spectral features. In contrast for the time-spectral features, the corresponding values are 29.41, 2.23, and 0.002086. The estimated function evaluation time also obtained is 0.26188 seconds. The optimization process significantly enhances the model's accuracy, increasing it from 92.14% to 95.42% for spectral features and from 99.29% to 99.88% for time-spectral features after applying the optimization techniques, as indicated in Table 7.3.

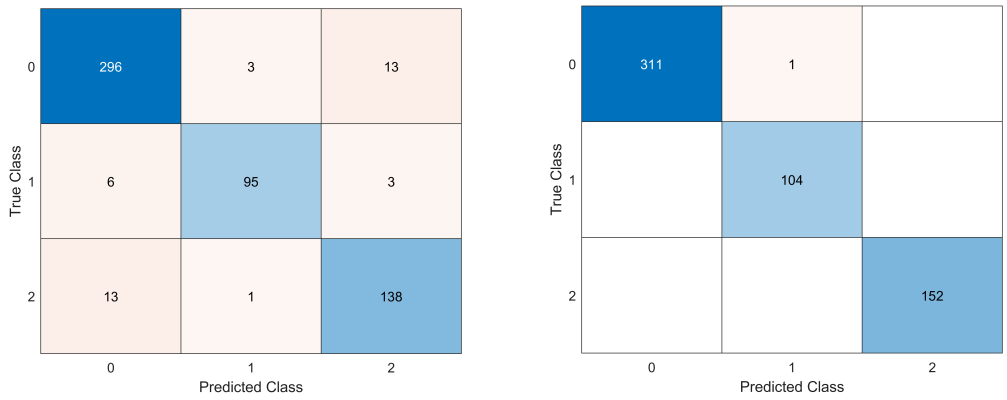

(a) (b)

Figure 7.12: Confusion matrix of (a) Spectral feature, (b) Time-spectral features for BO-SVM classifier (**0 - NR, 1 - CAD, and 2 - CHF subjects*)

For the BO-SVM classifier, the confusion matrix is depicted if Fig. 7.12. It can be seen

also that the spectral feature alone is not able to achieve accurate classification. The confusion matrix of BO-SVM and KNN models achieve the same performance and accurate classification for the three arrhythmias. The confusion matrix for KNN classifier is illustrated in Fig. 7.13.

Table 7.4: Comparison of existing literature in classification of CAD and CHF arrhythmias

	Material		Methodology		Performance Result (%)				
Ref.	**Data Type**	**Dataset Used**	**Features Extracted**	**Classifier**	**Accuracy**	**Specificity**	**Precision**	**Recall**	**F1-score**
(Rohila and Sharma, 2020)	HRV	NSR, SCD, CAD, CHF	Poincare plot, Entropy and S-transform	SVM, DT	91.67	94.64	84.75	83.33	-
(Kumari et al., 2021)	ECG	CHF	DWT (4 level decomposition)	SVM	77.78	-	100	77.78	87.5
(Nesaragi et al., 2022)	HR signals	CAD	Scalogram-based Tensor factorization	Bagged Trees	96.53	96.62	-	96.67	-
(Panjaitan et al., 2023)	HRV	NSR, SCD, CAD, CHF, VT	Time dmain	1D-CNN Wavelet	99.3	99.6	97.87	97	-
(Rao and Kumar, 2023)	ECM, ECG	CHF	-	-	96.89	-	99.1	97.53	97.76
(Sun et al., 2024)	HRV	CHF	Higher-Order Moments Detrended Fluctuation Analysis	ANN	72.67	-	-	-	-
(Karimulla and Patra, 2024)	Self-collected	CAD	Entropy, optimal multi-modal features	DL and SVM	95.96	87.31	-	100	92.93
(Karimulla and Patra, 2024)	HRV	NSR, SCD, CAD, CHF, AF	Time domain, frequency domain, and non-linear	GBC	96.43	95.45	-	97.14	-
Proposed work	HRV	Normal, CAD, CHF	Time-series and spectral	LF-CNN with-BO-SVM, KNN, RF	99.88	-	99.89	99.68	99.79

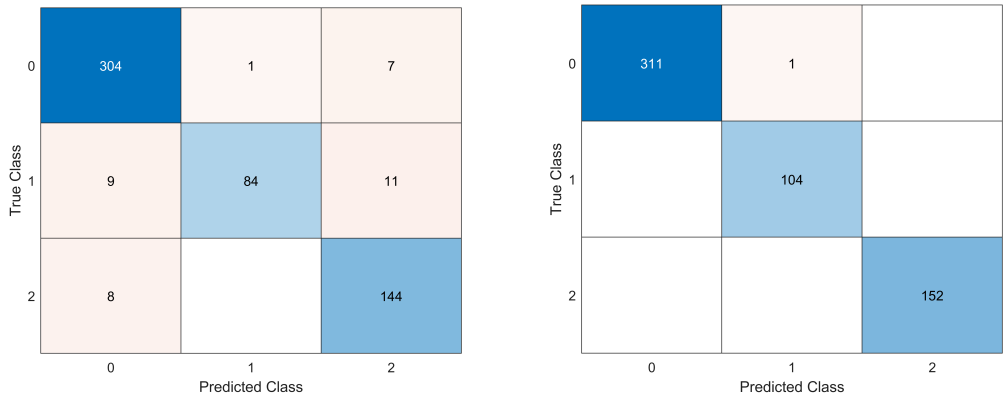

(a) (b)

Figure 7.13: Confusion matrix of (a) Spectral feature, (b) Time-spectral features for KNN classifier

As it can be shown, for spectral features, the performance of this classification model is lower as it identifies that for Normal (healthy) condition, 9 subjects were incorrectly identified as having normal condition (but they actually have CAD condition). Similarly, for CAD, 1 subject was incorrectly identified as having CAD (it actually has CHF). In contrast, for the time-spectral features, the KNN classifier achieves higher performance.

Table 7.3 illustrates the results of the proposed model for the spectral and the fusion of spectral and time series features for the deep CNN and various machine learning algorithms. It is evident that the accuracy, precision, recall, and F1-score from the spectral feature are lower compared to the fusion features. Furthermore, by fusion the two features (time-frequency), even greater values can be achieved. This indicates that if one feature contains less information while another holds more, combining the features can enhance overall performance.

The performance metrics for the 1D-CNN model are generally lower than those of the LF-CNN model. This suggests that integrating various features (fusion of features) significantly enhances the performance of classification results. After fusion of features using deep CNN and applying a SVM machine learning model with a linear kernel type (LF-1DCNN + SVM (kernel linear)), the results from the spectral feature alone are lower than those from the spectral features of LF-1DCNN model. However, when using time-spectral features, the performance exceeds that of the LF-1DCNN. This indicates that integrating machine learning algorithms with deep learning approaches can effectively enhance classification performance, rather than relying solely on deep learning methods.

The SVM model utilizing a radial basis function kernel (LF-1DCNN + SVM (RBF)) demonstrates better classification performance for spectral features compared to the linear kernel SVM (LF-1DCNN + SVM (kernel linear)). However, its performance is somewhat lower when applied to time-spectral features. This highlights that the choice of kernel type significantly affects the model's classification outcome. The AdaBoost machine learning algorithm achieves superior classification performance for time-spectral features compared to 1D-CNN, LF-1DCNN, and SVM models using both linear and RBF kernels. This indicates that AdaBoost is more effective in making accurate classifications than these other ML approaches. For spectral features, the DT algorithm demonstrates better performance than the Naive Bayes algorithm. However, when it comes to time-spectral features, Naive Bayes outperforms DT in classifying the three arrhythmias. This indicates that the effectiveness of each algorithm can vary depending on the type of features used.

The SVM model with a polynomial kernel achieves better classification results for time-spectral (fused) features, but its performance is lower for spectral features. In contrast, for fused features (attributes), the BO-SVM with a RBF kernel, K-NN (K=3), and RF all demonstrate the highest performance across all metrics, yielding similar outcomes. This suggests that the choice of model and attribute type significantly influences classification effectiveness.

In conclusion, the classification performance for the three arrhythmia types can be significantly improved by using a fusion of feature rather than relying on a single feature. Additionally, integrating machine learning algorithms with deep learning techniques yields higher classification results than using deep learning alone. This approach enhances the overall effec-

tiveness of cardiovascular arrhythmia classification models.

7.3.2 Discussion

Several researchers has been discussed the detection or classification of different cardiac arrhythmias from HRV and ECG data using various deep learning and machine learning algorithms. The proposed layer-fusion 1D-CNN model has been compared to various methodologies as shown in Table 7.4. The authors in (Rohila and Sharma, 2020) obtained an Ac of 91.67% in the classification of CAD and CHF subjects. The study involved the extraction of entropy features, Poincare plot, and S-transform from HRV signals and employed SVM and DT algorithms for their analysis. In (Kumari et al., 2021), the classification of ECG signals was performed using the SVM algorithm, achieving an Ac of 77.78% for the classification of CHF. Although they achieved a Pr of 100%, the results from the other metrics indicate a very poor performance in classifying the considered arrhythmia. The authors in (Nesaragi et al., 2022) propose a Bagged Trees classifier and achieved an Ac of 96.53% for automated detection of CAD. A 1D-CNN wavelet model was introduced for the classification of CAD and CHF diseases, with time domain features derived from HRV signals being utilized in (Panjaitan et al., 2023). In this approach the authors obtained an Ac of 99.3%, Se of 97.00%, Sp of 99.6%, and Pr of 97.87%. In (Rao and Kumar, 2023), an ECM matrix was proposed for the identification of CHF, and obtained an Ac of 96.89%. Classification of CHF has been done using ANN in (Mahananto et al., 2024) based on higher order moments DFA and achieve an Ac of 72.67%. An Ac of 95.96% was achieved for the identification of CAD by combining PCG, ECG, and coupling signals through the integration of optimal multi-modal attributes and the SVM learning algorithm in (Sun et al., 2024). Despite achieving a recall of 100%, the results from the other metrics reveal a very poor performance compared to our work. In the study (Karimulla and Patra, 2024), time, frequency, and non-linear attributes had been derived from HRV signals, and the GBC algorithm was applied to classify CAD and CHF, achieving an Ac of 96.43%, a Se of 97.14%, a Sp of 95.45%.

When compared to the techniques outlined in the literature, our layer fusion 1D-CNN model with- BO-SVM, KNN, and RF showcase significantly enhanced detection capabilities, Moreover, the proposed model consistently exceeds all referenced methods across multiple evaluation metrics, achieving accuracy of 99.88%.

7.4 Summary

Early detection of cardiac diseases are essential for medical professionals, as they significantly enhance the ability to diagnose patients in a timely and accurate manner. This study proposed a classification method for three cardiac arrhythmias, specifically Normal, CAD, and CHF, utilizing inedration of LF-CNN model with BO-SVM, KNN, and RF algorithms applied to HRV signals. The features extracted for the deep CNN include time-series and spectral measures which are then fed to the proposed machine learning algorithms. Batch normalization, the Relu activation function, and max-pooling layers have been utilized in the 1D-CNN architecture due to their capacity to enhance computational speed and effectiveness in multi-class classification tasks. The simulation results demonstrated that the proposed method achieved accurate cardiac arrhythmias classification by leveraging a fusion of time-spectral features, along with the integration of machine learning with deep learning algorithms. This combination enhances the model's accuracy in arrhythmia classification. In the future, this proposed model can be applied to investigate and classify other cardiac diseases using fusion of various features that will be helpful for cardiac patient outcome and cardiac medical specialist.

CONCLUSIONS AND RECOMMENDATIONS

This dissertation has discussed the development of advanced signal processing techniques for the spectral and non-linear analysis of CVDs and utilization of machine learning techniques for the classification of these diseases. The major conclusions from this study and the recommendations of future work are summarized as follows:

Conclusions

The study presented in this dissertation work makes significant contributions to cardiac signal processing and disease detection through innovative methodologies and rigorous validation. A highly efficient method for ECG denoising and R-peak detection have developed, combining DC component removal, normalization, and maximal overlap discrete wavelet-based denoising, followed by a threshold-based R-peak detection technique. Extensive testing on five PhysioNet databases (MITDB, QTDB, TWADB, AFTDB, and FANTASIADB) demonstrated exceptional performance, with sensitivity reaching 99.97% and a positive predictive value of 99.64% for the TWADB database, along with a remarkably low detection error rate of 0.063 for QTDB. These results confirm the method's reliability and suitability for diverse clinical and research applications. Building on this foundation, the study further investigated HRV as a non-invasive tool for assessing autonomic nervous system regulation. By employing advanced spectral and time-frequency techniques, the research successfully captured non-stationary behaviours that conventional methods often miss.

Further refining time-frequency analysis, energy concentration based an optimized Gaussian window reassignment technique (optimized by particle swarm optimization) has introduced for precise time-frequency localization. Experiments on synthetic and real-time signals demonstrated the proposed OptGWRS effectiveness in tracking abrupt frequency changes in non-stationary data compared to other TFA techniques such as, STFT, OptADMST, SST, SET, and RS. In addition to this, investigations of HRV and respiratory signal coupling revealed age-related declines in high-frequency coherence linked to autonomic nervous system degradation, while statistical integration enabled accurate localization of significant coupling regions ($p = 0.0125$). In contrast, this coupling in the low frequency band remains largely unaffected by the ageing of healthy subjects. Furthermore, the coherence in HRV-SABPV is also significantly lower in both the low ($p=0.00001$) and high frequency bands ($p=0.0001$) for the young and elderly subjects, while the NSSC among HRV and APIV signals is lower in eldly subjects compared with yng subjects in the low frequency and high frequency range.

Refocusing on cardiac disease classification, this study has proposed automated frameworks for myocardial infarction identification using OptMST, multiscale entropy (MSEn) fea-

tures, and machine learning models (BO-SVM, A-KNN, RF), which outperformed existing techniques in classifying arrhythmias. The RF classifier achieved accuracy of 98.44%, sensitivity of 94.60%, precision of 94.67%, specificity of 98.93%, and F-score of 94.62%. The introduced method enables timely intervention and improved patient outcomes. Expanding on this, an advanced approach combining stationary wavelet transforms, Tsallis entropy, and OBLOSELM classifier was proposed. Feature reduction via generalized discriminant analysis (GDA) and optimal block length significantly improved classification accuracy, with the RBF kernel and sigmoid activation function further enhancing the performance. The proposed method achieved an accuracy of 99.93%, sensitivity of 99.86%, specificity and positive predictive value of 100% for the classification of an inferior myocardial infraction cardiac disease. This non-invasive approach offers a reliable solution for early IMI diagnosis, contributing to improved cardiac health monitoring.

Finally, a LF-CNN model integrated with BO-SVM, KNN, and RF machine learning algorithms was proposed to classify cardiac arrhythmias (Normal, CAD, CHF). Leveraging the fusion of time and spectral features from HRV signals and integration of machine learning with deep learning algorithms, along with batch normalization and max-pooling, the model achieved high classification accuracy (99.88% accuracy, 99.89% precision, and 99.79% F-score) and improved computational efficiency.

The proposed methods can establish robust, automated systems for cardiac signal analysis and early disease detection, with implications for both clinical practice and medical research. Future work will focus on validating these methods across larger, more diverse datasets and extending their applications to broader cardiovascular and neurological conditions, ultimately advancing precision medicine through innovative, non-invasive diagnostic tools.

Recommendations

The Pioneering work outlined in this thesis lays a strong foundation for numerous exciting research pathways that promise to transform cardiac care. As we look ahead, several key directions emerge that could significantly enhance both the technical capabilities and clinical applicability of these systems. Building on the robust methodologies already developed, future efforts should focus on expanding and refining these approaches to overcome current challenges while exploring new frontiers in cardiovascular health monitoring. Future direction can incorporate the following ideas:

- One of the most critical concern is the validation of these algorithms across larger, more diverse datasets that better represent real-world populations. While the proposed methods

were validated on established databases (such as, MITDB, QTDB, Fantasia, etc.) and have demonstrated excellent performance, incorporating multi-ethnic cohorts, long-term wearable device recordings, and rare cardiac arrhythmias would substantially ensure the generalizability of these systems.

- Current methods rely on offline processing, but real-time analysis is crucial for emergency care. Future directions may involve optimizing algorithms for edge devices (including, smartwatches, portable ECG monitors) as well as developing lightweight models suitable for low-power hardware without sacrificing accuracy.

- Looking beyond ECG analysis, combining electrical signals with other biosignals (e.g., PPG, EEG, respiratory signals), optical plethysmography, and even biochemical markers could create a more holistic picture of cardiovascular health by capturing the full complexity of cardiac conditions. Such integration would be particularly powerful when paired with longitudinal monitoring capabilities, enabling not just diagnosis but prediction of adverse events. These capabilities would fundamentally shift cardiac care from reactive to preventive medicine.

- In addition to cardiovascular applications, the methodologies developed here could find applications to serve in neurology, sports medicine, and maternal-fetal health. The same principles that enable precise analysis of cardiac rhythms could be adapted to study brain-heart interactions in neurological disorders, optimize athletic training regimens, or monitor fetal development. These cross-disciplinary applications would not only extend the outcome of this work but also provide valuable feedback to refine the core technologies.

Research Contribution

The dissertation contributions out of this work are listed as follows:

1. H. M. Besfat, D. J. Gelmecha, and R. S. Singh, “Delineation of QRS features and denoising of ECG signal using Fejer Korovkin wavelet,” International Journal of Information Technology, vol. 16, no. 5, pp. 3027–3031, Apr. 2024, doi: 10.1007/s41870-024-01804-2, **Springer nature**, (**Scopus**, Status: **Published**)

2. H. M. Besfat, D. J. Gelmecha, and R. S. Singh, "Detection of myocardial infarction cardiac diseases based on renyi entropy and optimum block length of online sequential-extreme learning machine," Biomedical Engineering: Applications, Basis and Communications, (2025), DOI: 10.4015/S1016237225500152, **World Scientific Publishing**, (**I.F. 0.6**, **Scopus, Web of Science (WoS)**, Status: **Published**)

3. H. M. Besfat, D. J. Galmecha, and R. S. Singh, “Detection of myocardial infarction diseases based on entropy, optimized Stockwell time-frequency transform and extreme learning machine,” International Journal of Information Technology, Mar. 2025, doi: 10.1007/s41870-025-02504-1, **Springer nature**, (**Scopus**, Status: **Published**)

4. H. M. Besfat et al., “Spectral Analysis of Congestive Heart Failure Cardiac Disease using Flexible Analytic Wavelet Transform,” 2024 11th International Conference on Computing for Sustainable Global Development (INDIACom), pp. 1455–1460, Feb. 2024, doi: 10.23919/indiacom61295.2024.10498656, **IEEE**, (**Scopus**, Status: **Published**)

5. H. M. Besfat, D. J. Gelmecha, and R. S. Singh, "A Hybrid Layer-Fusion Convolutional Neural Network and Machine Learning Framework for Automated Detection and Classification of CAD and CHF Cardiac Diseases", Expert System with Applications, **Elsevier**, (**I.F. 7.5**, **SCIE**, Status: **Revision Submitted**)

6. H. M. Besfat, D. J. Gelmecha, and R. S. Singh, "Energy Concentration-Based Optimization of Gaussian Window Reassignment for Time-Frequency Analysis, and Its Application in Analyzing the Non-Stationary Spectral and Coherence of Cardiovascular Signals," Computers in Biology and Medicine, **Elsevier** (**I.F. 7, SCIE**, Status: **Revision**)

7. H. M. Besfat, D. J. Gelmecha, and R. S. Singh, "Multi-scale Entropy-Driven Multi-Classification of Myocardial Infarction Diseases Based on Optimized Modified Stockwell Time-Frequency Transform and Machine Learning Models," **IEEE Access**, (**I.F. 3.4**, **SCIE**, Status: **Under review**)

8. H. M. Besfat, D. J. Gelmecha, and R. S. Singh, "Automated Detection of Inferior Wall Myocardial Infarction Through Tsallis Entropy and an Optimized Block Length for OS-ELM," Computer methods in Biomechanics and Biomedical Engineering, **Taylor and Fransis**, (**I.F. 1.7**, **SCIE**, Status: **Under review**)

9. H. M. Besfat, D. J. Gelmecha, and R. S. Singh, "Automatic Detection of Myocardial Infarction Diseases from ECG Signal Based on Renyi, Dispersion Entropy features and Adaptive-KNN Machine Learning", (The 7th Annual National Research Conference, G**ambella University**, Status: **Accepted, Presented**)

10. H. M. Besfat, D. J. Gelmecha, and R. S. Singh, "Literature review on QRS detection, Spectral and Non-linear Analysis of ECG Signals using Machine Learning," (Status:, **Under process**)

REFERENCES

Abdar, M., Książek, W., Acharya, U. R., Tan, R.-S., Makarenkov, V., and Pławiak, P. (2019). A new machine learning technique for an accurate diagnosis of coronary artery disease. *Computer methods and programs in biomedicine*, 179:104992.

Acharya, R., Kannathal, N., and Krishnan, S. (2004). Comprehensive analysis of cardiac health using heart rate signals. *Physiological measurement*, 25(5):1139.

Acharya, U., Faust, O., Sree, V., and Swapna, G. (2014). Linear and nonlinear analysis of normal and cad-affected heart rate signals. *Computer Methods and Programs in Biomedicine*, 113(1):55–68.

Acharya, U., Joseph, K., Kannathal, N., Lim, C., and Suri, J. (2006). Heart rate variability: A review. *Medical and Biological Engineering and Computing*, 44(12):1031–1051.

Acharya, U. R., Faust, O., Kadri, N. A., Suri, J. S., and Yu, W. (2013). Automated identification of normal and diabetes heart rate signals using nonlinear measures. *Computers in biology and medicine*, 43(10):1523–1529.

Acharya, U. R., Fujita, H., Adam, M., Lih, O. S., Sudarshan, V. K., Hong, T. J., Koh, J. E., Hagiwara, Y., Chua, C. K., Poo, C. K., et al. (2017a). Automated characterization and classification of coronary artery disease and myocardial infarction by decomposition of ecg signals: A comparative study. *Information Sciences*, 377:17–29.

Acharya, U. R., Fujita, H., Sudarshan, V. K., Lih Oh, S., Muhammad, A., Koh, J. E., Hong Tan, J., Chua, C. K., Poo Chua, K., and San Tan, R. (2017b). Application of empirical mode decomposition (emd) for automated identification of congestive heart failure using heart rate signals. *Neural Computing and Applications*, 28:3073–3094.

Acharya, U. R., Fujita, H., Sudarshan, V. K., Oh, S. L., Adam, M., Koh, J. E., Tan, J. H., Ghista, D. N., Martis, R. J., Chua, C. K., et al. (2016). Automated detection and localization of myocardial infarction using electrocardiogram: a comparative study of different leads. *Knowledge-Based Systems*, 99:146–156.

Acharya, U. R., Krishnan, S. M., Spaan, J. A., and Suri, J. S. (2007). *Advances in cardiac signal processing*, volume 8. Springer.

Adamczyk, K. and Polak, A. G. (2025). Online algorithm for deriving heart rate variability components and their time–frequency analysis. *Applied Sciences*, 15(3):1210.

Adnane, M., Jiang, Z., and Choi, S. (2009). Development of qrs detection algorithm designed for wearable cardiorespiratory system. *Computer methods and programs in biomedicine*, 93(1):20–31.

Afonso, V. X., Tompkins, W. J., Nguyen, T. Q., and Luo, S. (1999). Ecg beat detection using filter banks. *IEEE transactions on biomedical engineering*, 46(2):192–202.

Aggarwal, R. and Kumar, S. (2022). Hrv based feature selection for congestive heart failure and normal sinus rhythm for meticulous presaging of heart disease using machine learning. *Measurement: Sensors*, 24:100573.

Agrawal, S., Nijs, K., Subramaniam, S., Englesakis, M., Venkatraghavan, L., and Chowdhury, T. (2024). Predictor role of heart rate variability in subarachnoid hemorrhage: A systematic review. *Journal of Clinical Monitoring and Computing*, 38(1):177–185.

Ahamad, S. (2023). A low-cost methodology for developing personal health monitoring devices to examine psychological states and the impact of exercises. *International Journal of Information Technology*, pages 1–13.

Ahmed, A. A., Ali, W., Abdullah, T. A., and Malebary, S. J. (2023). Classifying cardiac arrhythmia from ecg signal using 1d cnn deep learning model. *Mathematics*, 11(3):562.

Akella, A. and Akella, S. (2021). Machine learning algorithms for predicting coronary artery disease: efforts toward an open source solution. *Future science OA*, 7(6):FSO698.

Akselrod, S., Gordon, D., Madwed, J., Snidman, N., Shannon, D., and Cohen, R. (1985). Hemodynamic regulation: investigation by spectral analysis. *The American journal of physiology*, 249(4 Pt 2):H867–H875.

Akselrod, S., Gordon, D., Ubel, F. A., Shannon, D. C., Berger, A. C., and Cohen, R. J. (1981). Power spectrum analysis of heart rate fluctuation: a quantitative probe of beat-to-beat cardiovascular control. *science*, 213(4504):220–222.

Alghamdi, A., Hammad, M., Ugail, H., Abdel-Raheem, A., Muhammad, K., Khalifa, H. S., and Abd El-Latif, A. A. (2024). Detection of myocardial infarction based on novel deep transfer learning methods for urban healthcare in smart cities. *Multimedia tools and applications*, pages 1–22.

Alghoul, K., Alharthi, S., Al Osman, H., and El Saddik, A. (2017a). Heart rate variability extraction from videos signals: Ica vs. evm comparison. *IEEE Access*, 5:4711–4719.

Alghoul, K., Alharthi, S., Al Osman, H., and El Saddik, A. (2017b). Heart rate variability extraction from videos signals: Ica vs. evm comparison. *IEEE Access*, 5:4711–4719.

Altan, G., Kutlu, Y., and Allahverdi, N. (2016). A new approach to early diagnosis of congestive heart failure disease by using hilbert–huang transform. *Computer methods and programs in biomedicine*, 137:23–34.

Alves, D. K., Costa, F. B., de Araujo Ribeiro, R. L., de Sousa Neto, C. M., and Rocha, T. d. O. A. (2016). Real-time power measurement using the maximal overlap discrete wavelet-packet transform. *IEEE Transactions on Industrial Electronics*, 64(4):3177–3187.

Aoki, K., Stephens, D., and Johnson, J. (2001). Diurnal variation in cutaneous vasodilator and vasoconstrictor systems during heat stress. *American Journal of Physiology-Regulatory, Integrative and Comparative Physiology*, 281(2):R591–R595.

Arco, J. E., Gallego-Molina, N. J., Ortiz, A., Arroyo-Alvis, K., and López-Pérez, P. J. (2024). Identifying hrv patterns in ecg signals as early markers of dementia. *Expert Systems with Applications*, 243:122934.

Arvind, S., Maheshkumar, K., Vaishali, S., Lavanya, S., and Padmavathi, R. (2020). Development and validation of an integrated portable heart rate variability (hrv) analysis system–streme. *Medical Hypotheses*, 143:109887.

Attar, E. T., Balasubramanian, V., Subasi, E., and Kaya, M. (2021). Stress analysis based on simultaneous heart rate variability and eeg monitoring. *IEEE Journal of Translational Engineering in Health and Medicine*, 9:1–7.

Auger, F. and Flandrin, P. (1995). Improving the readability of time-frequency and time-scale representations by the reassignment method. *IEEE Transactions on signal processing*, 43(5):1068–1089.

Auger, F., Flandrin, P., Lin, Y.-T., McLaughlin, S., Meignen, S., Oberlin, T., and Wu, H.-T. (2013). Time-frequency reassignment and synchrosqueezing: An overview. *IEEE Signal Processing Magazine*, 30(6):32–41.

Aurobinda, A., Mohanty, B. P., and Mohanty, M. N. (2016). R-peak detection of ecg using adaptive thresholding. In *2016 International Conference on Communication and Signal Processing (ICCSP)*, pages 0284–0287. IEEE.

Aygun, A., Ghasemzadeh, H., and Jafari, R. (2019). Robust interbeat interval and heart rate variability estimation method from various morphological features using wearable sensors. *IEEE Journal of Biomedical and Health Informatics*, 24(8):2238–2250.

Azuaje, F., Dubitzky, W., and Lopes, P. (1999). Predicting coronary disease risk based on short-term rr interval measurements: A neural network approach. *Artificial Intelligence in Medicine*, 15(3):275–297.

Baghdadi, N. A., Farghaly Abdelaliem, S. M., Malki, A., Gad, I., Ewis, A., and Atlam, E. (2023). Advanced machine learning techniques for cardiovascular disease early detection and diagnosis. *Journal of Big Data*, 10(1):144.

Bai, Q. (2010). Analysis of particle swarm optimization algorithm. *Computer and information science*, 3(1):180.

Bakiya, A., Kamalanand, K., Rajinikanth, V., Nayak, R. S., and Kadry, S. (2020). Deep neural network assisted diagnosis of time-frequency transformed electromyograms. *Multimedia Tools and Applications*, 79(15):11051–11067.

Barbieri, R., Triedman, J., and Saul, J. (2002). Heart rate control and mechanical cardiopulmonary coupling to assess central volume: a systems analysis. *American Journal of Physiology-Regulatory, Integrative and Comparative Physiology*, 283(5):R1210–R1220.

Barua, P. D., Aydemir, E., Dogan, S., Kobat, M. A., Demir, F. B., Baygin, M., Tuncer, T., Oh, S. L., Tan, R.-S., and Acharya, U. R. (2023). Multilevel hybrid accurate handcrafted model for myocardial infarction classification using ecg signals. *International Journal of Machine Learning and Cybernetics*, 14(5):1651–1668.

Bayram, I. (2012). An analytic wavelet transform with a flexible time-frequency covering. *IEEE Transactions on Signal Processing*, 61(5):1131–1142.

Beheshti, M., Umapathy, K., and Krishnan, S. (2016). Electrophysiological cardiac modeling: a review. *Critical Reviews™ in Biomedical Engineering*, 44(1-2).

Belkadi, M. A. and Daamouche, A. (2021). A robust qrs detection approach using stationary wavelet transform. *Multimedia Tools and Applications*, 80(15):22843–22864.

Benjamin, E. J., Virani, S. S., Callaway, C. W., Chamberlain, A. M., Chang, A. R., Cheng, S., Chiuve, S. E., Cushman, M., Delling, F. N., Deo, R., et al. (2018). Heart disease and stroke statistics—2018 update: a report from the american heart association. *Circulation*, 137(12):e67–e492.

Berntson, G., Thomas, B., Eckberg, D., and Grossman, P. (1997). Heart rate variability: Origins, methods, and interpretive caveats. *Psychophysiology*, 34(6):623–648.

Besfat, H. M., Gelmecha, D. J., and Singh, R. S. (2024a). Delineation of qrs features and denoising of ecg signal using fejer korovkin wavelet. *International Journal of Information Technology*, 16(5):3027–3031.

Besfat, H. M., Gelmecha, D. J., Singh, R. S., Rathee, D. S., Arora, A., Teka, B. A., Belete, B. A., and Warse, E. T. (2024b). Spectral analysis of congestive heart failure cardiac disease using flexible analytic wavelet transform. In *2024 11th International Conference on Computing for Sustainable Global Development (INDIACom)*, pages 1455–1460. IEEE.

Beyramienanlou, H. (2021). A robust method to reliable cardiac qrs complex detection based on shannon energy and teager energy operator. *Circuits, Systems, and Signal Processing*, 40(2):980–992.

Borah, B. B., Das, K., Hazarika, U., and Roy, S. (2024). A deep knowledge distillation heartcare framework for detection of multi-label myocardial infarction from multi-lead ecg signals. *SN Computer Science*, 6(1):14.

Braga, A., da Silva Lemos, M., da Silva, J., Fontes, W., and dos Santos, R. (2002). Effects of angiotensins on day-night fluctuations and stress-induced changes in blood pressure. *American Journal of Physiology-Regulatory, Integrative and Comparative Physiology*, 282(6):R1663–R1671.

Breiman, L. (2001). Random forests. *Machine learning*, 45:5–32.

Brillinger, D. R. (2001). *Time Series: Data Analysis and Theory*. University of California at Berkeley, Berkeley, California, 2nd edition.

Brown, T., Beightol, L., Koh, J., and Eckberg, D. (1993). Important influence of respiration on human r-r interval power spectra is largely ignored. *Journal of Applied Physiology*, 75(5):2310–2317.

Cao, H., Peyrodie, L., et al. (2023). Variational mode decomposition-based simultaneous r peak detection and noise suppression for automatic ecg analysis. *IEEE Sensors Journal*, 23(8):8703–8713.

Cao, W., Ming, Z., Xu, Z., Zhang, J., and Wang, Q. (2019). Online sequential extreme learning machine with dynamic forgetting factor. *IEEE access*, 7:179746–179757.

Castiglioni, P., Coruzzi, P., Bini, M., Parati, G., and Faini, A. (2017). Multiscale sample entropy of cardiovascular signals: does the choice between fixed-or varying-tolerance among scales influence its evaluation and interpretation? *Entropy*, 19(11):590.

Cesari, M., Mehlsen, J., Mehlsen, A.-B., and Sorensen, H. B. D. (2017). A new wavelet-based ecg delineator for the evaluation of the ventricular innervation. *IEEE journal of translational engineering in health and medicine*, 5:1–15.

Chen, C.-L. and Chuang, C.-T. (2017). A qrs detection and r point recognition method for wearable single-lead ecg devices. *Sensors*, 17(9):1969.

Chen, H., Hu, S., Hua, R., and Zhao, X. (2021a). Improved naive bayes classification algorithm for traffic risk management. *EURASIP Journal on Advances in Signal Processing*, 2021(1):30.

Chen, H. and Maharatna, K. (2020). An automatic r and t peak detection method based on the combination of hierarchical clustering and discrete wavelet transform. *IEEE Journal of Biomedical and Health Informatics*, 24(10):2825–2832.

Chen, S., Webb, G. I., Liu, L., and Ma, X. (2020). A novel selective naïve bayes algorithm. *Knowledge-Based Systems*, 192:105361.

Chen, X., Guo, W., Zhao, L., Huang, W., Wang, L., Sun, A., Li, L., and Mo, F. (2021b). Acute myocardial infarction detection using deep learning-enabled electrocardiograms. *Frontiers in cardiovascular medicine*, 8:654515.

Chen, X., Shen, T., Hao, Y., Zhang, J., and Xie, P. (2024). Global synchronization of functional corticomuscular coupling under precise grip tasks using multichannel eeg and emg signals. *Cognitive Neurodynamics*, pages 1–14.

Christov, I. I. (2004). Real time electrocardiogram qrs detection using combined adaptive threshold. *Biomedical engineering online*, 3:1–9.

Chui, K. T., Tsang, K. F., Wu, C. K., Hung, F. H., Chi, H. R., Chung, H. S.-h., Man, K. F., and Ko, K. T. (2015). Cardiovascular diseases identification using electrocardiogram health identifier based on multiple criteria decision making. *Expert Systems with Applications*, 42(13):5684–5695.

Clariá, F., Vallverdú, M., Baranowski, R., Chojnowska, L., and Caminal, P. (2000). Time-frequency analysis of the rt and rr variability to stratify hypertrophic cardiomyopathy patients. *Computers and Biomedical Research*, 33(6):416–430.

Colak, O. H. (2009). Preprocessing effects in time–frequency distributions and spectral analysis of heart rate variability. *Digital Signal Processing*, 19(4):731–739.

Costa, M., Goldberger, A. L., and Peng, C.-K. (2002). Multiscale entropy analysis of complex physiologic time series. *Physical review letters*, 89(6):068102.

Costa, M., Goldberger, A. L., and Peng, C.-K. (2005). Multiscale entropy analysis of biological signals. *Physical Review E—Statistical, Nonlinear, and Soft Matter Physics*, 71(2):021906.

Dalmeida, K. M. and Masala, G. L. (2021). Hrv features as viable physiological markers for stress detection using wearable devices. *Sensors*, 21(8):2873.

Das, M. and Ari, S. (2013). Analysis of ecg signal denoising method based on s-transform. *Irbm*, 34(6):362–370.

De Giovanni, E., Teijeiro, T., Millet, G. P., and Atienza, D. (2022). Adaptive r-peak detection on wearable ecg sensors for high-intensity exercise. *IEEE Transactions on Biomedical Engineering*, 70(3):941–953.

de Lannoy, G., Frénay, B., Verleysen, M., and Delbeke, J. (2009). Supervised ecg delineation using the wavelet transform and hidden markov models. In *4th European Conference of the International Federation for Medical and Biological Engineering: ECIFMBE 2008 23–27 November 2008 Antwerp, Belgium*, pages 22–25. Springer.

Degerli, A., Zabihi, M., Kiranyaz, S., Hamid, T., Mazhar, R., Hamila, R., and Gabbouj, M. (2021). Early detection of myocardial infarction in low-quality echocardiography. *IEEE Access*, 9:34442–34453.

Deka, D. and Deka, B. (2021). Stratification of high-risk hypertensive patients using hybrid heart rate variability features and boosting algorithms. *IEEE Access*, 9:62665–62675.

Deka, D. and Deka, B. (2023). Detection of meditation-induced hrv dynamics using averaging technique-based oversampled feature set and machine learning classifiers. *IEEE Access*, 11:29576–29590.

Dhyani, S., Kumar, A., Choudhury, S., Verma, C., and Illés, Z. (2025). Assessing ecg-qrs signal detection algorithm chip and simulation on several fpgas. *Discover Computing*, 28(1):13.

Diker, A., Cömert, Z., Avci, E., and Velappan, S. (2018). Intelligent system based on genetic algorithm and support vector machine for detection of myocardial infarction from ecg signals. In *2018 26th Signal processing and communications applications conference (SIU)*, pages 1–4. Ieee.

Dilaveris, P. E., Pantazis, A., Zervopoulos, G., Tzannetis, G., Kallikazaros, J., Stefanadis, C., and Toutouzas, P. K. (2003). Differences in the morphology and duration between premature p waves and the preceding sinus complexes in patients with a history of paroxysmal atrial fibrillation. *Clinical Cardiology: An International Indexed and Peer-Reviewed Journal for Advances in the Treatment of Cardiovascular Disease*, 26(7):341–347.

Djoussé, L., Hopkins, P. N., North, K. E., Pankow, J. S., Arnett, D. K., and Ellison, R. C. (2011). Chocolate consumption is inversely associated with prevalent coronary heart disease:

the national heart, lung, and blood institute family heart study. *Clinical Nutrition*, 30(2):182–187.

Dohare, A. K., Kumar, V., and Kumar, R. (2018). Detection of myocardial infarction in 12 lead ecg using support vector machine. *Applied Soft Computing*, 64:138–147.

Dou, C., Wu, D., Yue, D., Jin, B., and Xu, S. (2020). A hybrid method for false data injection attack detection in smart grid based on variational mode decomposition and os-elm. *CSEE Journal of Power and Energy Systems*, 8(6):1697–1707.

Durrer, D. (1968). Electrical aspects of human cardiac activity: a clinical-physiological approach to excitation and stimulation. *Cardiovascular Research*, 2(1):1–18.

Ebrahimzadeh, E., Fayaz, F., Ahmadi, F., and Dolatabad, M. R. (2018). Linear and nonlinear analyses for detection of sudden cardiac death (scd) using ecg and hrv signals. *Trends Res*, 1(1):1–8.

Eckberg, D. (1983). Human sinus arrhythmia as an index of vagal cardiac outflow. *Journal of Applied Physiology*, 54(4):961–966.

Eckberg, D. (1985). Human respiratory-cardiovascular interactions in health and disease. In *Cardiorespiratory and Motor Coordination*, pages 253–258. Springer.

Eguchi, K. and Aoki, R. (2023). Practical rr interval editing for heart rate variability analysis using single-channel wearable ecg devices. *IEEE Access*, 11:25543–25582.

El Bouny, L., Khalil, M., and Adib, A. (2020). A wavelet denoising and teager energy operator-based method for automatic qrs complex detection in ecg signal. *Circuits, Systems, and Signal Processing*, 39(10):4943–4979.

Electrophysiology, T. F. o. t. E. S. o. C. t. N. A. S. o. P. (1996). Heart rate variability: standards of measurement, physiological interpretation, and clinical use. *Circulation*, 93(5):1043–1065.

Elgendi, M. (2013). Fast qrs detection with an optimized knowledge-based method: Evaluation on 11 standard ecg databases. *PloS one*, 8(9):e73557.

Elgendi, M., Eskofier, B., and Abbott, D. (2015). Fast t wave detection calibrated by clinical knowledge with annotation of p and t waves. *Sensors*, 15(7):17693–17714.

Elgendi, M., Meo, M., and Abbott, D. (2016). A proof-of-concept study: Simple and effective detection of p and t waves in arrhythmic ecg signals. *Bioengineering*, 3(4):26.

Eltrass, A. S., Tayel, M. B., and Ammar, A. I. (2021). A new automated cnn deep learning approach for identification of ecg congestive heart failure and arrhythmia using constant-q non-stationary gabor transform. *Biomedical signal processing and control*, 65:102326.

Estévez, M., Machado, C., Leisman, G., Estévez-Hernández, T., Arias-Morales, A., Machado, A., and Montes-Brown, J. (2016). Spectral analysis of heart rate variability. *International Journal on Disability and Human Development*, 15(1):5–17.

Fan, J. and Watanabe, T. (2022). Atherosclerosis: Known and unknown. *Pathology international*, 72(3):151–160.

Fang, R., Lu, C.-C., Chuang, C.-T., and Chang, W.-H. (2022). A visually interpretable detection method combines 3-d ecg with a multi-vgg neural network for myocardial infarction identification. *Computer Methods and Programs in Biomedicine*, 219:106762.

Farashi, S. (2016). A multiresolution time-dependent entropy method for qrs complex detection. *Biomedical Signal Processing and Control*, 24:63–71.

Faust, O. and Acharya, U. R. (2021). Automated classification of five arrhythmias and normal sinus rhythm based on rr interval signals. *Expert Systems with Applications*, 181:115031.

Feng, K., Pi, X., Liu, H., and Sun, K. (2019). Myocardial infarction classification based on convolutional neural network and recurrent neural network. *Applied Sciences*, 9(9):1879.

Flandrin, P., Auger, F., and Chassande-Mottin, E. (2018). Time-frequency reassignment: from principles to algorithms. In *Applications in time-frequency signal processing*, pages 179–204. CRC Press.

Force, T. (1996). Standards of measurement, physiological interpretation and clinical use. task force of the european society of cardiology and the north american society of pacing and electrophysiology. *Circulation*, 93(5):1043–1065.

Friganovic, K., Kukolja, D., Jovic, A., Cifrek, M., and Krstacic, G. (2018). Optimizing the detection of characteristic waves in ecg based on processing methods combinations. *IEEE access*, 6:50609–50626.

Fujiwara, K., Abe, E., Kamata, K., Nakayama, C., Suzuki, Y., Yamakawa, T., Hiraoka, T., Kano, M., Sumi, Y., Masuda, F., et al. (2018). Heart rate variability-based driver drowsiness detection and its validation with eeg. *IEEE Transactions on Biomedical Engineering*, 66(6):1769–1778.

Furuichi, S. (2005). On uniqueness theorems for tsallis entropy and tsallis relative entropy. *IEEE Transactions on Information Theory*, 51(10):3638–3645.

Gad, A. G. (2022). Particle swarm optimization algorithm and its applications: a systematic review. *Archives of computational methods in engineering*, 29(5):2531–2561.

Geng, D.-Y., Zhao, J., Wang, C.-X., and Ning, Q. (2020). A decision support system for automatic sleep staging from hrv using wavelet packet decomposition and energy features. *Biomedical Signal Processing and Control*, 56:101722.

Ghaffari, A., Homaeinezhad, M., Akraminia, M., Atarod, M., and Daevaeiha, M. (2009). A robust wavelet-based multi-lead electrocardiogram delineation algorithm. *Medical engineering & physics*, 31(10):1219–1227.

Giri, D., Acharya, U., and Martis, R. (2013). Automated diagnosis of coronary artery disease affected patients using lda, pca, ica and discrete wavelet transform. *Knowledge-Based Systems*, 37:274–282.

Go, A., Mozaffarian, D., Roger, V., Benjamin, E., et al. (2013). Heart disease and stroke statistics-2013 update: A report from the american heart association. *Circulation*, 127(1):e6–e245.

Goldberger, A. L., Amaral, L. A., Glass, L., Hausdorff, J. M., Ivanov, P. C., Mark, R. G., Mietus, J. E., Moody, G. B., Peng, C.-K., and Stanley, H. E. (2000a). Physiobank, physiotoolkit, and physionet: components of a new research resource for complex physiologic signals. *Circulation*, 101(23):e215–e220.

Goldberger, A. L., Amaral, L. A., Glass, L., Hausdorff, J. M., Ivanov, P. C., Mark, R. G., Mietus, J. E., Moody, G. B., Peng, C.-K., and Stanley, H. E. (2000b). Physiobank, physiotoolkit, and physionet: components of a new research resource for complex physiologic signals. *circulation*, 101(23):e215–e220.

Greenhill, S., Rana, S., Gupta, S., Vellanki, P., and Venkatesh, S. (2020). Bayesian optimization for adaptive experimental design: A review. *IEEE access*, 8:13937–13948.

Guede-Fernandez, F., Ferrer-Mileo, V., Mateu-Mateus, M., Ramos-Castro, J., García-González, M. Á., and Fernández-Chimeno, M. (2020). A photoplethysmography smartphone-based method for heart rate variability assessment: Device model and breathing influences. *Biomedical Signal Processing and Control*, 57:101717.

Guerrero-Mendez, C. D., Blanco-Diaz, C. F., Rivera-Flor, H., De Souza, A. F., Jaramillo-Isaza, S., Ruiz-Olaya, A. F., and Bastos-Filho, T. F. (2023). Coupling effects of cross-corticomuscular association during object manipulation tasks on different haptic sensations. *NeuroSci*, 4(3):195–210.

Guerrero-Mendez, C. D. and Ruiz-Olaya, A. F. (2022). Coherence-based connectivity analysis of eeg and emg signals during reach-to-grasp movement involving two weights. *Brain-Computer Interfaces*, 9(3):140–154.

Gupta, V., Mittal, M., and Mittal, V. (2020). R-peak detection based chaos analysis of ecg signal. *Analog Integrated Circuits and Signal Processing*, 102:479–490.

Gupta, V., Priya, T., Yadav, A. K., Pachori, R. B., and Acharya, U. R. (2017). Automated detection of focal eeg signals using features extracted from flexible analytic wavelet transform. *Pattern Recognition Letters*, 94:180–188.

Habibi, Z., Karimizadeh, K., Nosratpour, A., and Alipourfard, I. (2024). Enhanced qrs detection and ecg compression using adaptive thresholding: a real-time approach for improved monitoring and diagnosis. *Computers and Electrical Engineering*, 119:109528.

Hamilton, P. S. and Tompkins, W. J. (1986). Quantitative investigation of qrs detection rules using the mit/bih arrhythmia database. *IEEE transactions on biomedical engineering*, (12):1157–1165.

Hammad, M., Alkinani, M. H., Gupta, B. B., and Abd El-Latif, A. A. (2022). Myocardial infarction detection based on deep neural network on imbalanced data. *Multimedia Systems*, pages 1–13.

Han, C. and Shi, L. (2019). Automated interpretable detection of myocardial infarction fusing energy entropy and morphological features. *Computer methods and programs in biomedicine*, 175:9–23.

Hao, Z., Zhang, X., and Lai, Z. (2022). Adaptive r-peak detection algorithm based on brown exponential smoothing model. *IEEE access*, 10:114355–114363.

Harper, K. and Armelagos, G. (2010). The changing disease-scape in the third epidemiological transition. *International journal of environmental research and public health*, 7(2):675–697.

He, D., Cao, H., Wang, S., and Chen, X. (2019). Time-reassigned synchrosqueezing transform: The algorithm and its applications in mechanical signal processing. *Mechanical Systems and Signal Processing*, 117:255–279.

He, R., Liu, Y., Wang, K., Zhao, N., Yuan, Y., Li, Q., and Zhang, H. (2020). Automatic detection of qrs complexes using dual channels based on u-net and bidirectional long short-term memory. *IEEE Journal of Biomedical and Health Informatics*, 25(4):1052–1061.

He, R., Wang, K., Li, Q., Yuan, Y., Zhao, N., Liu, Y., and Zhang, H. (2017). A novel method for the detection of r-peaks in ecg based on k-nearest neighbors and particle swarm optimization. *EURASIP Journal on Advances in Signal Processing*, 2017:1–14.

Homaeinezhad, M. R., ErfanianMoshiri-Nejad, M., and Naseri, H. (2014). A correlation analysis-based detection and delineation of ecg characteristic events using template waveforms extracted by ensemble averaging of clustered heart cycles. *Computers in biology and medicine*, 44:66–75.

Honi, D. G. and Szathmary, L. (2024). A one-dimensional convolutional neural network-based deep learning approach for predicting cardiovascular diseases. *Informatics in Medicine Unlocked*, 49:101535.

Hossain, M. B., Bashar, S. K., Walkey, A. J., McManus, D. D., and Chon, K. H. (2019). An accurate qrs complex and p wave detection in ecg signals using complete ensemble empirical mode decomposition with adaptive noise approach. *IEEE Access*, 7:128869–128880.

Hou, Z., Dong, Y., Xiang, J., Li, X., and Yang, B. (2018). A real-time qrs detection method based on phase portraits and box-scoring calculation. *IEEE Sensors Journal*, 18(9):3694–3702.

Howorka, K., Pumprla, J., Tamm, J., Schabmann, A., Klomfar, S., Kostineak, E., Howorka, N., and Sovova, E. (2013). Effects of guided breathing on blood pressure and heart rate variability in hypertensive diabetic patients. *Autonomic Neuroscience*, 179(1-2):131–137.

Hsu, C. F., Wei, S.-Y., Huang, H.-P., Hsu, L., Chi, S., and Peng, C.-K. (2017). Entropy of entropy: Measurement of dynamical complexity for biological systems. *Entropy*, 19(10):550.

Hu, M. and Liang, H. (2011). Intrinsic mode entropy based on multivariate empirical mode decomposition and its application to neural data analysis. *Cognitive Neurodynamics*, 5:277–284.

Huang, H., Chan, H., Lin, P., Wu, C., and Huang, C. (1997). Time-frequency spectral analysis of heart rate variability during induction of general anaesthesia. *British Journal of Anaesthesia*, 79(6):754–758.

Humeau-Heurtier, A. (2015). The multiscale entropy algorithm and its variants: A review. *Entropy*, 17(5):3110–3123.

Hurst, J. W. (2006). The value of using the entire new york heart association's classification of heart and vascular disease. *Clinical Cardiology: An International Indexed and Peer-Reviewed Journal for Advances in the Treatment of Cardiovascular Disease*, 29(9):415–417.

Hussain, L., Aziz, W., Khan, I. R., Alkinani, M. H., and Alowibdi, J. S. (2021). Machine learning based congestive heart failure detection using feature importance ranking of multimodal features. *Math Biosci Eng*, 18(1):69–91.

INEGI (2014). Instituto nacional de estadística y geografía (méxico).

Injadat, M., Salo, F., Nassif, A. B., Essex, A., and Shami, A. (2018). Bayesian optimization with machine learning algorithms towards anomaly detection. In *2018 IEEE global communications conference (GLOBECOM)*, pages 1–6. IEEE.

Isler, Y. (2016). Discrimination of systolic and diastolic dysfunctions using multi-layer perceptron in heart rate variability analysis. *Computers in biology and medicine*, 76:113–119.

İşler, Y. and Kuntalp, M. (2007). Combining classical hrv indices with wavelet entropy measures improves to performance in diagnosing congestive heart failure. *Computers in biology and medicine*, 37(10):1502–1510.

Isler, Y., Narin, A., Ozer, M., and Perc, M. (2019). Multi-stage classification of congestive heart failure based on short-term heart rate variability. *Chaos, Solitons & Fractals*, 118:145–151.

Iyengar, N., Peng, C., Morin, R., Goldberger, A. L., and Lipsitz, L. A. (1996). Age-related alterations in the fractal scaling of cardiac interbeat interval dynamics. *American Journal of Physiology-Regulatory, Integrative and Comparative Physiology*, 271(4):R1078–R1084.

Jaafar, H., Ramli, N. H., and Nasir, A. S. A. (2018). An improvement to the k-nearest neighbor classifier for ecg database. In *IOP Conference Series: Materials Science and Engineering*, volume 318, page 012046. IOP Publishing.

Jahmunah, V., Ng, E. Y. K., San, T. R., and Acharya, U. R. (2021). Automated detection of coronary artery disease, myocardial infarction and congestive heart failure using gaborcnn model with ecg signals. *Computers in biology and medicine*, 134:104457.

Jain, P., Deshmukh, A., and Padole, H. (2024). Design of an integrated myocardial infarction detection model using ecg connectivity features and multivariate time series classification. *IEEE Access*, 12:9070–9081.

Jain, S., Ahirwal, M., Kumar, A., Bajaj, V., and Singh, G. K. (2017). Qrs detection using adaptive filters: A comparative study. *ISA transactions*, 66:362–375.

Javeed, A., Khan, S. U., Ali, L., Ali, S., Imrana, Y., and Rahman, A. (2022). Machine learning-based automated diagnostic systems developed for heart failure prediction using different types of data modalities: a systematic review and future directions. *Computational and Mathematical Methods in Medicine*, 2022.

Javorka, M., Trunkvalterova, Z., Tonhajzerova, I., Javorkova, J., Javorka, K., and Baumert, M. (2008). Short-term heart rate complexity is reduced in patients with type 1 diabetes mellitus. *Clinical Neurophysiology*, 119(5):1071–1081.

Jayanthi, S. et al. (2023). Mental health status monitoring for people with autism spectrum disorder using machine learning. *International Journal of Information Technology*, pages 1–9.

Jia, M., Li, F., Wu, J., Chen, Z., and Pu, Y. (2020). Robust qrs detection using high-resolution wavelet packet decomposition and time-attention convolutional neural network. *IEEE Access*, 8:16979–16988.

Johnson, C. L., Paulose-Ram, R., Ogden, C. L., Carroll, M. D., Kruszan-Moran, D., Dohrmann, S. M., and Curtin, L. R. (2013). National health and nutrition examination survey. analytic guidelines, 1999-2010.

Jovic, A. and Bogunovic, N. (2011). Electrocardiogram analysis using a combination of statistical, geometric, and nonlinear heart rate variability features. *Artificial intelligence in medicine*, 51(3):175–186.

Jovic, A., Brkic, K., and Krstacic, G. (2019). Detection of congestive heart failure from short-term heart rate variability segments using hybrid feature selection approach. *Biomedical Signal Processing and Control*, 53:101583.

Joy, T. T., Rana, S., Gupta, S., and Venkatesh, S. (2016). Hyperparameter tuning for big data using bayesian optimisation. In *2016 23rd International Conference on Pattern Recognition (ICPR)*, pages 2574–2579. IEEE.

Jung, H., Yoo, H. J., Choi, P., Nashiro, K., Min, J., Cho, C., Thayer, J. F., Lehrer, P., and Mather, M. (2024). Changes in negative emotions across five weeks of hrv biofeedback intervention were mediated by changes in resting heart rate variability. *Applied Psychophysiology and Biofeedback*, pages 1–24.

Kamath, M., Fallen, E., and McKelvie, R. (1991). Effects of steady state exercise on the power spectrum of heart rate variability. *Medicine and Science in Sports and Exercise*, 23(4):428–434.

Karimipour, A. and Homaeinezhad, M. R. (2014). Real-time electrocardiogram p-qrs-t detection–delineation algorithm based on quality-supported analysis of characteristic templates. *Computers in biology and medicine*, 52:153–165.

Karimulla, S. and Patra, D. (2024). An optimal methodology for early prediction of sudden cardiac death using advanced heart rate variability features of ecg signal. *Arabian Journal for Science and Engineering*, 49(5):6725–6741.

Kathirvel, P., Sabarimalai Manikandan, M., Prasanna, S., and Soman, K. (2011). An efficient r-peak detection based on new nonlinear transformation and first-order gaussian differentiator. *Cardiovascular Engineering and Technology*, 2:408–425.

Keissar, K., Davrath, L. R., and Akselrod, S. (2009). Coherence analysis between respiration and heart rate variability using continuous wavelet transform. *Philosophical Transactions of the Royal Society A: Mathematical, Physical and Engineering Sciences*, 367(1892):1393–1406.

Khamis, H., Weiss, R., Xie, Y., Chang, C.-W., Lovell, N. H., and Redmond, S. J. (2016). Qrs detection algorithm for telehealth electrocardiogram recordings. *IEEE Transactions on Biomedical Engineering*, 63(7):1377–1388.

Kiliçarslan, S. (2023). Pso+ gwo: a hybrid particle swarm optimization and grey wolf optimization based algorithm for fine-tuning hyper-parameters of convolutional neural networks for cardiovascular disease detection. *Journal of Ambient Intelligence and Humanized Computing*, 14(1):87–97.

Kiranyaz, S., Avci, O., Abdeljaber, O., Ince, T., Gabbouj, M., and Inman, D. J. (2021). 1d convolutional neural networks and applications: A survey. *Mechanical systems and signal processing*, 151:107398.

Kitney, R. (1980). An analysis of the thermoregulatory influences on heart-rate variability. *The study of heart rate variability*, pages 81–113.

Kodama, T., Kamata, K., Fujiwara, K., Kano, M., Yamakawa, T., Yuki, I., and Murayama, Y. (2018). Ischemic stroke detection by analyzing heart rate variability in rat middle cerebral artery occlusion model. *IEEE Transactions on Neural Systems and Rehabilitation Engineering*, 26(6):1152–1160.

Koh, J., Brown, T., Beightol, L., Ha, C., and Eckberg, D. (1994). Human autonomic rhythms: vagal cardiac mechanisms in tetraplegic subjects. *The Journal of Physiology*, 474(3):483–495.

Kora, P. (2017). Ecg based myocardial infarction detection using hybrid firefly algorithm. *Computer methods and programs in biomedicine*, 152:141–148.

Kumar, M., Pachori, R. B., and Acharya, U. R. (2017). Automated diagnosis of myocardial infarction ecg signals using sample entropy in flexible analytic wavelet transform framework. *Entropy*, 19(9):488.

Kumar, R., Aggarwal, Y., and Nigam, V. K. (2023). Autonomic features in prediction of coronary artery disease and myocardial infarction. *IETE Journal of Research*, 69(11):8354–8361.

Kumari, C. U., Murthy, A. S. D., Prasanna, B. L., Reddy, M. P. P., and Panigrahy, A. K. (2021). An automated detection of heart arrhythmias using machine learning technique: Svm. *Materials Today: Proceedings*, 45:1393–1398.

Kurt, I., Ture, M., and Kurum, A. T. (2008). Comparing performances of logistic regression, classification and regression tree, and neural networks for predicting coronary artery disease. *Expert systems with applications*, 34(1):366–374.

Laguna, P., Mark, R. G., Goldberg, A., and Moody, G. B. (1997). A database for evaluation of algorithms for measurement of qt and other waveform intervals in the ecg. In *Computers in cardiology 1997*, pages 673–676. IEEE.

Lanfranchi, P. and Somers, V. (2002). Arterial baroreflex function and cardiovascular variability: interactions and implications. *American Journal of Physiology-Regulatory, Integrative and Comparative Physiology*, 283(4):R815–R826.

Lee, H., Noh, K., and Ryu, K. (2007). Mining biosignal data: coronary artery disease diagnosis using linear and nonlinear features of hrv. In *Pacific-Asia Conference on Knowledge Discovery and Data Mining*, pages 218–228. Springer.

Li, B. N., Dong, M. C., and Vai, M. I. (2010). On an automatic delineator for arterial blood pressure waveforms. *Biomedical Signal Processing and Control*, 5(1):76–81.

Li, C. (2022). An energy-concentrated synchrosqueezing transform using a reassignment operator for the analysis of nonstationary signals. *The International Journal of Advanced Manufacturing Technology*, 122(1):133–146.

Li, L., Cai, H., Han, H., Jiang, Q., and Ji, H. (2020a). Adaptive short-time fourier transform and synchrosqueezing transform for non-stationary signal separation. *Signal Processing*, 166:107231.

Li, S. (2020). Multifractal detrended fluctuation analysis of congestive heart failure disease based on constructed heartbeat sequence. *IEEE Access*, 8:205244–205249.

Li, Z., Gao, J., Li, H., Zhang, Z., Liu, N., and Zhu, X. (2020b). Synchroextracting transform: The theory analysis and comparisons with the synchrosqueezing transform. *Signal Processing*, 166:107243.

Libby, P. and Theroux, P. (2005). Pathophysiology of coronary artery disease. *Circulation*, 111(25):3481–3488.

Lin, C.-T., Chang, K.-C., Lin, C.-L., Chiang, C.-C., Lu, S.-W., Chang, S.-S., Lin, B.-S., Liang, H.-Y., Chen, R.-J., Lee, Y.-T., et al. (2010). An intelligent telecardiology system using a wearable and wireless ecg to detect atrial fibrillation. *IEEE transactions on information technology in biomedicine*, 14(3):726–733.

Liu, W., Zhang, M., Zhang, Y., Liao, Y., Huang, Q., Chang, S., Wang, H., and He, J. (2017). Real-time multilead convolutional neural network for myocardial infarction detection. *IEEE journal of biomedical and health informatics*, 22(5):1434–1444.

Liu, X., Wang, X., Zhou, X., and Jiang, A. (2018). Appropriate use of the increment entropy for electrophysiological time series. *Computers in biology and medicine*, 95:13–23.

Liu, Y., Wang, Y., and Zhang, J. (2012). New machine learning algorithm: Random forest. In *Information Computing and Applications: Third International Conference, ICICA 2012, Chengde, China, September 14-16, 2012. Proceedings 3*, pages 246–252. Springer.

Liu, Y., Xiang, H., Jiang, Z., and Xiang, J. (2023a). Refining the time–frequency characteristic of non-stationary signal for improving time–frequency representation under variable speeds. *Scientific Reports*, 13(1):5215.

Liu, Y., Xiang, H., Jiang, Z., and Xiang, J. (2023b). Refining the time–frequency characteristic of non-stationary signal for improving time–frequency representation under variable speeds. *Scientific Reports*, 13(1):5215.

Lu, H., Gao, H., Ye, M., and Wang, X. (2019). A hybrid ensemble algorithm combining adaboost and genetic algorithm for cancer classification with gene expression data. *IEEE/ACM transactions on computational biology and bioinformatics*, 18(3):863–870.

Lu, X., Pan, M., and Yu, Y. (2018). Qrs detection based on improved adaptive threshold. *Journal of healthcare engineering*, 2018(1):5694595.

Lui, H. W. and Chow, K. L. (2018). Multiclass classification of myocardial infarction with convolutional and recurrent neural networks for portable ecg devices. *Informatics in Medicine Unlocked*, 13:26–33.

Magagnin, V., Mauri, M., Cipresso, P., Mainardi, L., Brown, E. N., Cerutti, S., Villamira, M., and Barbieri, R. (2010). Heart rate variability and respiratory sinus arrhythmia assessment of affective states by bivariate autoregressive spectral analysis. In *2010 Computing in Cardiology*, pages 145–148. IEEE.

Magrupov, T., Talatov, Y., Magrupova, M., and Ripka, D. (2020). A technique for classifying the ecg signal into various possible states of the cardiovascular system. In *2020 IEEE International Conference on Electrical Engineering and Photonics (EExPolytech)*, pages 127–131. IEEE.

Mahananto, F., Anggraeni, W., and Astuti, N. D. (2024). Classification of congestive heart failure using artificial neural network based on higher-order moments detrended fluctuation analysis of heart rate variability. *Procedia Computer Science*, 234:614–621.

Mahesh, T., Dhilip Kumar, V., Vinoth Kumar, V., Asghar, J., Geman, O., Arulkumaran, G., and Arun, N. (2022). Adaboost ensemble methods using k-fold cross validation for survivability with the early detection of heart disease. *Computational Intelligence and Neuroscience*, 2022(1):9005278.

Malik, M. (1995). Geometrical methods for heart rate variability. *Heart rate variability*, 10(2):415–416.

Malik, M. (1997). Time-domain measurement of heart rate variability. *Cardiac Electrophysiology Review*, 3:329–334.

Malik, M., Bigger, J. T., Camm, A. J., Kleiger, R. E., Malliani, A., Moss, A. J., and Schwartz, P. J. (1996). Heart rate variability: Standards of measurement, physiological interpretation, and clinical use. *European heart journal*, 17(3):354–381.

Malik, M., Farrell, T., and Camm, A. (1990). Circadian rhythm of heart rate variability after acute myocardial infarction and its influence on the prognostic value of heart rate variability. *The American Journal of Cardiology*, 66:1049–1054.

Malliani, A., Pagani, M., and Lombardi, F. (1994). Physiology and clinical implications of variability of cardiovascular parameters with focus on heart rate and blood pressure. *The American Journal of Cardiology*, 73(10):3–9.

Malliani, A., Pagani, M., Lombardi, F., and Cerutti, S. (1991). Cardiovascular neural regulation explored in the frequency domain. *Circulation*, 84(2):482–492.

Malpas, S. (2002). Neural influences on cardiovascular variability: possibilities and pitfalls. *American Journal of Physiology-Heart and Circulatory Physiology*, 282(1):H6–H20.

Malpas, S. C. and Maling, T. J. (1990). Heart-rate variability and cardiac autonomic function in diabetes. *Diabetes*, 39(10):1177–1181.

Manis, G., Nikolopoulos, S., Alexandridi, A., and Davos, C. (2007). Assessment of the classification capability of prediction and approximation methods for hrv analysis. *Computers in Biology and Medicine*, 37(5):642–654.

Mansourian, N., Sarafan, S., Torkamani-Azar, F., Ghirmai, T., and Cao, H. (2023). Novel qrs detection based on the adaptive improved permutation entropy. *Biomedical Signal Processing and Control*, 80:104270.

Martin, H., Izquierdo, W., Cabrerizo, M., Cabrera, A., and Adjouadi, M. (2021). Near real-time single-beat myocardial infarction detection from single-lead electrocardiogram using long short-term memory neural network. *Biomedical Signal Processing and Control*, 68:102683.

Martin, S. S., Aday, A. W., Allen, N. B., Almarzooq, Z. I., Anderson, C. A., Arora, P., Avery, C. L., Baker-Smith, C. M., Bansal, N., Beaton, A. Z., et al. (2025). 2025 heart disease and stroke statistics: A report of us and global data from the american heart association. *Circulation*.

Martínez, A., Alcaraz, R., and Rieta, J. J. (2010). A new method for automatic delineation of ecg fiducial points based on the phasor transform. In *2010 Annual International Conference of the IEEE Engineering in Medicine and Biology*, pages 4586–4589. IEEE.

Martínez, J. P., Almeida, R., Olmos, S., Rocha, A. P., and Laguna, P. (2004). A wavelet-based ecg delineator: evaluation on standard databases. *IEEE Transactions on biomedical engineering*, 51(4):570–581.

Masetic, Z. and Subasi, A. (2016). Congestive heart failure detection using random forest classifier. *Computer methods and programs in biomedicine*, 130:54–64.

Meddah, K., Talha, M. K., Zairi, H., Nouah, M., Hadji, S., Ait, M. A., Bessekri, B., and Cherrih, H. (2020). Fpga implementation system for qrs complex detection. *Biomedical Engineering: Applications, Basis and Communications*, 32(01):2050005.

Melillo, P., Fusco, R., Sansone, M., Bracale, M., and Pecchia, L. (2011). Discrimination power of long-term heart rate variability measures for chronic heart failure detection. *Medical & biological engineering & computing*, 49:67–74.

Mendis, S., Thygesen, K., Kuulasmaa, K., Giampaoli, S., Mähönen, M., Ngu Blackett, K., Lisheng, L., and group on behalf of the participating experts of the WHO consultation for revision of WHO definition of myocardial infarction, W. (2011). World health organization

definition of myocardial infarction: 2008–09 revision. *International journal of epidemiology*, 40(1):139–146.

Merritt, C. and Tan, S. (2012). Willem einthoven (1860-1927): father of electrocardiography. *Singapore medical journal*, 53(1):17–18.

Mienye, I. D. and Jere, N. (2024). A survey of decision trees: Concepts, algorithms, and applications. *IEEE Access*.

Milagro, J., Gracia-Tabuenca, J., Seppä, V.-P., Karjalainen, J., Paassilta, M., Orini, M., Bailón, R., Gil, E., and Viik, J. (2019). Noninvasive cardiorespiratory signals analysis for asthma evolution monitoring in preschool children. *IEEE Transactions on Biomedical Engineering*, 67(7):1863–1871.

Modak, S., Taha, L. Y., and Abdel-Raheem, E. (2021). A novel method of qrs detection using time and amplitude thresholds with statistical false peak elimination. *IEEE Access*, 9:46079–46092.

Moghadam, S. R. and Asl, B. M. (2023). Automatic diagnosis and localization of myocardial infarction using morphological features of ecg signal. *Biomedical Signal Processing and Control*, 83:104671.

Mondhe, D. (2022). Cardiovascular disease detection using machine learning. In *International Conference on Advanced Communications and Machine Intelligence*, pages 243–252. Springer.

Moody, G. (2008). The physionet/computers in cardiology challenge 2008: T-wave alternans. In *2008 Computers in Cardiology*, pages 505–508.

Moody, G. B. and Mark, R. G. (2001). The impact of the mit-bih arrhythmia database. *IEEE engineering in medicine and biology magazine*, 20(3):45–50.

Moody, G. E. (2004). Spontaneous termination of atrial fibrillation: a challenge from physionet and computers in cardiology 2004. In *Computers in Cardiology, 2004*, pages 101–104. IEEE.

Moshawrab, M., Adda, M., Bouzouane, A., Ibrahim, H., and Raad, A. (2023). Predicting cardiovascular events with machine learning models and heart rate variability. *Int. J. Ubiquitous Syst. Pervasive Netw.(JUSPN)*, 18:49–59.

Moss, A. J. (1993). Measurement of the qt interval and the risk associated with qtc interval prolongation: a review. *The American journal of cardiology*, 72(6):B23–B25.

Moss, A. J. and Stern, S. (1996). Noninvasive electrocardiology: Clinical aspects of holter monitoring. *(No Title)*.

Moukadem, A., Bouguila, Z., Abdeslam, D. O., and Dieterlen, A. (2015). A new optimized stockwell transform applied on synthetic and real non-stationary signals. *Digital Signal Processing*, 46:226–238.

Mozaffarian, D., Benjamin, E. J., Go, A. S., Arnett, D. K., Blaha, M. J., Cushman, M., Das, S. R., De Ferranti, S., Després, J.-P., Fullerton, H. J., et al. (2016). Heart disease and stroke statistics—2016 update: a report from the american heart association. *circulation*, 133(4):e38–e360.

Muhammad, G., Naveed, S., Nadeem, L., Mahmood, T., Khan, A. R., Amin, Y., and Bahaj, S. A. O. (2023). Enhancing prognosis accuracy for ischemic cardiovascular disease using k nearest neighbor algorithm: a robust approach. *IEEE Access*.

Muhammad, L., Al-Shourbaji, I., Haruna, A. A., Mohammed, I. A., Ahmad, A., and Jibrin, M. B. (2021). Machine learning predictive models for coronary artery disease. *SN Computer Science*, 2(5):350.

Mulder, G. and Mulder, L. (1981). Information processing and cardiovascular control. *Psychophysiology*, 18(4):392–402.

Mulder, L. (1992). Measurement and analysis methods of heart rate and respiration for use in applied environments. *Biological Psychology*, 34(2–3):205–236.

Najarian, K. and Splinter, R. (2012). *Biomedical signal and image processing*. Taylor & Francis.

Narin, A., Isler, Y., and Ozer, M. (2014). Investigating the performance improvement of hrv indices in chf using feature selection methods based on backward elimination and statistical significance. *Computers in biology and medicine*, 45:72–79.

Nayak, C., Saha, S. K., Kar, R., and Mandal, D. (2019). An efficient and robust digital fractional order differentiator based ecg pre-processor design for qrs detection. *IEEE transactions on biomedical circuits and systems*, 13(4):682–696.

Nesaragi, N., Sharma, A., Patidar, S., and Acharya, U. R. (2022). Automated diagnosis of coronary artery disease using scalogram-based tensor decomposition with heart rate signals. *Medical Engineering & Physics*, 110:103811.

Nikolopoulos, S., Alexandridi, A., Nikolakeas, S., and Manis, G. (2003). Experimental analysis of heart rate variability of long-recording electrocardiograms in normal subjects and patients with coronary artery disease and normal left ventricular function. *Journal of Biomedical Informatics*, 36(3):202–217.

Novak, V. and Novak, P. (1993). Influence of respiration on heart rate and blood pressure fluctuations. *Journal of Applied Physiology*, 74(2):617–626.

Novak, V., Novak, P., DeMarchie, M., and Schondorf, R. (1995). The effect of severe brainstem injury on heart rate and blood pressure oscillations. *Clinical Autonomic Research*, 5(1):24–30.

Olhede, S. C. and Walden, A. T. (2002). Generalized morse wavelets. *IEEE Transactions on Signal Processing*, 50(11):2661–2670.

Organization, W. H. (2015). Who | cardiovascular diseases (cvds) factsheet no. 317. Accessed: 2025-04-08.

Orini, M., Bailón, R., Mainardi, L. T., Laguna, P., and Flandrin, P. (2011). Characterization of dynamic interactions between cardiovascular signals by time-frequency coherence. *IEEE transactions on biomedical engineering*, 59(3):663–673.

Orlandic, L., De Giovanni, E., Arza, A., Yazdani, S., Vesin, J.-M., and Atienza, D. (2019). Reward: Design, optimization, and evaluation of a real-time relative-energy wearable r-peak detection algorithm. In *2019 41st annual international conference of the IEEE engineering in medicine and biology society (EMBC)*, pages 3341–3347. IEEE.

Overton, J., Williams, T., Chambers, J., and Rashotte, M. (2001). Cardiovascular and metabolic responses to fasting and thermoneutrality are conserved in obese zucker rats. *American Journal of Physiology-Regulatory, Integrative and Comparative Physiology*, 280(4):R1007–R1015.

Padhy, S. and Dandapat, S. (2017). Third-order tensor based analysis of multilead ecg for classification of myocardial infarction. *Biomedical Signal Processing and Control*, 31:71–78.

Pan, J. and Tompkins, W. J. (1985). A real-time qrs detection algorithm. *IEEE transactions on biomedical engineering*, (3):230–236.

Panahi, F., Rashidi, S., and Sheikhani, A. (2021). Application of fractional fourier transform in feature extraction from electrocardiogram and galvanic skin response for emotion recognition. *Biomedical Signal Processing and Control*, 69:102863.

Pandit, D., Zhang, L., Liu, C., Chattopadhyay, S., Aslam, N., and Lim, C. P. (2017). A lightweight qrs detector for single lead ecg signals using a max-min difference algorithm. *Computer methods and programs in biomedicine*, 144:61–75.

Panjaitan, F., Nurmaini, S., and Partan, R. U. (2023). Accurate prediction of sudden cardiac death based on heart rate variability analysis using convolutional neural network. *Medicina*, 59(8):1394.

Parmar, N., Sirpal, P., Sikora, W. A., Dewald, J. P., Refai, H. H., and Yang, Y. (2024). Beta-band cortico-muscular phase coherence in hemiparetic stroke. *Biomedical Signal Processing and Control*, 97:106719.

Patel, V., Kantipudi, N., Jones, G., and Kamath, M. (2016). Air pollution and cardiovascular disease: A review. *Critical Reviews^{TM} in Biomedical Engineering*, 44(5):327–346.

Patidar, S., Pachori, R. B., and Acharya, U. R. (2015). Automated diagnosis of coronary artery disease using tunable-q wavelet transform applied on heart rate signals. *Knowledge-based systems*, 82:1–10.

Penaz, J. (1978). *Mayer waves: History and methodology*. Automedica.

Petrović, V. L., Janković, M. M., Lupšić, A. V., Mihajlović, V. R., and Popović-Božović, J. S. (2019). High-accuracy real-time monitoring of heart rate variability using 24 ghz continuous-wave doppler radar. *IEEE Access*, 7:74721–74733.

Pham, T. D. (2017). Time-shift multiscale entropy analysis of physiological signals. *Entropy*, 19(6):257.

Phukpattaranont, P. (2015). Qrs detection algorithm based on the quadratic filter. *Expert Systems with Applications*, 42(11):4867–4877.

Pichon, A., Roulaud, M., Antoine-Jonville, S., de Bisschop, C., and Denjean, A. (2006). Spectral analysis of heart rate variability: interchangeability between autoregressive analysis and fast fourier transform. *Journal of electrocardiology*, 39(1):31–37.

Poddar, M., Kumar, V., and Sharma, Y. (2013). Linear-nonlinear heart rate variability analysis and svm based classification of normal and hypertensive subjects. *Journal of Electrocardiology*, 46(4):e25.

Poddar, M. G., Kumar, V., and Sharma, Y. P. (2015). Automated diagnosis of coronary artery diseased patients by heart rate variability analysis using linear and non-linear methods. *Journal of medical engineering & technology*, 39(6):331–341.

Poli, R., Cagnoni, S., and Valli, G. (1995). Genetic design of optimum linear and nonlinear qrs detectors. *IEEE Transactions on Biomedical Engineering*, 42(11):1137–1141.

Pomeranz, B., Macaulay, R., Caudill, M. A., Kutz, I., Adam, D., Gordon, D., Kilborn, K. M., Barger, A. C., Shannon, D. C., and Cohen, R. J. (1985). Assessment of autonomic function in humans by heart rate spectral analysis. *American Journal of Physiology-Heart and Circulatory Physiology*, 248(1):H151–H153.

Porter, G. and Rivkees, S. (2001). Ontogeny of humoral heart rate regulation in the embryonic mouse. *American Journal of Physiology-Regulatory, Integrative and Comparative Physiology*, 281(2):R401–R407.

Porumb, M., Iadanza, E., Massaro, S., and Pecchia, L. (2020). A convolutional neural network approach to detect congestive heart failure. *Biomedical Signal Processing and Control*, 55:101597.

Prabhakaran, D., Yusuf, S., Mehta, S., Pogue, J., Avezum, A., Budaj, A., Cerumzynski, L., Flather, M., Fox, K., Hunt, D., et al. (2005). Two-year outcomes in patients admitted with non-st elevation acute coronary syndrome: results of the oasis registry 1 and 2. *Indian heart journal*, 57(3):217–225.

Prabhakararao, E. and Dandapat, S. (2020). Myocardial infarction severity stages classification from ecg signals using attentional recurrent neural network. *IEEE Sensors Journal*, 20(15):8711–8720.

Qiu, W., Tang, Q., Liu, J., and Yao, W. (2019). An automatic identification framework for complex power quality disturbances based on multifusion convolutional neural network. *IEEE Transactions on Industrial Informatics*, 16(5):3233–3241.

Rahman, M. O., Augustyniak, P., and Olejarczyk, E. (2024). The qrs detection using the modified pan-tompkins algorithm. In *2024 IEEE International Workshop on Metrology for Industry 4.0 & IoT (MetroInd4. 0 & IoT)*, pages 328–332. IEEE.

Rai, H. M. and Chatterjee, K. (2022). Hybrid cnn-lstm deep learning model and ensemble technique for automatic detection of myocardial infarction using big ecg data. *Applied Intelligence*, 52(5):5366–5384.

Rajinikanth, V., Kadry, S., Taniar, D., Kamalanand, K., Elaziz, M. A., and Thanaraj, K. P. (2023). Detecting epilepsy in eeg signals using synchro-extracting-transform (set) supported classification technique. *Journal of Ambient Intelligence and Humanized Computing*, 14(8):10123–10141.

Ramadevi, P. and Das, R. (2024). An extensive analysis of machine learning techniques with hyper-parameter tuning by bayesian optimized svm kernel for the detection of human lung disease. *IEEE Access*.

Rangayyan, R. M. and Krishnan, S. (2024). Introduction to biomedical signals.

Rao, B. M. and Kumar, A. (2023). Congestive heart failure detection based on electrocardiomatrix method with ecg signal. *Computer Assisted Methods in Engineering and Science*, 30(3):291–304.

Reasat, T. and Shahnaz, C. (2017). Detection of inferior myocardial infarction using shallow convolutional neural networks. In *2017 IEEE region 10 humanitarian technology conference (R10-HTC)*, pages 718–721. IEEE.

Reed, M. J., Robertson, C., and Addison, P. (2005). Heart rate variability measurements and the prediction of ventricular arrhythmias. *Qjm*, 98(2):87–95.

Rehman Javed, A., Jalil, Z., Atif Moqurrab, S., Abbas, S., and Liu, X. (2022). Ensemble adaboost classifier for accurate and fast detection of botnet attacks in connected vehicles. *Transactions on Emerging Telecommunications Technologies*, 33(10):e4088.

Rentero, N., Cividjian, A., Trevaks, D., Pequignot, J., Quintin, L., and McAllen, R. (2002). Activity patterns of cardiac vagal motoneurons in rat nucleus ambiguus. *American Journal of Physiology-Regulatory, Integrative and Comparative Physiology*, 283(6):R1327–R1334.

Reyes, O., Morell, C., and Ventura, S. (2015). Scalable extensions of the relieff algorithm for weighting and selecting features on the multi-label learning context. *Neurocomputing*, 161:168–182.

Riek, N. T., Akcakaya, M., Bouzid, Z., Gokhale, T., Helman, S., Kraevsky-Philips, K., Ji, R. Q., Sejdic, E., Zègre-Hemsey, J. K., Martin-Gill, C., et al. (2024). Ecg-smart-net: A deep learning architecture for precise ecg diagnosis of occlusion myocardial infarction. *arXiv preprint arXiv:2405.09567*.

Rodrigues, T., Samoutphonh, S., Silva, H., and Fred, A. (2021). A low-complexity r-peak detection algorithm with adaptive thresholding for wearable devices. In *2020 25th international conference on pattern recognition (ICPR)*, pages 1–8. IEEE.

Rohila, A. and Sharma, A. (2019). Phase entropy: A new complexity measure for heart rate variability. *Physiological measurement*, 40(10):105006.

Rohila, A. and Sharma, A. (2020). Detection of sudden cardiac death by a comparative study of heart rate variability in normal and abnormal heart conditions. *Biocybernetics and Biomedical Engineering*, 40(3):1140–1154.

Roth, G. A., Mensah, G. A., Johnson, C. O., Addolorato, G., Ammirati, E., Baddour, L. M., Barengo, N. C., Beaton, A. Z., Benjamin, E. J., Benziger, C. P., et al. (2020). Global burden of cardiovascular diseases and risk factors, 1990–2019: update from the gbd 2019 study. *Journal of the American college of cardiology*, 76(25):2982–3021.

Sabor, N., Gendy, G., Mohammed, H., Wang, G., and Lian, Y. (2022). Robust arrhythmia classification based on qrs detection and a compact 1d-cnn for wearable ecg devices. *IEEE Journal of Biomedical and Health Informatics*, 26(12):5918–5929.

Sadhukhan, D., Pal, S., and Mitra, M. (2018). Automated identification of myocardial infarction using harmonic phase distribution pattern of ecg data. *IEEE Transactions on Instrumentation and Measurement*, 67(10):2303–2313.

Sahu, G. and Ray, K. C. (2021). An efficient method for detection and localization of myocardial infarction. *IEEE Transactions on Instrumentation and Measurement*, 71:1–12.

Salo, T. M., Viikari, J. S., Antila, K. J., Voipio-Pulkki, L.-M., Jalonen, J. O., and Välimäki, I. A. (1996). Antihypertensive treatment and heart rate variability in diabetic patients: role of cardiac autonomic neuropathy. *Journal of the autonomic nervous system*, 60(1-2):61–70.

Sankari, Z. and Adeli, H. (2011). Heartsaver: A mobile cardiac monitoring system for autodetection of atrial fibrillation, myocardial infarction, and atrio-ventricular block. *Computers in biology and medicine*, 41(4):211–220.

Scalvini, S., Volterrani, M., Zanelli, E., Pagani, M., Mazzuero, G., Coats, A. J., and Giordano, A. (1998). Is heart rate variability a reliable method to assess autonomic modulation in left ventricular dysfunction and heart failure?: Assessment of autonomic modulation with heart rate variability. *International journal of cardiology*, 67(1):9–17.

Seo, Y., Choi, Y., and Choi, J. (2017). River stage modeling by combining maximal overlap discrete wavelet transform, support vector machines and genetic algorithm. *Water*, 9(7):525.

Shah, S., Gnanasegaran, G., Sundberg-Cohon, J., and Buscombe, J. R. (2009). The heart: Anatomy, physiology and exercise physiology. In *Integrating Cardiology for Nuclear Medicine Physicians: A Guide to Nuclear Medicine Physicians*, pages 3–22. Springer.

Shahbazi, F. and Asl, B. M. (2015). Generalized discriminant analysis for congestive heart failure risk assessment based on long-term heart rate variability. *Computer methods and programs in biomedicine*, 122(2):191–198.

Shahnawaz, M. B. and Dawood, H. (2021). An effective deep learning model for automated detection of myocardial infarction based on ultrashort-term heart rate variability analysis. *Mathematical Problems in Engineering*, 2021(1):6455053.

Sharada, K., Sushma, K., Muthukumaran, V., Mahesh, T., Swapna, B., and Roopashree, S. (2023). High ecg diagnosis rate using novel machine learning techniques with distributed arithmetic (da) based gated recurrent units. *Microprocessors and Microsystems*, 98:104796.

Sharma, D. and Kohli, N. (2024). Delineation of ecg waveform components using encoder-decoder architecture with postprocess algorithm. *International Journal of Information Technology*, 16(6):3425–3435.

Sharma, L. and Sunkaria, R. (2020). Myocardial infarction detection and localization using optimal features based lead specific approach. *Irbm*, 41(1):58–70.

Sharma, L., Tripathy, R., and Dandapat, S. (2015). Multiscale energy and eigenspace approach to detection and localization of myocardial infarction. *IEEE transactions on biomedical engineering*, 62(7):1827–1837.

Sharma, L. D. and Sunkaria, R. K. (2016). A robust qrs detection using novel pre-processing techniques and kurtosis based enhanced efficiency. *Measurement*, 87:194–204.

Sharma, L. D. and Sunkaria, R. K. (2018). Inferior myocardial infarction detection using stationary wavelet transform and machine learning approach. *Signal, Image and Video Processing*, 12(2):199–206.

Sharma, N., Sunkaria, R. K., and Sharma, L. D. (2022). Qrs complex detection using stationary wavelet transform and adaptive thresholding. *Biomedical Physics & Engineering Express*, 8(6):065011.

Sharma, R. R., Kumar, M., and Pachori, R. B. (2019). Joint time-frequency domain-based cad disease sensing system using ecg signals. *IEEE Sensors Journal*, 19(10):3912–3920.

Shimauchi, S., Eguchi, K., Aoki, R., Fukui, M., and Harada, N. (2021). Rr interval estimation for wearable electrocardiogram based on single complex wavelet filtering and morphology-based peak selection. *IEEE Access*, 9:60802–60827.

Silverman, M. E. and Willis Hurst, J. (1992). Willem einthoven—the father of electrocardiography. *Clinical cardiology*, 15(10):785–787.

Singh, M. S., Thongam, K., Choudhary, P., and Bhagat, P. (2024). An integrated machine learning approach for congestive heart failure prediction. *Diagnostics*, 14(7):736.

Singh, P. N. and Mahapatra, R. P. (2024). A novel deep learning approach for arrhythmia prediction on ecg classification using recurrent cnn with gwo. *International Journal of Information Technology*, 16(1):577–585.

Singh, R., Saini, B., and Sunkaria, R. (2018a). Times varying spectral coherence investigation of cardiovascular signals based on energy concentration in healthy young and elderly subjects by the adaptive continuous morlet wavelet transform. *IRBM*, 39(1):54–68.

Singh, R. S., Gelmecha, D. J., Aseffa, D. T., Ayane, T. H., and Sinha, D. K. (2021). Automated detection of normal and cardiac heart disease using chaos attributes and online sequential extreme learning machine. In *Computational Intelligence in Healthcare*, pages 213–234. Springer.

Singh, R. S., Saini, B. S., and Sunkaria, R. K. (2017a). Power spectral analysis of short-term heart rate variability in healthy and arrhythmia subjects by the adaptive continuous morlet wavelet transform. *Applied Medical Informatics*, 39(3-4):49–66.

Singh, R. S., Saini, B. S., and Sunkaria, R. K. (2017b). Power spectral analysis of short-term heart rate variability in healthy and arrhythmia subjects by the adaptive continuous morlet wavelet transform. *Applied Medical Informatics*, 39(3-4):49–66.

Singh, R. S., Saini, B. S., and Sunkaria, R. K. (2018b). Assessment of cardiac heart failure and cardiac artery disease by the higher order spectra. *Biomedical Engineering: Applications, Basis and Communications*, 30(02):1850016.

Singh, R. S., Saini, B. S., and Sunkaria, R. K. (2018c). Classification of cardiac heart disease using reduced chaos features and 1-norm linear programming extreme learning machine. *International Journal for Multiscale Computational Engineering*, 16(5).

Singh, R. S., Saini, B. S., and Sunkaria, R. K. (2018d). Detection of coronary artery disease by reduced features and extreme learning machine. *Clujul Medical*, 91(2):166.

Singh, R. S., Saini, B. S., and Sunkaria, R. K. (2019). Arrhythmia detection based on time–frequency features of heart rate variability and back-propagation neural network. *Iran Journal of Computer Science*, 2:245–257.

Sinha, N. and Das, A. (2020). Automatic diagnosis of cardiac arrhythmias based on three stage feature fusion and classification model using dwt. *Biomedical Signal Processing and Control*, 62:102066.

Sinha, R. (2012). An approach for classifying ecg arrhythmia based on features extracted from emd and wavelet packet domains.

Sood, S., Kumar, M., Pachori, R. B., and Acharya, U. R. (2016). Application of empirical mode decomposition–based features for analysis of normal and cad heart rate signals. *Journal of mechanics in medicine and biology*, 16(01):1640002.

Sopic, D., Aminifar, A., Aminifar, A., and Atienza, D. (2018). Real-time event-driven classification technique for early detection and prevention of myocardial infarction on wearable systems. *IEEE transactions on biomedical circuits and systems*, 12(5):982–992.

Soria, M. L. (2012). Signal processing for automatic heartbeat classification and patient adaptation in the electrocardiogram.

Sörnmo, L. and Laguna, P. (2005). *Bioelectrical signal processing in cardiac and neurological applications*, volume 8. Academic press.

Sridhar, C., Lih, O. S., Jahmunah, V., Koh, J. E., Ciaccio, E. J., San, T. R., Arunkumar, N., Kadry, S., and Rajendra Acharya, U. (2021). Accurate detection of myocardial infarction using non linear features with ecg signals. *Journal of Ambient Intelligence and Humanized Computing*, 12:3227–3244.

Stanfield, C. L., Germann, W. J., Niles, M., and Cannon, J. (2012). Principles of human physiology. *2002*.

Sumalatha, U., Prakasha, K. K., Prabhu, S., and Nayak, V. C. (2024). Deep learning applications in ecg analysis and disease detection: An investigation study of recent advances. *IEEE Access*.

Sun, C., Liu, X., Liu, C., Wang, X., Liu, Y., Zhao, S., and Zhang, M. (2024). Enhanced cad detection using novel multi-modal learning: Integration of ecg, pcg, and coupling signals. *Bioengineering*, 11(11):1093.

Sundarasekar, R., Thanjaivadivel, M., Manogaran, G., Kumar, P. M., Varatharajan, R., Chilamkurti, N., and Hsu, C.-H. (2018). Internet of things with maximal overlap discrete wavelet transform for remote health monitoring of abnormal ecg signals. *Journal of medical systems*, 42:1–13.

Sunkaria, R. K., Saxena, S. C., Vinod, K., and Telles, S. (2012). Hrv dynamics in four yogic-based meditation states using optimised ar model. *International Journal of Biomedical Engineering and Technology*, 9(1):45–59.

Susič, D., Gradišek, A., and Gams, M. (2024). Pcgmix: A data-augmentation method for heart-sound classification. *IEEE Journal of Biomedical and Health Informatics*.

Suyari, H. (2004). Generalization of shannon-khinchin axioms to nonextensive systems and the uniqueness theorem for the nonextensive entropy. *IEEE Transactions on Information Theory*, 50(8):1783–1787.

Talukder, S., Singh, R., Bora, S., and Paily, R. (2020). An efficient architecture for qrs detection in fpga using integer haar wavelet transform. *Circuits, Systems, and Signal Processing*, 39(7):3610–3625.

Thuraisingham, R. A. and Gottwald, G. A. (2006). On multiscale entropy analysis for physiological data. *Physica A: Statistical Mechanics and its Applications*, 366:323–332.

Tripathi, P., Ansari, M., Gandhi, T. K., Mehrotra, R., Heyat, M. B. B., Akhtar, F., Ukwuoma, C. C., Muaad, A. Y., Kadah, Y. M., Al-Antari, M. A., et al. (2022). Ensemble computational intelligent for insomnia sleep stage detection via the sleep ecg signal. *IEEE Access*, 10:108710–108721.

Tripathi, P. M., Kumar, A., Komaragiri, R., and Kumar, M. (2021). A review on computational methods for denoising and detecting ecg signals to detect cardiovascular diseases. *Archives of Computational Methods in Engineering*, pages 1–40.

Tripathy, R., Paternina, M. R., Arrieta, J. G., Zamora-Méndez, A., and Naik, G. R. (2019). Automated detection of congestive heart failure from electrocardiogram signal using stockwell transform and hybrid classification scheme. *Computer methods and programs in biomedicine*, 173:53–65.

Tsipouras, M. G., Exarchos, T. P., Fotiadis, D. I., Kotsia, A. P., Vakalis, K. V., Naka, K. K., and Michalis, L. K. (2008). Automated diagnosis of coronary artery disease based on data mining and fuzzy modeling. *IEEE Transactions on information technology in biomedicine*, 12(4):447–458.

Tueche, F., Mohamadou, Y., Djeukam, A., Kouekeu, L. C. N., Seujip, R., and Tonka, M. (2021). Embedded algorithm for qrs detection based on signal shape. *IEEE Transactions on Instrumentation and Measurement*, 70:1–12.

Umair, M., Chalabianloo, N., Sas, C., and Ersoy, C. (2021). Hrv and stress: A mixed-methods approach for comparison of wearable heart rate sensors for biofeedback. *IEEE Access*, 9:14005–14024.

Urbanowicz, R. J., Meeker, M., La Cava, W., Olson, R. S., and Moore, J. H. (2018). Relief-based feature selection: Introduction and review. *Journal of biomedical informatics*, 85:189–203.

van Dijk, W., Huizink, A. C., Oosterman, M., Lemmers-Jansen, I. L., and de Vente, W. (2023). Validation of photoplethysmography using a mobile phone application for the assessment of heart rate variability in the context of heart rate variability–biofeedback. *Psychosomatic Medicine*, 85(7):568–576.

Varon, C., Lázaro, J., Bolea, J., Hernando, A., Aguiló, J., Gil, E., Van Huffel, S., and Bailón, R. (2018). Unconstrained estimation of hrv indices after removing respiratory influences from heart rate. *IEEE Journal of Biomedical and Health Informatics*, 23(6):2386–2397.

Venkatesh, C., Lavanya, M., Naga Swetha, P., Naganjaneyulu, M., and Mohan Kumar Reddy, K. (2023). A neural network-based cardiovascular disease detection using ecg signals. In *International Conference on Communications and Cyber Physical Engineering 2018*, pages 291–304. Springer.

Vornanen, M., Ryökkynen, A., and Nurmi, A. (2002). Temperature-dependent expression of sarcolemmal k+ currents in rainbow trout atrial and ventricular myocytes. *American Journal of Physiology-Regulatory, Integrative and Comparative Physiology*, 282(4):R1191–R1199.

Wang, D., Tan, D., and Liu, L. (2018). Particle swarm optimization algorithm: an overview. *Soft computing*, 22(2):387–408.

Wang, F., Zeng, X., Wu, C., Wang, B., and Liu, K. R. (2021a). mmhrv: Contactless heart rate variability monitoring using millimeter-wave radio. *IEEE Internet of Things Journal*, 8(22):16623–16636.

Wang, G., Shanker, S., Nag, A., Lian, Y., and John, D. (2024). Ecg biometric authentication using self-supervised learning for iot edge sensors. *IEEE Journal of Biomedical and Health Informatics*.

Wang, H., He, S., Liu, T., Pang, Y., Lin, J., Liu, Q., Han, K., Wang, J., and Jeon, G. (2022). Qrs detection of ecg signal using u-net and dbscan. *Multimedia Tools and Applications*, 81(10):13319–13333.

Wang, H., Zhou, Y., Niu, X., Liu, D., Li, L., Duan, Y., and Wang, Z. (2025). A low-cost and stable dal arrhythmia detection algorithm based on the weak stratification query strategy of morphological statistical features. *Expert Systems with Applications*, 261:125482.

Wang, S. and Chen, H. (2019). A novel deep learning method for the classification of power quality disturbances using deep convolutional neural network. *Applied energy*, 235:1126–1140.

Wang, X., Mao, D., and Li, X. (2021b). Bearing fault diagnosis based on vibro-acoustic data fusion and 1d-cnn network. *Measurement*, 173:108518.

Wang, Y. and Veluvolu, K. C. (2017a). Time-frequency analysis of non-stationary biological signals with sparse linear regression based fourier linear combiner. *Sensors*, 17(6):1386.

Wang, Y. and Veluvolu, K. C. (2017b). Time-frequency analysis of nonstationary biological signals with sparse linear regression based fourier linear combiner. *Sensors*, 17(6):1386.

Weimann, K. and Conrad, T. O. (2024). Federated learning with deep neural networks: A privacy-preserving approach to enhanced ecg classification. *IEEE Journal of Biomedical and Health Informatics*.

Williams, T., Chambers, J., Henderson, R., Rashotte, M., and Overton, J. (2002). Cardiovascular responses to caloric restriction and thermoneutrality in c57bl/6j mice. *American Journal of Physiology-Regulatory, Integrative and Comparative Physiology*, 282(5):R1459–R1467.

Willis Hurst, J. (1997). Abnormalities of the s-t segment—part i. *Clinical cardiology*, 20(6):511–520.

Wood, J. and Barry, D. (1996). Time-frequency analysis of skeletal muscle and cardiac vibrations. *Proceedings of the IEEE*, 84(9):1281–1294.

World Health Organization (2012). Cardiovascular diseases (cvds). Technical Report Fact sheet N^{o}317, World Health Organization.

Xiao, F., Lu, T., Wu, M., and Ai, Q. (2020). Maximal overlap discrete wavelet transform and deep learning for robust denoising and detection of power quality disturbance. *IET Generation, Transmission & Distribution*, 14(1):140–147.

Xie, W., Nie, W., Saffari, P., Robledo, L. F., Descote, P.-Y., and Jian, W. (2021a). Landslide hazard assessment based on bayesian optimization–support vector machine in nanping city, china. *Natural Hazards*, 109(1):931–948.

Xie, X., Liu, H., Shu, M., Zhu, Q., Huang, A., Kong, X., and Wang, Y. (2021b). A multi-stage denoising framework for ambulatory ecg signal based on domain knowledge and motion artifact detection. *Future Generation Computer Systems*, 116:103–116.

Yan, H., Yang, Z., Gao, J., and Wang, X. (2025). Qrs detection in noisy electrocardiogram using an adaptively regularized numerical differentiation method. *Biomedical Signal Processing and Control*, 105:107666.

Yang, Y., Peng, Z., Dong, X., Zhang, W., and Meng, G. (2014). General parameterized time-frequency transform. *IEEE Transactions on Signal Processing*, 62(11):2751–2764.

Yao, L., Liu, C., Li, P., Wang, J., Liu, Y., Li, W., Wang, X., Li, H., and Zhang, H. (2020). Enhanced automated diagnosis of coronary artery disease using features extracted from qt interval time series and st–t waveform. *IEEE Access*, 8:129510–129524.

Yildirim, O., Baloglu, U. B., Tan, R.-S., Ciaccio, E. J., and Acharya, U. R. (2019). A new approach for arrhythmia classification using deep coded features and lstm networks. *Computer methods and programs in biomedicine*, 176:121–133.

Yıldırım, Ö., Pławiak, P., Tan, R.-S., and Acharya, U. R. (2018). Arrhythmia detection using deep convolutional neural network with long duration ecg signals. *Computers in biology and medicine*, 102:411–420.

Yu, G., Yu, M., and Xu, C. (2017). Synchroextracting transform. *IEEE Transactions on Industrial Electronics*, 64(10):8042–8054.

Yu, S.-N. and Lee, M.-Y. (2012). Conditional mutual information-based feature selection for congestive heart failure recognition using heart rate variability. *Computer methods and programs in biomedicine*, 108(1):299–309.

Yuen, B., Dong, X., and Lu, T. (2020). Detecting noisy ecg qrs complexes using waveletcnn autoencoder and convlstm. *IEEE Access*, 8:143802–143817.

Yusuf, S., Rangarajan, S., Teo, K., Islam, S., Li, W., Liu, L., Bo, J., Lou, Q., Lu, F., Liu, T., et al. (2014). Cardiovascular risk and events in 17 low-, middle-, and high-income countries. *New England Journal of Medicine*, 371(9):818–827.

Zahid, M. U., Kiranyaz, S., Ince, T., Devecioglu, O. C., Chowdhury, M. E., Khandakar, A., Tahir, A., and Gabbouj, M. (2021). Robust r-peak detection in low-quality holter ecgs using 1d convolutional neural network. *IEEE Transactions on Biomedical Engineering*, 69(1):119–128.

Zalabarria, U., Irigoyen, E., Martinez, R., and Lowe, A. (2020). Online robust r-peaks detection in noisy electrocardiograms using a novel iterative smart processing algorithm. *Applied Mathematics and Computation*, 369:124839.

Zeng, W., Shan, L., Yuan, C., and Du, S. (2024). Detection of myocardial infarction using shannon energy envelope, fa-mvemd and deterministic learning. *Complex & Intelligent Systems*, 10(4):4755–4773.

Zeng, W. and Yuan, C. (2023). Myocardial infarction detection using itd, dwt and deterministic learning based on ecg signals. *Cognitive Neurodynamics*, 17(4):941–964.

Zeng, W., Yuan, J., Yuan, C., Wang, Q., Liu, F., and Wang, Y. (2021). A novel technique for the detection of myocardial dysfunction using ecg signals based on hybrid signal processing and neural networks. *Soft Computing*, 25(6):4571–4595.

Zhang, D., Jia, X., Ding, H., Ye, D., and Thakor, N. V. (2009). Application of tsallis entropy to eeg: quantifying the presence of burst suppression after asphyxial cardiac arrest in rats. *IEEE transactions on biomedical engineering*, 57(4):867–874.

Zhang, F. and Lian, Y. (2009). Qrs detection based on multiscale mathematical morphology for wearable ecg devices in body area networks. *IEEE Transactions on Biomedical Circuits and Systems*, 3(4):220–228.

Zhang, G., Si, Y., Wang, D., Yang, W., and Sun, Y. (2019). Automated detection of myocardial infarction using a gramian angular field and principal component analysis network. *IEEE Access*, 7:171570–171583.

Zhang, H. and Li, D. (2007). Naïve bayes text classifier. In *2007 IEEE international conference on granular computing (GRC 2007)*, pages 708–708. IEEE.

Zhang, J., Wu, Y., Chen, Y., and Chen, T. (2020a). Health-radio: Towards contactless myocardial infarction detection using radio signals. *IEEE Transactions on Mobile Computing*, 21(2):585–597.

Zhang, M., Wen, Y., Chen, J., Yang, X., Gao, R., and Zhao, H. (2018). Pedestrian dead-reckoning indoor localization based on os-elm. *IEEE Access*, 6:6116–6129.

Zhang, X., Noah, J. A., Dravida, S., and Hirsch, J. (2020b). Optimization of wavelet coherence analysis as a measure of neural synchrony during hyperscanning using functional near-infrared spectroscopy. *Neurophotonics*, 7(1):015010–015010.

Zhang, Z., Yu, Q., Zhang, Q., Ning, N., and Li, J. (2020c). A kalman filtering based adaptive threshold algorithm for qrs complex detection. *Biomedical Signal Processing and Control*, 58:101827.

Zhao, K., Li, Y., Wang, G., Pu, Y., and Lian, Y. (2021). A robust qrs detection and accurate r-peak identification algorithm for wearable ecg sensors. *Science China Information Sciences*, 64(8):182401.

Zhong, S. and Oyadiji, S. O. (2011). Crack detection in simply supported beams using stationary wavelet transform of modal data. *Structural Control and Health Monitoring*, 18(2):169–190.

Zidelmal, Z., Amirou, A., Adnane, M., and Belouchrani, A. (2012). Qrs detection based on wavelet coefficients. *Computer methods and programs in biomedicine*, 107(3):490–496.

Ziemssen, T. and Siepmann, T. (2019). The investigation of the cardiovascular and sudomotor autonomic nervous system—a review. *Frontiers in neurology*, 10:53.